University of Maribor

UNIVERSITY OF THE WEST of SCOTLAND
UWS

10TH International Conference on Sustainable Energy and Environmental Protection:

Modelling and Simulation

(June 27TH - 30TH, 2017, Bled, Slovenia)

(Conference Proceedings)

Editors:
Emeritus Prof. dr. Jurij Krope
Prof. dr. Abdul Ghani Olabi
Prof. dr. Darko Goričanec
Prof. dr. Stanislav Božičnik

University of Maribor Press


University of Maribor Press

10TH International Conference on Sustainable Energy and Environmental Protection

Modelling and Simulation

(June 27TH – 30TH, 2017, Bled, Slovenia)

(Conference Proceedings)

Editors:
Emeritus Prof. dr. Jurij Krope
Prof. dr. Abdul Ghani Olabi
Prof. dr. Darko Goričanec
Prof. dr. Stanislav Božičnik

June 2017

Title: 10TH International Conference on Sustainable Energy and Environmental Protection (June 27TH – 30TH, 2017, Bled, Slovenia) (Conference Proceedings)

Subtitle: Modelling and Simulation

Editors: Emeritus Prof. Jurij Krope, Ph.D. (University of Maribor, Slovenia),
Prof. Abdul Ghani Olabi, Ph.D. (University of the West of Scotland, UK),
Asso. Prof. Darko Goričanec, Ph.D. (University of Maribor, Slovenia),
Asso. Prof. Stanislav Božičnik (University of Maribor, Slovenia).

Review: Prof. Željko Knez, Ph.D. (University of Maribor, Slovenia),
Prof. Niko Samec, Ph.D. (University of Maribor, Slovenia).

Tehnical editors : Jan Perša (University of Maribor Press),
Armin Turanović (University of Maribor Press).

Design and layout: University of Maribor Press

Conference: 10TH International Conference on Sustainable Energy and Environmental Protection

First published in 2017 by
University of Maribor Press
Slomškov trg 15, 2000 Maribor, Slovenia
tel. +386 2 250 42 42, fax +386 2 252 32 45
http://press.um.si, zalozba@um.si

Co-published by
University of Maribor, Faculty of Chemistry and Chemical Engineering
Smetanova ulica 17,2000 Maribor, Slovenia
tel. +386 (0)2 22 94 400, faks + 386 (0)2 25 27 774
http://www.fkkt.um.si, fkkt@um.si

Published: 5. July 2017

CIP - Kataložni zapis o publikaciji
Univerzitetna knjižnica Maribor

551.511.33:519.876.5(082)

INTERNATIONAL Conference on Sustainable Energy and Environmental Protection (10 ; 2017 ; Bled)
Modelling and simulation [Elektronski vir] : (Conference proceedings) / 10th International Conference on Sustainable Energy and Environmental Protection, (June 27th-30th, 2017, Bled, Slovenia) ; [organised by] University of Maribor [and] University of the West of Scotland ; editors Jurij Krope ... [et al.]. - El. zbornik. - Maribor : University of Maribor Press, 2017

Način dostopa (URL): http://press.um.si/index.php/ump/catalog/book/249

ISBN 978-961-286-058-5 (pdf)

doi: 10.18690/978-961-286-058-5
1. Gl. stv. nasl. 2. Krope, Jurij 3. Univerza (Maribor)
COBISS.SI-ID 92432129

ISBN 978-961-286-058-5

DOI: https://doi.org/10.18690/978-961-286-058-5

Price: Free copy

For publisher: Prof. Igor Tičar, Ph.D., rector (University of Maribor)

University of Maribor Press

Preface

The 10th International Conference on Sustainable Energy and environmental Protection – SEEP 2017 was organised on June 27th – 30th 2017 in Bled, Slovenia, by:

- Faculty of Chemistry and Chemical Engineering, University of Maribor, Slovenia,
- University of the West of Scotland, School of Engineering and

The aim of SEEP2017 is to bring together the researches within the field of sustainable energy and environmental protection from all over the world.

The contributed papers are grouped in 18 sessions in order to provide access to readers out of 300 contributions prepared by authors from 52 countries.

We thank the distinguished plenary and keynote speakers and chairs who have kindly consented to participate at this conference. We are also grateful to all the authors for their papers and to all committee members.

We believe that scientific results and professional debates shall not only be an incentive for development, but also for making new friendships and possible future scientific development projects.

General chair
Emeritus Prof. dr. Jurij Krope

10TH INTERNATIONAL CONFERENCE ON SUSTAINABLE ENERGY AND ENVIRONMENTAL PROTECTION (JUNE 27TH – 30TH, 2017, BLED, SLOVENIA), MODELLING AND SIMULATION
J. Krope, A.Ghani Olabi, D. Goričanec & S. Božičnik

University of Maribor Press

Plenary Talk on
The Relation between Renewable Energy and Circular Economy

ABDUL GHANI OLABI - BIBLIOGRAPHY

Prof Olabi is director and founding member of the Institute of Engineering and Energy Technologies (www.uws.ac.uk\ieet) at the University of the West of Scotland. He received his M.Eng and Ph.D. from Dublin City University, since 1984 he worked at SSRC, HIAST, CNR, CRF, DCU and UWS. Prof Olabi has supervised postgraduate research students (10 M.Eng and 30PhD) to successful completion. Prof Olabi has edited 12 proceedings, and has published more than 135 papers in peer-reviewed international journals and about 135 papers in international conferences, in addition to 30 book chapters. In the last 12 months Prof Olabi has patented 2 innovative projects. Prof Olabi is the founder of the International Conference on Sustainable Energy and Environmental Protection SEEP, www.seepconference.co.uk

He is the Subject Editor of the Elsevier Energy Journal https://www.journals.elsevier.com/energy/editorial-board/abdul-ghani-olabi, also Subject editor of the Reference Module in Materials Science and Materials Engineering http://scitechconnect.elsevier.com/reference-module-material-science/ and board member of a few other journals. Prof Olabi has coordinated different National, EU and International Projects. He has produced different reports to the Irish Gov. regarding: Hydrogen and Fuel Cells and Solar Energy.

CORRESPONDENCE ADDRESS: Abdul Ghani Olabi, Ph.D., Professor, University of the West of Scotland, School of Engineering and Computing, D163a, McLachlan Building, Paisley, United Kingdom, e-mail: Abdul.Olabi@uws.ac.uk.

https://doi.org/10.18690/978-961-286-058-5 ISBN 978-961-286-058-5

Available at: http://press.um.si.

10TH INTERNATIONAL CONFERENCE ON SUSTAINABLE ENERGY AND ENVIRONMENTAL PROTECTION (JUNE 27TH – 30TH, 2017, BLED, SLOVENIA), MODELLING AND SIMULATION
J. Krope, A.Ghani Olabi, D. Goričanec & S. Božičnik

University of Maribor Press

Plenary Talk on Energy Footprints Reduction and Virtual Footprints Interactions

JIŘÍ JAROMÍR KLEMEŠ & PETAR SABEV VARBANOV

Increasing efforts and resources have been devoted to research during environmental studies, including the assessment of various harmful impacts from industrial, civic, business, transportation and other economy activities. Environmental impacts are usually quantified through Life Cycle Assessment (LCA). In recent years, footprints have emerged as efficient and useful indicators to use within LCA. The footprint assessment techniques has provided a set of tools enabling the evaluation of Greenhouse Gas (GHG) – including CO_2, emissions and the corresponding effective flows on the world scale. From all such indicators, the energy footprint represents the area of forest that would be required to absorb the GHG emissions resulting from the energy consumption required for a certain activity, excluding the proportion absorbed by the oceans, and the area occupied by hydroelectric dams and reservoirs for hydropower.

An overview of the virtual GHG flow trends in the international trade, associating the GHG and water footprints with the consumption of goods and services is performed. Several important indications have been obtained: (a) There are significant GHG gaps between producer's and consumer's emissions – US and EU have high absolute net imports GHG budget. (b) China is an exporting country and increasingly carries a load of GHG emission and virtual water export associated with consumption in the relevant importing countries. (c) International trade can reduce global environmental pressure by redirecting import to products produced with lower intensity of GHG emissions and lower water footprints, or producing them domestically.

To develop self-sufficient regions based on more efficient processes by combining neighbouring countries can be a promising development. A future direction should be focused on two main areas: (1) To provide the self-sufficient regions based on more efficient processes by combining production of surrounding countries. (2) To develop the shared mechanism and market share of virtual carbon between trading partners regionally and internationally.

CORRESPONDENCE ADDRESS: Jiří Jaromír Klemeš, DSc, Professor, Brno University of Technology - VUT Brno, Faculty of Mechanical Engineering, NETME Centre, Sustainable Process Integration Laboratory – SPIL, Technická 2896/2, 616 69 Brno, Czech Republic, e-mail: klemes@fme.vutbr.cz. Petar Sabev Varbanov, Ph.D., Associate Professor, Brno University of Technology - VUT Brno, Faculty of Mechanical Engineering, NETME Centre, Sustainable Process Integration Laboratory – SPIL, Technická 2896/2, 616 69 Brno, Czech Republic, e-mail: varbanov@fme.vutbr.cz.

https://doi.org/10.18690/978-961-286-058-5 ISBN 978-961-286-058-5

Available at: http://press.um.si.

University of Maribor Press

JIŘÍ JAROMÍR KLEMEŠ - BIBLIOGRAPHY

Head of "Sustainable Process Integration Laboratory – SPIL", NETME Centre, Faculty of Mechanical Engineering, Brno University of Technology - VUT Brno, Czech Republic and Emeritus Professor at "Centre for Process Systems Engineering and Sustainability", Pázmány Péter Catholic University, Budapest, Hungary.

Previously the Project Director, Senior Project Officer and Hon Reader at Department of Process Integration at UMIST, The University of Manchester and University of Edinburgh, UK. Founder and a long term Head of the Centre for Process Integration and Intensification – CPI2, University of Pannonia, Veszprém, Hungary. Awarded by the EC with Marie Curies Chair of Excellence (EXC). Track record of managing and coordinating 91 major EC, NATO and UK Know-How projects. Research funding attracted over 21 M€.

Co-Editor-in-Chief of Journal of Cleaner Production (IF=4.959). The founder and President for 20 y of PRES (Process Integration for Energy Saving and Pollution Reduction) conferences. Chairperson of CAPE Working Party of EFCE, a member of WP on Process Intensification and of the EFCE Sustainability platform.

He authored nearly 400 papers, h-index 40. A number of books published by McGraw-Hill; Woodhead; Elsevier; Ashgate Publishing Cambridge; Springer; WILEY-VCH; Taylor & Francis).

Several times Distinguished Visiting Professor for Universiti Teknologi Malaysia, Xi'an Jiaotong University; South China University of Technology, Guangzhou; Tianjin University in China; University of Maribor, Slovenia; University Technology Petronas, Malaysia; Brno University of Technology and the Russian Mendeleev University of Chemical Technology, Moscow. Doctor Honoris Causa of Kharkiv National University "Kharkiv Polytechnic Institute" in Ukraine, the University of Maribor in Slovenia, University POLITEHNICA Bucharest, Romania. "Honorary Doctor of Engineering Universiti Teknologi Malaysia", "Honorary Membership of Czech Society of Chemical Engineering", "European Federation of Chemical Engineering (EFCE) Life-Time Achievements Award" and "Pro Universitaire Pannonica" Gold Medal.

CORRESPONDENCE ADDRESS: Jiří Jaromír Klemeš, DSc, Professor, Brno University of Technology - VUT Brno, Faculty of Mechanical Engineering, NETME Centre, Sustainable Process Integration Laboratory – SPIL, Technická 2896/2, 616 69 Brno, Czech Republic, e-mail: klemes@fme.vutbr.cz.

https://doi.org/10.18690/978-961-286-058-5 ISBN 978-961-286-058-5

Available at: http://press.um.si.

10TH INTERNATIONAL CONFERENCE ON SUSTAINABLE ENERGY AND ENVIRONMENTAL PROTECTION (JUNE 27TH – 30TH, 2017, BLED, SLOVENIA), MODELLING AND SIMULATION
J. Krope, A.Ghani Olabi, D. Goričanec & S. Božičnik

University of Maribor Press

Plenary Talk on Renewable energy sources for environmental protection

HAKAN SERHAD SOYHAN

Development in energy sector, technological advancements, production and consumption amounts in the countries and environmental awareness give shape to industry of energy. When the dependency is taken into account in terms of natural resources and energy, there are many risks for countries having no fossil energy sources. Renewable and clean sources of energy and optimal use of these resources minimize environmental impacts, produce minimum secondary wastes and are sustainable based on current and future economic and social societal needs. Sun is one of the main energy sources in recent years. Light and heat of sun are used in many ways to renewable energy. Other commonly used are biomass and wind energy. To be able to use these sources efficiently national energy and natural resources policies should be evaluated together with the global developments and they should be compatible with technological improvements. Strategic plans with regard to energy are needed more intensively and they must be in the qualification of a road map, taking into account the developments related to natural resources and energy, its specific needs and defining the sources owned by countries. In this presentation, the role of supply security was evaluated in term of energy policies. In this talk, new technologies in renewable energy production will be shown and the importance of supply security in strategic energy plan will be explained.

CORRESPONDENCE ADDRESS: Hakan Serhad Soyhan, Ph.D., Professor, Sakarya University, Engineering Faculty, Esentepe Campus, M7 Building, 54187 - Esentepe /Sakarya, Turkey, e-mail: hsoyhan@sakarya.edu.tr.

https://doi.org/10.18690/978-961-286-058-5 ISBN 978-961-286-058-5

Available at: http://press.um.si.

University of Maribor Press

HAKAN SERHAD SOYHAN - BIBLIOGRAPHY

Professor at Sakarya University, Engineering Faculty. 50 % fot teaching and the rest for reasearch activities.

Teaching, courses taught:

Graduate courses:

- Combustion technology;
- Modelling techniques;

Undergraduate courses:

- Combustion techniques;
- Internal combustion engines;
- Fire safety.

Tehnical skills and competences professional societies:

- 25 jurnal papers in SCI Index. 23 conference papers;
- Editor at FCE journal. Co-editor at J of Sakarya University;
- Head of Local Energy Research Society (YETA);
- Member od American Society of Mechanical engineers (ASME);
- Member of Turkish Society of Mechanical Engineers (TSME).

CORRESPONDENCE ADDRESS: Hakan Serhad Soyhan, Ph.D., Professor, Sakarya University, Engineering Faculty, Esentepe Campus, M7 Building, 54187 - Esentepe /Sakarya, Turkey, e-mail: hsoyhan@sakarya.edu.tr.

https://doi.org/10.18690/978-961-286-058-5 ISBN 978-961-286-058-5

Available at: http://press.um.si.

University of Maribor Press

Table of Contents

CONFERENCE PROCEEDINGS

10TH INTERNATIONAL CONFERENCE ON SUSTAINABLE ENERGY AND ENVIRONMENTAL PROTECTION (JUNE 27TH – 30TH, 2017, BLED, SLOVENIA), MODELLING AND SIMULATION
J. Krope, A.Ghani Olabi, D. Goričanec & S. Božičnik

University of Maribor Press

New Approximation Algorithms for a Fast Direct Determination of State Functions of Water and Steam

RENÉ HOFMANN, PAUL LINZER, HEIMO WALTER & THOMAS WILL

Abstract This contribution focuses on the definition of new approximation algorithms for the determination of state functions of water/steam. For dynamic simulation of power cycles or industrial processes, one often needs to integrate the nonlinear formulations of the IAPWS-IF97 mathematically. The practicability of the IF97 formulation requires case differences, complex algebraic transformations and a large number of computing operations. The main aspect of this work is to reduce this computation time using a direct method with a given accuracy, and thus to enable extensive dynamic process simulation calculations also for real-time applications using demand-side management and optimal control. Using the industry standard, possible approaches for linear and quadratic approximation of the state functions of water and steam are processed for both the single-phase and the two-phase region. According to the definition of these linear or quadratic approximation functions, investigations are carried out with regard to occurring errors in the variation of the parameters characteristic of the respective approximation. The practicability is demonstrated by a simple illustrative example of a thermal energy steam drum in transient load cycling behaviour using the developed approaches.

Keywords: • thermal engineering • state equations • local approximation functions • dynamic process simulation • comparison IF97 with new approximations •

CORRESPONDENCE ADDRESS: René Hofmann, Prof., Head of Research Area Industrial Energy Systems, TU Wien, Institute for Energy Systems and Thermodynamics, Getreidemarkt 9/302; 1060 Vienna, Austria; email: rene.hofmann@tuwien.ac.at. Paul Linzner, MSc, MS-Thesis-Student, TU Wien, Institute for Energy Systems and Thermodynamics, Getreidemarkt 9/302; 1060 Vienna, Austria; email: lp1000@gmx.at. Heimo Walter, Associate. Prof., Department Thermodynamics and Thermal Engineering, TU Wien, Institute for Energy Systems and Thermodynamics, Getreidemarkt 9/302; 1060 Vienna, Austria; email: heimo.walter@tuwien.ac.at. Thomas Will, MSc, Head of Steam Generation, Steinmüller Engineering GmbH, IHI Group Company, Fabrikstraße 5, 51643 Gummersbach, Germany; email: Thomas.Will@steinmueller.com.

https://doi.org/10.18690/978-961-286-058-5.1 ISBN 978-961-286-058-5

Available at: http://press.um.si.

1 Introduction and problem formulation

It is not unusual to use dimensionless quantities as independent variables when formulating fundamental equations. This path is also carried out in the fundamental equations of the IAPWS-IF97, [8] and [2]. When using the Helmholtz function, the thermodynamic temperature and the specific volume are used as independent variables. All other state variables, such as the specific enthalpy, the specific entropy or the specific heat capacities etc., can be obtained by forming derivatives of the fundamental equation and corresponding combination of the obtained expressions. The IAPWS-IF97 formulation published by the International Association for the Properties of Water and Steam [8] and programmed e.g. in [7], is used in the industry as standard for the calculation of the state variables of water and water vapour and is based on the Helmholtz function. In practice, special attention must be given to

- The calculation of the state variables which requires a large number of calculation operations and case distinctions.
- Some relationships are not a direct state equation. It can only be handled by iterative calculations. This also means high compu-tational expenditure.
- The state equations are in a format which makes it difficult to insert them into other relationships or algebraic transformations.

by using the IAPWS-IF97 formulation.

Thus mathematical approaches for the avoidance of these limitations are needed. However, it should be noted in particular that such equations only ever apply in a defined mathematical area in order to meet accuracy requirements for the calculation to be obtainable.

Before presenting the approximations, short explanations with relevant literature are given for an advantageous calculation of the state variables of water and water vapour. Detailed explanations on numerous representations of the state variables of water and water vapour and the partial derivatives required are presented in [1]. A special method for calculating the state variables using Taylor series expansion is illustrated in [2]. This publication deals in particular with the calculation speed and an accuracy analysis in comparison with an industrial standard. Some aspects of linear interpolation when using steam traps are given in [3]. In [4] comments on linear interpolation of fixed support points for dynamic modelling of steam processes can be found. Furthermore, explicit statements regarding the step size and the resulting accuracy are provided. In [5] an interpolation technique is applied to shorten the computation time with special consideration of the choice of the grid in the p,T plane for different state variables.

2 Local approximation of the state equations

The thermal state equation can be used as a starting point for the approximation considerations. This equation describes a relationship between pressure p, specific

volume *v* and temperature *T*. Mathematical relationships between the state variables *p* (pressure), *T* (thermodynamic temperature), *v* (specific volume), *u* (specific internal energy), *h* (specific enthalpy), and *x* (vapour quality) are developed. Since the possible state equations are characterized by local validity, their boundaries can thus be regarded as boundaries for the scope of the respective approximation functions. The following derivations are based on the considerations of [9].

2.1 Linear Approximation in the two-phase-region

The starting point of the calculations for the approximation in the two-phase region is a pressure p_0. To this initial state 0 a saturation temperature $T_{s0} = T_s(p_0)$ is dedicated, which can be calculated via IAPWS-IF97. Furthermore, this state 0 is assigned as saturation state for the specific enthalpy and the specific volume:

- a specific enthalpy of the boiling water $h'_0 = h'(p_0)$,
- a specific enthalpy of the saturated steam $h''_0 = h''(p_0)$,
- a specific volume of the boiling water $v'_0 = v'(p_0)$,
- a specific volume of saturated steam $v''_0 = v''(p_0)$.

State 1 is characterized by a pressure $p_1 = p_0 + \Delta p$ with $\Delta p < 22.064\ MPa - p_0$ and a corresponding boiling temperature $T_{s1} = T_s(p_1)$, with $h'_1 = h'(p_1)$, $h''_1 = h''(p_1)$, $v'_1 = v'(p_1)$, and $v''_1 = v''(p_1)$.

The approximation of the boiling and saturation states in the pressure interval [p_0, p_1] is defined by

$$T_{s,n}(p) = G_0 p + H_0 \tag{1}$$

$$h'_n(p) = G_1 p + H_1 \tag{2}$$

$$h''_n(p) = G_2 p + H_2 \tag{3}$$

$$v'_n(p) = G_3 p + H_3 \tag{4}$$

$$v''_n(p) = G_4 p + H_4 \tag{5}$$

whereby the occurring constants G_0 to G_4 or H_0 to H_4 are defined by

$$G_0 = \frac{T_{s1} - T_{s0}}{p_1 - p_0}, \tag{6}$$

$$H_0 = T_{s0} - G_0 p_0, \tag{7}$$

$$G_1 = \frac{h'_1 - h'_0}{p_1 - p_0}, \tag{8}$$

$$H_1 = h_0' - G_1 p_0, \tag{9}$$

$$G_2 = \frac{h_1'' - h_0''}{p_1 - p_0}, \tag{10}$$

$$H_2 = h_0'' - G_2 p_0, \tag{11}$$

$$G_3 = \frac{v_1' - v_0'}{p_1 - p_0}, \tag{12}$$

$$H_3 = v_0' - G_3 p_0, \tag{13}$$

$$G_4 = \frac{v_1'' - v_0''}{p_1 - p_0}, \tag{14}$$

$$H_4 = v_0'' - G_4 p_0. \tag{15}$$

The determination is made from the boiling and saturation states $T_{s0}, h_0', h_0'', v_0', v_0''$ associated with a pressure p_0 as well as the associated boiling and saturation states at pressure $p_1 = p_0 + \Delta p$; each is determined using the IAPWS-IF97 formulation. An arbitrary state point in the two-phase region is already uniquely determined by pre-setting of the pressure p and the quality x. The interpolation domain for applying the equations to linear approximation is thus described by $x \in [0,1]$ and $p \in [p_0, p_1]$.

Substituting the results obtained from Equation (2) and (3) yields an interpolation value for the specific enthalpy

$$hh_n(x,p) = x(G_2 p + H_2) + (1-x)(G_1 p + H_1) = p\big(G_1 + x(G_2 - G_1)\big) + H_1 + x(H_2 - H_1). \tag{16}$$

Substituting the expressions known from Equation (4) and (5) yields for the specific volume v

$$v_n(x,p) = x(G_4 p + H_4) + (1-x)(G_3 p + H_3) = p\big(G_3 + x(G_4 - G_3)\big) + H_3 + x(H_4 - H_3). \tag{17}$$

The approximated internal energy is calculated by substituting Equation (16) and (17) in

$$u_n(x,p) = h_n(x,p) - p v_n(x,p). \tag{18a}$$

Thus

$$u_n(x,p) = x(G_2p + H_2) + (1-x)(G_1p + H_1) - p\big(x(G_4p + H_4) + (1-x)(G_3p + H_3)\big) = x\big((G_2p + H_2) - p(G_4p + H_4)\big) + (1-x)\left((G_1p + H_1) - p(G_3p + H_3)\right) \quad (18b)$$

is obtained. An approximation value for the boiling temperature within the interpolation domain is obtained by using the expressions from Equation (6) and (7) with

$$T_{s,n}(x,p) = T_{s,n}(p) = G_0p + H_0, \quad (19)$$

which corresponds to the independence of the steam quality to the already known Equation (1).

2.2 Quadratic Approximation in the two-phase-region

In case of the quadratic approximation, an additional pressure level

$$p_{1/2} = p_0 + \tfrac{1}{2}\Delta p \quad (20)$$

between state 0 and 1 is introduced to obtain a boiling temperature of $T_{s1/2} = T_s\big(p_{1/2}\big)$. An arbitrary function curve $f(x)$ defined in the interval $[x_0, x_1]$, with three supporting points $x_0, x_{1/2}, x_1$, valid for $x_0 < x_{1/2} < x_1$, is specified for the quadratic approximation and is written as follows

$$\begin{bmatrix} f(x_0) \\ f\big(x_{1/2}\big) \\ f(x_1) \end{bmatrix} = \begin{bmatrix} x_0^2 & x_0 & 1 \\ x_{1/2}^2 & x_{1/2} & 1 \\ x_1^2 & x_1 & 1 \end{bmatrix} \begin{bmatrix} a \\ b \\ c \end{bmatrix} \quad (21)$$

In this case, the equation system $\boldsymbol{\lambda} = \boldsymbol{X^{-1}} \cdot \boldsymbol{f}$ has to be solved for the parameter vector $\boldsymbol{\lambda}$. For more detailed information on the values of the inverse matrix as well as the comprehensively mathematical terms of the components of the parameter vector it is referred to [10].

2.3 Linear Approximation in the single-phase-region

In the single-phase region, the quality x is dispensable. Thus, five relevant state variables remain. These are $p, T, v, u,$ and h. The starting point of the calculations for the approximation in the single-phase region is any point within the *p,T*-region which is characterized by a pressure p_0 and a temperature T_0. To this state 0

- a specific enthalpy $h_0 = h(p_0, T_0)$,
- a specific volume $v_0 = v(p_0, T_0)$ and
- a specific internal energy

$$u_0 = u(p_0, T_0) = h_0 - p_0 v_0 \tag{22}$$

is assigned, which can be evaluated via IAPWS-IF97. The starting point for the two-dimensional approximation of the specific enthalpy and internal energy is

$$h_n(p, T) = h_0 + \lambda_1 (T - T_0) + \lambda_2 (p - p_0) \tag{23}$$

$$u_n(pv, p) = u_0 + \lambda_3 (pv - p_0 v_0) + \lambda_4 (p - p_0) \tag{24}$$

The approximation functions have to fulfil the following three boundary conditions:

- $h_n(p_0, T_0) = h_0, u_n(p_0 v_0, p_0) = u_0$ at state 0
- $h_n(p_0, T_1) = h_1, u_n(p_0 v_1, p_0) = u_1$ at state 1
- $h_n(p_2, T_2) = h_2, u_n(p_2 v_2, p_2) = u_2$ at state 2.

Writing the two approximation formulas from (23) and (24) in the following form

$$u_n = Apv + Bp + C, \tag{25}$$

$$h_n = DT + Ep + F. \tag{26}$$

Taking into account the definition for the specific enthalpy, it is immediately apparent that three equations are available as relations between the five relevant states. If two quantities are known, the remaining three state variables can be calculated from equation (22), (25), and (26). This notation is also advantageous for programming. The constants occurring in (25) and (26) are obtained by

$$A = \frac{1}{p_0} \frac{u_1 - u_0}{v_1 - v_0} \tag{27}$$

$$B = \frac{(u_2 - A p_2 v_2) - (u_0 - A p_0 v_0)}{p_2 - p_0} \tag{28}$$

$$C = u_0 - A p_0 v_0 - B p_0 \tag{29}$$

$$D = \frac{h_1 - h_0}{T_1 - T_0} \tag{30}$$

$$E = -D \frac{T_2 - T_0}{p_2 - p_0} \tag{31}$$

$$F = h_0 - D T_0 - E p_0. \tag{32}$$

To check the phase state, an approximated function for the saturation temperature is introduced as a function of the pressure

$$T_{S,n}(p) = Gp + H \tag{33}$$

with

$$G = \frac{T_{S,1} - T_{S,0}}{p_1 - p_0} \tag{34}$$

$$H = T_{s,0} - Gp_0. \tag{35}$$

The saturation temperatures $T_{S,0}$ and $T_{S,1}$ with regarding pressures p_0 and $p_1 = p_0 + \Delta p$ are determined using the IAPWS-IF97.

3 Error and sensitivity analysis

In the following, the approaches of the approximation in the single and two-phase region are compared. Characteristic deviations of the approximate state variables are determined over the entire relevant pressure area within the region.

3.1 Validity Properties

Based on a sensitivity analysis, the validity of errors is shown. The aim is to determine the corresponding relative pressure difference $\Delta p_{zul}/p_o$ for a given pressure level p_o and a permissible error tolerance Δ_{zul}.

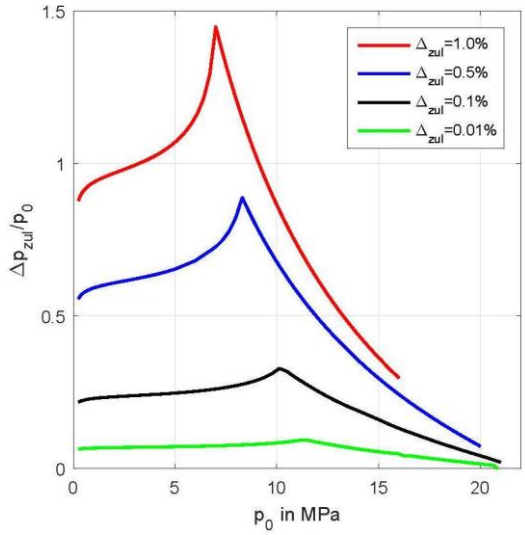

Figure 1. Validity ranges for error retention for enthalpy; lin. approx. variation of □zul; two-phase-region.

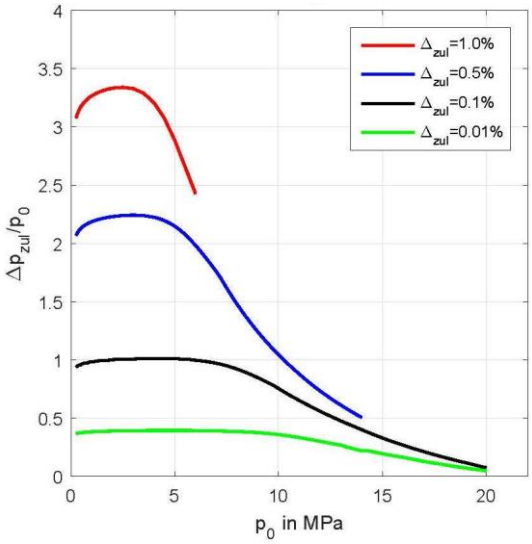

Figure 2. Validity ranges for error retention for enthalpy; quadr. approx. variation of □zul; two-phase-region.

A larger $\Delta p_{zul}/p_o$-value is evaluated by applying a square approximation in the two-phase region, thus a factor of 2 is obtained between the values of linear and quadratic approximation. In Figure 1 and Figure 2 the ranges of validity for error retention by variation of the permissible error tolerance for the enthalpy at linear and quadratic approximation is shown. The resulting peaks in Figure 1 are obtained by both boundary curves for boiling water and saturated steam to maintain the required error tolerance. In Figure 3 the relative deviation of the approximated enthalpy in the single-phase region for superheated steam at $h_0 = 3000kJ/kg$, $h_1 = 3500kJ/kg$, $p_0 = 8MPa$, and $p_2 = 14MPa$ is presented.

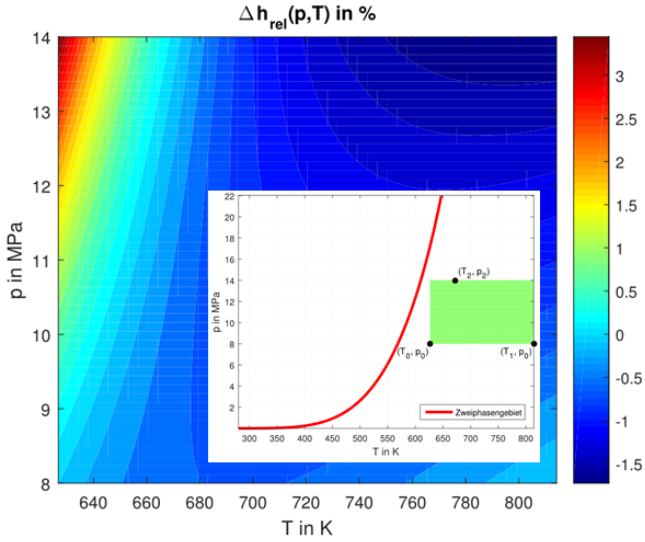

Figure 3. Relative deviation of approximated enthalpy; single-phase-region.

4 Illustrative example of a steam drum

On the basis of a transient drum model of a natural circulation steam generator, the developed approximations for the two-phase region will be discussed. According to the parameters shown in Figure (4) the pressure profile $p(t)$ of the drum, the feedwater mass flow $\dot{m}_{Spw}$, the blowdown mass flow $\dot{m}_{Ab}$, the drum level l, the drum geometry, the water and steam properties and the drum material are assumed to be known. A feedwater mass flow $\dot{m}_{Spw}$ is fed to the steam drum, while the blowdown mass flow $\dot{m}_{Ab}$ and the steam mass flow $\dot{m}_D$ leaves the drum. The heating is effected by applying a heat flow $\dot{Q}$ to the heating surfaces. The medium in the interior of the drum is in the boiling state associated with the pressure $p(t)$; the drum level l, the distribution in boiling water $m_{W,Tr}$ and saturated water steam $m_{D,Tr}$.

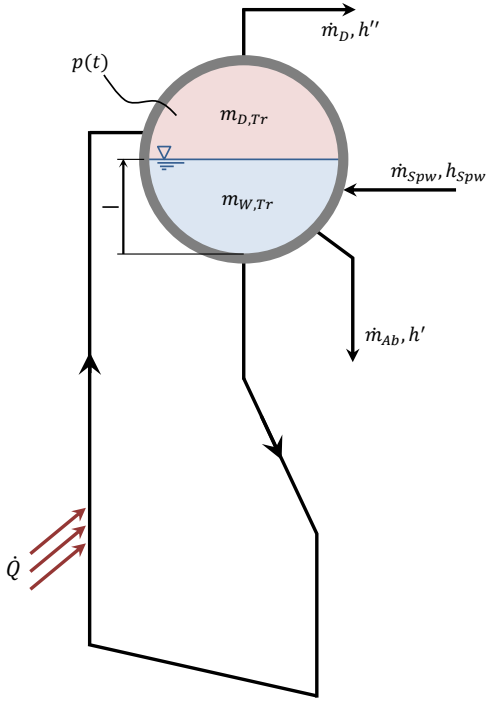

Figure 4. Principle of a steam drum in a natural circulation system.

The extracted saturation steam $\dot{m}_D$ leaves the drum with the enthalpy h'' and the blowdown water with an enthalpy h'. The enthalpy of the feedwater is h_{Spw}. The following explanations are largely based on the equations described in [6]. Governing equations for the mass and energy balance for the steam drum gives

$$\frac{dm_{W,Tr}}{dt} + \frac{dm_{D,Tr}}{dt} = \dot{m}_{Spw} - \dot{m}_D - \dot{m}_{Ab}, \tag{36}$$

and

$$\frac{d(m_{W,Tr}h')}{dt} + \frac{d(m_{D,Tr}h'')}{dt} + m_{St}c_{St}\frac{dT_s}{dt} = \dot{Q} + V_{Tr}\frac{dp}{dt} + \dot{m}_{Spw}h_{Spw} - \dot{m}_D h'' - \dot{m}_{Ab}h' \tag{37}$$

For a given pressure profile $p(t)$ the pressure gradient can be calculated with

$$\frac{dp}{dt} = [t^3 \quad t^2 \quad t \quad 1] \begin{bmatrix} -6.004\times10^{-11}\,\frac{bar}{s^4} \\ 6.5094\times10^{-8}\,\frac{bar}{s^3} \\ 4.0928\times10^{-5}\,\frac{bar}{s^2} \\ 9.4697\times10^{-3}\,\frac{bar}{s} \end{bmatrix} \tag{38}$$

with $t \in [0, 1500]$s, $h = const.$ and $\dot{m}_{Spw} \in [1, 20]\ t\ /\ h$. For the calculation of the required heatflow $\dot{Q}$, and the resulting steam mass flow $\dot{m}_D$ Equation (36) will be inserted in Equation (37). In Figure (5) and (6), the time dependent calculated profile of the steam mass flow and the heat flow are compared, based on the water and steam properties according to IF97, the linear approximation, and the quadratic approximation. When applying the linear approximation in the two-phase region, a characteristic pressure difference $\Delta p/p_0 = 0.1$ was used. A significant advantage by using the approximation is that the saturation variables according to IF97 need only be calculated at 32 points. This means that the approximation instead of IF97 is applied to points which are not support points for the approximation, which requires considerably less computation time compared to IF97 evaluations. Figures (5) and (6) show the corresponding results for the quantities to be determined. From this it is very clear that an integral error results within a pressure range $[p_0, p_0 + \Delta p]$. On the other hand, if the quadratic approximation presented in Section 2.2 is applied to calculate the mass flow of steam and the heat flow with the same characteristic pressure difference of 0.1, the superiority is clearly demonstrated. The error analysis for the steam mass flow $\dot{m}_D$ and the heat flow $\dot{Q}$ with a linear approximation of the mass values and $\Delta p/p_0 = 0.1$ calculates a relative deviation within ±2% for $\dot{m}_D$ and ±3.5% for $\dot{Q}$. Compared to this the quadratic approximation lies within ±0.05% for $\dot{m}_D$ and ±0.1% for $\dot{Q}$. The better accuracy is, however, bought by an additional support point, at which the computer-intensive evaluations according to IF97 have to be carried out. All evaluations were carried out with the same time step of 1s. Table 1 shows the calculation times of the different variants and the resulting time savings when applying the approximations in the two-phase region compared to the exact calculation according to IF97. Regardless of the approximation used, the calculation time is in each case reduced by more than 50%.

Table 1. Comparison of the calculation time for the application example steam drum.

Variant	Calculation Time	Reduction
Exact (IF97)	25.24 s	-
Linear Approx.	9.77 s	61.3%
Quadratic Approx.	11.03 s	56.3%

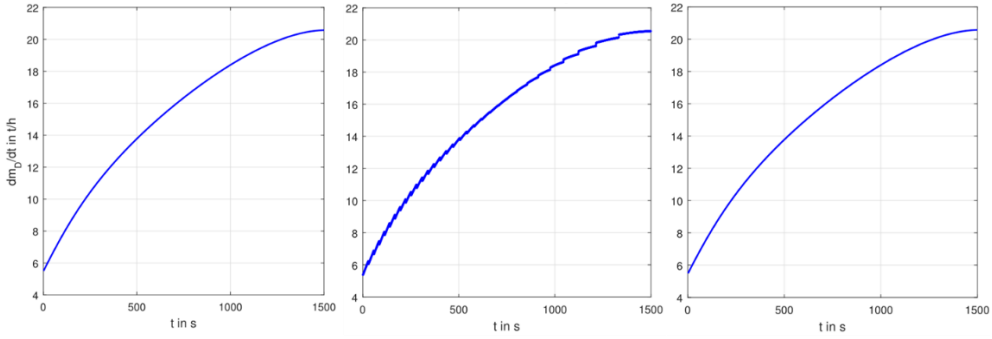

Figure 5. Comparison of the results for the steam mass flow, [left] exact calculation (IF97), [middle] linear and [right] quadratic approximation.

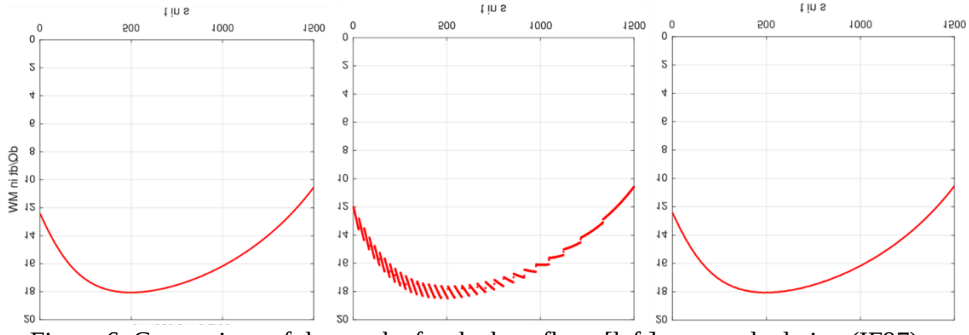

Figure 6. Comparison of the results for the heat flow, [left] exact calculation (IF97), [middle] linear, and [right] quadratic approximation.

5 Conclusion

In the present work, new approximation algorithm for a fast calculation of the properties for water and steam were presented. As a basis for the new algorithms the IAPWS-IF97 formulation for calculating the properties of water and steam was used. For the approximation of the state properties a linear and a quadratic approach was used for both the single- and the two phase region. A comparison of the calculation time of the new approximations with the IAPWS-IF97 formulation has shown that a time saving of more than 50% can be achieved. An error analysis of the new approaches has shown that the quadratic approach has a better representation of the state properties compared to the linear approach but needs more computation time. At the end of the article the application of the new approximations was demonstrated with a transient example. This direct method for calculating the properties for water and steam provides the possibility to enable extensive dynamic process simulation calculations also for real-time applications using demand-side management and optimal control.

Acknowledgements

The authors would like to thank the company Steinmüller Engineering GmbH, for the basic considerations on the approximations as well as FDBR e.V. for the provided chapters from the handbook "Wärme- und Strömungstechnik".

List of symbols

Latin Symbols

a	[~] various constants of approx. functions
A	[−] constant of approx. function
b	[~] various constants of approx. functions
B	[m³/kg] constant of approx. function
c	[~] various constants of approx. functions
c	[J/(kg K)] specific heat capacity
C	[J/kg] constant of approx. function
D	[J/(kg K)] constant of approx. function
E	[m³/kg] constant of approx. function
f, f	[~] function/function value
F	[J/kg] constant of approx. function
G	[~] various constants of approx. functions
h	[J/kg] specific enthalpy
l	[m] drum level
H	[~] various constants of approx. functions
i	[−] (summation-)Index
m	[kg] mass
$\dot{m}$	[kg/s] mass flow
n	[−] endvalue summation index
p	[Pa] pressure
q	[J/kg] specific heat
Q	[J] heat
$\dot{Q}$	[W] heat flow
T	[K] temperature
u	[J/kg] specific internal energy
v	[m³/kg] specific volume
x	[–] steam content
x	[~] independet value
X	[~] value matrix

Greek Symbols

Δ	prefix for deviation or deviation, difference
ε	value for termination criterion
λ	various constants of approx. functions
λ	various vectors with constants of approx. functions

Index Superscript

´	saturated liquid phase
´´	saturated steam phase

Index Subscript

0	variable at state
1	variable at initialstate
1, 2, 3	component of vectorial quantity
1, 2, 3, 4	indexes to distinguish constants
½	variable at state
2	variable at endstate
Ab	blowdown
D	steam
IF97	evaluation according to IF97
n	approximating value
s	boiling state
Spw	feed water
St	steel
Tr	steam drum
zul	permissible value

References

[1] Ponweiser, K.; Walter, H.: Die thermo-dynamischen Zustandsgrößen von Wasser & Wasserdampf und deren partielle Ableitungen in unterschiedlichen Darstellungsformen. BWK 46 (1994), No.1/2, pp. 53–55.

[2] Miyagawa, K.; Hill P. G.: Rapid and Accurate Calculation of Water and Steam Properties Using the Tabular Taylor Series Expansion Method. Journ. of Engineering for Gas Turbines and Power 123 (2001), no. 3, pp.707–712.

[3] Baehr, H. D.: Zur Interpolation in Dampftafeln. BWK 26 (1974), no.5, pp. 211–212.

[4] van der Looij, J.: Zweckmässige Formulierung der Eigenschaften von Wasser und Wasserdampf für die dyn. Modellbildung von Dampfkraft-prozessen. BWK 38 (1986), no.12, pp. 545–546.

[5] Pfleger, E.: Optimale Stoffwertberechnung von Wasser/Wasserdampf. BWK 40 (1988), no.10, pp. 405–408.

[6] FDBR Handbook Wärme- und Strömungs-technik. FDBR e.V. (Hrsg.), Chapter 10.3, 2016.

[7] Freiler, P.: Programmierung der Zustands- und Transportgrößen von Wasser und Wasserdampf, TU-Wien, MS-Thesis, 2015.

[8] Wagner, W.; Kruse, A.; Kretzschmar, H.-J.: Prop. of water and steam. Berlin: Springer, 1998.

[9] Will, T.: Approximation der Zustands-gleichungen für Wasser/Dampf nach IAPWS-IF97 durch Näherungsfunktionen. Steinmüller Engineering GmbH, 2009 (internal document).

[10] Linzner, P.: Approximation der Zustands-gleichungen von Wasser und Wasserdampf; TU Wien, MS-Thesis, 2017.

10TH INTERNATIONAL CONFERENCE ON SUSTAINABLE ENERGY AND ENVIRONMENTAL PROTECTION (JUNE 27TH – 30TH, 2017, BLED, SLOVENIA), MODELLING AND SIMULATION
J. Krope, A.Ghani Olabi, D. Goričanec & S. Božičnik

University of Maribor Press

CFD Modelling of a Multipass Heat Pipe Based Heat Exchanger

AMISHA CHAUHAN, SULAIMAN ALMAHMOUD & HUSSAM JOUHARA

Abstract The utilisation of multipass systems is implemented in a number of industries ranging from passive cooling systems in engines to power transmission. Many variables can alter performance of a multipass heat exchanger such as pipe arrangement, working fluid, number of passes etc.... The principle behind the addition of thermosyphons in a multipass arrangement is to increase the convective heat transfer to the thermosyphons. In effect, this will encourage an even thermal distribution throughout the thermosyphon sections during operation. Numerical and experimental studies have validated the increase in convective heat transfer when compared against single pass flow streams in other heat exchanger applications. Recently the experimentation of thermosyphon based multipass heat exchangers has been conducted on a small scale model, to study the influence of hot and cold streams. Subsequent research has been conducted to identify the thermal characteristics of the thermosyphon in a multipass application. The arrangement of thermosyphons and baffles can influence the heat transfer of surrounding thermosyphons, and can physically change the air distribution through each pass. The validation the system will characterise the thermal performance with copper based heat pipes charged with water when utilised in a multipass arrangement coupled with a single pass water cooling system.

Keywords: • CFD • multi pass • heat exchanger • pipe • thermosyphon •

CORRESPONDENCE ADDRESS: Amisha Chauhan, Brunel University London, Institute of Energy Futures, College of Engineering, Design and Physical Sciences, RCUK Centre for Sustainable Energy Use in Food Chains, Uxbridge, Middlesex, UB8 3PH, United Kingdom, e-mail:amisha.chauhan. Sulaiman Almahmoud, Brunel University London, Institute of Energy Futures, College of Engineering, Design and Physical Sciences, RCUK Centre for Sustainable Energy Use in Food Chains, Uxbridge, Middlesex, UB8 3PH, United Kingdom, e-mail: Sulaiman.Almahmoud@brunel.ac.uk. Hussam Jouhara, Brunel University London, Institute of Energy Futures, College of Engineering, Design and Physical Sciences, RCUK Centre for Sustainable Energy Use in Food Chains, Uxbridge, Middlesex, UB8 3PH, United Kingdom, e-mail: Hussam.Jouhara@brunel.ac.uk.

https://doi.org/10.18690/978-961-286-058-5.2 ISBN 978-961-286-058-5

Available at: http://press.um.si.

1 Introduction

The addition of passes within a system have been utilised in a number of heat exchangers such as shell and tube structures [1]. The addition of passes in heat pipe based heat exchangers theoretically will increase the thermal capacity to an already effective system with minimal maintenance [2]. The principle of a heat pipes is based on the effect of evaporation and condensation as heat is applied to the condenser, the working fluid inside will boil causing low density fluid to rise to the evaporator section. The latent heat is absorbed in the evaporator and the fluid returns to the condenser. The addition of heat pipes are commonly implemented in waste heat recovery applications with studies regarding fill ratios[3] and effect of inclination angles [4]. The studies around key variables offer an insight into the variation in thermal performance and the identification of potential uses. The CFD simulation around heat pipes has been heavily focused around simulating the difficult multiphase process within the heat pipe and the applicability of heat pipes within different industries but the effect of passes has not been thoroughly investigated. A pivotal point within the simulation of heat pipes, was the successful modelling of geyser boiling and multiphase process as modelled by *Jouhara et al* [5] and *Fadhl et al* [6] respectively. The increasing potential and advancements in technology has allowed the progression of multiphase modelling, allowing the study of key variables that directly influence the performance of heat pipes. The simulations around singular heat pipes are vast, but simulations based around Heat Pipe Heat Exchangers (HPHE) are scarce. The application of HPHE in a practical and industrial application is steadily increasing with the utilisation of simulation techniques. The effects studied in single pipe models largely influence the heat pipe configuration and composition. Studies investigating fill ratios with regards to dry out can heavily influence larger scale systems, with the fill ratio and possibility of dry out heavily affecting the thermal performance of the system. Even though the studies of these variables directly influence the performance of HPHE, the amount of simulations does not reflect this. External influences need to be considered with HPHE, such as flow direction and amount of passes. The effect of passes has been widely studied but has been simulated in select HPHE studies. *Ramos et al* [7] investigated the effects of a single pass air to water cross flow heat pipe heat exchanger. The simulation is based on the previous experiment conducted by *Mroue et al* [8] based on a two pass heat pipe heat exchanger. Both systems were simulated under steady state profiles with similar assumptions. Both simulations highlight the improved thermal performance. Both simulations are based on the similar test rings with the only variation being the increase in heat transfer area due to the addition of a secondary pass. The simulation results from the addition of passes shows promising results as predicted, but the system itself had a maximum length of 2.6m of 6 heat pipes, which in comparison is a large system considering it operates on two passes, with a small amount of heat pipes. The following findings highlight a proposed multi-pass system presents a more compact system (maximum system interior length=342mm) whilst maintaining the thermal performance of the multipass schematic. The following simulation results represent the operation of a system ranging from one, three and five passes, with a variation in flow rate in the condenser section.

2 CFD method

The geometry for the model is based on the experimental work conducted on the system. The heat pipes within the system are set as superconductor with a set temperature in the evaporative and conductive sections. The investigation is based on the thermal characteristics of the thermosyphon and the associated effects with a varying air/water inlet and the increase in the number of passes.

2.1 Geometry and Mesh

The geometry was constructed in ANSYS Design-modeller as shown in figure 2. The figure highlights the geometry proposed for the five pass system; each pass geometry has been altered for each configuration as shown in figure 1.

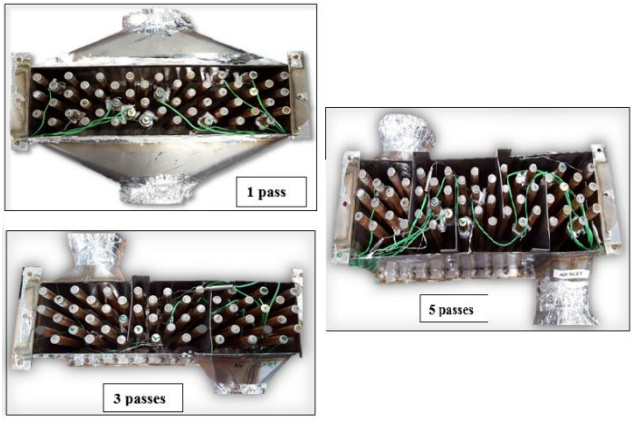

Figure 1: Pass Configuration and Schematic

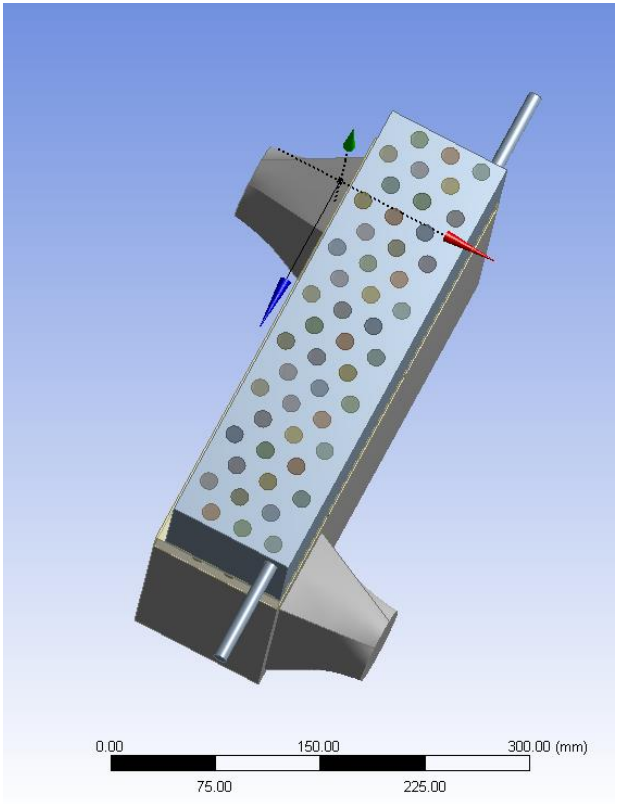

Figure 2: Proposed Geometry

2.2 Boundary Conditions and Numerical Method

The modelling of heat transfer systems is a highly complex task, with a number of external influences that can affect the heat transfer. In an ideal world, the most informative and desired simulation technique would be a *Direct Numerical Simulation* (DNS) but the computational power needed is far beyond the resources of industrial application. The addition of *Reynolds Averaged Navier-Stokes* (RANS) Simulations allows a simplified visualisation during operation but also the interaction between the fluid and heat pipe. The simulation for the multi-pass system was conducted using ANSYS Fluent with the utilisation of the *k-epsilon* realizable model using scalable wall functions. The simulation was conducted under steady state conditions with a pressure-velocity coupling and a SIMPLE and second order discretization method.

2.3 Assumptions

The following assumptions were made prior to the simulation:

a) A constant thermal conductivity was applied to all the heat pipes
b) The heat pipes were simulated as superconductors based on the copper heat pipes within the system
c) A constant inlet velocity in the evaporator section was applied throughout all pass configurations.
d) The only variable being the water flow located in the condenser section as represented
e) The adiabatic section has been assigned as a zero heat flux region.
f) The walls enclosing the heat pipe domain are assumed to be adiabatic, and a zero heat flux wall boundary conditions have been assigned accordingly.

3 Results and discussions

The placement of heat pipes has been placed in the optimum location by using an optimum staggered position. The position of staggered heat pipes has been calculated to ensure the optimum thermal distribution with each flow profile and baffle configuration. Three selections of passes were chosen to investigate the influence of passes. The subsequent simulations were conducted on one, three and five pass configurations with a constant selection of varied velocities applied to all pass configurations.

3.1 Effect of Flow Rate

The effect of the flow rate was the major variable within the study. The water flow rate was simulated through high (0.02 l/s) and low (0.01l/s) water flow rates.

3.1.1 Effect of Water flow at 0.01l/s

Figure 2 highlights the overview of outlet temperature at 0.01 l/s. It is evident that the addition of passes reduces the air outlet temeperature indicating the increased performance of the mutlipass system. The addition of passes increases the heat transfer area and thus improving the performance of the system. From figure 2, its evident that the increase in passes, decreases the air outlet temperature, the counter current of the water flow increases as a result highlighting the success of additional passes. The overall difference temperature difference between the air outlet temperature from the single pass to a five pass was approximately 16K decrease, whereas the water temperature was 2.4K. Although the water decrease is significantly smaller compared to the air outlet value, the differences in values can be due to the variation in data obtained to verify the system. The inlet temperature values used for the water varied by approximately 2.2K which caused a small amount of variance within the simulation data. By taking into account the

variation in data, the corresponding outlet temperature shows a decrease, highlighting the success of additional passes.

3.1.2 Effect of Water Flow at 0.02l/s

Theoretically the increase in flow rate should increase the heat transfer coefficient within the system, which is highlighted in figure 3. The increase in passes further decreased the air temperature by approximately 25.7K. In comparison to the low flow rate, this is a significantly higher temperature difference, highlighting the effectiveness of a flow rate increase. The initial predictions for the multi pass system predicted the superior performance of a higher flow rate due to the increased level of turbulence during operation resulting in an effective heat transfer throughout the system.

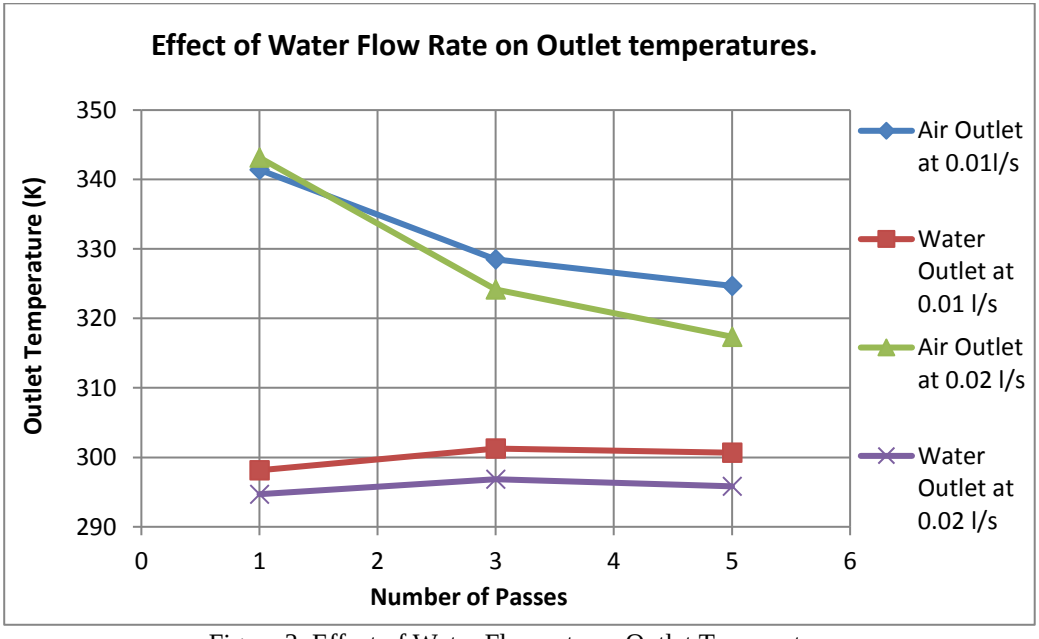

Figure 3: Effect of Water Flow rate on Outlet Temperature

Figure 3 highlights the respective outlet temperatures of all pass configurations during operation at a water flow rate of 0.02l/s. The variation in water temperature fluctuated by approximately 3.2K. The associated water outlet temperature during a high water flow rate faced similar issues as the low flow rate—with the variation in flow rate being the values obtained from experiment and the variation in inlet temperature.

3.2 Comparison of Results: Air Profile

The results obtained from the CFD simulation highlight the main observations from 1, 3 and 5 pass configurations in both high and low flow rates in the air section, the fluctuations directly correlate the changes observed in the water section. Both sets of images highlight the associated temperature gradient throughout the system. The arrows represent the flow direction due to the varied inlet and outlet locations. The results shown in figure 4-9. The plots signify both temperature contours and velocity path lines. The left side of the figure denotes the scale of the velocity path line overlay; the adjacent scale denotes the temperature contour plot located beneath the velocity path lines. The CFD results shown in figure 4 and 5 highlight the results obtained for the 5 pass configuration with 0.01l/s and 0.02l/s respectively. The operation of the five pass configuration shows an increase in average temperature as the flow rate increases. The increase in temperature is visible in both figure 4 and 5, the overall increase was approximately 30K. A similar trend is present in the three pass configuration (figure 6 and 7), with an average temperature difference of approximately 12K. In the single pass system, the overall difference is less pronounced with an average increase of approximately 10K. The single pass system for both flow rates (figure 8 and 9 respectively) highlights the large presence of wakes within the transition duct. This is more prominent in a higher flow regime. The transition section of the duct has been set as an adiabatic wall section but the amount of recirculation in those areas suggests that a large amount of unwanted heat transfer can occur in that area in a realistic application. The turbulence within the duct does increase the temperature in the surrounding areas but the dissipated heat in the duct has not been investigated. The wakes in the transition section in both 3 pass configurations (figure 6 and 7) and 5 pass (figure 8 and 9) are practically non-existent. Figure 6 and 7 highlight the air velocity profile. Figure 6 represents a low velocity plot, which highlights an increase in velocity as the passes increase but an increase in temperature regularity, a similar trend is shown in figure 7. The corresponding plot for high velocity also highlights the increase in temperature. Both high velocity and an increased heat flux area seem to be the ideal combination to achieve the optimum multipass configuration which is evident in the five pass simulations (figure 8 and 9). Both pass configurations show a drastically different temperature contour plot highlighting a key combination of passes and air inlet flow rate. The corresponding data is shown in figure 3 highlights the ideal combination of pass configuration and the corresponding outlet temperature. The temperature distribution in the amount of passes has led to some thermal irregularities due to the lack of circulation around passes. The general flow follows a serpentine style flow, as it passes through each pass, leaving zones out of this serpentine section in areas of low heat flux as represented on the corresponding temperature contour plots. The areas of low heat flux are further exaggerated. As the majority of the recirculation is occurring in the transition section, this is leading to a high level of low temperature zones towards the extremities of the system. Further precautions could be made to reduce the areas of poor recirculation such as the change of inlet location/ transition angle or the change of baffle location.

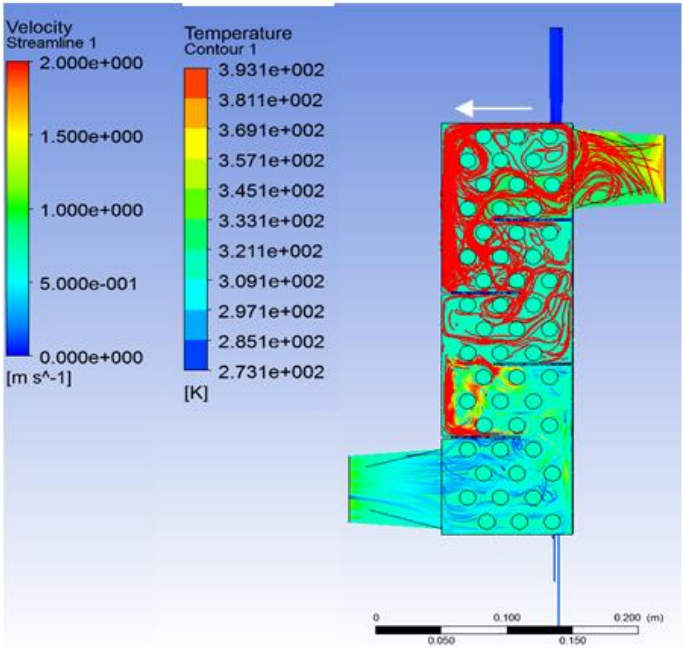

Figure 4: Velocity Pathlines and Temperature Contour Plot of 5Pass system at 0.01l/s

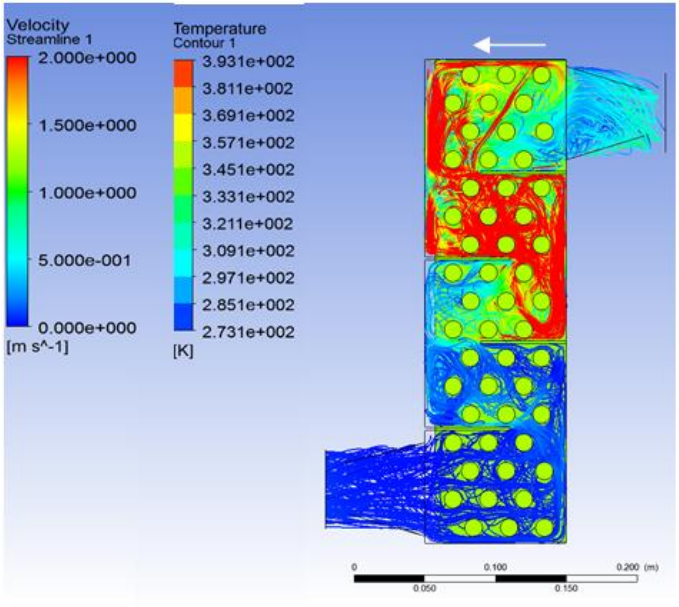

Figure 5: Velocity Pathlines and Temperature Contour Plot of 5Pass system at 0.02l/s

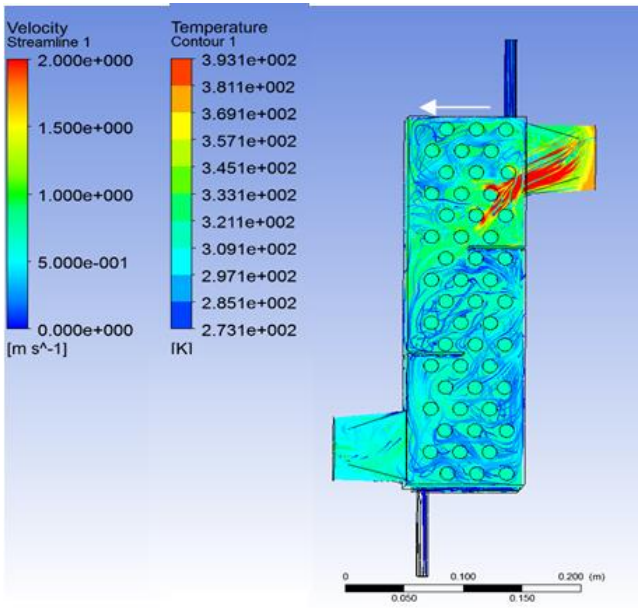

Figure 6: Velocity Pathlines and Temperature Contour Plot of 3Pass system at 0.01l/s

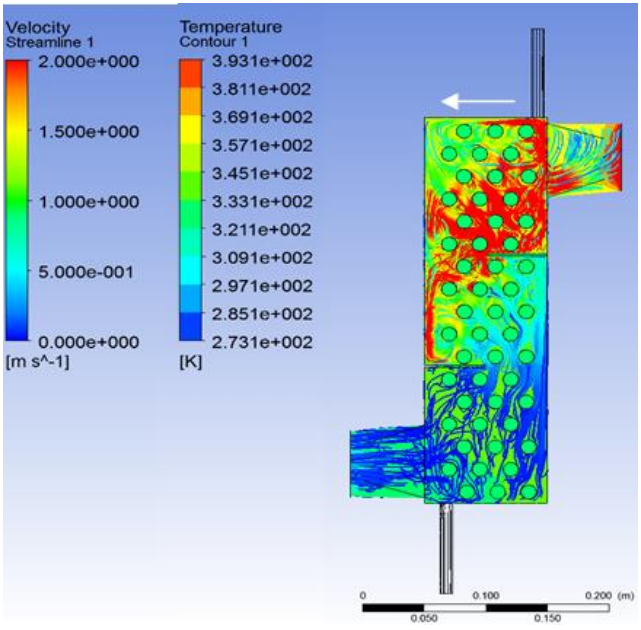

Figure 7: Velocity Pathlines and Temperature Contour plot of 3 Pass System at 0.02l/s

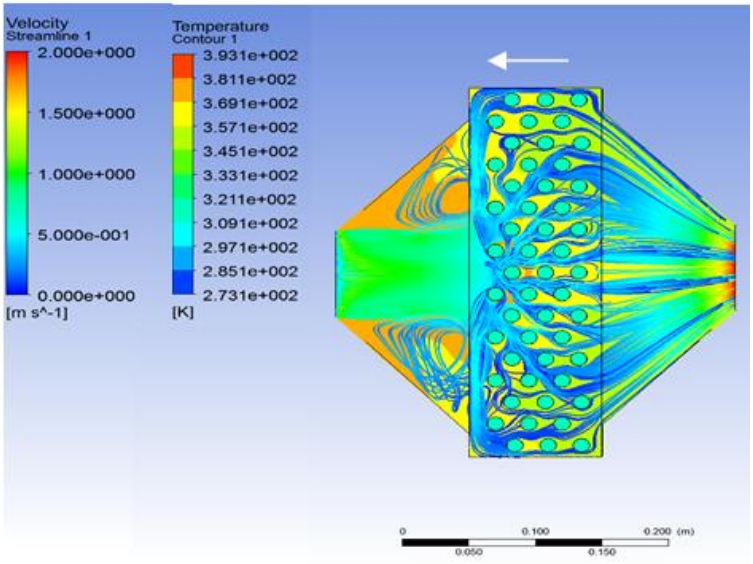

Figure 8: Velocity Pathlines and Temperature Contour Plot of 1Pass system at 0.01l/s

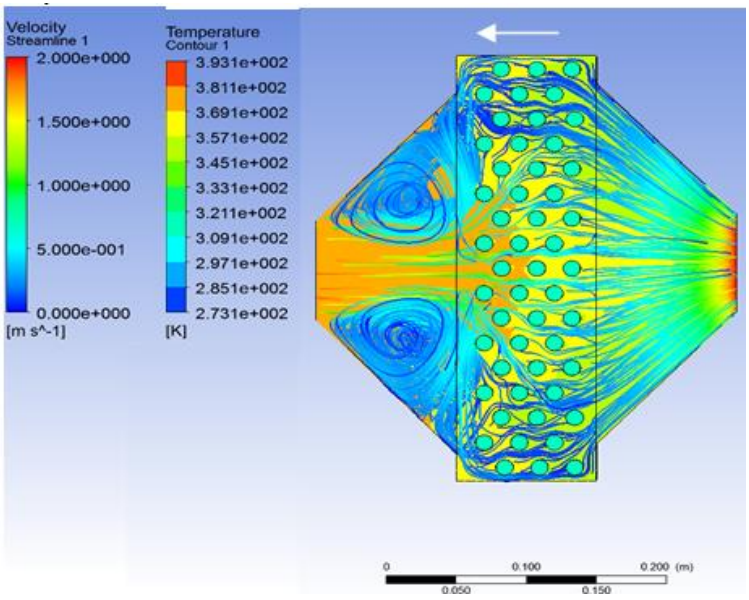

Figure 9: Velocity Pathlines and Temperature Contour plot of 1 Pass System at 0.02l/s

4 Discussion

From the corresponding contour and velocity path lines, there is a prominent prevalence of low temperature zones located in regions with low velocity regions which are commonly located away from the flow schematic of the system, which is extremely visible in a single pass schematic. Areas of recirculation have been located in undesired areas leading to a poor system performance, although the addition of passes and smaller transition areas has increased the thermal regularity within the system. In comparison between a single pass and five pass, the amount of thermal regularity increases with the addition of each pass, improving the thermal distribution, but creates a flow regime causing areas towards the walls to be areas of low temperatures. The corresponding water outlet data values show an increase in temperature with an increase in passes and velocities highlighting the optimum pass configuration to be: A five pass system operating at a high flow rate.

5 Conclusion

From the results gathered, it is evident that the implementation of additional passes increases the performance of the system due to the increase thermal area due to the increase in passes. Both the data and CFD contour plots both highlight the improved operation with the addition of passes. The lack of recirculation around certain passes can lead to a less effective system, leading to zones of poor heat flux. The implementation of passes is an effective method of maximising the potential of a heat pipe based heat exchanger, but the localised low heat flux zones need to be minimised either by the change in pass location or a variation in heat pipe location. The effect of inlet water flow rate shows promising results, but only two flow configurations have been simulated, further investigations into different inlet water and air flow rates and temperatures need to be conducted. The lack of recirculation areas need to be investigated with the consideration of thermal losses to the walls of the system and the impact on the system performance.

Acknowledgements

This research was funded by Innovate UK- Erva Mate Drying. (Project Reference #: 102716)

References

[1] E. Pal, I. Kumar, J. B. Joshi, and N. K. Maheshwari, "CFD simulations of shell-side flow in a shell-and-tube type heat exchanger with and without baffles," *Chem. Eng. Sci.*, vol. 143, pp. 314–340, 2016.

[2] A. Alizadehdakhel, M. Rahimi, and A. A. Alsairafi, "CFD modeling of flow and heat transfer in a thermosyphon," *Int. Commun. Heat Mass Transf.*, vol. 37, no. 3, pp. 312–318, 2010.

[3] A. A. Alammar, R. K. Al-Dadah, and S. M. Mahmoud, "Numerical investigation of effect of fill ratio and inclination angle on a thermosiphon heat pipe thermal performance," *Appl.*

Therm. Eng., vol. 108, pp. 1055–1065, 2016.

[4] M. Pishvar, M. Saffar Avval, Z. Mansoori, and M. Amirkhosravi, "Three dimensional heat transfer modeling of gas-solid flow in a pipe under various inclination angles," *Powder Technol.*, vol. 262, pp. 223–232, 2014.

[5] H. Jouhara, B. Fadhl, and L. C. Wrobel, "Three-dimensional CFD simulation of geyser boiling in a two-phase closed thermosyphon," *Int. J. Hydrogen Energy*, 2016.

[6] B. Fadhl, L. C. Wrobel, and H. Jouhara, "CFD modelling of a two-phase closed thermosyphon charged with R134a and R404a," *Appl. Therm. Eng.*, vol. 78, pp. 482–490, 2015.

[7] J. Ramos, A. Chong, and H. Jouhara, "Experimental and numerical investigation of a cross flow air-to-water heat pipe-based heat exchanger used in waste heat recovery," *Int. J. Heat Mass Transf.*, vol. 102, pp. 1267–1281, 2016.

[8] H. Mroue, J. B. Ramos, L. C. Wrobel, and H. Jouhara, "Experimental and numerical investigation of an air-to-water heat pipe-based heat exchanger," *Appl. Therm. Eng.*, vol. 78, pp. 339–350, 2015.

10TH INTERNATIONAL CONFERENCE ON SUSTAINABLE ENERGY AND ENVIRONMENTAL PROTECTION (JUNE 27TH – 30TH, 2017, BLED, SLOVENIA), MODELLING AND SIMULATION
J. Krope, A.Ghani Olabi, D. Goričanec & S. Božičnik

University of Maribor Press

Fast Pyrolysis in a Shaftless Screw Reactor: A 1-D Numerical Model

FABIO CODIGNOLE LUZ, STEFANO CORDINER, ALESSANDRO MANNI, VINCENZO MULONE & VITTORIO ROCCO

Abstract This paper is focused on the numerical modeling of a shaftless screw fast pyrolyzer with special attention on the chemical kinetics framework, as well as heat and mass transfer phenomena. A model with constant wall temperature has been developed to generate temperature profile and conversion patterns along the reactor. The model, including heat transport processes, is based on a 4 parallel DAEM reaction framework. The structure includes the three major biomass pseudo-component occurring in the biomass thermal degradation. Numerical results have been validated against experimental data, operating the pyrolyzer with spruce wood pellets. Results demonstrate that the selected kinetic framework, along with the proposed heat and mass transfer description, gives realistic conversion rates if compared with experimental data. The maximum bio-oil production from pellet has been observed at 500°C, with yield of 66%. Moreover, results show a strong dependence of performance parameters on the wall temperature, on gas-solid heating rate, and on the screw design characteristics.

Keywords: • fast pyrolysis • DAEM • screw reactor • spruce wood pellet • heat transfer •

CORRESPONDENCE ADDRESS: Fabio Codignole Luz, Ph.D. student, University of Rome Tor Vergata, 1.Dpt. of Industrial Engineering, Via Del Politecnico 1 ,00133 Roma, Italy, e-mail: fabio.codignole.luz@uniroma2.it. Stefano Cordiner, Ph.D., Full Professor, University of Rome Tor Vergata, Dpt. of Industrial Engineering, Via Del Politecnico 1 ,00133 Roma, Italy, e-mail: cordiner@uniroma2.it. Alessandro Manni, Ph.D., University of Rome Tor Vergata, Dpt. of Industrial Engineering, Via Del Politecnico 1 ,00133 Roma, Italy, e-mail: alessandro.manni@uniroma2.it. Vincenzo Mulone University of Rome Tor Vergata, Dpt. of Industrial Engineering, Via Del Politecnico 1 ,00133 Roma, Italy, e-mail: mulone@uniroma2.it. Vittorio Rocco, University of Rome Tor Vergata, Dpt. of Industrial Engineering, Via Del Politecnico 1 ,00133 Roma, Italy, e-mail: rocco@uniroma2.it.

https://doi.org/10.18690/978-961-286-058-5.3 ISBN 978-961-286-058-5

Available at: http://press.um.si.

1 Introduction

The intermediate conversion of solid biomass into liquid or gaseous products through biochemical or thermochemical processes is one of the means to improve the energy density and transportation problems related with solid fuels. However, the strong dependence of performance parameters on feedstock characteristics [1] and conversion technology specific characteristics [2], makes the design process challenging toward the cost effectiveness.

Numerous numerical fast pyrolysis models, focused on the improvement of bio-oil production parameters, have been developed and can be found in the literature [3-6]. Most of these models put emphasis on the analysis of the characteristic effects related to the optimization of operating parameters such as biomass and carrier gas flows, maximum temperature obtained, heating rate [7, 8]. In the given background, this paper aims at describing the operation of a screw reactor designed and realized for the fast pyrolysis (FP) process with a simplified but accurate 1D numerical model representing its behaviour.

Few models have been developed so far to describe the behaviour of a screw biomass reactor designed for fast pyrolysis and only recently multi-dimensional analysis tools have been proposed for such systems [9]. Special attention is here given to the definition of the chemical kinetics framework, as well as mass and heat transfer representation phenomena including conduction, convection and radiation by means of a rotary kiln approach [10]. The simple model developed, aims at understanding the impact of operating conditions on system performances. The experimental setup description, according to Figure 1, is reported in [11] as well as the implemented kinetic framework based on the model proposed by Miller & Bellan [12].

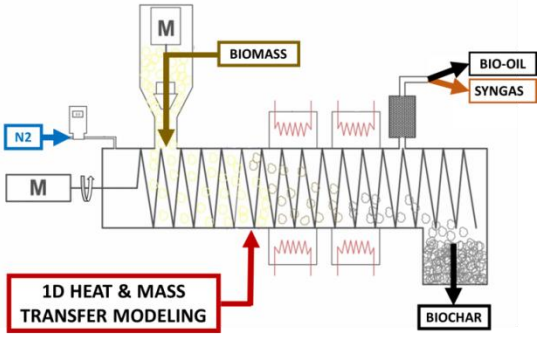

Figure 1. Experimental setup

In that case, the system has been tested with spruce wood pellet, previously analyzed by the authors through polymeric, ultimate and proximate analyses.

2 Energy and mass transfer modeling

Heat management represents for sure the most important aspect for the FP reactor design. Screw conveyors have unique features in terms of heat transfer characteristics, which can be shared with rotary kilns (except for time depth penetration), and thus the same approach as reported in [10] is here proposed. The screw velocity in fact, similarly to kilns rotation speed, has a strong influence on heat transfer coefficients especially between the wall and the solid bed. In Figure 3 the schematic of a control volume is given, along with a description of the heat transfer balances, described below.

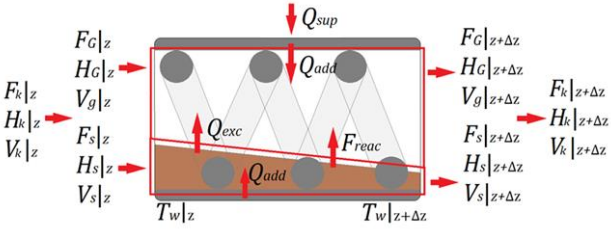

Figure 2. Model control volume

The model has been developed under the following main assumptions:

- Solid and gas phases well mixed over the radial direction
- Variable solid particle size
- Gas phase behaving as a perfect gas
- Gas phase including gas, inert and tar
- Finite axial dispersion
- DAEM kinetics based on the framework proposed in [12]

According to Figure 2, species *k* enters the control volume at position z with mass flow rate F_k. The mass flow rate of species k changes by chemical reaction with reaction rate k_k. The steady state mass balance over the control volume for a single species can be evaluated as reported in Table 1, where the differential form of all the species with the sub phase velocities evaluated according to the RTD Residence Time Distribution calculated in [13]with a DEM approach. The gaseous fraction velocity, assuming the same value for all the gaseous species and considered as ideal, can be simply derived by the total area (table 1). As the reactor has a constant section, that equation can be derived in differential form (DF) as well. This equation represents a constraint for the global mass conservation ensuring the total area conservation as well. The reactor, as a multiphase system, consists of two domains with two coupled energy balance equations: one for the solid phase, and the other one for the gaseous phase. Moreover, heats of reaction must be taken into account as well. First, energy balance in the control volume according to Figure 2 and Table 1 can be evaluated with a global formulation of the energy balance equation over the whole control volume. The first term LHS represent the heat of reactions. As the

system has two phases, two equations must be solved to solve the energy conservation. Energy balance over the solid bed can be evaluated as reported in table 1 where $\dot{q}_{a-ul,s}$ is the sum of unit length conductive and radiative heat fluxes from wall to solid bed, and $\dot{q}_{e-ul}$ the sum of convective and radiative fluxes exchanged with the gas phase. The last energy balance be solved for the gas phase, similarly to the solid one. The energy balance over the gaseous phase can be evaluated as reported in table 1, where $\dot{q}_{a-ul,g}$ represents the unit length heat flux given by the exposed wall to the gas phase through convection and radiation, and $\dot{q}_{e-ul}$ the convective flux exchanged with the solid phase. The set of equations commented are solved in MATLAB environment by means of the ode15s solver since the system is stiff. The problem gives a $[17n_v + 4] \times [17n_v + 4]$ system, where n_v is the number of sub-velocities given by the RTD simulation [13]. Furthermore, initial conditions must be provided at z=0. Definition of heat transfer fluxes are required to solve the ODE set. In such a reactor, as reported in Figure 3, the thermal energy externally provided, is given to the solid bed and to the gas phase via two different paths: one across the exposed bed surface and the other one through the covered bed surface. At the exposed surface, the solid phase absorbs heat by convection and radiation, while the covered bed region gets heat mostly via conduction at the wall.

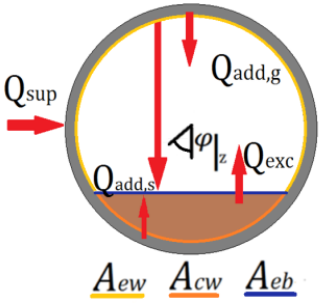

Figure 3. Heat transfer model diagram

The system can then be divided into three regions: solid bed, gas zone, and heated walls. The heat transfer exchanged by the system is the sum of the following terms:

- Q_{sup}: heat supplied from the external resistance rings, controlled at the constant temperature $T_{wall1,2,3}$.
- $Q_{add,g}$, heat transfer exchanged between the exposed walls and the gas phase due to convection and radiation.
- Q_{exc}, heat transfer exchanged between the exposed bed surface and the gas phase due to convection and radiation.
- $Q_{add,s}$, heat transfer exchanged between the covered wall and the solid bed, which is mostly conduction and radiation between exposed wall and bed.

Relations used in externally heated rotary kilns[10, 14] are used to determine the heat transfer coefficients. This assumption can be justified by the similarities occurring between the systems. A heat transfer model can be represented by an equivalent electric circuit in which, electrical resistances represented by terms as $1/(h_k A_k)$ and voltage generators connected with an earthing (zero potential) are used in substitution of gas, solid and wall temperatures. According to the energy balance, the heat transfer rate terms are contained in the unit length thermal transmittance coefficients h_k . In a such a way, the heat transfer per unit length can be evaluated by means of the equations reported in table 1.

The heat transfer coefficients must be determined in order to obtain the heating rate values per unit length. Heat transfer between covered wall and covered solid bed mostly occur by conduction.

Table 1. Model equations

Balance equations	
Mass Balance	$\sum_{i=1}^{n_v}\frac{\partial F_{w,i}}{\partial z}+\frac{\partial F_{m,i}}{\partial z}+\sum_{j=1}^{3}\frac{\partial F_{vb,j,i}}{\partial z}+\frac{\partial F_{ab,j,i}}{\partial z}+\frac{\partial F_{c,j,i}}{\partial z}+\frac{\partial F_{g,j,i}}{\partial z}+\frac{\partial F_{t,j,i}}{\partial z}=\sum_{k=1}^{n}\pm\frac{k_k F_k}{V_k}=0$
Total area constancy	$\sum_{k=1}^{n}A_k=\sum_{k=1}^{n}\frac{F_k}{\rho_k V_k}=cost.=\pi R^2$
Total area constancy D.F.	$\frac{\partial}{\partial z}\left(\frac{F_N}{\rho_N V_g}\right)+\sum_{i=1}^{n_v}\frac{1}{V_i}\left[\frac{1}{\rho_w}\frac{\partial F_{w,i}}{\partial z}+\sum_{j=1}^{3}\frac{1}{\rho_b}\frac{\partial F_{vb,j,i}}{\partial z}+\frac{1}{\rho_b}\frac{\partial F_{ab,j,i}}{\partial z}+\frac{1}{\rho_c}\frac{\partial F_{c,j,i}}{\partial z}\right]+\frac{\partial}{\partial z}\left(\frac{F_{m,i}}{\rho_m V_g}\right)+\frac{\partial}{\partial z}\left(\frac{F_{g,j,i}}{\rho_g V_g}+\frac{F_{t,j,i}}{\rho_t V_g}\right)=0$
Energy balance	$\sum_{k=1}^{n}\frac{k_k F_{k,z}}{V_k}\Delta H_k+\sum_{k=1}^{n}F_k C_{pk}\frac{\partial T_k}{\partial z}=\dot{q}_{a-ul}$
Energy balance over solid bed	$\left[\sum_{i=1}^{n_v}F_{w,i}C_{pw}+\sum_{j=1}^{3}F_{vb,j,i}C_{pb}+F_{ab,j,i}C_{pb}+F_{c,j,i}C_{pc}\right]\frac{\partial T_s}{\partial z}=\dot{q}_{a-ul,s}-\left[\sum_{i=1}^{n_v}\frac{F_{w,i}k_m}{V_i}\Delta H_m+\sum_{j=1}^{3}\frac{F_{ab,j,i}k_{2,j}}{V_i}\Delta H_2+\frac{F_{ab,j,i}k_{3,j}}{V_i}\Delta H_3\right]+\dot{q}_{e-ul}$
Energy balance over gaseous phase	$\left[F_N C_{pN}+\sum_{i=1}^{n_v}F_{m,i}C_{pm}+\sum_{j=1}^{3}F_{g,j,i}C_{pg}+F_{t,j,i}C_{pt}\right]\frac{\partial T_g}{\partial z}+\left[\sum_{i=1}^{n_v}\frac{\partial F_{m,i}}{\partial z}C_{pm}+\sum_{j=1}^{3}\frac{\partial F_{g,j,i}}{\partial z}C_{pg}+\frac{\partial F_{t,j,i}}{\partial z}C_{pt}\right](T_g-T_s)=-\sum_{i=1}^{n_v}\sum_{j=1}^{3}\frac{F_{t,j,i}k_4}{V_g}\Delta H_4+\dot{q}_{a-ul,g}-\dot{q}_{e-ul}$
Heat transfer model equations	
wall to bed	$\dot{q}_{a-ul,s}=(h_{cw-cb}^{cd}A_{cw}+h_{ew-eb}^{r}A_{eb})(T_w-T_s)$
exchanged	$\dot{q}_{e-ul}=-(h_{eb-g}^{cv}+h_{eb-g}^{r})A_{eb}(T_s-T_g)$
wall to gas	$\dot{q}_{a-ul,g}=(h_{ew-g}^{cv}+h_{ew-g}^{r})A_{ew}(T_w-T_g)$
Conductive and convective coefficients	
Covered.wall.-covered bed	$h_{cw-cb}^{cd}=1/(\chi D_p/k_g)+\left(2\sqrt{[(1-y)k_b\rho_b C_{pb}+yk_c\rho_c C_{pc}]\cdot n\cdot sin\,\alpha\, cos\,\alpha/pitch}\right)^{-1}$
Exp. wall-gas	$h_{ew-g}^{cv}=\left(1.54Re_g^{0.575}Re_s^{-0.292}\right)k_g/D_e$
Exp. bed-gas	$h_{eb-g}^{cv}=\left(0.46Re_g^{0.535}Re_s^{0.341}\eta^{-0.341}\right)k_g/D_e$
Radiative coefficient	
Exp. wall- bed	$h_{ew-eb}^{r}=(J_w-J_s)(\tau_g F_{eb-ew})/T_w-T_s$
Exp. bed-gas	$h_{eb-g}^{r}=(J_s-E_g)(\epsilon_g F_{eb-g})/T_s-T_g$
Exp. wall-gas	$h_{ew-g}^{r}=(J_w-E_g)(\epsilon_g F_{ew-g})/T_w-T_g$

Thermal resistance will be constituted of a term which depends on the solid contact [15] and another one related to the gas film at the surfaces interface. The conductive heat transfer coefficient between the covered wall and the covered bed can be evaluated as reported in table 1. As already highlighted, the convective heat transfer is made of two terms: one between the gas phase and the exposed wall surface Q_{ew-g}^{cv}, and one between the gas phase and exposed bed surface Q_{eb-g}^{cv}. The convective coefficients can be

evaluated by means of the equations proposed in [16] for a rotary kiln and reported in Table 1. The radiative heat transfer has been modelled under the following main assumptions: bodies are considered grey, the axial temperature gradient is negligible , the view factors are taken constant and equal to unity [10], emissivity ϵ_k and transmissivity τ_g are assumed constant over the reactor length abscissa z.

3 Simulation parameters

In Table 2 the reactor geometrical parameters and the properties of the biomass are reported .

Table 2. Simulation parameters

Parameter	Symbol	Unit	Value
Biomass mass flow	F_{bio}	Kg/h	0.5
Central value SAVD	V_s	m/s	0.016
Internal Pressure	p_{amb}	Pa	101315
Moisture %w	Φ	-	0.06
Nitrogen volumetric flow	F_N	Nl/min	0.5
Reactor diameter	D	m	0.02
Reactor length	L	m	0.25
Screw angle	α	deg	40
Screw pitch	pitch	m	0.025
First wall temperature	$T_{wall,1}$	°C	7
Second wall temperature	$T_{wall,2}$	°C	350
Third wall temperature	$T_{wall,3}$	°C	450,500,550
Biomass density	ρ_b	Kg/m^3	600
Biomass thermal conductivity[17]	k_b	W/m·K	0.11
Char and biomass porosity	ε	-	0.65
Char density	ρ_c	Kg/m^3	350
Char thermal conductivity[17]	k_c	W/m·K	0.071
Gas molecular weight	PM_g	g/mol	20
Gas thermal conductivity[17]	k_g	W/m·K	0.026
Initial particles diameter	d_p	m	$8.5 \cdot 10^{-4}$
Kinematic viscosity[17]	ν	m^2/s	$4 \cdot 10^{-6}$
Nitrogen molecular weight	PM_N	g/mol	28
Tar molecular weight	PM_t	g/mol	60
Solid and wall emissivity	ϵ_s, ϵ_w	-	0.8
Gas emissivity	ϵ_g	-	0.2
Gas transmissivity	τ_g	-	0.8

Biomass, char, gas, tar and nitrogen heat capacities C_p are assumed temperature dependent [17] while water and moisture are assumed constant functions of temperature.

4 Analysis of results

For validation purposes, only Spruce wood pellet has been considered. Numerical results are compared with the experimental ones in terms of product yields over the reactor length (x axis). The characteristic operating parameters considered are the following:

- •450 °C, 500°C, 550°C pyrolysis temperatures
- •0.5NL/min nitrogen flow rate
- •0.5 Kg/h biomass flow rate

In the following figures, representing only results at 500°C, the continuous lines represent the numerical results, to be compared with the experimental ones (starred lines) as collected at the reactor outlet; the dashed lines indicate the numerical temperature at the wall. In conversion rates plots, experimental char gas and tar yields are also highlighted.

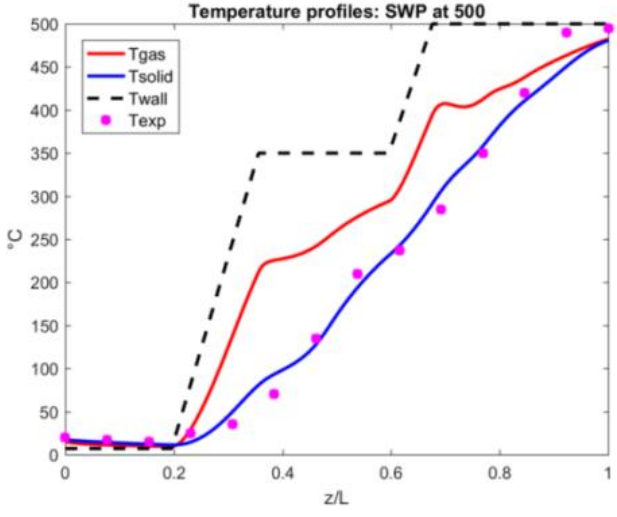

Figure 4.Temperature profiles

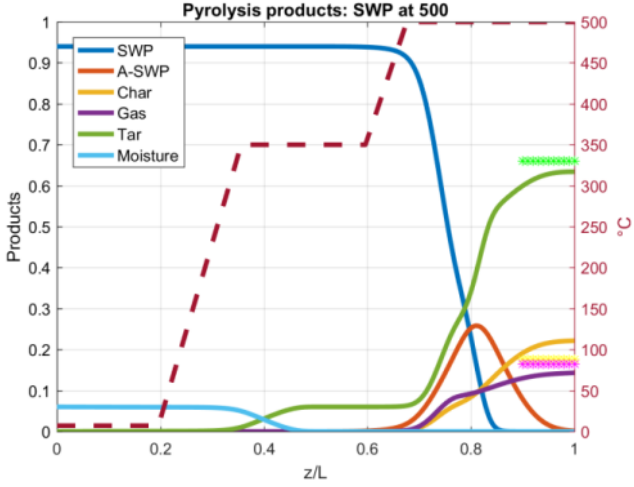

Figure 5.Pyroysis products

It must be underlined that the SWP bio-oil production peak is predicted at 500°C, in agreement with the experimental data (table 3). Furthermore it must be pointed out that at the lowest temperature the biomass can be not fully consumed by the chemical reactions for intrinsic limits of the simplified chemical model. In that case the use of a DAEM framework is mandatory to predict accurately the low temperature reactions activation. It has already been highlighted that the peak of bio-oil production, as predicted by the model, is obtained at intermediate temperature. This can be reasonably attributed to the incomplete biomass conversion process at lower temperature for the first step reactions, while at the higher temperature secondary reactions can take place enabling the bio-oil cracking and increasing the secondary gas yield. The contribution of the DAEM capability is evidently relevant. In fact, since the reactions start at a low temperature, the primary reactions have enough time to evolve completely, while the secondary reactions start to take place. Furthermore, the heating rates supplied for both gaseous products and solid bed are shown in Figure 6 and Figure 7.

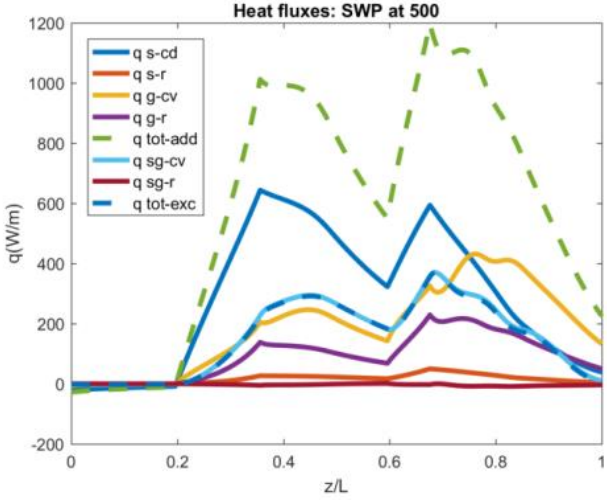

Figure 6. Heat fluxes

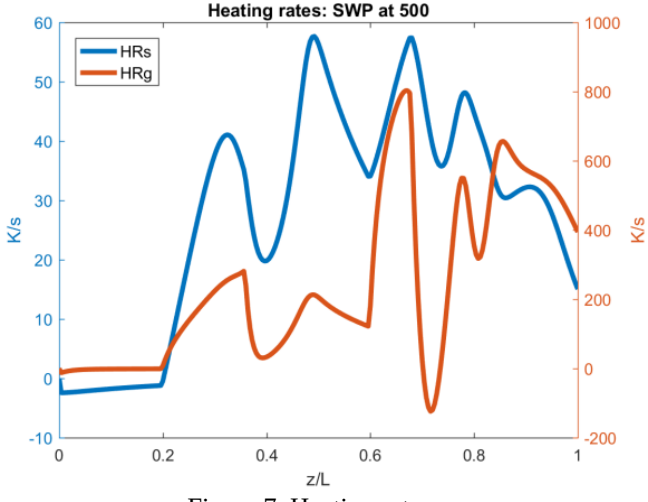

Figure 7. Heating rates

At low temperature, the conductive heat flux gives the highest contribution, while the convective heat flux gets important by increasing gaseous velocity as a result of tar, gas production and moisture evaporation, due to the high temperature. In the hotter reactor zone, due to the high volatile matter production rate (mainly bio-oil as vapor), the velocity increases considerably and thus the convection term reaches the highest values. The radiative heat flux gets important only at high temperature, contributing substantially to the reactor heat management,. In table 3 experimental and numerical results are

compared: it is worth highlighting that the moisture content of biomass is included into the tar yield. In Figure 6 the convective, conductive and radiative heat fluxes exchanged between the phases are given. As expected, the conversion rates are strongly affected by the wall temperature and thus the heating rate.

Table 3. Exp. Vs Model Results

Bio&T.	**Bio-Oil**		**Syngas**		**Char**		**Unreac.**
	Exp.	Model	Exp.	Model	Exp.	Model	Model
SWP 450°C	58,5	58,74	16	13,66	25	20,41	7,19
SWP 500°C	66	63,41	16,5	14,32	17,5	22,14	0,13
SWP 550°C	64	62,27	18,5	15,64	17,5	22,1	0

In all the cases, although the numerical heating up is greater than the experimental one, a slower biomass reactivity and thus a consequent higher unreacted fraction is observed (Table 3). Due to the same reason, the maximum oil production predicted numerically is slightly moved toward the hotter regions . In general, the numerical results, are in good agreement with the experimental data in terms of oil fraction evolutions with limited errors . The thermal power requested for both the heating up and the endothermal reactions is in the order of 150 W for all the cases, which is in substantial agreement with the experimental one, that is in the range of about 160W [11].

5 Conclusions

In this work, a 1D model for fast pyrolysis in a screw reactor has been developed. Coupled mass and energy equations with a DEAM kinetic framework and heat transfer model adapted from kiln reactors theory, validated vs the experimental data, have been implemented. A particle spatial velocity distribution adapted from a 3D-DEM simulation has been considered as well to evaluate the model capabilities. The main obtained results are the following:

- The oil concentration predicted over temperature is in line with literature available data as well as with the experimental one, with yields of about 64% and 58% respectively for pellet and spent coffee. The maximum bio-oil production, as seen in the experiments, is given at the intermediate temperature of 500°C.
- Numerical temperature profiles are in substantial agreement with the experimental ones
- Heating rates and residence times are in line with literature available data for the fast pyrolysis process.
- Heat fluxes between walls and solid-gas phases are comparable with experimental findings .

The MATLAB code developed can simulate fast pyrolysis process in a screw reactor by varying the main simulation parameters (i.e. mass flow, pyrolysis temperature, carrier gas flow, biomass composition, biomass velocity in the reactor) in order to optimize the process yield.

Acknowledgements
The authors would like to acknowledge the batchelor students Lorenzo Berchicci and Gianmarco Palma for their valuable contribution to the numerical results commented in this paper and C

SF/CAPES (BEX-11965/13-4) – Brazilian Federal Agency for Support and Evaluation of Graduate Education within the Ministry of Education of Brazil.

References

[1] A. W. Bhutto, K. Qureshi, K. Harijan, R. Abro, T. Abbas, A. A. Bazmi, *et al.*, "Insight into progress in pre-treatment of lignocellulosic biomass," *Energy*, 2017.
[2] H. Nam, S. C. Capareda, N. Ashwath, and J. Kongkasawan, "Experimental investigation of pyrolysis of rice straw using bench-scale auger, batch and fluidized bed reactors," *Energy*, vol. 93, pp. 2384-2394, 2015.
[3] C. Di Blasi, "Modeling chemical and physical processes of wood and biomass pyrolysis," *Progress in Energy and Combustion Science*, vol. 34, pp. 47-90, 2008.
[4] A. Bridgwater and G. Peacocke, "Fast pyrolysis processes for biomass," *Renewable and sustainable energy reviews*, vol. 4, pp. 1-73, 2000.
[5] A. V. Bridgwater, "Review of fast pyrolysis of biomass and product upgrading," *Biomass and bioenergy*, vol. 38, pp. 68-94, 2012.
[6] S. Aramideh, Q. Xiong, S.-C. Kong, and R. C. Brown, "Numerical simulation of biomass fast pyrolysis in an auger reactor," *Fuel*, vol. 156, pp. 234-242, 2015.
[7] M. A. Cordiner S , Mulone V, Rocco V, "Biomass pyrolysis modeling of systems at laboratory scale," *International Journal of Numerical Methods for Heat and Fluid Flow*, SUBMITTED 2017.
[8] S. Yang, M. Wu, and C. Wu, "Application of biomass fast pyrolysis part I: Pyrolysis characteristics and products," *Energy*, vol. 66, pp. 162-171, 2014.
[9] A. Funke, E. Henrich, N. Dahmen, and J. Sauer, "Dimensional Analysis of Auger- Type Fast Pyrolysis Reactors," *Energy Technology*, vol. 5, pp. 119-129, 2017.
[10] S. Q. Li, L. B. Ma, W. Wan, and Q. Yao, "A Mathematical Model of Heat Transfer in a Rotary Kiln Thermo- Reactor," *Chemical engineering & technology*, vol. 28, pp. 1480-1489, 2005.
[11] F. Codignole Luz, S. Cordiner, A. Manni, V. Mulone, and V. Rocco, "Analysis of Residual Biomass fast pyrolysis at laboratory scale: experimental and numerical evaluation of spent coffee powders energy content," *Energy Procedia (in press)*, 2017.
[12] R. S. Miller and J. Bellan, "A generalized biomass pyrolysis model based on superimposed cellulose, hemicelluloseand liqnin kinetics," *Combustion science and technology*, vol. 126, pp. 97-137, 1997.
[13] F. C. Luz, S.Cordiner, A. Manni, V. Mulone, and V. Rocco, "Biomass fast pyrolysis process at laboratory scale:residence time and heating up evaluation in a shaftless screw reactor by means of a discrete element model approach," in *CHT-17*, Naples, 2017.
[14] J. Gorog, J. Brimacombe, and T. Adams, "Radiative heat transfer in rotary kilns," *Metallurgical Transactions B*, vol. 12, pp. 55-70, 1981.

[15] G. Wes, A. A. Drinkenburg, and S. Stemerding, "Heat transfer in a horizontal rotary drum reactor," *Powder Technology,* vol. 13, pp. 185-192, 1976.
[16] S. Tscheng and A. Watkinson, "Convective heat transfer in a rotary kiln," *The Canadian Journal of Chemical Engineering,* vol. 57, pp. 433-443, 1979.
[17] H. Lu, E. Ip, J. Scott, P. Foster, M. Vickers, and L. L. Baxter, "Effects of particle shape and size on devolatilization of biomass particle," *Fuel,* vol. 89, pp. 1156-1168, 2010.

10TH INTERNATIONAL CONFERENCE ON SUSTAINABLE ENERGY AND ENVIRONMENTAL PROTECTION (JUNE 27TH – 30TH, 2017, BLED, SLOVENIA), MODELLING AND SIMULATION
J. Krope, A.Ghani Olabi, D. Goričanec & S. Božičnik

University of Maribor Press

Industrial NGSR Reactor for Hydrogen Production: Steady-State Simulation Devoted to Fault Diagnosis

FREDERICO PUGLIESE, GABRIELE MOSER, ANDREA TRUCCO, VALTER MANTELLI & PAOLA COSTAMAGNA

Abstract The purpose of the research reported in the present paper is to develop a diagnosis and prognosis tool for a Natural Gas Steam Reforming (NGSR) reactor. This tool is based on a mathematical model, based on (i) microscopic balances of mass, energy and momentum; (ii) appropriate boundary conditions; and (iii) appropriate expressions for constitutive laws, in particular chemical kinetics. Here, the steady-state version of the model is presented. The model equations are integrated numerically by a finite element method, implemented through COMSOL Multiphysics 5.2. The results are simulated 2-D maps of all the chemical-physical variables inside the NGSR reactor, in particular temperature and composition of the reactant gas. In the validation phase, the results of the model are compared to literature results and also to experimental data provided by a full-size industrial multi-tubular NGSR reactor.

Keywords: • Hydrogen Production • Chemical Reactor • Natural Gas Steam Reforming (NGSR) • Mathematical Modeling • Fault Detection and Isolation (FDI) •

CORRESPONDENCE ADDRESS: Frederico Pugliese, University of Genoa, Department of Civil, Chemical and Environmental Engineering (DICCA), Via Montallegro 1, I-16145 Genoa, Italy, e-mail: federico.pugliese@edu.unige.it. Gabriele Moser, University of Genoa, Department of Electrical, Electronics and Telecommunications Engineering (DITEN), Via Opera Pia 11a, I-16145 Genoa, Italy, e-mail: gabriele.moser@unige.it. Andrea Trucco, University of Genoa, Department of Electrical, Electronics and Telecommunications Engineering (DITEN), Via Opera Pia 11a, I-16145 Genoa, Italy, e-mail: andrea.trucco@unige.it. Valter Mentelli, IPLOM S.p.A., Via C. Navone 3/B, I-16012 Busalla (GE), Italy, e-mail: valter.mantelli@iplom.it, Paola Costamagna, University of Genoa, Department of Civil, Chemical and Environmental Engineering (DICCA), Via Montallegro 1, I-16145 Genoa, Italy, e-mail: paola.costamagna@unige.it.

https://doi.org/10.18690/978-961-286-058-5.4 ISBN 978-961-286-058-5

Available at: http://press.um.si.

1 Introduction

The concept of sustainable energy is associated to that of hydrogen economy. However, at present, the main hydrogen production pathway is from fossil fuels, mainly natural gas. Natural gas (NG) is a mixture without definite composition; methane is the major component, with a typical molar fraction around 85-90% [1]. Other components are nitrogen and higher hydrocarbons, typically ethane, propane, butane, pentane and hexane [1]. Conversion into hydrogen can then follow different reaction pathways; natural gas steam reforming (NGSR) is the more widely employed process. Despite NGSR chemical reactors implement an established technology, they still present some issues, in particular the deposition of carbon, which can coat the active sites of the catalyst, inhibiting its activity and limiting the diffusion of reactants into the catalytic bed [2,3,4]. This deposition starts at some critical points and then expands over time, generating an increase of pressure losses and causing a reduction of conversion. The final purpose of our research is the development of a system for early detection and prediction of coke deposition, i.e. a fault detection and isolation (FDI) tool, suitably tailored for the NGSR reactor. A number of FDI methods have been proposed and applied to a variety of systems. A survey can be found in [5], where they are classified as: (i) quantitative model-based; (ii) qualitative model-based, and (iii) process history-based methods. In practice, the classification regards the approach used to produce the fault data for the FDI: in the first two cases, the data are obtained from a model developed for the system under analysis, while the latter approach is based on historical experimental data. In the present work, we propose a model for the NGSR reactor. Modelling of industrial NGSR reactors has already been addressed [6,7]. However, the previous literature works are mainly aimed to optimize the operating conditions and identify innovative geometries, while the model presented here is intended to provide the basis for an FDI tool based on pattern recognition techniques, which will be developed in a subsequent phase.

2 NGSR reactor geometry and operating conditions

An industrial multi-tubular NGSR reactor built and operated at Iplom is considered. The reactor is formed by 30 tubes positioned vertically in a top-fired furnace (Figure 1). Each tube has diameter 0.12 m and length 12 m; these are typical state-of-the-art dimensions for industrial NGSR reactor tubes. The tubes are filled with commercial Johnson Matthey catalyst pellets (Katalco series).

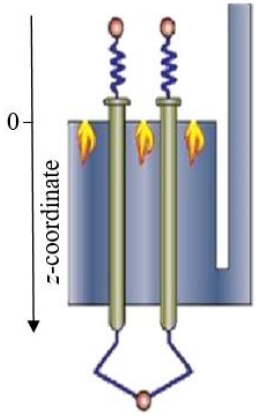

Figure 1. Scheme of an industrial top-fired NGSR reactor

The multi-tubular reactor is fed with a mixture provided by two different sources: NG from the national grid and an internal refinery stream called *refinery gas* (coming from other unit operations). NG and refinery gas have a flowrate of 49.97 kmol h^{-1} and 21.9 kmol h^{-1} respectively. Compositions are reported in Table 1. The mixture is further added with 303.8 kmol h^{-1} of steam in order to obtain an S/C=4.1. The feeding mixture is preheated to 815 K and then it is divided equally among the tubes of the NGSR reactor. Referring to Figure, tubes are fed at the top (z=0) and flow direction is from top to bottom along the z-coordinate. Internal tube operating pressure is 25.6 bar. The furnace is fed with a mixture provided by two different sources: NG from the national grid and an internal refinery stream called *purge gas* (coming from other unit operations). In this case, NG and purge gas have a flowrate of 19 kmol h^{-1} and 88.5 kmol h^{-1} respectively. Compositions are reported in Table 1. The mixture, at 298 K, is divided equally among the uniformly distributed burners of the furnace. Air is fed to the burners as well (flowrate 17257 kg h^{-1}). The furnace pressure is 2.9 bar. It is common operative knowledge to consider 1/3 of the furnace length as a radiative zone, and the rest as a convective zone. In the first, the prevailing heat transfer mechanism is radiation from the flame, while in the second, convective heat exchange with the combustion fumes is prevalent. In the NGSR reactor furnace under study, the upper region is the radiative zone, and the bottom region is the convective zone, where, on average, the combustion fumes flow downwards, in co-flow with the reacting flow inside the tubes.

Table 1. NGSR reactor and furnace feedstock composition [mol%]

Component	NG	Refinery gas	Purge gas
CH_4	89.3	7.16	10.03
C_2H_6	4.58	4.61	-
C_3H_8	0.81	10.37	-
i-C_4H_{10}	0.14	7.06	-
n-C_4H_{10}	0.2	4.94	-
i-C_5H_{12}	0.05	0.26	-
n-C_5H_{12}	0.02	0.26	-
C_{5+}	0.04	-	-
CO	-	-	23.99
CO_2	1.54	-	6.64
N_2	3.36	-	2.34
H_2	-	64.02	56.99
He	0.03	-	-

3 Mathematical model

The mathematical model is developed for the industrial NGSR reactor described in Section 2. The main underlying assumption is that all the tubes of the reactor display identical behaviour. Under this assumption, one single tube is simulated with the hypothesis of cylindrical symmetry, based on which a 2-D simulation model is developed in function of the radial and axial coordinates. The radial *r*-coordinate has its origin at the axis of the tube, and the axial coordinate is the *z*-coordinate of Figure.

3.1 Reaction scheme

The main reactions included in the simulation model are methane steam reforming (MSR) and water gas shift (WGS):

$CH_4 + H_2O \leftrightarrows CO + 3H_2$ (MSR)

$$\Delta H_{298K}^{MSR} = 206.27\, kJmol^{-1}$$

$CO + H_2O \leftrightarrows CO_2 + 4H_2$ (WGS)

$$\Delta H_{298K}^{WGS} = -41.19\, kJmol^{-1}$$

MSR is a strongly endothermal reaction, while WGS is slightly exothermal. SR reactions of higher hydrocarbons (ethane, propane, butane, pentane and C_{5+}) are not taken into consideration. Furthermore, methane cracking and the Boudouard reaction, leading to carbon formations, are not embedded into the model described in the present paper.

3.2 Model development: assumptions and equations

Current fixed-bed reactor modelling approaches are often based on simplifying assumptions, such as pseudo homogeneity, effective transport parameters and unidirectional plug-flow. In our modelling approach, some of these hypothesis are retained, such as: (i) the fixed-bed catalytic reactor is simulated as a pseudo-continuum, where both fluid and solid phases are modelled as inter-penetrating continua; (ii) diffusive limitations inside the catalyst pores are neglected. The model implements mass, energy and momentum balances, coupled to a kinetic subroutine. The equations are all written in local form for the fixed catalytic bed of the reactor, with reference to Eulerian coordinates, accounting for transport of mass, energy and momentum. All the equations are written in the typical form for non-ideal tubular reactors. A description of the equations embedded in the model is provided in a previous paper [4]. Here, in addition to the simulation of the reactor itself, the model includes also a simplified simulation of the furnace, which is considered as an annular heating jacket surrounding the reactor, fed by the reaction fumes at a temperature equal to the adiabatic flame temperature, with no distinction between the radiative and convective parts of the furnace. The plug-flow assumption is applied, and velocity and temperature T_g are considered to be function only of the *z*-coordinate, while all the chemical-physical variables are assumed to be uniform on each annular section of the heating jacket. The energy balance includes the term:

$$Q_{vd} = h \cdot S \cdot (T_{wall} - T_g) \tag{1}$$

which is the heat supplied by the annular heating jacket to the tubular reactor, with h being the convective heat exchange coefficient, S the reactor outer surface, T_{wall} the temperature of the reactant gases inside the reactor tube, at the tube wall. This term is accounted for in both the energy balance of the heating jacket and, with opposite sign, in the energy balance of the NGSR reactor tube. No heat exchange is considered to occur between the heating jacket and the surroundings.

3.3 Parameter and input data estimation

The combustion fumes are assumed to enter annular heating jacket at the adiabatic flame temperature T_{af}. On the basis of a macroscopic energy balance, considering complete combustion of the fuel fed to the furnace burners, T_{af}=1819 K. The Reynolds number is estimated Re=45.600 inside the tube, and Re=14.000 in the annular heating jacket. Thus, the flow regimen is turbulent and it is assumed to be completely developed. Under these conditions, the Colburn equation is applied to both the reactant gases flowing inside the tube and to the combustion fumes flowing in through external annular heating jacket [8]:

$$Nu = 0.023 \cdot Re^{0.8} \cdot Pr^{0.33} \tag{2}$$

where Nu and Pr are respectively the Nusselt and Prandtl numbers. Finally, the overall convective heat exchange coefficient through the tube wall, accounting for both internal and external resistances, is estimated as h=35 W m^{-2} K^{-1}.

3.4 Model integration

The NGSR reactor model equations form a partial differential and algebraic equation (PDAE) system. The resolution of the PDAE system needs implementation of a numerical method. To this end, the finite element method (FEM) is selected, which is implemented through COMSOL Multiphysics, version 5.2 [9]. The model runs typically in 5 minutes on an Intel Core i5® CPU running at 3.20 GHz with 16 GB of RAM. This running time is acceptable in order to generate the large pool of data required to train diagnostics and prognostics tools.

Input data of the model are the geometrical data of the reactor and the operating conditions, i.e. flowrate, composition and temperature for the reactant mixture being fed inside the tube, and for the combustion fumes being fed into the heating jacket. Model results are simulated 2-D maps of all the chemical-physical variables inside the NGSR reactor, in particular temperature and composition of the reactant gas.

4 Results and discussion

Figure 2 presents both 2-D map and 1-D profile of the simulated temperature inside the NGSR reactor tube.

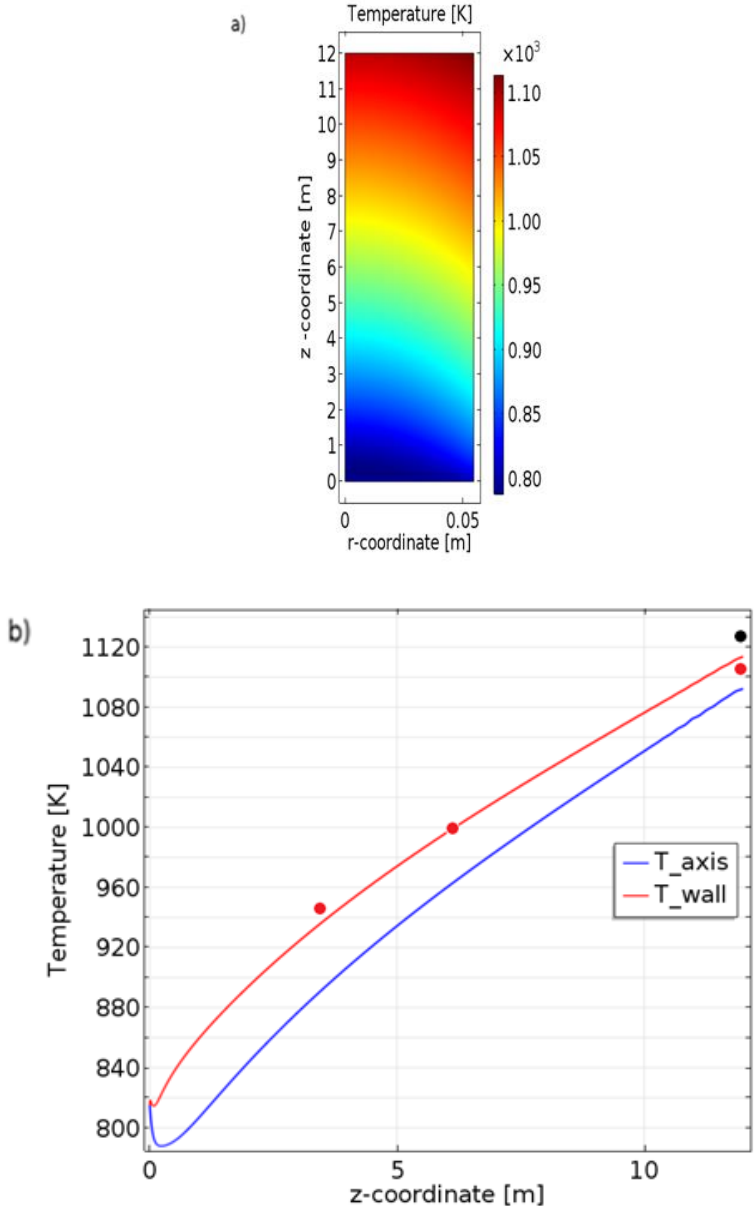

Figure 2. a) simulated map of NGSR reactor tube temperature; b) simulated temperature profile: — T along the reactor axis; — T_{wall}; ● literature simulation results [7]; ● experimental data

Figure 2 a), clearly displays a significant deviation from the plug-flow behaviour, mainly due to the thermal effects taking place in the reactor, namely the heat exchange occurring at the reactor wall with the hot combustion fumes, and the strongly endothermal MSR reaction occurring inside the tube. This is displayed in Figure 2 a) and further evidenced in Figure 2 b), which reports the temperature profile along the *z*-coordinate at the reactor wall (r=0.06 m) and along the reactor axis (r=0.0 m), clearly showing that that the wall temperature is about 20-50 K higher. This is a direct consequence of the heat exchange mechanism: the combustion fumes provide heat through the wall to the reagent gas inside the reactor, increasing its temperature. This effect is higher at the tube wall and tends to decrease moving to the reactor centre, where, for symmetry reasons, the radial heat flow vanishes. Figure 2 a) and b) also display a temperature drop in proximity of the reactor inlet, mainly in the centre of the reactor, due to the endothermal effect of the MSR reaction. This is followed by an increase up to about 1103.6 K at the reactor outlet. This is a consequence of the heat transferred from the external annular jacket, and of the reduced kinetics, and thus reduced cooling effect, of the MSR reaction along the *z*-coordinate. Furthermore, Figure 2 b) presents a comparison between simulated T_{wall} and the results reported by a reference literature reference work [7] focusing on the simulation of a similar NGSR multi-tubular reactor. The comparison demonstrates overall good agreement. In addition, Figure b) reports the experimental value (1125.7 K) measured at the lower end of the industrial multi-tubular NGSR reactor under consideration in the present work, and the agreement is reasonably satisfactory again. Further simulation results (not reported here) for the temperature of the combustion fumes along the *z*-coordinate, display a temperature drop of about 390 K between inlet and outlet.

Figure 3 reports 2-D maps of molar fractions for methane and hydrogen. Obviously, methane consumption and hydrogen production occur simultaneously along the reactor. Molar fraction profiles show again a significant deviation from the plug-flow behaviour, and are strictly associated to the temperature profiles reported in Figure 2. Indeed, methane molar fraction is remarkably lower at the tube wall compared to the tube centre, while hydrogen molar fraction shows the opposite behaviour. This is explained considering that at the tube wall, where temperature is higher, the endothermal MSR reaction is favoured from both the thermodynamic and the kinetic point of view, resulting in a higher reaction extent and thus lower reactant (i.e. methane) and higher product (i.e. hydrogen) molar fractions.

Figure 4 reports the simulated reactant gas composition along the reactor axis, which is in good qualitative agreement with the results reported by a reference literature work [7], not reproduced here, focusing on the simulation of a similar NGSR multi-tubular reactor.

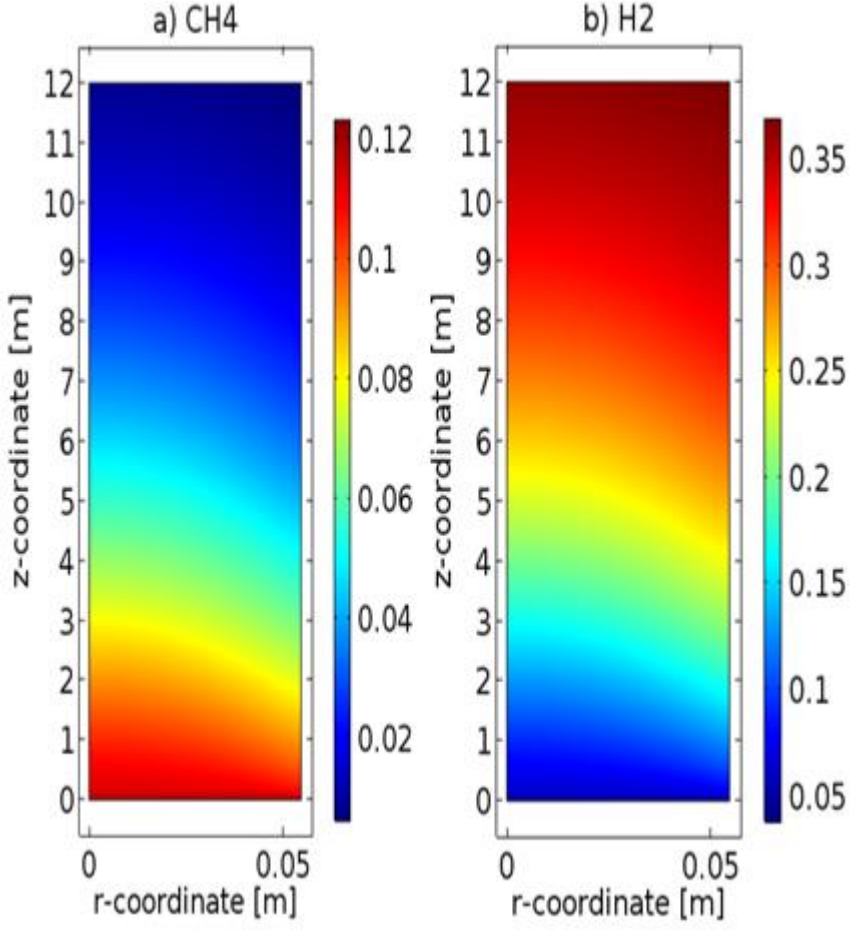

Figure 3. Simulated maps of molar fractions in the NGSR reactor a) CH_4; b) H_2

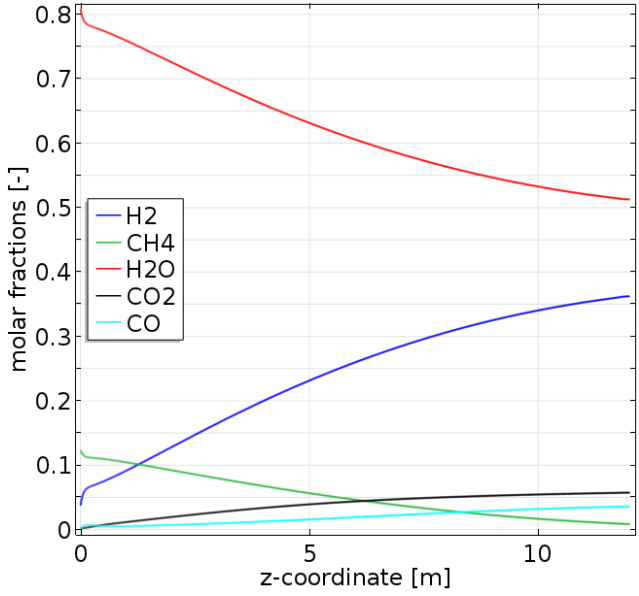

Figure 4. Simulated composition profiles along the reactor axis

Experimental data and simulation results for the reactant gas composition (on dry basis) at the outlet of the reactor are reported in Table 2 and Table 3 respectively. In both cases, compositions at thermodynamic equilibrium are reported for comparison, calculated through an independent Matlab® code implementing an interpolation of experimental data reported in the literature [10] for the calculation of the equilibrium constants $K_{p,MSR}$ and $K_{p,WGS}$. In Table 2, thermodynamic equilibrium is evaluated at the temperature measured experimentally at the outlet of the industrial reactor (1125.7 K). The results reported in Table 2 demonstrate that the reacting mixture at the outlet of the industrial multi-tubular NGSR reactor is, with very good approximation, at thermodynamic equilibrium. Minor discrepancies are ascribed to minor experimental errors or minor numerical errors in interpolating the literature experimental data of thermodynamic equilibrium. We point out that, in this case, when evaluating the thermodynamic equilibrium, the SR reactions of higher hydrocarbons are considered to be complete.

Table 2. Outlet compositions [mol%, on dry basis]. Experimental data and equilibrium values (considering complete SR of higher hydrocarbons) at 1125.7 K

Component	Experimental	Thermodynamic equilibrium
CH_4	3.26	3.26
H_2	73.97	74.01
CO	11.64	12.29
CO_2	11.11	9.86
C_2+	0	0
N_2	0.02	0.58

Table 3. Outlet compositions [mol%, on dry basis]. Simulation results and equilibrium values (neglecting SR of higher hydrocarbons) at 1103.6 K

Component	Simulation	Thermodynamic equilibrium
CH_4	1.56	1.73
H_2	74.06	74.1
CO	7.33	8.55
CO_2	11.76	10.86
C_2+	3.99	4.00
N_2	0.74	0.76

On the other hand, in Table 3, thermodynamic equilibrium is evaluated at the temperature evaluated by the simulation model at the outlet of the industrial reactor (1103.6 K). Table 3 demonstrates that also the simulation model predicts that the reacting mixture is at thermodynamic equilibrium at the outlet of the reactor. In this case, discrepancies are mainly due to discrepancies between the algorithms implemented in COMSOL and in Matlab for the evaluation of $K_{p,MSR}$ and $K_{p,WGS}$. In this case, when evaluating the compositions at thermodynamic equilibrium, SR reactions of higher hydrocarbons are neglected, since this is the basic assumption made in developing the simulation code.

Even if the simulation model well captures the attainment of thermodynamic equilibrium at the outlet of the reactor demonstrated by the experimental data reported in Table 2, nevertheless some discrepancies arise between these experimental data and the simulated outlet compositions. In particular, even if Table 2 and Table 3 display a good agreement between simulation results and industrial NGSR experimental data for the molar fraction of the reaction products (hydrogen and carbon dioxide), nevertheless, the amount of unreacted methane at the outlet of the reactor is about the double in the experimental reactor than in the simulated results. This difference is mainly due to the hypothesis of neglecting the SR of higher hydrocarbons made in developing the simulation model.

5 Conclusions and future developments

We are developing methods for early prediction and detection of faults in chemical reactors based on numerical tools for the steady-state and transient reactor simulation. In this paper, we present a steady-state model for an industrial multi-tubular NGSR reactor. The model includes mass, energy and momentum balances, coupled to a local kinetics for the MSR and WGS reactions. The model equations are integrated through the COMSOL Multiphysics software, version 5.2. The model results are 2-D maps of temperature and compositions, which are validated against reference literature results and also experimental data provided by a full-size NGSR reactor built and operated at the refinery Iplom. Future developments for this work are planned in terms of: (i) refinement of the kinetic subroutine of the model to include the SR of higher hydrocarbons (ethane, propane, butane, pentane and C_{5+}); (ii) refinement of the kinetic subroutine of the model to include the simulation of coke deposition; (iii) extension to transient simulation and

(iv) use of simulated temperature and composition results under faulty and unfaulty operating conditions to produce data to train diagnostic and prognostic tools.

Acknowledgments

Dott. Stefano Rossi is acknowledged for his contribution to the simulations. Prof. Guido Busca and Prof. Gabriella Garbarino of the University of Genoa are acknowledged for fruitful discussions during this work.

References

[1] S. H. Chan, and H. M. Wang, "Effect of natural gas composition on autothermal fuel reforming products", Fuel Processing Technology, vol. 64, pp. 221–239, 2000.
[2] S. Helveg, J. Sehested, and J. R. Rostrup-Nielsen, "Whisker carbon in perspective", Catalysis Today, vol. 178, pp. 42–46, 2011.
[3] D. L. Trimm, "Catalysts for the control of coking during steam reforming", Catalysis Today, vol. 49, pp. 3–10, 1999.
[4] F. Pugliese, A. Trucco, G. Moser, and P. Costamagna, "Diagnostics and Prognostics-Oriented Modeling of an NGSR Fuel Processor for Application in SOFC Systems", Fuel Cells (in press).
[5] V. Venkatasubramanian, R. Rengaswamy, K. Yin, and S. N. Kaviri, "A review of process fault detection and diagnosis: Part I: Quantitative model-based methods" Computers & Chemical Engineering, vol. 27, pp. 293–311, 2003.
[6] J. Xu and G.F. Froment, "Methane steam reforming: II. Diffusional limitations and reactor simulation", AIChE Journal, vol. 35, pp. 97–103, (1989).
[7] G. Pantoleontos, E. S. Kikkinides, and M. C. Georgiadis, "A heterogeneous dynamic model for the simulation and optimisation of the steam methane reforming reactor", International Journal of Hydrogen Energy, vol. 37, pp. 16346–16358, 2012.
[8] A.F. Mills, Heat Transfer, Second Edition, Prentice-Hall, New Jersey, 1999
[9] COMSOL Multiphysics, can be found under http://www.comsol.com/comsol-multiphysics, 2017.
[10] J. R. Rostrup-Nielsen, Catalysis Science and Technology, Vol. 5. New York: Springer-Verlag, 1984

10TH INTERNATIONAL CONFERENCE ON SUSTAINABLE ENERGY AND ENVIRONMENTAL PROTECTION (JUNE 27TH – 30TH, 2017, BLED, SLOVENIA), MODELLING AND SIMULATION
J. Krope, A.Ghani Olabi, D. Goričanec & S. Božičnik

University of Maribor Press

Energy Recovery Optimization of an Ammonia-Water Power Cooling Cycle Using Exergy-Pinch Method

JOUAN RASHIDI, POUYA IFAEI, CHANGKYOO YOO & JEONG TAI KIM

Abstract This study combines Pinch and Exergy approach to analyse a new combined power and cooling cogeneration with ejector absorption refrigeration cycle. The cycle, Kalina power-cooling with ejector (KPCE), combines Kalina cycle and ejector absorption refrigeration cycle with ammonia-water mixture as the working fluid to produce power and refrigeration outputs simultaneously. In this study inefficiencies and losses are identified through exergy and pinch analyses. The total exergy loss for the equipment is quantified to find the potential of equipment improvement. Additional losses of energy due to the inefficient heat recovery design of the system are then identified by cross pinch heat in the process. Evaporator, condenser, and the first flash tank preheater devoted the highest potential of improvement from exergy analysis and four preheaters showed inefficient design of the heat recovery through pinch analysis. After redesigning, the optimized KPCE showed 8% and 11% increase in power-cooling efficiency and exergetic efficiency, respectively.

Keywords: • Ejector, • Energy recovery • Exergy • Kalina cycle • Pinch •

CORRESPONDENCE ADDRESS: Jouan Rashidi, Ph.D. student, Kyung Hee University, Department of environmental science and engineering, Suwon-si, Gyeongi-do, South Korea, e-mail: jouanra@khu.ac.kr. Pouya Ifaei, Ph.D. student, Kyung Hee University, Department of environmental science and engineering, Suwon-si, Gyeongi-do, South Korea, e-mail: pooya_if@hotmail.com. Changkyoo Yoo, Ph.D., Professor, Kyung Hee University, Department of environmental science and engineering, Suwon-si, Gyeongi-do, South Korea, e-mail: ckyoo@khu.ac.kr. Jeong Tai Kim, Ph.D., Professor, Kyung Hee University, Department of agricultural engineering, Suwon-si, Gyeongi-do, South Korea, e-mail: jtkim@khu.ac.kr.

https://doi.org/10.18690/978-961-286-058-5.5 ISBN 978-961-286-058-5

Available at: http://press.um.si.

1 Introduction

The low quality and free energy source such as industrial waste heat can be recovered and used in power as well as cooling production systems. Several researchers have studied the power production performance using low grade heat sources with concentrating on unconventional working fluids such as ammonia-water mixture in Rankine, Kalina or other cycles [1, 2]. Ammonia-water evaporates and condenses as a non-azeotropic mixture, over a range of temperature; therefore, it is enable to achieve a better temperature match between the working substance and the heat sources.

Kalina cycle (KC), introduced by Alexander Kalina, is a fairly new thermodynamic power cycle using ammonia-water mixture with potential to accomplish efficient energy conversion of the low-grade heat sources; Low-temperature geothermal energy [3], solar energy [4], and industrial waste heat [5].

Utilizing and recovering of low-grade heat for cooling purpose have been performed by various thermodynamic cycles, such as absorption, adsorption, desiccant and ejection cycles [6].

Power and cooling cogeneration systems utilizing low grade heat sources have been studied by various researchers. Rashidi et al., have introduced a high efficient power-cooling cycle integrating Kalina and absorption refrigeration cycles to produce both outputs simultaneously [7]. They reported a power-cooling efficiency of 18.8%. With the same propose the performance of a combined Rankine cycle with ejector has been investigated [8]. Dai et al., proposed a system combined the Rankine cycle and the ejector-refrigeration cycle by adding a turbine between the generator and the ejector [9]. The performance of different working fluids in a combined organic Rankine cycle and ejector refrigeration cycle has been studied [10]. Li et al. proposed a Kalina cycle where the ejector has been used to substitute for the throttle valve and the absorber [11]. The ejector could increase the pressure difference of working fluid; therefore, the cycle could obtain higher thermal efficiency.

Pinch Analysis (PA) and Exergy Analysis (EA), are two powerful analytical methods to identify and select concrete technical solutions for improving efficiencies and providing optimum manufacturing solutions [12]. Pinch analysis with the idea of setting targets prior to design were first introduced and developed in the late 1970s. It has reported significant changes in energy saving and several applications in chemical process industries [13]. Researchers have done studies on using PA in various power plants to simulate and modify the existing sites [14]. EA can obtain a deeper insight with regard to process efficiency and potential to improve energy utilization [15]. It has been applied since 1975 toward the design, modelling, simulation, and performance evaluation of systems [16-18]. Exergy can be a key parameter toward improving engineering systems by determining true efficiencies through consideration of the surroundings [19].

According to literature studies on performance of the combined Kalina and ejector cycle as a power-cooling cycle is rare. In this paper, we introduce the Kalina power-cooling cycle with ejector. The performance of the system is analysed using exergy analysis to find the total avoidable and unavoidable exergy losses. The equipment is quantified according to exergy losses to find the potential of equipment improvement. Additional losses of energy due to the inefficient heat recovery design of the system are identified through pinch analysis. According to losses which are identified by EA and PA the process is redesigned to improve the performance of equipment and eliminate the cross heat transfer.

2 Method and materials

2.1 System Configuration

Figure 1 shows a schematic of the proposed system, Kalina power-cooling cycle with ejector, KPCE. The cycle is a combination of KC and ejector absorption refrigeration cycle to produce power and cooling simultaneously. After the condenser the working fluid (stream 17) enters to the ejector to decrease the pressure drop inefficiencies and increase the cooling subsystem performance. Two inputs are considered to pass the ejector; primary flow which is a portion of condensed working fluid, and secondary flow which is a portion of evaporated working fluid in cooling subsystem. The output of ejector at state 18 generates cooling through the evaporator. Following cooling generation, the working fluid (state 31) is divided in two parts to be recycled in the system; one enters the ejector as the secondary flow (state 31) and the other one is absorbed by the absorber (state 33). The primary concentration (X_{ABS}) within an intermediate range (47%) at state 1 leaves the absorber and is separated through the flash tank to the highest (X_{TUR}) and lowest (X_{LOW}) concentration streams (step 4→5, 15). The solution with a concentration of X_{TUR} is divided into two portions to produce power and cooling through turbine and evaporator, respectively. Cycling the working fluid heat recovery happens in two heat exchangers (FTP1 and FTP2) before separation in the flash tank and in another heat exchanger (PH) after the before condensation.

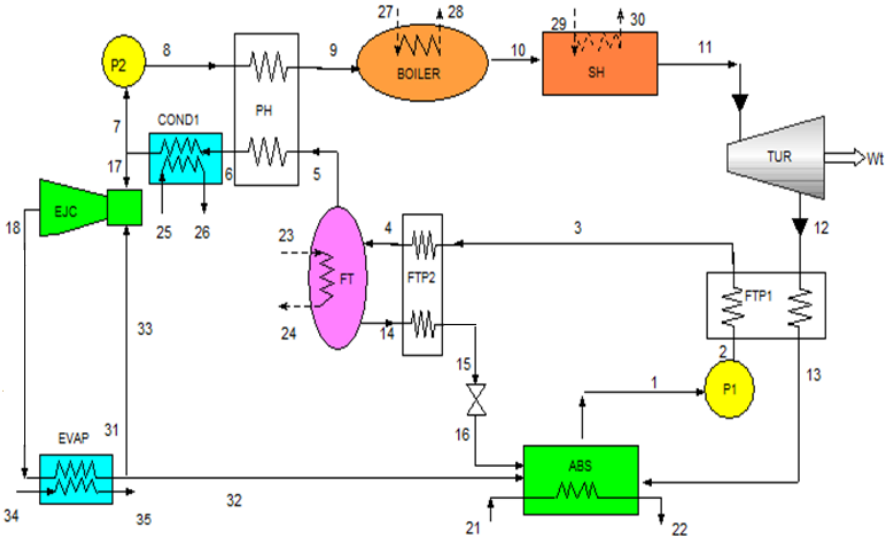

Figure 1. Schematic representation of Kalina power-cooling cycle with ejector (KPCE)

2.2 Exergy Analysis

The exergy of a system is the maximum work that can be performed by a system considering a specified reference environment as a dead state. The reference environment is assumed to be infinite, in equilibrium, and enclosed to all other systems [20]. Physical exergy is the maximum theoretical useful work that can be performed when the system is brought into physical equilibrium with the environment and chemical exergy is the separation of the chemical composition of a system from its chemical equilibrium [21]. Applying the first and second laws of thermodynamics, the following exergy balance is obtained:

$$\dot{E}x_Q + \sum_i \dot{m}_i ex_i = \sum_e \dot{m}_e ex_e + \dot{E}x_W + \dot{E}x_D \qquad (1)$$

where subscripts *e* and *i* represent the inlet and outlet specific exergy of the control volume, respectively. $\dot{E}x_D$, $\dot{E}x_Q$, and $\dot{E}x_W$ are related to exergy destruction, exergy of heat transfer, and exergy of work which cross the boundary, respectively. $\dot{E}x_Q$ and $\dot{E}x_W$ are obtained from equations. (2) and (3):

$$\dot{E}x_Q = \left(1 - \frac{T_0}{T}\right) Q_i \qquad (2)$$

$$\dot{E}x_w = \dot{W} \tag{3}$$

The term *Ex* is defined as follows:

$$\dot{E}x = \dot{E}x_{ph} + \dot{E}x_{ch} \tag{4}$$

$$\dot{E}x_{ph} = \dot{m} \cdot \left(h - h_0\right) - T_0\left(s - s_0\right) \tag{5}$$

where, $\dot{E}x_{ph}$ is the physical exergy, $\dot{m}$ is the mass flow rate (kg/s), *h* is the specific enthalpy, *s* is the specific entropy, *T* is the absolute temperature (K), and ($_0$) refers to the ambient state [21].

Since the concentration of NH3-H2O varies through the cycle, chemical exergy of working fluid also vary. It can be obtained as follows:

$$\dot{E}x_{ch} = x.\frac{ex_{NH_3}}{M_{NH_3}} + \left(1 - x\right)\frac{ex_{H_2O}}{M_{H_2O}} \tag{6}$$

where ex_{NH3}, ex_{H2O}, M_{NH3}, and M_{H2O} are the standard molar specific chemical exergies and molecular mass of ammonia and water, respectively [22]. The exergy destruction and exergy efficiency of each component of the cycle can be obtained using equations (7) and (8), respectively[23].

$$\dot{E}x_{D,k} = F_k - P_k \tag{7}$$

$$\eta_{ex} = P_k / F_k \tag{8}$$

where *F*, *P*, and *K* refer to the fuel, products, and components. The overall exergetic efficiency and exergy loss of the cycle can be calculated as follows:

$$\eta_{ex,total} = E\dot{x}_w / E\dot{x}_Q \tag{9}$$

$$E\dot{x}_{loss} = E\dot{x}_Q - E\dot{x}_w \tag{10}$$

2.3 Pinch Analysis

PA has become a general methodology for the targeting and design of thermal and chemical processes, and associated utilities. When considering the energy efficiency of a process, pinch-based approaches target the identification of the possible energy recovery by heat exchange, and define the Minimum Energy Requirement (MER) of the process. The Composite Curves (CC) and the Grand Composite Curve (GCC) are two basic tools in PA, and they are constructed using temperature versus enthalpy axes[12]. The MER targeting procedure with CC is shown in Figure 2. The energy targeting in PA set by the CC and GCC are only in terms of heat loads. However, to deal with systems involving heat and power, the concepts of both the CC and the GCC should be extended.

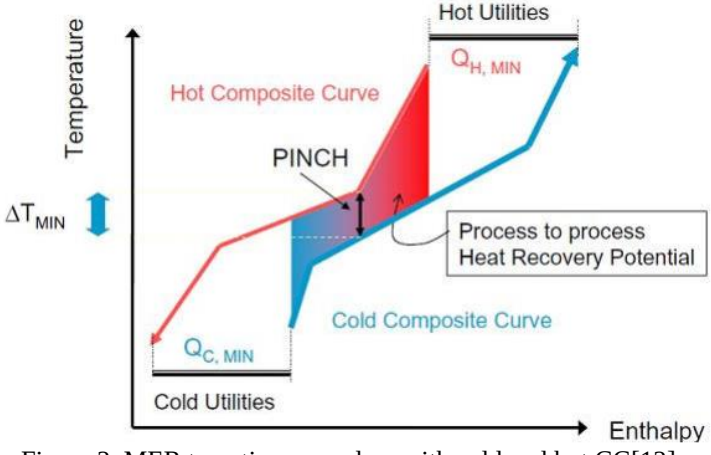

Figure 2. MER targeting procedure with cold and hot CC[12]

3 Result and discussion

Using the thermodynamic properties and definitions for fuel, product, and losses presented in equations (1)-(10), exergy analysis was performed to calculate the exergy destruction, exergetic efficiency, and total exergy loss of KPCE components. The input conditions for are shown in Table 1, including the ammonia mass fractions, mass flow rates, pressure and temperature levels, and mass ratios.

Table 1. Reference input condition of KPCE system

Parameter	Unit	Value
Turbine pressure (P_{TUR})	kPa	1500
Intermediate pressure (P_{FT})	kPa	470
Absorber pressure (P_{ABS})	kPa	80
Evaporator pressure (P_{EVAP})	kPa	200
Desorber pressure (P_{DES})	kPa	7.445
Turbine ammonia mass fraction (X_{TUR})	%	72
Absorber mass flow rate	Kg/s	4
Turbine temperature (T_{TUR})	°C	280
Absorber temperature (T_{ABS})	°C	20

The exergy destruction of components is demonstrated in figure 3. As can be seen FTP2, condenser, and evaporator have the major exergy destruction quantities among all components. The cycle showed the total exergy efficiency and the total exergy destruction equal to 20% and 972kw, respectively.

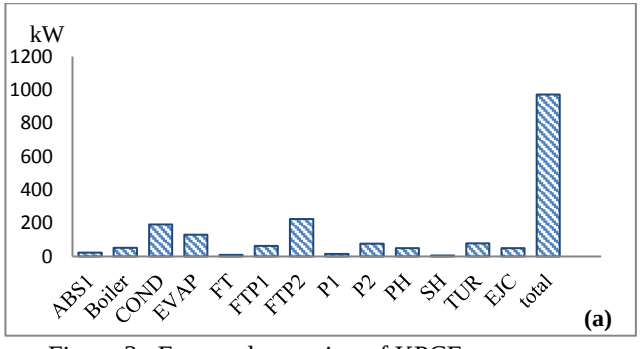

Figure 3. Exergy destruction of KPCE components

Figure 4 is a diagram of the system with the supply and target temperatures in degree of Celsius. C and H refer to cold and hot utilities which are cold water and steam. The figure also presents the streams with their numbers that have been described in Table 2.

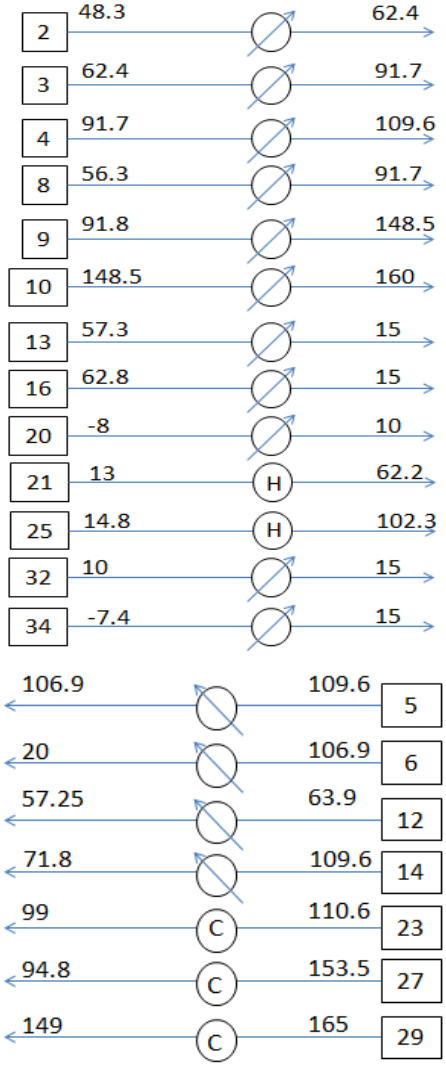

Figure 4. Diagram of the heat exchanger network of KPCE system

Table 2. Stream data of the heat exchanger network in the KPCE system

stream	type	ΔT	ΔH	C_p (kw/°C)
2	cold	14.1	235.03	16.66879
3	cold	29.3	468.6	15.99317
4	cold	17.9	1146.5	64.05028
5	hot	-2.7	-101	37.40741
6	hot	-86.9	-1498	17.2382
8	cold	35.4	609.7	17.22316
9	cold	56.7	998.3	17.6067
10	cold	11.5	31	2.695652
12	hot	-6.67	-215	32.23388
13	hot	-42.3	-1225.1	28.96217
14	hot	-37.79	-162.1	4.289495
16	hot	-47.8	-84.6	1.769874
20	cold	18	388	21.55556
21	cold	49.2	885.3	17.9939
23	hot	-11.6	-2384	205.5172
25	cold	87.45	2618.6	29.9442
27	hot	-58.63	-2386	40.69589
29	hot	-15.7	-31	1.974522
32	hot	-3	-607.6	202.5333
34	hot	-22.37	-637	28.47564

Table 2 summarizes the target temperature difference (ΔT) of heat exchanger network streams as well as their corresponding enthalpy difference (ΔH). In the last column C_p is the ratio of ΔH to ΔT. to continue the pinch analysis the minimum temperature difference ΔT_{min} is set to 10°C. After finding the pinch point and redesigning the heat exchanger network the required hot utility decreased from 4201 kw to 3300kw also the required cold utility dropped from 7594kw to 4910kw. The system before modification had several pinch problems where cold stream crossed hot stream in 4 points. Obtaining these results the modified KPCE system has been analysed from exergy point again. The new system demonstrates an exergy destruction decrease in all components especially for evaporator, condenser, and FTP2.

Figure 5a shows the comparison between exergy destruction of KPCE system before and after modification. As can be seen total exergy destruction has been dropped around 10%. Figure 5b compares the power-cooling and exergetic efficiencies of KPCE before and after optimization. It can be seen, power-cooling efficiency has increased by 8% and exergetic efficiency encounters an increment of 11%.

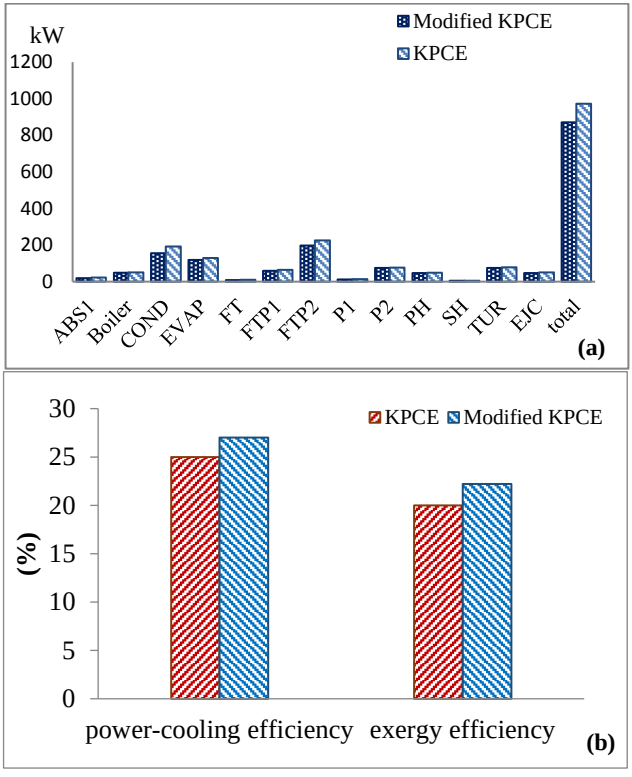

Figure 5. comparison between (a) component exergy destruction and (b) power cooling and exergy efficiencies of KPCE and modified KPCE system

4 Conclusion

Pinch and Exergy analyses are performed in this study to optimize the performance of a power and cogeneration system which combines Kalina cycle with and ejector absorption refrigeration cycle called KPCE, Kalina power-cooling cycle with ejector. The system uses ammonia-water mixture as the working fluid to produce power and refrigeration outputs simultaneously. Using both exergy and pinch analysis inefficiencies of components as well as heat exchanger network are identified. Exergy analysis identified three components including evaporator, condenser, and FTP1 corresponded with the highest exergy destruction among all components. Using pinch method, cross heat pinch points were detected and the heat exchanger network was redesigned in order to decrease losses through heat recovery in the cycle. By cycle modification and optimization, the optimized KPCE achieved 8% and 11% increase in power-cooling efficiency and exergetic efficiency, respectively.

Acknowledgements

This work was supported by a National Research Foundation of Korea (NRF) grant funded by the Korean Government (MSIP) (No.2015R1A2A2 A11001120).

References

[1] A. Nemati, H. Nami, F. Ranjbar, M. Yari, A comparative thermodynamic analysis of ORC and Kalina cycles for waste heat recovery: A case study for CGAM cogeneration system, Case Studies in Thermal Engineering, 9 (2017) 1-13.
[2] T. Eller, F. Heberle, D. Brüggemann, Second law analysis of novel working fluid pairs for waste heat recovery by the Kalina cycle, Energy, 119 (2017) 188-198.
[3] H. Saffari, S. Sadeghi, M. Khoshzat, P. Mehregan, Thermodynamic analysis and optimization of a geothermal Kalina cycle system using Artificial Bee Colony algorithm, Renewable Energy, 89 (2016) 154-167.
[4] F. Sun, Y. Ikegami, H. Arima, W. Zhou, Performance Analysis of the Low Temperature Solar-Boosted Power Generation System—Part II: Thermodynamic Characteristics of the Kalina Solar System, Journal of Solar Energy Engineering, 135 (2013) 011007.
[5] V. Zare, S. Mahmoudi, M. Yari, On the exergoeconomic assessment of employing Kalina cycle for GT-MHR waste heat utilization, Energy Conversion and Management, 90 (2015) 364-374.
[6] E. Aridhi, M. Abbes, A. Mami, Solutions based on renewable energy and technology to improve the performance of refrigeration systems, Journal of Renewable and Sustainable Energy, 8 (2016) 065906.
[7] J. Rashidi, P. Ifaei, I. JanghorbanEsfahani, A. Ataei, C.K. Yoo, Thermodynamic and economic studies of two new high efficient power-cooling cogeneration systems based on Kalina and absorption refrigeration cycles, Energy Conversion and Management, 127 (2016) 170-186.
[8] K. Zhang, X. Chen, C.N. Markides, Y. Yang, S. Shen, Evaluation of ejector performance for an organic Rankine cycle combined power and cooling system, Applied Energy, 184 (2016) 404-412.
[9] Y. Dai, J. Wang, L. Gao, Exergy analysis, parametric analysis and optimization for a novel combined power and ejector refrigeration cycle, applied thermal engineering, 29 (2009) 1983-1990.
[10] A. Habibzadeh, M. Rashidi, N. Galanis, Analysis of a combined power and ejector-refrigeration cycle using low temperature heat, Energy Conversion and Management, 65 (2013) 381-391.
[11] X.G. Li, Q.L. Zhang, X.J. Li, A Kalina cycle with ejector, Energy, 54 (2013) 212-219.
[12] A. Ataei, C. Yoo, Combined pinch and exergy analysis for energy efficiency optimization in a steam power plant, International Journal of Physical Sciences, 5 (2010) 1110-1123.
[13] R. Smith, Chemical process: design and integration, John Wiley & Sons, 2005.
[14] B. Linnhoff, F.J. Alanis, Integration of a new process into an existing site: a case study in the application of pinch technology, Journal of Engineering for gas turbines and power, 113 (1991) 159-169.
[15] R. Saidur, J. Ahamed, H. Masjuki, Energy, exergy and economic analysis of industrial boilers, Energy Policy, 38 (2010) 2188-2197.
[16] S.M. Sanaei, T. Furubayashi, T. Nakata, Assessment of energy utilization in Iran's industrial sector using energy and exergy analysis method, Applied Thermal Engineering, 36 (2012) 472-481.

[17] F. Zarifi, T. Mahlia, F. Motasemi, M. Shekarchian, M. Moghavvemi, Current and future energy and exergy efficiencies in the Iran's transportation sector, Energy Conversion and Management, 74 (2013) 24-34.
[18] Z. Rashidi, A. Karbassi, A. Ataei, P. Ifaei, R. Samiee-Zafarghandi, M. Mohammadizadeh, Power plant design using gas produced by waste leachate treatment plant, International Journal of Environmental Research, 6 (2012) 875-882.
[19] I. Dincer, M. Hussain, I. Al-Zaharnah, Energy and exergy utilization in transportation sector of Saudi Arabia, Applied Thermal Engineering, 24 (2004) 525-538.
[20] Ibrahim Dincer, M.A. Rosen, Exergy: energy, environment and sustainable development, Elsevier, 2007.
[21] P. Ahmadi, I. Dincer, Thermodynamic and exergoenvironmental analysis and multi-objective optimization of a gas turbine power plant, Applied Thermal Engineering, 31 (2011) 2529-2540.
[22] O.K. Singh, S.C. Kaushik, Reducing CO 2 emission and improving exergy based performance of natural gas fired combined cycle power plants by coupling Kalina cycle, Energy, 55 (2013) 1002-1013.
[23] P. Ifaei, J. Rashidi, C. Yoo, Thermoeconomic and environmental analyses of a low water consumption combined steam power plant and refrigeration chillers–Part 1: Energy and economic modelling and analysis, Energy Conversion and Management, 123 (2016) 610-624.

10TH INTERNATIONAL CONFERENCE ON SUSTAINABLE ENERGY AND ENVIRONMENTAL PROTECTION (JUNE 27TH – 30TH, 2017, BLED, SLOVENIA), MODELLING AND SIMULATION
J. Krope, A.Ghani Olabi, D. Goričanec & S. Božičnik

University of Maribor Press

Extracting Knowledge from Non-Parametric Models of Climate-Related Building Energy Use

MATJAŽ PREK, VINCENC BUTALA & GORAZD KRESE

Abstract Major discrepancies between real and modelled systems are common when modelling thermal response of buildings and the installed HVAC systems with existing simulation tools, which are based on simplified physical laws, despite the fact that their use requires detailed knowledge of the simulated system. On the other hand, supervised data-driven models are capable of high quality prediction performances, but lack the interpretability of deterministic models.

In this study, we present and analyse a methodology for discovering functional dependencies between building cooling energy use and its influential variables. The approach is based on a sensitivity analysis of non-parametric data-driven models for predicting the electricity demand of HVAC chillers, whereby we focused only on models build with the random forests ensemble machine learning algorithm.

Keywords: • building energy modelling • HVAC • data mining • sensitivity analysis • random forests •

CORRESPONDENCE ADDRESS: Matjaž Prek, Ph.D., Assistant Professor, University of Ljubljana, Faculty of Mechanical Engineering, Aškerčeva cesta 6, 1000 Ljubljana, Slovenia, e-mail: matjaz.prek@fs.uni-lj.si. Vincenc Butala, Ph.D., Professor, University of Ljubljana, Faculty of Mechanical Engineering, Aškerčeva cesta 6, 1000 Ljubljana, Slovenia, e-mail: vincenc.butala@fs.uni-lj.si. Gorazd Krese, Ph.D., Assistant, University of Ljubljana, Faculty of Mechanical Engineering, Aškerčeva cesta 6, 1000 Ljubljana, Slovenia, e-mail: gorazd.krese@fs.uni-lj.si.

https://doi.org/10.18690/978-961-286-058-5.6 ISBN 978-961-286-058-5

Available at: http://press.um.si.

1 Introduction

Buildings are responsible for 40% of energy consumption and 36% of CO_2 emissions in the European Union (EU). Currently, about 35% of the EU's buildings are over 50 years old. By improving the energy efficiency of buildings, the total EU energy consumption could be reduced by 5% to 6% and lower CO_2 emissions by about 5% [1]. Hence, reducing the energy consumption of buildings is crucial for achieving national and international goals (e.g. Paris Agreement) for reducing the greenhouse gas (GHG) emissions.

Building energy modelling has an important role in building energy conservation, since it can aid at evaluating building energy efficiency, commissioning and fault detection and diagnosis (FDD). Although building energy simulations based on physics models have been used, developed and refined since the early 1970s, simulation based assessment of building energy performance is still associated with large uncertainties. These uncertainties arise from input data uncertainties (i.e. meteorological data, geometrical data, thermo-physical properties, equipment operation scenario, and occupancy) and the uncertainties induced by the modelling assumptions which represent reality only to a certain extent [2]. The resulting discrepancy between prediction and reality can be especially pronounced when modelling complex multi-zonal buildings, with multiple uses and HVAC systems. In contrast, supervised data-driven models can make accurate predictions without much knowledge on the building geometry or the detailed physical phenomena. The only major requirement that is common to all (supervised) data-driven modelling techniques, such as artificial neural network (ANN) [3], [4] and support vector machines (SVM) [5], is a sufficiently large and diverse data set from which they can deduce the underlying functional dependencies between the building energy use and the corresponding influential variables. This requirement used to limit the applicability of data-driven modelling techniques, but developments in various fields of information and communications technology (e.g. smart metering, real-time monitoring) make data availability less of an issue today. Thus, the main issue or rather an untapped opportunity is how to extract (human) understandable knowledge from data-driven energy use models, which could potentially unveil useful insights or even help to reduce the performance gap of first-principle simulation models.

This paper aims to present and analyse a methodology for discovering functional dependencies between building cooling energy use and its influential variables, based on a sensitivity analysis of models for predicting the electricity demand of HVAC chillers build with the random forests algorithm.

2 Methods

2.1 Random Forests

Random forests (RF) [6] is an ensemble machine learning method based on decision trees. Decision trees are statistical models for solving regression and classification problems.

In a decision tree data of an output variable is iteratively partitioned based on decision rules or test functions in terms of a set of input features. The set of chosen input features in each split node indicates their importance on predicting the output variable's values. The test functions outcomes represent branches while the final split nodes, which store the final test results, are called leaves. For regions with dense data in the input space, a decision tree can have more splits to produce a finer prediction. For regions with sparse data in the input space, a tree will have a coarser prediction. RF uses a modified CART (classification and regression tree) algorithm [6], which like the original [7], can build only binary trees, i.e. the data in each node is split in exactly two parts. The speciality of the mentioned modified CART algorithm is that it limits the selection of the best predictor variables to determine the split at each node to a subset of randomly chosen candidate predictors. For regression problems the recommended number of candidate predictors according to [8] is:

$$m = a/3 \tag{1}$$

where, m is the number of randomly selected candidate predictor variables and a is the number of all possible predictors.

The RF algorithm generates a series of individual decision trees (usually at least 100) and aggregates their predictions to obtain the final prediction. The training algorithm is based on bagging (bootstrap aggregating) [9], where a sample of observations, called bootstrap, is randomly selected with replacement from the training set. The bootstrap samples contain on average 63.2 % [9] of different observations from the training set. The omitted cases from each bootstrap are called out-of-bag (OOB) data [6], [9]. The RF algorithm uses OOB examples in an internal cross-validation to calculate an unbiased estimate of the generalization error or the so-called out-of the bag error:

$$err_{OOB} = \frac{1}{n}\sum_{i=1}^{n}\left(y_i - \bar{\bar{y}}_{i,OOB}\right)^2 \tag{2}$$

where, err_{OBB} is the OOB error, n is the number of examples in the training set, y_i is the value of the output variable for the i-th observation and $\bar{\bar{y}}_{i,OOB}$ is the mean prediction for the i-th observation of the decision trees trained on a bootstrap sample not containing the i-th sample.

OOB samples are also used to determine the variable importance. In this case the OOB values for each variable in a bootstrap sample are randomly permuted. The importance is then measured as the difference between the prediction accuracy before and after the permutation and averaged over all the trees [10]:

$$I_v\left(X_j\right)=\frac{1}{n_t}\sum_{t=1}^{n_t}\left(err_{OOB,t}^{j}-err_{OOB,t}\right) \tag{3}$$

where, $I_v(X_j)$ is the importance of the *i*-th variable, n_t is the number of generated decision trees, $err^j_{OOB,t}$ is the OOB error of the *t*-th decisions tree with the *j*-th variable permuted randomly over its OOB sample and $err_{OOB,t}$ is the OOB error of the *t*-th decisions tree.

To conclude, the main advantages of the RF algorithm, apart from the mentioned built-in mechanisms for estimating the generalization error and the variable importance, is its speed, ease of use (i.e. only two parameters to tune; m and n_t), the ability to handle missing values and its robustness to noise as well as to over fitting [11]. However, RF has a downside common to all non-parametric machine learning methods, namely the incomprehensibility of the build models.

2.2 Sensitivity Analysis

To tackle the incomprehensibility of the RF models we resorted to the methodology proposed by Cortez and Embrechts [12], [13] for extracting human understandable knowledge from non-parametric data-driven models based on visualizing the results of a Sensitivity Analysis (SA). Namely, we decided for the application of the Cluster-based SA (CSA) and the Data-based SA (DSA) approaches, which are briefly summarised in the following subsection.

Cluster-based SA

CSA examines the influence of an input variable X_j on the target (dependant) variable Y, whose values are predicted with the model $\hat{Y}=f(\boldsymbol{X})$, through the following steps:

(i) Store the predicted values of the build model for the whole training dataset.
(ii) For a selected input variable define the number of clusters L and determine their boundaries based on its minimum and maximum values.
(iii) Allocate the vectors of the training data values for the model input variables and the corresponding predictions into the clusters defined for the currently examined input variable.
(iv) Aggregate the model predictions corresponding to each cluster of the examined input variable according to the chosen sensitivity response aggregation function.

The following sensitivity response aggregation functions are proposed by the authors [13]:

$$\hat{y}_{ave}\left(X_j^{\,L}\right)=\frac{1}{n_L}\sum_{i=1}^{n_L}x_{j,i} \tag{4}$$

$$\hat{y}_{\max}\left(X_j^L\right) = \max\left\{x_{j,1},\ldots x_{j,i},\ldots x_{j,n_L}\right\} \tag{5}$$

$$\hat{y}_{\min}\left(X_j^L\right) = \min\left\{x_{j,1},\ldots x_{j,i},\ldots x_{j,n_L}\right\} \tag{6}$$

where, $\hat{y}_{ave}(X_j^L)$ is the average predicted value in the L-th cluster corresponding to the examined input variable X_j, $\hat{y}_{max}(X_j^L)$ and $\hat{y}_{min}(X_j^L)$ are analogously the maximal and minimal predicted value in the L-th cluster, and n_L is number of training samples allocated to the L-th cluster.

The main challenge in applying CSA is determining the number of clusters. Since input variables values generally have different distributions, choosing the same number of cluster for all variables can result in empty cluster subsets for individual variables. We resolved this issue by using the Freedman–Diaconis rule [14] to determine the number of clusters for each input variable:

$$H_j = \frac{2 \cdot IQR(X_j)}{\sqrt[3]{n}} \tag{7}$$

$$L_j == \frac{\max(X_j) - \min(X_j)}{H_j} \tag{8}$$

where, H_j is the cluster width of the j-th input variable, IQR is interquartile range and L_j is the selected number of clusters for the j-th input variable.

Data-based SA

DSA examines the influence of an input variable X_j on the target (dependant) variable Y, whose values are predicted with the model $\hat{Y}=f(\boldsymbol{X})$, through the following steps:

(i) For a selected input variable define the number of levels L and determine their boundaries based on its minimum and maximum values.
(ii) From the training dataset randomly select N_s examples and replace the values of the input variable X_j with the level at which its influence on Y is examined.
(iii) With the considered model predict and store the values of the target variable Y on the chosen N_s samples.
(iv) Aggregate the predicted values corresponding to each level of the examined input variable according to the chosen sensitivity response aggregation function.
(v) Repeat steps (i)-(iv) for each level of the examined input variable.

The main disadvantage of the DSA method is that it does not consider the possible relations between the input variables. Hence, there is a risk that we get unrepresentative or physically impossible combinations of input variables values. For this reason our version of the algorithm for executing DSA includes an additional mechanism for restricting the combinations of input variables value.

3 Data

For the analysis two tertiary sector buildings, for which electrical demand of HVAC system components in 15-minute intervals was collected within the IEE project ISERVcmb [15], were chosen. The corresponding meteorological data at 30-minute resolution was obtained from a local weather station. To maintain the anonymity of the selected buildings they are hereinafter referred to only as buildings P_1 and P_2.

Both office buildings are located in Ljubljana and are orientated in a northwest-southeast direction. The HVAC systems serving the buildings provide the same thermal comfort service, i.e. cooling and ventilation while humidity is allowed to free float. In both buildings ventilation is provided by single duct (SD) constant air volume (CAV) air handling units which also remove the cooling load in combination with fan coil units (FCUs). Additional information about the selected buildings and the installed HVAC systems is listed in Table 4.

Table 4. Building and HVAC systems description

Building	P_1	P_2
Location	Ljubljana	
Building type	Office	
Number of floors	2	6
Area conditioned [m^2]	1438	7171
Volume conditioned [m^3]	3664	20080
Glazing ratio [1]	0.108	0.371
Roof ratio [1]	0.771	0.230
C/A_w* [Wh/m^2K]	40.62	37.67
HVAC system	SD CAV AHU + FCUs	6 SD CAV AHU + FCUs
Chiller type	air cooled vapour-comp. liq. chiller	3 air cooled vapour-comp. liq. chiller
Cooling capacity [kW]	122.2	120/120/182
EER	2.8	3.58/3.58/3.67

* - heat capacity per unit of wall area

Since in both cases the AHU(s) and FCUs are served by the same vapour-compression liquid chiller(s), chiller electricity demand E was chosen as the target variable for the modelling process (i.e. to serve as the substitute for the overall cooling load). The used

data sets consisted from measurements for the whole year 2012; hence they contained both winter and summer operation. As the considered chillers are not in operation during the winter regime or are in standby mode, the first step of pre-processing was to remove the data points corresponding to this subset (Figure 4). Additionally, non-working days (weekends and holydays) were filtered out to avoid occupancy variation and consequently to isolate the influence of external (i.e. climate-related) heat gains.

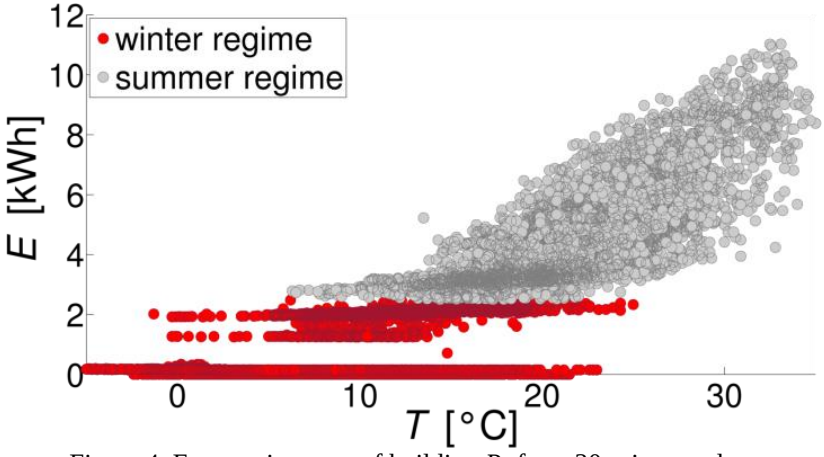

Figure 4. Energy signature of building P_1 from 30-minute values

4 Results

For each building two RF models were built. Namely, one trained on half-hourly measured values of the chiller(s) electric energy use and the one trained on hourly values of the latter, whereby the following meteorological variables were chosen as the candidate input variables:

- the outdoor air temperature T (for the inclusion of the transmission and sensible ventilation heat gains),
- the global (total) solar radiation on a horizontal surface G_{glob} (for the inclusion of the solar heat gains),
- and the outdoor air absolute humidity x (for the inclusion of the latent heat gains).

  Based on a parameter tuning analysis the subsequent values were chosen for the modelling process:
- n_t=1000, m=2.

CSA was applied first to extract knowledge from the build RF models. The results of the analysis were visualised in the form of so-called Variable Effect Characteristic (VEC) curves [13], which are simply plots of the model's response against the corresponding (level) values of the input variable whose influence is being examined. All of the obtained

CSA VEC curves exhibit distinctly discontinuous changes in the model's response (i.e. predicted chiller energy use), whereby the VEC curves for absolute humidity are the most prominent (Figure 5a). The reason for these deviations lies in the very definition of the CSA, where we are limited only to the input variables values present in the training dataset. Thus some clusters, resulting from the allocation of the training data values vectors, may have a too small variable's values domain (Figure 5). Because of this limitation a more detailed analysis of the CSA results was meaningless in our case.

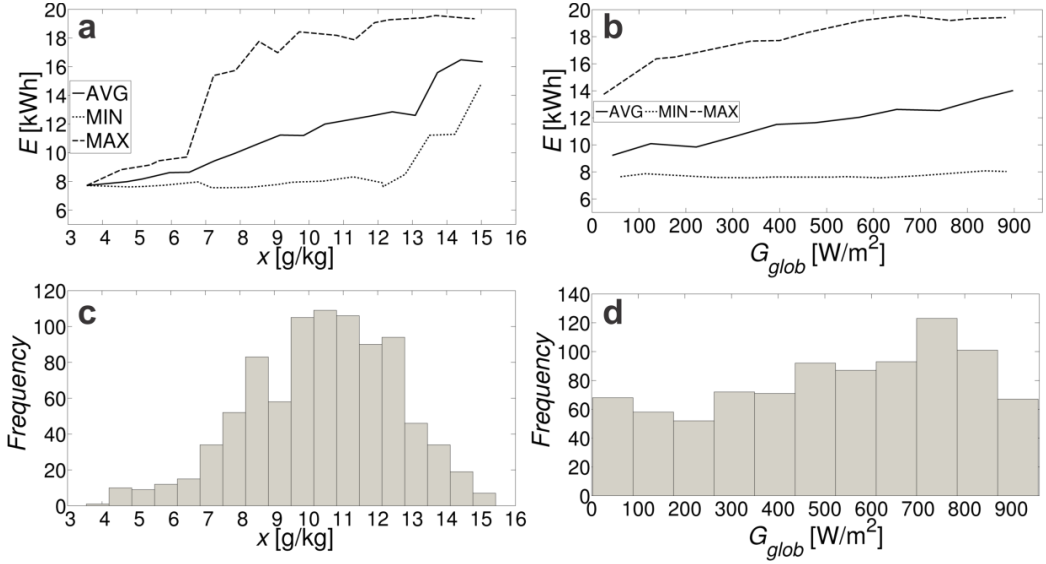

Figure 5. CSA VEC curves analysis of the building P_1's hourly data based model: (a) VEC for absolute humidity; (b) VEC for solar radiation; (c) value distribution of absolute humidity clusters; (d) value distribution of solar radiation clusters

In contrast to CSA, where the number of clusters or levels for each input variable was determined by applying the Freedman–Diaconis rule, we decide to use 31 levels for all input variables due to the significantly larger number of examples associated with each input level. The so obtained VEC curves (Figure 6) coincide well with the RF variable importance estimates, i.e. outdoor temperature the most influential variable, while solar radiation variation has the smallest impact on the model response. The only exception is the behaviour of the VEC curve for solar radiation of the building's *P2* hourly data based model (Figure 7), where at around 500 W/m^2 an almost stepwise change of the aggregated maximal response (Equation (5)) curve occurs. This anomaly is the consequence of the examples used for determining the model response during the DSA. In this case specifically, by changing the solar radiation values of the training examples we obtained data points outside the training region of the model (Figure 8). Hence, the model performed extrapolation. If the deviant data points are in the minority, this issue can be alleviated by using a sensitivity response aggregation function based on a combination of multiple predictions, e.g. the average predicted value for an input level (Equation (4)).

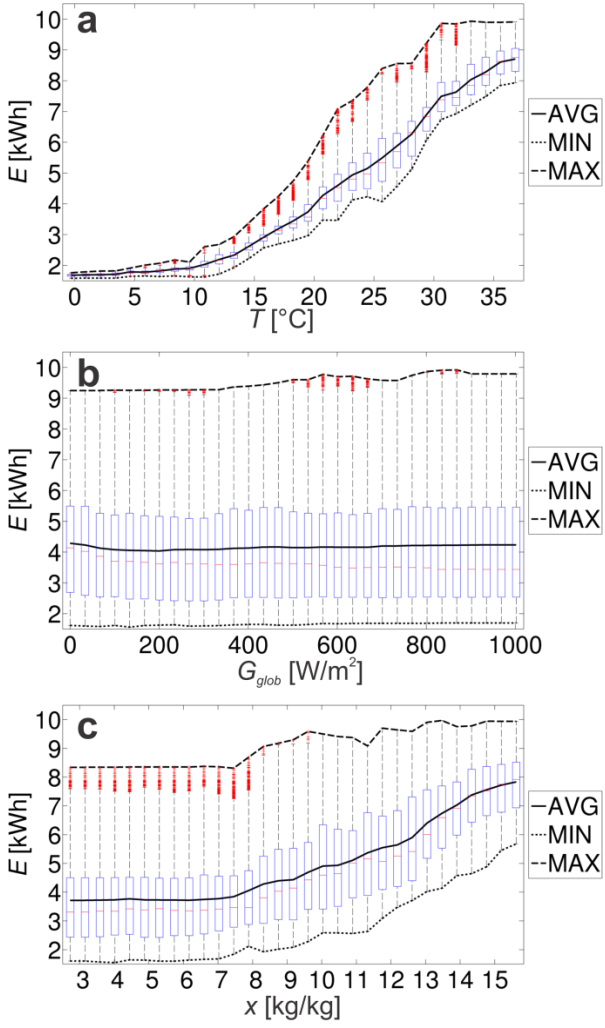

Figure 6. DSA VEC curves of the building *P1*'s half hourly data based model for: (a) outdoor temperature; (b) solar radiation; (c) absolute humidity

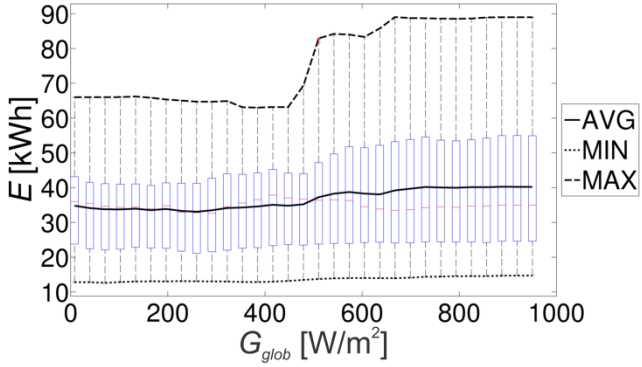

Figure 7. DSA VEC curve of the building P_2's hourly data based model for solar radiation

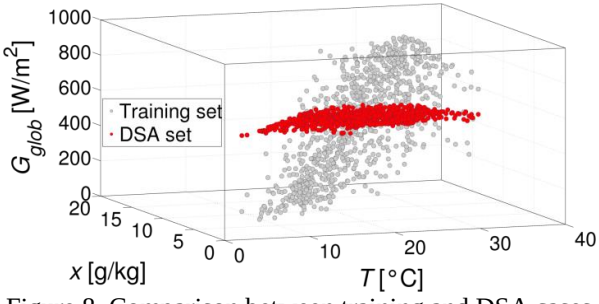

Figure 8. Comparison between training and DSA cases

From outdoor temperature VEC curves (Figure 6a) it was also evident that the modelled HVAC systems are undersized with regard to the cooling loads, because of the energy use stagnation at higher temperatures. Moreover, it can also be observed that the range of sensitivity increases along with increasing temperature (excluding the mentioned stagnating part at high temperatures). According to [13] this indicates that the output variable depends more on input interactions rather than single input effects. This cannot be confirmed from the VEC curves for solar radiation (Figure 6b). However, the absolute humidity VEC curves (Figure 6c) of all the examined models, after an initial stagnation, display an increase in the predicted values from some threshold value, which partly coincides with the increase of the corresponding temperature VEC curves range of sensitivity. In our case the mechanism for restricting the combinations of input variables values, included in our version of the algorithm for executing DSA, has a more evident effect on the dispersion of predicted values. In particular, the mechanism allows a temperature value change only if the resulting temperature is greater than or equal to the dew point temperature corresponding to the absolute humidity of the considered data point. Due to this restriction the lower temperature levels contain significantly less data points than the higher temperature levels (Figure 9), thus resulting also in a smaller dispersion of the predicted values.

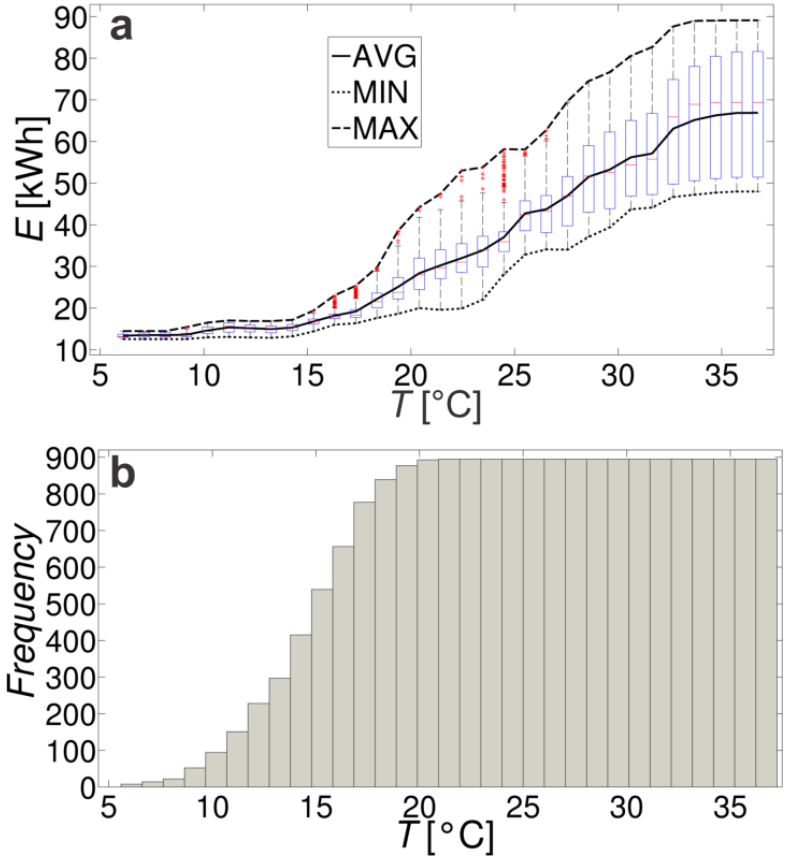

Figure 9. Distribution of the outdoor temperature values for the DSA of the building P_2's hourly data based model

5 Conclusions

In this work, we presented and analysed an approach, based on sensitivity analysis, for extracting knowledge from non-parametric models of climate-related building energy use. For this purpose four RF models, on two different time scales, were trained on measured electric energy use of two tertiary sector buildings chillers, whereby influential meteorological variables were selected as the candidate input variables.

In order to reveal the functional dependencies learned by the build RF models we applied two SA based visualization techniques, proposed in [12][13], for extracting human understandable knowledge from non-parametric regression (and classification) models. Specifically, we used the so-called Cluster-based SA (CSA) and the Data-based SA

(DSA), whereby the first proved to be unsuitable due to the non-uniform distribution of the used (measured) chiller energy consumption.

Although the relationships visualized through the application of the DSA coincided well with the RF variable importance estimates, issues regarding the data (points) for determining the model responses at different input variable levels were also detected. Despite the inclusion of a mechanism for restricting the combinations of the input variables values in the DSA execution algorithm, data points outside the training regions of the models still occurred during the generation of the sensitivity analysis data sets.
In addition to eliminating the above-mentioned limitations of the presented approach for discovering functional dependencies between building cooling energy use and its influential variables, attention should also be paid to exploring the possibilities for performing and interpreting visualisation techniques based on multivariate sensitivity analysis.

References

[1] "Buildings - European Commission." [Online]. Available: https://ec.europa.eu/energy/en/topics/energy-efficiency/buildings. [Accessed: 27-Feb-2017].
[2] I. A. Macdonald, "Quantifying the Effects of Uncertainty in Building Simulation," Department of Mechanical Engineering, University of Strathclyde, 2002.
[3] A. E. Ben-Nakhi and M. A. Mahmoud, "Cooling load prediction for buildings using general regression neural networks," *Energy Convers. Manag.*, vol. 45, no. 13, pp. 2127–2141, 2004.
[4] S. S. K. Kwok, R. K. K. Yuen, and E. W. M. Lee, "An intelligent approach to assessing the effect of building occupancy on building cooling load prediction," *Build. Environ.*, vol. 46, no. 8, pp. 1681–1690, 2011.
[5] Q. Li, Q. Meng, J. Cai, H. Yoshino, and A. Mochida, "Applying support vector machine to predict hourly cooling load in the building," *Appl. Energy*, vol. 86, no. 10, pp. 2249–2256, 2009.
[6] L. Breiman, "Random Forests," *Mach. Learn.*, vol. 45, no. 1, pp. 5–32, 2001.
[7] S. L. Crawford and S. L., "Extensions to the CART algorithm," *Int. J. Man. Mach. Stud.*, vol. 31, no. 2, pp. 197–217, Aug. 1989.
[8] L. Breiman and A. Cutler, "Manual for Setting Up, Using, and Understanding Random Forest V4.0." [Online]. Available: https://www.stat.berkeley.edu/~breiman/Using_random_forests_v4.0.pdf. [Accessed: 25-Feb-2017].
[9] L. Breiman, "Bagging Predictors," *Mach. Learn.*, vol. 24, no. 2, pp. 123–140, 1996.
[10] T. R. Tooke, N. C. Coops, and J. Webster, "Predicting building ages from LiDAR data with random forests for building energy modeling," *Energy Build.*, vol. 68, no. Part A, pp. 603–610, 2014.
[11] M. Robnik-Sikonja, "Improving random forests," *Mach. Learn. ECML 2004*, p. 12, 2004.
[12] P. Cortez and M. J. Embrechts, "Opening black box data mining models using sensitivity analysis," *Proc. IEEE Symp. Comput. Intell. Data Min. (CIDM), 2011*, pp. 341–348, 2011.
[13] P. Cortez and M. J. Embrechts, "Using sensitivity analysis and visualization techniques to open black box data mining models," *Inf. Sci. (Ny).*, vol. 225, pp. 1–17, 2013.

[14] D. Freedman and P. Diaconis, "On the histogram as a density estimator:L 2 theory," *Zeitschrift für Wahrscheinlichkeitstheorie und Verwandte Gebiete*, vol. 57, no. 4, pp. 453–476, Dec. 1981.

[15] I. Knight, A. Konidari, A. Knight, S. Blatch, J.-L. Alexandre, A. Freire, M. Masoero, J. Toniolo, M. N. Assimakopoulos, M. Argyriou, D. Wright, M. Sheldon, V. Butala, M. Prek, J. Mandelj, P. Andre, V. Lemort, O. Mair, C. Gruber, and R. Hitchin, "The inspection of building services through continuous monitoring and benchmarking : the ISERVCMB project : ISERVCMB final report - July 2014," 2014.

10TH INTERNATIONAL CONFERENCE ON SUSTAINABLE ENERGY AND ENVIRONMENTAL PROTECTION (JUNE 27TH – 30TH, 2017, BLED, SLOVENIA), MODELLING AND SIMULATION
J. Krope, A.Ghani Olabi, D. Goričanec & S. Božičnik

University of Maribor Press

Extraction of ZnO Thin Film Parameters for ZnO/Si Solar Cells Modelling

SLIMANE CHALA, NOUREDINE SENGOUGA, FAHRETTIN YAKUPHANOĞLU, SAÂD RAHMANE, MADANI BDIRINA & İBRAHIM KARTERI

Abstract Zinc oxide (ZnO) is a semiconductor with promising electrical and optical properties. Pure ZnO is an n-type degenerate semiconductor and is almost entirely transparent in the optical region of the electromagnetic spectrum. Sol–gel spin-coating method was used to grow ZnO thin film from Zinc acetate decomposition. The optical properties were investigated to use them in simulation of a ZnO/Si heterostructure solar cell. However, the real solar cell shows poor photovoltaic performance. Numerical simulation is used to elucidate this poor performance. The same structure has been simulated, by using the experimental results, by considering the ZnO as a semiconductor with continuous distribution of states in its band gap similar to an amorphous semiconductor. The density of states model used here is composed of four bands: two tail bands and two Gaussian distribution deep level bands. Evidently the first case gave results far from reality. In the second case and by adjusting the constituents of the band gap states, it was possible to reproduce a good agreement between simulated and measured J-V characteristics of the solar cell.

Keywords: • Sol–gel • ZnO thin film • defects • solar cell • simulation •

CORRESPONDENCE ADDRESS: Slimane Chala, Ph.D. Student, University of Biskra, Physics Department, Laboratory of Metallic and Semiconducting Materials, BP 145 RP, 07000 Biskra, Algeria, e-mail: chala_slimane@yahoo.com, Nouredine Sengouga, Ph.D., Professor, University of Biskra, Physics Department, Laboratory of Metallic and Semiconducting Materials, BP 145 RP, 07000 Biskra, Algeria, e-mail: n.sengouga@univ-biskra.dz, Fahrettin Yakuphanoğlu, Ph.D., Professor, Firat University, Physics Department, 23169 Elazig, Turkey, e-mail: fyhanoglu@firat.edu.tr, Saâd Rahmane, Ph.D., Professor, University of Biskra, Physics Department, BP 145 RP, 07000 Biskra, Algeria, e-mail: rahmanesa@yahoo.fr, Madani Bdirina, Ph.D. Student, University of Biskra, Physics Department, BP 145 RP, 07000 Biskra, Algeria, e-mail: madany.bdirina@gmail.com, İbrahim Karteri, Ph.D., Assist Professor, Kahramanmaras Sutcu Imam University, Department of Energy Systems Engineering, Kahramanmaras, Turkey, e-mail: i.karteri@ksu.edu.tr.

https://doi.org/10.18690/978-961-286-058-5.7 ISBN 978-961-286-058-5

Available at: http://press.um.si.

1 Introduction

II-VI transparent conducting metal oxides such as ZnO and CdO are promising for application in thin film and various optoelectronic devices [1-2]. ZnO has been studied in recent years due to its unique properties such as wide-band gap, high transparency and low resistivity [3]. It also can be used as a window layer in solar cells [4].

It is well known that undoped ZnO thin films generally indicate n-type conduction. ZnO thin films have been grown on Si substrates by several physical and chemical methods such as chemical vapor deposition, sputtering, atomic layer deposition [5-8]. pulsed laser deposition (PLD) [9] and chemical spray pyrolysis [10]. ZnO thin films with p-Si have been used in many applications such as photodetectors and solar cells owing to its good optical and electrical properties, ease of fabrication, low cost [11-13].

The aim of this study was focused on fabrication and characterization a ZnO film using sol–gel spin-coating technique then extract the optical parameters to use them in the modeling of a ZnO/p-Si heterojunction solar cell.

The ZnO/p-Si heterojunction solar cell which was fabricated by sol–gel method shows poor photovoltaic performance [14]. In this work numerical simulation using Silvaco ATLAS software is used to model the aforementioned solar cell and to elucidate this poor performance.

2 Experimental

ZnO thin films were developed by sol–gel spin coating method. Before forming a ZnO layer on the glass substrate, the native oxide on the front surface of the substrate was removed in HF:H2O (1:10) solution, then, the wafer was rinsed in DI water. To obtain the sol, the precursor zinc acetate dehydrate was first dissolved into 2-methoxyethanol as a solvent and by adding monoethanolamine, which acts as the stabilizer. Molar ratio of monoethanolamine to zinc acetate was maintained at1:1 and the concentrations of zinc acetate was 0.3M. After stirring for 1h, a clear and homogeneous solution was obtained. The substrate was placed on the sample holder and was rotated at a speed of 3000 rpm for 30 s. After each spin coating the substrate was dried in a furnace at 300 C for 10 min to evaporate the solvents.

After this process was repeated 10 times, thermal treatment was carried out at 450 C for 1 h to decompose completely the organic component from the film. Then, the ZnO film was annealed at 750 C for1h.

2.1 Results

Optical properties

Figures 1, 2 and 3 show the transmittance, reflectance and absorption coefficients spectra as a function of wavelength range from 250 to 1000 nm for the ZnO thin film grown using the sol solutions with molarity: 0.3M.

The optical transmittance of a material is generally determined by the thickness, surface roughness, and absorption coefficient of the material.
The average value of transmittance of thin films in the visible range is found to be 85% - 92%. These high transmittance values in UV/VIS region make this film an excellent candidate for transparent window in thin film solar cells.
The reflectance (R) decreases as the wavelength increases (energy decreases) in the wavelength range (375-1000) nm

The absorption coefficient for the thin films was obtained using the equation,

$$I = I_0 e^{-\alpha d} \quad (1)$$

where I and I_0 represent the intensities of the transmitted and incident light, respectively.

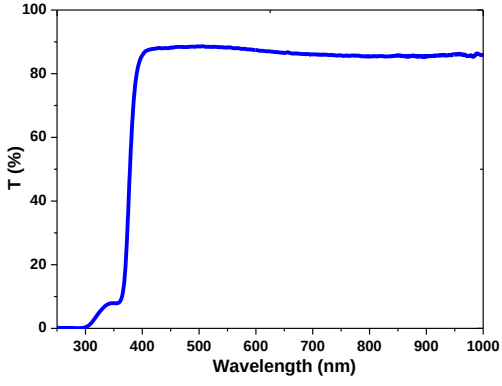

Figure 1. Optical Transmittance As Function Of Wavelength

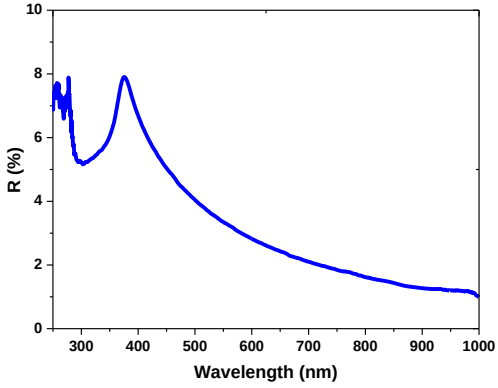

Figure 2. Optical Reflectance As Function Of Wavelength

Considering interfaces related to the thin film and the thin film thickness in practical experiments, the transmittance and reflectance of the ZnO-based materials obey the following equation [15]:

$$T = (1 - R)^2 \exp[-\alpha d] \quad (2)$$

where T represents the optical transmittance, R denotes the reflectance, and d is the thickness of the thin films. Thus, α can be calculated using the following equation:

$$\alpha = -\frac{1}{d} \ln[T/(1 - R)^2] \quad (3)$$

The optical bandgap (Eg) value of the thin film was calculated from a plot using the absorption coefficient of ZnO thin films as shown in Figure 4.

The presence of a single slope in the plot suggests that the films have direct and allowed transition. The band gap energy is obtained by extrapolating the straight line portion of the plot to zero absorption coefficient. The band gap value of ZnO thin film is found to be 3.25 eV.. The absorption coefficient of ZnO thin films is found to be zero in forbidden energy region and it is found to increase rapidly with the decrease in wavelength beyond energy band gap. Zero absorption coefficients of ZnO thin films in the visible range of spectrum make these thin films suitable as window layer in solar cells.

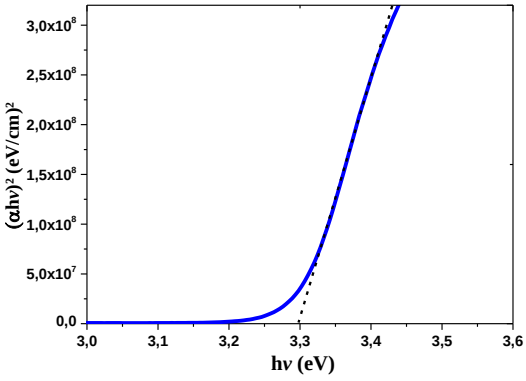

Figure 4. (αhν)² As Function Of Wavelength

Figures 5 and 6 show the refractive index (n) and extinction coefficient (k), respectively, for the ZnO thin film grown using the sol-gel method. Knowledge of the dispersion of the refractive indices of semiconductor materials is essential to accurately model and optimize the optical properties of such materials. The complex refractive index of a semiconductor material can be expressed [16]:

$$\hat{n} = n(\omega) + ik(\omega) \tag{4}$$

where n and k represent the real and imaginary parts, i.e., the refractive index and extinction coefficient of the complex refractive index, respectively. The real part quantifies the phase velocity of light whereas the imaginary part quantifies the absorption of light in the material. The refractive index of a semiconductor material can be calculated using the following relation [17]:

$$n = \left(\frac{1+R}{1-R}\right) + \sqrt{\frac{4R}{(1-R)^2} - k^2} \tag{5}$$

where $k(= \alpha\lambda/4\pi)$ is the extinction coefficient, which can be calculated from the optical transmittance of the material.

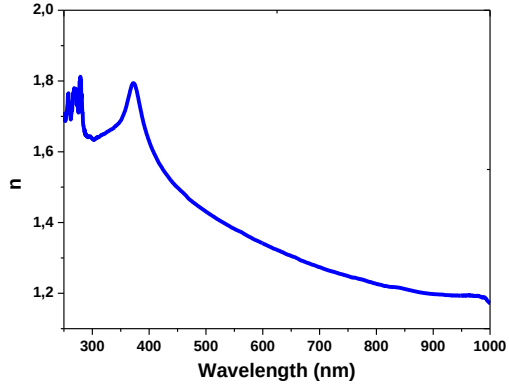

Figure 5. Refractive Index (n) As Function Of Wavelength

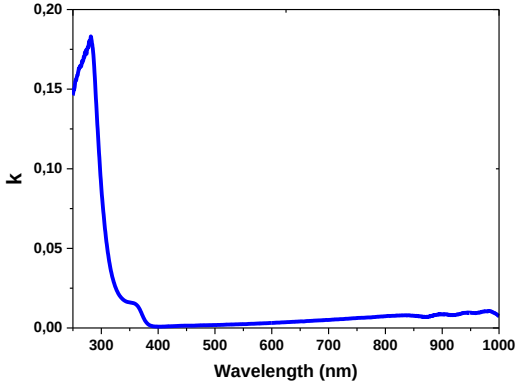

Figure 6. Extinction Coefficient (k) As Function Of Wavelength

Figures 7 and 8 show the dependence of the real (ε_1) and imaginary (ε_2) parts of the complex dielectric constant, respectively, on photon energy. The fundamental electron excitation spectra for the thin films are determined by the frequency dependence of the complex dielectric constant. The values of ε_1 and ε_2 are related to n and k and are calculated using the following formulas [16]:

$$\varepsilon_1 = n^2 - k^2 \text{ and } \varepsilon_2 = 2nk \quad (6)$$

Thus, the dielectric properties of the ZnO thin film change with change in the refractive index and extinction coefficient of the thin films. The steep increase in ε_1 and ε_2 for photon energies is due to the band gap transitions.

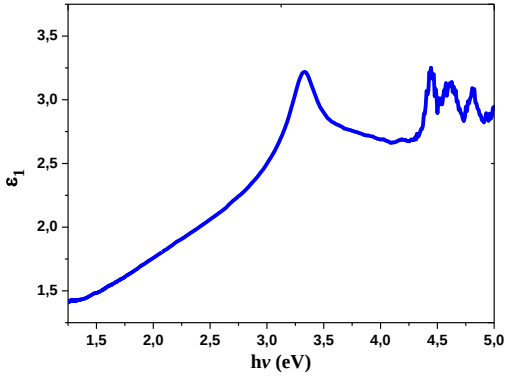

Figure 7. Real Dielectric Constant (ε_1) As Function Of Photon Energy

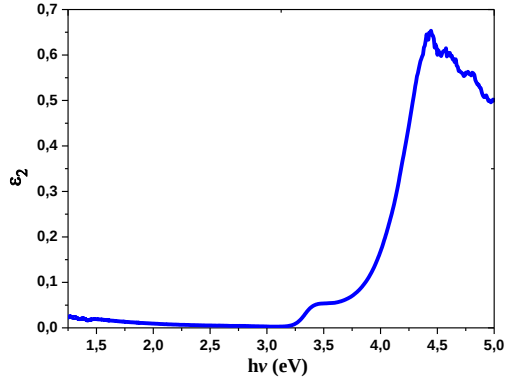

Figure 8. Imaginary Dielectric Constant (ε_2) As Function Of Photon Energy

3 Simulation

The validity of simulation results must be performed by comparing them with those obtained in experimental studies, our experimental results data in this case. Otherwise, obtained simulation results are undermined and called into question, and it is neither possible nor feasible to re-use them in constructing real devices such as solar cells. In this respect parameters to be used in the simulation have to be published data from different research efforts. Furthermore these data, if necessary have to be adjusted in a reasonable way, to yield simulation results comparable to measurements.

The SILVACO TCAD ATLAS software was used [18] in this work to elucidate the poor performance of the ZnO/p-Si solar cell. It is a physically-based two and three dimensional

device simulator. It predicts the electrical behavior of a specified structure and the internal physical mechanisms involved. It solves a set of fundamental equations, which link together the electrostatic potential and the carrier densities, through Poisson's equation, the carrier continuity equations and the transport equations. The simplest model of charge transport that is useful is the Drift-Diffusion Model [19].

3.1 Simulation Results

It is well known that, in most cases, thin films have non crystalline structure. It is therefore expected that the polycrystalline or amorphous nature of these films give rise to defects in the film lattice. These will give rise to different types of energy levels in the band gap of the material.

In amorphous semiconductors, the density of states (DOS) is composed of four bands: two tail bands (a donor-like valence band and an acceptor-like conduction band) and two deep level bands (one acceptor-like and the other donor-like). The firsts are modeled as decaying exponentials from the band edge while the latters are modeled using a Gaussian distribution. The density is then given by:

$$g(E) = g_{GA}(E) + g_{GD}(E) + g_{TA}(E) + g_{TD}(E) \quad (7)$$

The subscripts G and T are for Gaussian and tail respectively while A and D are for acceptor and donor respectively.

$$\boldsymbol{g(E) = G_{GA} exp\left[-\left[\frac{E_{GA}-E}{\sigma_D}\right]^2\right] + G_{GD} exp\left[-\left[\frac{E-E_{GD}}{\sigma_D}\right]^2\right] + G_{TA}\, exp\left[\frac{E-E_C}{E_A}\right] + G_{TD} exp\left[\frac{E_V-E}{E_D}\right]} \quad (8)$$

where $E_{V(C)}$is the valence (conduction) band edge, $G_{TD(A)}(\ cm^{-3}eV^{-1})$ the effective density at $E_{V(C)}$, $E_{D(A)}$ the characteristic slope energy of the valence (conduction) band-tail states, $G_{GA(D)}$ the total density $(cm^{-3}eV^{-1})$, $\sigma_D(\sigma_A)$ the standard deviation and $E_{GD(A)}$ the peak energy of the Gaussian distribution.

The effect of the different constituents of the DOS on the J-V characteristics of the non-ideal ZnO/p-Si solar cell is shown in Figure 9.

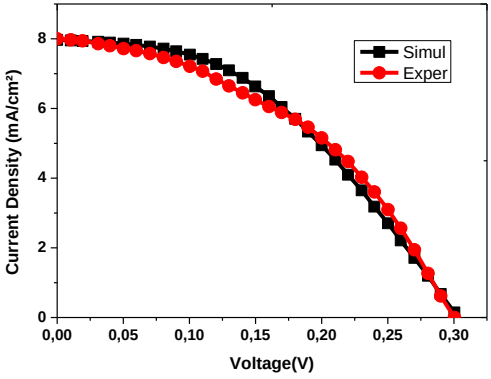

Figure 9. Comparison Of Simulated And Measured J-V Characteristics Of The ZnO/p-Si Solar Cell

As it is very clear there is a very good agreement between simulation and measurements. The extracted parameters gave almost a perfect match between simulation and measurement.

4 Conclusion

ZnO thin film was successfully prepared by sol-gel spin-coating technique with 0.3M zinc acetate solutions. The film has been characterized using optical measurements.

The optical constants of the Zno film (band gap (Eg), refractive index (n), extinction coefficient (k) and dielectric constant (ε)), to use them in simulation, were analyzed and investigated from the transmittance and reflectance spectra.

A ZnO/p-Si heterojunction solar cell which was fabricated by sol–gel method shows poor photovoltaic performance [14]. In this work numerical simulation using Silvaco ATLAS software is used to model this solar cell and to elucidate this poor performance. Several possible causes were considered. In this work the effect of presence of defects in the semiconductor (tail or Gaussian states). As was supposed, the defects were found to mainly affect the photovoltaic parameters. Good comparison between experimental and simulation results was obtained with these values: a total density of the Gaussian states, G_{Ga}=1x10^{15} and G_{Gd}=5x10^{16} cm^{-3}/eV, and a density of tail states, G_{Ta}= 1x10^{20} cm^{-3}/eV and G_{Td}= 1x10^{20} cm^{-3}/eV. These values produced a good agreement between simulated and measured J-V characteristics of the solar cell.

Acknowledgements

Slimane Chala and Nouredine Sengouga would like to thank the University of Biskra for its financial support for the scientific visit to the Firat University, Elazig-Turkey.

References

[1] F. Yakuphanoglu, Y. Caglar, M. Caglar, and S. Ilican, "Materials Science in Semiconductor Processing ZnO / p-Si heterojunction photodiode by sol – gel deposition of nanostructure n-ZnO film on p-Si substrate," *Mater. Sci. Semicond. Process.*, vol. 13, no. 3, pp. 137–140, 2010.

[2] S. Chala, N. Sengouga, and F. Yakuphanoglu, "Modeling the effect of defects on the performance of an n-CdO/p-Si solar cell," *Vacuum*, vol. 120, pp. 81–88, 2015.

[3] D. M. Bagnall *et al.*, "Optically pumped lasing of ZnO at room temperature," *Appl. Phys. Lett.*, vol. 70, no. 17, p. 2230, 1997.

[4] Z. A. Shukri, L. S. Yip, C. X. Qiu, I. Shih, and C. H. Champness, "Preliminary Photovoltaic Cells With Single-Crystal Cis Substrates," *Sol. Energy Mater. Sol. Cells*, vol. 37, pp. 395–401, 1995.

[5] Y. Choi *et al.*, "High current fast switching n-ZnO/p-Si diode," *J. Phys. D. Appl. Phys.*, vol. 43, no. 34, p. 345101, 2010.

[6] F. Zhu-x, L. Bi-xi, and L. Gui-hong, "Photovoltaic Effect of ZnO / Si Heterostructure Photovoltaic Effect of ZnO / Si Heterostructure *," *Chinese Phys. Lett.*, vol. 16, no. 10, pp. 753–755, 1999.

[7] J. Skriniarova et al., "No Title," *J. Phys. Conf. Ser.*, vol. 100, p. 1, 2008.

[8] Z. Y., "Properties of ZnO thin films grown on Si substrates by MOCVD and ZnO/Si heterojunctions," *Semicond. Sci. Technol.*, vol. 20, p. 1132, 2005.

[9] Y. Liu, L. Zhao, and J. Lian, "Al-doped ZnO films by pulsed laser deposition at room temperature," *Vacuum*, vol. 81, no. 1, pp. 18–21, 2006.

[10] S. Yilmaz, E. McGlynn, E. Bacaksiz, J. Cullen, and R. K. Chellappan, "Structural, optical and magnetic properties of Ni-doped ZnO micro-rods grown by the spray pyrolysis method," *Chem. Phys. Lett.*, vol. 525–526, pp. 72–76, 2012.

[11] Y. S. Ocak, "Electrical characterization of DC sputtered ZnO/p-Si heterojunction," *J. Alloys Compd.*, vol. 513, pp. 130–134, 2012.

[12] M. Nawaz, E. S. Marstein, and A. Holt, "Design Analysis of ZnO/cSi Heterojunction Solar Cell," *35th IEEE Photovolt. Spec. Conf.*, pp. 2213–2218, 2010.

[13] K. Liu, M. Sakurai, and M. Aono, "ZnO-based ultraviolet photodetectors," *Sensors*, vol. 10, no. 9, pp. 8604–8634, 2010.

[14] S. Farooq, S. S. Hussain, S. Riaz, and S. Naseem, "ZnO / c-Si Solar cell Fabricated through Sol-Gel and Spin Coating," 2012.

[15] M. S. Kim *et al.*, "Growth and Characterization of Indium-Doped Zinc Oxide Thin Films Prepared by Sol – Gel Method," *Acta Phys. Pol. A*, vol. 121, no. 1, pp. 3–6, 2012.

[16] F. Yakuphanoglu, A. Cukurovali, and I. Yilmaz, "Refractive index and optical absorption properties of the complexes of a cyclobutane containing thiazolyl hydrazone ligand," *Opt. Mater. (Amst).*, vol. 27, no. 8, pp. 1363–1368, 2005.

[17] M. R. Islam and J. Podder, "Optical properties of ZnO nano fiber thin films grown by spray pyrolysis of zinc acetate precursor," *Cryst. Res. Technol.*, vol. 44, no. 3, pp. 286–292, 2009.

[18] D. S. Software, "Atlas User ' s Manual," no. 408, pp. 567–1000, 2013.

[19] S. M. Sze and K. K. Ng, *Physics of Semiconductor Devices*. 2007.

University of Maribor Press

CFD Simulation of Combustion in a Furnace Using Mixture Gases With Variable Calorific Value

SERGIO MORALES, DANIEL BARRAGAN & VIATCHESLAV KAFAROV

Abstract In the different processes carried out in the petroleum refining industry, mixtures of residual gases are produced commonly known as "refinery gases". In many cases, refinery gases are used as fuel in burning equipment such as boilers or furnaces in order to save energy and avoid additional costs associated to their storage. However, the chemical composition of refinery gases varies depending on the process from which they are produced and can have a heating value varying from 800 Btu/ft3 to 2000 Btu/ft3, which causes important alterations in the combustion process. This work analyses the effect of the variability of the heating value of refinery gases in the combustion process of furnaces using Computational Fluid Dynamics (CFD), which is a technique that has been widely used to obtain detailed information about the operation of furnaces through the development of models and simulations. Comparative CFD simulation cases are carried out varying the fuel composition which results provide detailed information about temperature and chemical species distribution and efficiency and how these parameters are affected when the fuel composition changes. The results are very important to evaluate the convenience of the usage of refinery gases as fuels in furnaces and enhance their operation.

Keywords: • CFD • Calorific value • Combustion • Furnace • Simulation •

CORRESPONDENCE ADDRESS: Sergio Morales, MSc., Student of Chemical Engineering, Research Centre for Sustainable Development in Industry and Energy (CIDES) Industrial University of Santander, School of Chemical Engineering, Carrera 27 #9, Bucaramanga, Colombia, e-mail: sergiom80@hotmail.com. Daniel Barragan, MSc., Student of Chemical Engineering, Research Centre for Sustainable Development in Industry and Energy (CIDES), Industrial University of Santander, School of Chemical Engineering Carrera 27 #9, Bucaramanga, Colombia, e-mail: engineer.barragan@gmail.com. Viatcheslav Kafarov, Dr.Sc, Associate Professor, Research Centre for Sustainable Development in Industry and Energy (CIDES), Industrial University of Santander, School of Chemical Engineering, Carrera 27 #9, Bucaramanga, Colombia, e-mail: kafarov@uis.edu.co.

https://doi.org/10.18690/978-961-286-058-5.8 ISBN 978-961-286-058-5

Available at: http://press.um.si.

1 Introduction

In the oil industry combustion is a mechanism for transforming energy through industrial equipment such as: furnaces, boilers, etc. Some of them are designed to use natural gas as fuel. In the petroleum refining processes, various mixtures of waste gases are also generated, called "refinery gases (RG)", which are used as they are produced due to their storage cost [1]; These gas mixtures are a source of natural gas savings, with which they are mixed or used directly in the equipment, especially in the furnaces, which are considered a key equipment in the refineries, since they supply the necessary heat to carry out various processes such as: distillation, hydrocracking, separation, among others [1-3]. However, the composition of RG is not homogeneous and varies depending on the process stream from which it comes, usually with high contents of methane, hydrogen, ethane, ethylene, propane and propylene [1].

These variations in the composition of the RG alter its calorific value, presenting changes in a range between 800-2500 BTU / ft^3 [4], causing alterations in the combustion process, which changes the degree of conversion and generates unwanted products affecting safety and increasing emissions of pollutants.

The gas combustion process involves a set of disciplines that are strongly associated with each other: kinetics, thermodynamics, turbulent interactions and transport phenomena in each of their situations (mass, momentum and energy) [1]. These phenomena can be represented using the fundamental equations of conservation of mass, momentum and energy. However, the introduction of turbulence equations must be taken into account, which together with the fundamental conservation equations can only be solved analytically in very simplified cases. In this context, numerical simulation using Computational Fluid Dynamics (CFD) has proven to be a highly accurate technique that can provide and predict information that, in most cases, can be costly and difficult to obtain experimentally, since it is not necessary to invest resources in a final product and experimental tests, in other words, it is an excellent tool to obtain detailed information about the processes of operation in furnaces [5].

In literature, several studies have been published about modeling combustion processes in typical industrial furnaces using CFD. Oprins and Heynderickx performed a CFD simulation of the radiant zone of an industrial thermal cracking furnace, obtaining flow and pressure profiles. In their work, they concluded that the use of a non-structured tetrahedral mesh allows to avoid problems and errors in the calculation of pressure profiles when using a semi-structured prismatic mesh for the solution of flow equations [6].

Stefanidis et al performed the CFD simulation of combustion process in a cracking furnace using different combustion models. Flow, temperature and concentration profiles of chemical species were obtained in the radiant zone of an industrial cracking furnace using two combustion models: The Eddy Dissipation Concept with detailed reaction

kinetics and The Eddy Break Up Model with simplified reaction kinetics. When comparing the results obtained with both models, they suggest that more sophisticated combustion models such as the Eddy Dissipation Concept with detailed reaction kinetics for the combustion modeling should be used in cracking furnaces under normal operating conditions [7].

X. Lan et al performed the numerical simulation of heat transfer and reaction processes in ethylene furnaces. The results of the simulation showed detailed information on flow profiles, temperature, heat flux distribution and species concentration distribution, which allows understanding the different processes and behaviors present in the ethylene furnaces [8].
Many other researchers have focused on modeling and simulating laboratory furnaces because it is easier to validate results with experimental data. A. Rebola et al performed a numerical simulation of a laboratory flameless furnace and compared different turbulence and combustion models, the results were validated using experimental data [9].

Bo Liu et al carried out numerical simulations to study the performance of a forward flow furnace using a deflector to reduce emissions and also evaluated the effect of ethane content of fuel gas on the flow and temperature of the furnace [10].

Many other researchers like F. Diaz and J. Castro [2] and X. Li et al [11] also used CFD to model and simulate combustion processes in furnaces obtaining flow, temperature and species concentration profiles using fuels with defined composition, but there are very few studies using fuels with different composition and heating value. The aim of this work is to evaluate the effect of using RG with different heating values on the flue gas side of a typical box furnace using CFD.

2 CFD simulation development

2.1 Furnace characteristics

The configuration of the furnace in this study is typical box type with floor burners, the one used by A.Sayre et al [12]. Since the furnace and the burner are symmetric, a 2D axisymmetric grid can be used. The computational mesh consists of 10000 elements. A more refined grid size is used in the burner exit and centerline because fuel and air mixing process occurs here. The boundary conditions and operation characteristics of the furnace are based on a study case by ANSYS [13]. The 2D mesh and dimensions of the furnace of this study are shown in Figure 1.

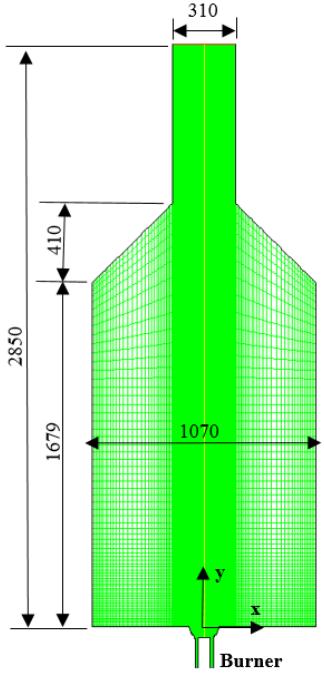

Figure 1. 2D Mesh and dimensions (in mm) of the furnace

2.2 Flow model

The model used to calculate stationary flow inside the furnace is based on the Reynolds-Average-Navier-Stokes (RANS) steady-state governing equations that contain mass, momentum, energy, species balances. The SIMPLE algorithm was used for the pressure-velocity coupling. The general form of these equations is shown next. For more detailed information of all the equations presented in this paper please consult [2], [6-8], [11].

Continuity:

$$\frac{\partial}{\partial x_i}(\rho u_i) = 0 \tag{1}$$

Conservation of momentum:

$$\frac{\partial}{\partial x_j}(\rho u_i u_j) = \frac{\partial p_{eff}}{\partial x_i} +$$

$$\frac{\partial}{\partial x_j}\left[\mu_{eff}\left(\frac{\partial u_i}{\partial x_j}+\frac{\partial u_j}{\partial x_i}-\frac{2}{3}\delta_{ij}\frac{\partial u_l}{\partial x_l}\right)\right] \quad (2)$$

Conservation of energy:

$$\frac{\partial}{\partial x_i}[u_i(\rho E+p)]=\frac{\partial}{\partial x_j} \quad (3)$$

$$\left(k_{eff}\frac{\partial T}{\partial x_j}\sum_{j=1}^{N} h_j J_j+u_i\mu_{eff}\left[\left(\frac{\partial u_j}{\partial x_i}+\frac{\partial u_i}{\partial x_j}\right)-\frac{2}{3}\frac{\partial u_l}{\partial x_l}\delta_{ij}\right]\right)+S_h$$

Conservation of chemical species:

$$\frac{\partial \rho u_j Y_i}{\partial x_j}=\frac{\partial}{\partial x_j}\left[\left(\rho D_{i,m}+\frac{\mu_t}{Sc_t}\right)\frac{\partial Y_i}{\partial x_j}\right]+R_i \quad (4)$$

The model selected to account for turbulence is the two-equation standard k-ε, this needs two additional equations for k and ε respectively.

Equation of k:

$$\frac{\partial}{\partial t}(\rho k)\frac{\partial}{\partial x_i}(\rho k u_i)=\frac{\partial}{\partial x_j}\left[\left(\mu+\frac{\mu_t}{\sigma_k}\right)\frac{\partial k}{\partial x_j}\right]+$$

$$G_k+G_b-\rho\varepsilon-Y_M+S_k \quad (5)$$

Equation of ε:

$$\frac{\partial}{\partial t}(\rho\varepsilon)+\frac{\partial}{\partial x_i}(\rho\varepsilon u_i)=\frac{\partial}{\partial x_j}\left[\left(\mu+\frac{\mu_t}{\sigma_\varepsilon}\right)\frac{\partial \varepsilon}{\partial x_j}\right]+$$

$$C_{1\varepsilon}\frac{\varepsilon}{k}(G_k+C_{3\varepsilon}G_b)-C_{2\varepsilon}\rho\frac{\varepsilon^2}{k}+S_\varepsilon \quad (6)$$

Where:

$$G_k=\mu_t\left(\frac{\partial u_i}{\partial x_j}+\frac{\partial u_j}{\partial x_i}\right)\frac{\partial u_i}{\partial x_j}$$

$$\mu_t=\rho C_\mu\frac{k^2}{\varepsilon}$$

The constants defined for the k-ε standard model are:

$C_{1\varepsilon}=1.44$; $C_{2\varepsilon}=1.92$; $C_\mu=0.09$; $\sigma_k=1.0$; $\sigma_\varepsilon=1.3$

2.3 Combustion model

The mathematical model selected in this work is the Probability Density Function (PDF) mixture fraction model. This model is the most used in non-premixed combustion cases. This model is described with the following equations [2]:

Mixture fraction equation:

$$f=\frac{m_f}{m_f+m_o} \tag{7}$$

Average mixture fraction equation:

$$\frac{\partial}{\partial t}\left(\rho\bar{f}\right)+\frac{\partial}{\partial x_j}\left(\rho u_j\bar{f}\right)=\frac{\partial}{\partial x_j}\left(\frac{\mu_t}{\sigma_f}\frac{\partial\bar{f}}{\partial x_j}\right) \tag{8}$$

Variance average mixture fraction equation:

$$\frac{\partial}{\partial t}\left(\rho\bar{f'^2}\right)+\frac{\partial}{\partial x_j}\left(\rho u_j\bar{f'^2}\right)= \tag{9}$$

$$\frac{\partial}{\partial x_j}\left(\frac{\mu_t}{\sigma_{\bar{f'^2}}}\frac{\partial\bar{f'^2}}{\partial x_j}\right)+C_g\mu_e\left(\frac{\partial\bar{f}}{\partial x_j}\right)^2-C_d\rho\frac{\varepsilon}{k}\bar{f'^2}$$

2.4 Radiation model

In order to calculate the radiation, which dominates the heat transfer process inside the furnace, it is necessary to select a radiation model. In this case, the Discrete Ordinate (DO) radiation model was selected because is the most robust radiation model available and works fine with all the range of optical thickness. This model is described by the following equation [2], [11].

Equation of DO radiation model:

$$\nabla\cdot(I(\vec{r},\vec{s})\,\vec{s})+aI(\vec{r},\vec{s})=an^2\frac{\sigma T^4}{\pi} \tag{10}$$

Additionally, it is important to take into account that the combustion gases also participate in the radiation heat transfer. The main products of the combustion process of gases are CO_2 and H_2O The emissivity of the combustion products gases is calculated with the Weighted Sum of Gray Gases Model (WSGGM), which is described by the following equation [2], [11].

$$\varepsilon_m=\sum_{i=0}^{I}a_{\varepsilon,i}I(T)(1-e^{-k_i ps}) \tag{11}$$

2.5 Results and discussion

This work contemplates the simulation of comparative cases in order to evaluate the effect of variable heating value of RG in the combustion process in furnaces. The gas mixture compositions used in this work are the ones obtained by O. Cala et al, which are described in table 1 [2].

Table 1. Compositions (%) of RG used in this study [2]

Gas type	Natural Gas	RG1	RG2
CH_4	97	70	35
C_2H_6	1	0	3
C_3H_8	1	16	35
C_4H_{10}	0	5	12
C_2H_4	0.5	3	7
C_3H_6	0.5	0	8
H_2S	0	1	0
H_2	0	5	0
Inferior Calorific value ($Btu/ft^{3)}$	913	1200	1800

In this work 3 comparative cases were simulated using 3 mixture gases with the compositions shown in table 1 using ANSYS FLUENT commercial code. The first case was simulated using Natural Gas, the second with RG1 composition and the third with RG2 composition. The contours of temperature inside the furnace for the 3 cases are shown in Figure 2.

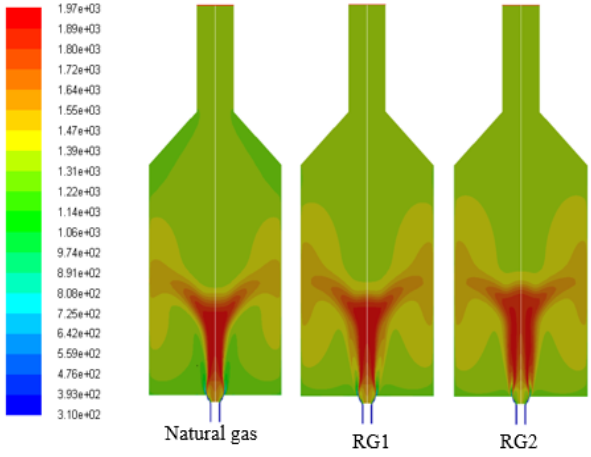

Figure 2. Temperature contours inside the furnace with different gas mixtures

The maximum temperatures calculated were 1975K with natural gas, 1942.36 with RG2 and 1928.18 with RG3. It can be said that content of CH_4 in the gas mixtures affects the temperature contours distribution inside the furnace. When the content of CH_4 increases, the maximum temperature inside the furnace decreases, but a more uniform heat distribution is observed. On the other hand, when CH_4 content decreases, the maximum temperature increases, but heat distribution is less uniform, that is to say, less hot zones can be observed. It is important to say that if the calorific value increases it does not necessarily mean that the maximum temperature will increase too because there are other factors like air excess and fuel flow that have an effect on this parameter.

In Figure 3 the contours of mole fraction of CO inside the furnace are shown.

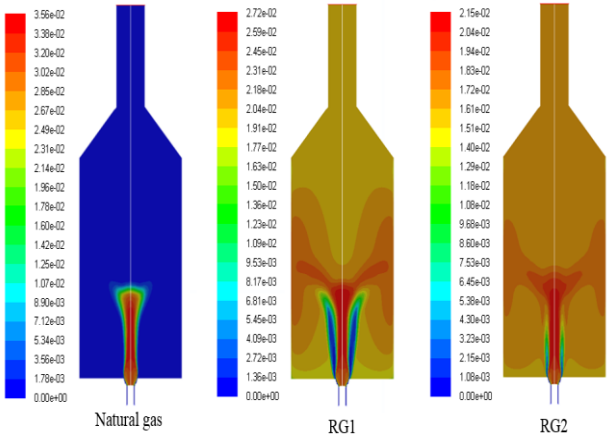

Figure 3. CO_2 mole fraction contours inside the furnace with different gas mixtures.

According to the information presented in figure 3, the CO mole fraction inside the furnace is higher with natural gas (0.035) concentrated in the burner exit and decreases when the mole fraction of CH_4 decreases. This means that when the fuel has a higher concentration of CH_4 the CO mole fraction decreases. With natural gas the combustion process is more efficient, CO is only present at the burner exit while with RG1 and RG2 the combustion process is not efficient and more CO is present all inside the furnace, indicating that air excess needs to be adjusted to improve combustion efficiency.

3 Conclusions

This paper analyzed the effect of using refinery mixture gases with different composition and calorific values in the combustion process of furnaces using CFD. The simulation was carried out in 2D and contours of temperature and CO mole fraction were obtained.

The simulation with natural gas showed the best heat distribution inside the furnace and the lowest CO mole fraction distribution, that is to say that the combustion was complete. On the other hand, with RG1 and RG2 the combustion is not complete and more CO is produced, which means that the combustion is not efficient and needs to be adjusted.

Accordingly, a more detailed study of the air excess requirement and fuel flow is needed when the fuel composition and calorific value change in order to achieve complete combustion and hence reduce the formation of unwanted products like CO.

Acknowledgements
The authors of this paper would like to thank the Research Centre for Sustainable Development in Industry and Energy (CIDES) and the Industrial University of Santander (UIS).

References

[1] CALA PARRA, OM, "Determination of an energy efficiency index for the combustion processes of gas mixture in refinery", Master Thesis in Chemical Engineering, Universidad Industrial de Santander, Bucaramanga, Colombia, 2014.
[2] F.A. Díaz Mateus and J.A. Castro-Gualdrón, "MATHEMATICAL MODEL FOR REFINERY FURNACES SIMULATION", CTF - Cienc. Tecnol. Futuro, vol. 4, pp. 89–99, 2010.
[3] MERIÑO STAND, LI, "Design of a methodology to achieve an eco-efficient and safe combustion of gas mixtures", Doctoral Thesis in Chemical Engineering, Universidad Industrial de Santander, Bucaramanga, Colombia, 2015.
[4] O. M. Cala, L. Meriño, V. Kafarov, and J. Saavedra, "Effect of the composition of the refinery gas on the characteristics of the combustion process.", Rev. Ing. Univ. Medellín Vol 12 Núm 23 2013.
[5] L. R. Cancino, Á. H. Restrepo, and A. A. M. Oliveira, "Numerical analysis of the combustion in an atmospheric burner crown type of domestic application", Sci. Tech., vol. 13, núm. 35, pp. 201–206, 2007.
[6] A. J. M. Oprins y G. J. Heynderickx, "Calculation of three-dimensional flow and pressure fields in cracking furnaces", Int. Symp. Math. Chem. Kinet. Eng., vol. 58, núm. 21, pp. 4883–4893, nov. 2003.
[7] G. D. Stefanidis, B. Merci, G. J. Heynderickx, and G. B. Marin, "CFD simulations of steam cracking furnaces using detailed combustion mechanisms", Comput. Chem. Eng., vol. 30, núm. 4, pp. 635–649, feb. 2006.
[8] X. Lan, J. Gao, C. Xu, and H. Zhang, "Numerical Simulation of Transfer and Reaction Processes in Ethylene Furnaces", Chem. Eng. Res. Des., vol. 85, núm. 12, pp. 1565–1579, 2007.
[9] A. Rebola, P.J. Coelho, M. Costa, Assessment of the performance of several turbulence and combustion models in the numerical simulation of a flameless combustor, Combust. Sci. Technol. 185 (2012) 600-626.
[10] B. Liu, Y. Wang, H. Xu. "Mild combustion in forward flow furnace of refinery-off gas for low-emissions by deflector", Applied Thermal Engineering, vol. 91, pp.1048-1058, sep. 2015.
[11] X. Li, L. Zhang, Y. Sun, B. Jiang, X. Li, y J. Wang, "Numerical simulation of the flue gas side of refining vacuum furnace using CFD", Chem. Eng. Sci., vol. 123, pp. 70–80, feb. 2015.

[12] A. Sayre, N. Lallement, and J. Dugu, and R. Weber "Scaling Characteristics of Aerodynamics and Low-NOx Properties of Industrial Natural Gas Burners", The SCALING 400 Study, Part IV: The 300 KW BERL Test Results, IFRF Doc No F40/y/11, International Flame Research Foundation, The Netherlands.

[13] ANSYS INC. Tutorial 15: Using the non- premixed combustion model. March 12, 2009.

10TH INTERNATIONAL CONFERENCE ON SUSTAINABLE ENERGY AND ENVIRONMENTAL PROTECTION (JUNE 27TH – 30TH, 2017, BLED, SLOVENIA), MODELLING AND SIMULATION
J. Krope, A.Ghani Olabi, D. Goričanec & S. Božičnik

University of Maribor Press

Wind Power Plant Influence to the Latvian EPS Stability

INGA ZICMANE, KRISTINA BERZINA, ALEKSEJS SOBOLEVSKIS & SERGEY KOVALENKO

Abstract Power systems are composed of groups of elements or components that act in series or parallel or both with each other to carry power from generation sources to load buses. During the last two decades, increase in electricity demand and environmental concern resulted in fast growth of power production from renewable sources. Wind power is one of the most efficient alternatives. The purpose of this paper is devoted to the evaluation of the integration of a wind farm in the Latvian Electric Power System (EPS) in terms of stability. As well as provide methods for detection of network parameters that are most vulnerable (voltage drop) to external impacts (sensors), determine their relationship with EPS parameters, try to use this information for improvement of EPS behavioural properties. Thus, availability of information on the location of sensors allows determining and controlling nodes, in which the biggest oscillations of operational parameters are observed due to disturbances in the system.

Keywords: • Environmental economics • Hydroelectric power generation • Power generation dispatch • Power system economics • Transmission lines •

CORRESPONDENCE ADDRESS: Inga Zicmane, Ph.D., Professor, Riga Technical University, Faculty of Power and Electrical Engineering, Azenes street 12.1-312., Riga, Latvia, e-mail: Inga.Zicmane@rtu.lv. Kristina Berzina, Ph.D., Assistant Professor, Riga Technical University, Faculty of Power and Electrical Engineering, Azenes street 12.1-402, Riga, Latvia, e-mail: Kristina.Berzina@rtu.lv. Aleksejs Sobolevskis, Ph.d. student, Riga Technical University, Faculty of Power and Electrical Engineering, Riga, Latvia, e-mail Aleksejs.Sobolevskis@gmail.com. Sergey Kovalenko, Ph.D., Riga Technical University, Faculty of Power and Electrical Engineering, Riga, Latvia, e-mail: Sergejs.Kovalenko@rtu.lv.

https://doi.org/10.18690/978-961-286-058-5.9 ISBN 978-961-286-058-5

Available at: http://press.um.si.

1 Introduction

The 2009/28/EC Directive on the promotion of the use of energy from renewable sources sets (RES) the objective of reaching at least 20% of the EU's final energy consumption through renewable energy sources by 2020. The highest type of RES in Latvia is run of the river power plants. The most important is Daugava river cascade with tree power plants with installed capacity 1.53 GW.

One of the main Latvia's RES is wind power plants. The wind parks are mainly located in the western part of Latvia and they are close to the coast side. Currently installed capacity of the wind riches around 91 MW, all of them is onshore. By 2025, it is planned to increase the share of wind power up to 340 MW (onshore – 267 MW and offshore 73MW) under conservative scenario. It is obvious that based on such a development scenario, operation of the power system shall be checked in a view of the stability preservation.

Stable operation of any power system depends on the ability of continuous provision of generated and consumed power balance, as well as the level required for the quality of electric power. In order to assess the stable operation of the power system, a whole range of different software package is designed, which can be used to model a variety of operating modes. In the past, the stability of proposed system has been estimated by extrapolating the experience obtained from existing systems and using rule-of-thumb method. In the future, however, more precise methods of predicting and evaluating stability will be required [1], taking into account the prospects of growth of share of renewables.

In the framework of the given publication, two Latvian power system models were analyzed and compared: the current one (according to the situation in 2017) and the planned one (according to the situation in 2020 with the expected modernization and new interconnections of transmission lines). The purpose of this paper is to provide methods for detection of network parameters that are most weak to external impacts, determine their relationship with EPS parameters, to use this information for improvement of EPS behavioural properties.
Software has been used as a calculation tool (for instance, ETAP, REGUS and MathCad).

2 Brief discription

Traditionally, list of the most "dangerous" system is obtained by simulation of single or joint failures using a complete or simplified mathematical model of the EPS based on expert judgements and heuristics [1].

Thus, for example, the EPS vulnerability may be assessed on the basis of general theory of complex systems [2]. As a result, only one weak point (branch) of the network (according to overload level by comparison with other lines), loss of which leads to a

relative decrease in operability and overall efficiency of the entire network, is determined for a 34-node diagram.

The second approach [3] provides a formalized technique of analysis of cascade-developing emergency processes, which allows obtaining a fairly adequate reflection of the actual events, states and processes in the EPS occurred that appear in cascade development of the accident, but does not allow analysing emergency situations before they occur.

The third approach [4] aimed to identify the weak points offers finding the critical (weak) sections (by static stability) based on simplified models. The disadvantage of this approach is the difficulty of analysis and systematization of the results of numerous calculations.

2.1 Theoretical foundation

Sensority (sensitivity) is the degree of operational parameter response to the single disturbance that can be found either by numerical experiment or by some indirect indicators, in particular by the following proposed indicators connected with the singular values and eigenvalues of sensitivity matrices. Thus, operational parameters and the EPS elements related to them, the sensitivity of which is significantly higher than sensitivity of others, are called sensory [5].

The most interesting in the context of the EPS vulnerability research is localization of diagram branches, change in parameters of which mostly affects sensority. As it is known, arithmetic values of square roots of the common eigenvalues λ of real matrices A^TA and AA^T are called matrix singular values A. $\sigma_i(A) = \sqrt{\lambda_i(A^TA)} = \sqrt{\lambda_i(AA^T)}$, if $i=1,...,k$, and indicator of the sensority increase is reduction of the minimum singular value σ_1 of the Jacobian matrix [5, 6].

Therefore, to assess the impact of the diagram parameters and operational parameters on the sensority of its elements, the matrix derived from the Jacobian matrix by conductance of branches y_{ij} of the analysed diagram has been studied.

The presence and placement of sensors and weak points was determined using numerical and analytical methods for studying the scheme of the EPS and its parameters of singular analysis of the Jacobian matrix (1) and the bus admittance matrix (2), as well as generalized indicators of weakness (3) and (4)

$$J = W\Sigma V^{\mathrm{T}} = \sum_{i=1}^{k} w_i \sigma_i v_i^{\mathrm{T}}, \quad (1)$$

$$Y = W_Y \Sigma_Y V_Y^T = \sum_{i=1}^{k} w_{Yi} \sigma_{Yi} v_{Yi}^{\mathrm{T}}, \tag{2}$$

where $\Sigma = \mathrm{diag}(\sigma_1, \sigma_2, \ldots, \sigma_k)$ and $\Sigma_Y = \mathrm{diag}(\sigma_{Y1}, \sigma_{Y2}, \ldots, \sigma_{Yk})$ are diagonal matrices of singular values; $W = (w_1, w_2, \ldots, w_k), V = (v_1, v_2, \ldots, v_k)$ and $W_Y = (w_{Y1}, w_{Y2}, \ldots, w_{Yk}), V_Y = (v_{Y1}, v_{Y2}, \ldots, v_{Yk})$ are orthogonal matrices of size $k \times k$, their i-th columns are respectively the i-th left and the i-th right singular vectors of the corresponding matrices; the conditions $w_i^{\mathrm{T}} w_i = v_i^{\mathrm{T}} v_i = 1$, $w_i^{\mathrm{T}} w_j = v_i^{\mathrm{T}} v_j = 0$ are valid for them, if $i \neq j$.

The greatest interest from the point of view of the research of the vulnerability of the EPS has the localization of the branches of the network, the change in the parameters of which maximizes the sensority. The indicator of increasing the sensority is the decrease of the minimum singular value σ_1 of the Jacobian matrix. Therefore, to evaluate the influence of the parameters of the network scheme and the parameters of the regime on the sensority of its elements, the derivative matrix of the Jacobian matrix with respect to the conductivities of the branches of the analyzed network was studied.

As generalized indicators to highlight of weak branches on the basis of singular analysis, the following indicators $\chi_{J\sigma}$ and $\chi_{Y\sigma}$ [3, 5] were used:

$$\chi_{J\sigma} = \frac{\partial \sigma_1}{\partial y_{ij}} = w_{1\delta}^{\mathrm{T}} \left(\frac{\partial^2 P}{\partial \delta \partial y_{ij}} \right) v_{1\delta} + w_{1\delta}^{\mathrm{T}} \left(\frac{\partial^2 P}{\partial U \partial y_{ij}} \right) v_{1U} + \\ + w_{1U}^{\mathrm{T}} \left(\frac{\partial^2 Q}{\partial \delta \partial y_{ij}} \right) v_{1\delta} + w_{1U}^{\mathrm{T}} \left(\frac{\partial^2 Q}{\partial U \partial y_{ij}} \right) v_{1U} \tag{3}$$

$$\chi_{Y\sigma} = (w_{Yp1} - w_{Yq1})(v_{Yp1} - v_{Yq1}), \tag{3}$$

where $\partial^2 P / \partial \delta \partial y_{ij}$, $\partial^2 P / \partial U \partial y_{ij}$, $\partial^2 Q / \partial \delta \partial y_{ij}$, $\partial^2 Q / \partial U \partial y_{ij}$ are elements of the derivative matrix of the Jacobian matrix with respect to the conductivities of the branches y_{ij}; w_1, v_1 – the 1st left and the 1st right singular vectors of the Jacobian matrix; w_{Y1}, v_{Y1} – the 1st left and the 1st right singular vectors of the bus admittance matrix.

2.2 The research in the Latvian 330 kV transmission power system

Research of the Latvian power system was carried out on the basis of two model schemes obtained on the basis of both the present situation of the energy system (2017), Fig.1 and the planned development scenarios, taking into account the share of the growth prospect of renewable power generating capacity (2020), Fig. 2.

The Latvian power system has interconnection lines with Estonian, Lithuanian and Russian grids and is part of the Nord Pool Spot market. Transmitting power system of Latvia operates in two voltage classes: 110 kV and 330 kV.

Mathematical model include 330 kV transmitting line lengths, electrical generation, consumer and voltage class.

To study the chosen approach/method, a simplified model of the Latvian power system has been considered.

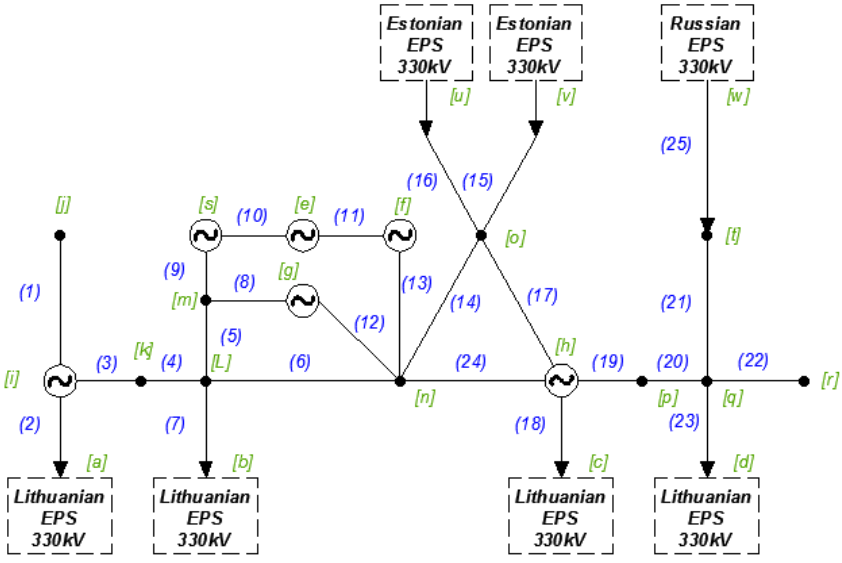

Figure 1. The studied 330 kV network diagram at 2017 year

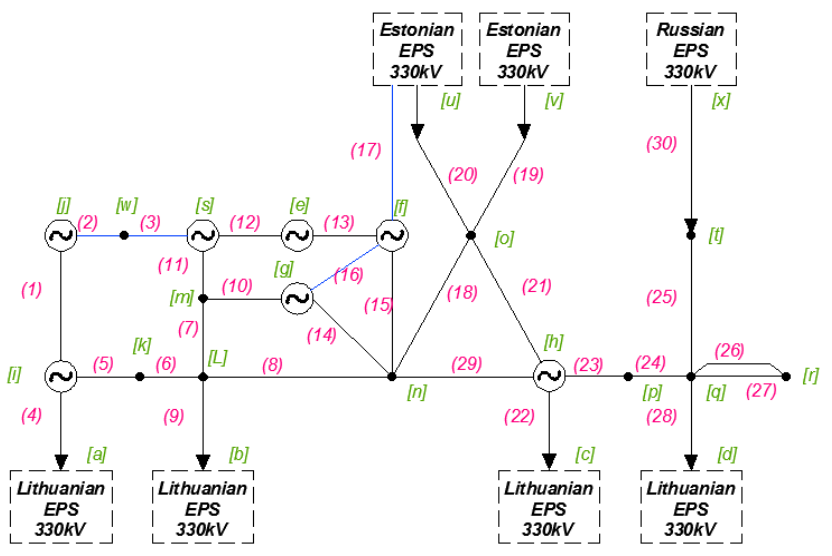

Figure 2. The studied 330 kV network diagram in 2020 (additional lines 2, 3, 16 and 17)

Table 1. Models generation points

Nr. node	Name	P, MW	Nr. node	Name	P, MW
a-d	Lithua-nia	-	*n*	Salas-pils	-
e	CHP-1	≈144	*o*	Valmie-ra	-
f	CHP-2	≈881	*p*	Krust-pils	-
g	HPP Riga	≈402	*q*	Liksna	-
h	HPP Plavina	≈894	*r*	Daugav-pils	-
i	Grobina	≈19	*s*	Imanta	≈40
j	Vents-pils	-	*t*	Rezek-ne	-
k	Broceni	-	*u*	Estonia	≈150
l	Jelgava	-	*v*	Estonia	≈150
m	Bishu-ciems	-	*w*	Russian Federa-tion	≈100

Using the methods of singular analysis of the Jacobian matrix and the bus admittance matrix for the schemes of 2017 and 2020 (Fig. 1 and 2). For the scheme shown Fig.1 (2017 year) the maximal components of the right singular vector corresponding to the minimal singular value of the Jacobian matrix are identified as voltage sensing nodes a, b, e, f, g, i, j, k, l, m, n, s (Fig. 3a). Sensory in terms of the loss of voltage are the branches 19, 20, 21, 24, 25 (Fig. 3b).

Nodes and branches having the maximal calculated values of the components of the first right singular vector of the matrix are identified by the nodes a; b; e; f; g; i; j; k; l; m; n; o; p; t; v; w as the sensory for voltage (Fig. 3a).

Difference estimate corresponding to the nodes at the ends of the branches of the components of the first right singular vector $\sigma_{\min}$ of the matrix makes it possible to identify the branches sensory to the loss of voltage 19; 20; 21; 24; 25 (Fig. 3, b).

Comparison of the estimates of sensitivities obtained using the singular analysis of the Jacobian matrix (Fig. 4a) and the singular analysis of the bus admittance matrix (Fig. 4b) shows that practically the same nodes and branches are sensory in terms of deviation of voltage modules. The difference in results is explained by the fact that the sensority of some elements of the EPS depends only on the topological parameters of the network, while others on the regime ones as well.

Using expression (3) for the scheme observed(Fig. 1), the following branches 1; 4; 5; 6; 14; 17; 20; 24 (Fig. 5a) were identified as the weak ones. It should be noted that the branches 20 and 24 and higher were identified as the sensory ones by loss of voltage.

Fig. 4b, shows calculation of the weakness indicator of the branches $\chi_{Y\sigma}$ with the use of dependence (4). Analysis of the obtained results allows us establishing that the branches 3, 4, 19, 20, whose components are maximal, are weak. At the same time, the branches 4, 19, 20 were previously determined as the weak ones (see Fig. 3b, 4b), but the branches 4, 20 as the weak ones in terms of the indicator (see Fig. 5a). The difference in the ranking results of the weak branches is due to the fact that the singular analysis of the matrix does not take into account the regime parameter, localizing only the structural inhomogeneity of the EPS.

Summarizing the above information about the sensors and weak points of the researched network, it can be stated that the following nodes a; b; e; f; g; i; j; k; l; m; n; o; p; s; t; v; w and the branches 1; 3; 4; 5; 6; 14; 17; 19; 20; 21; 24; 25 are sensory in terms of voltage.

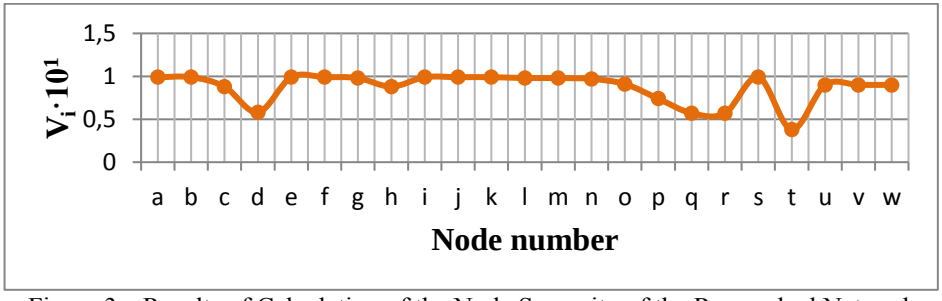

Figure 3a. Results of Calculation of the Node Sensority of the Researched Network (2017 year) on the Basis of Singular Analysis of the Jacobian Matrix

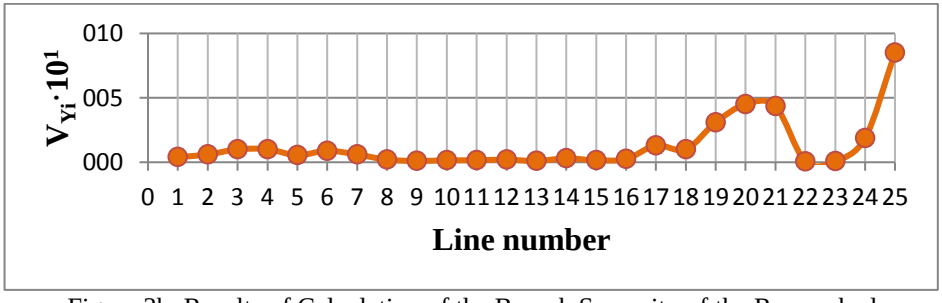

Figure 3b. Results of Calculation of the Branch Sensority of the Researched Network(2017 year) on the Basis of Singular Analysis of the Jacobian Matrix

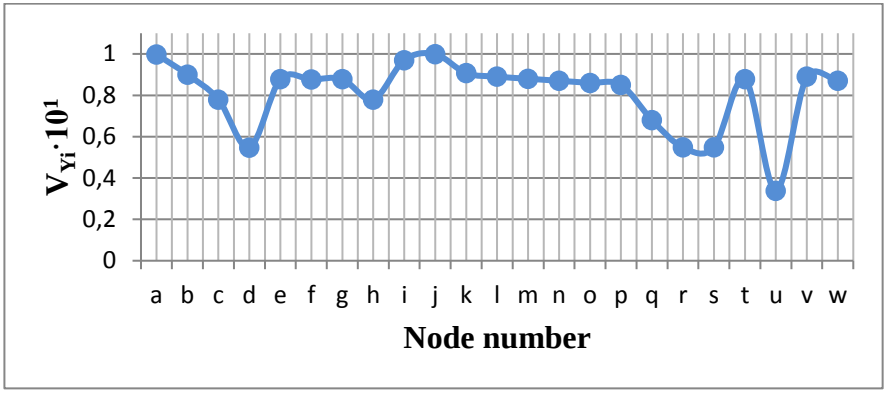

Figure 4a. Results of Calculation of the Node Sensority of the Researched Network (2017 year) on the Basis of Singular Analysis of the Bus Admittance Matrix Y, Sensory in Terms of Voltage

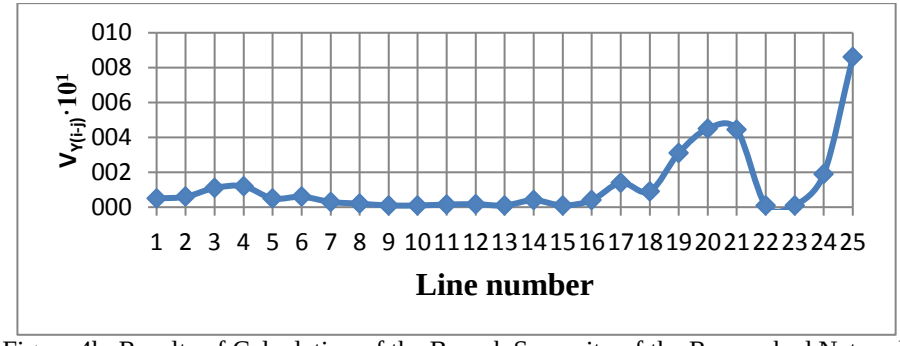

Figure 4b. Results of Calculation of the Branch Sensority of the Researched Network (2017 year) on the Basis of Singular Analysis of the Bus Admittance Matrix Y, Sensory in Terms of Loss of Voltage

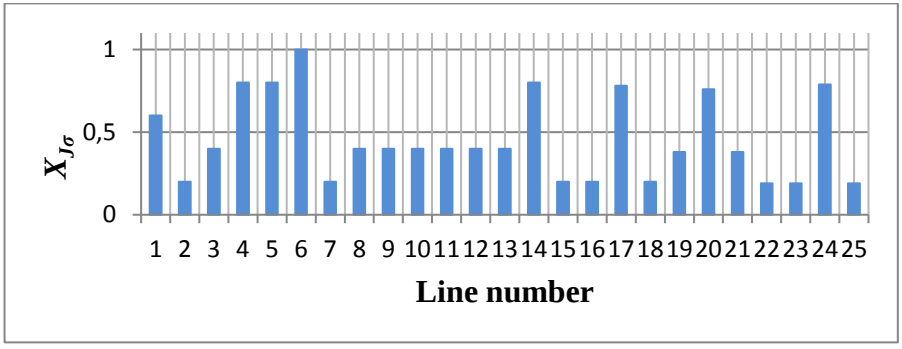

Figure 5a. Ranking of the Branches of the Scheme(2017 year), According to the Branch Weakness Indicators, Based on Singular Analysis of the Jacobian Matrix

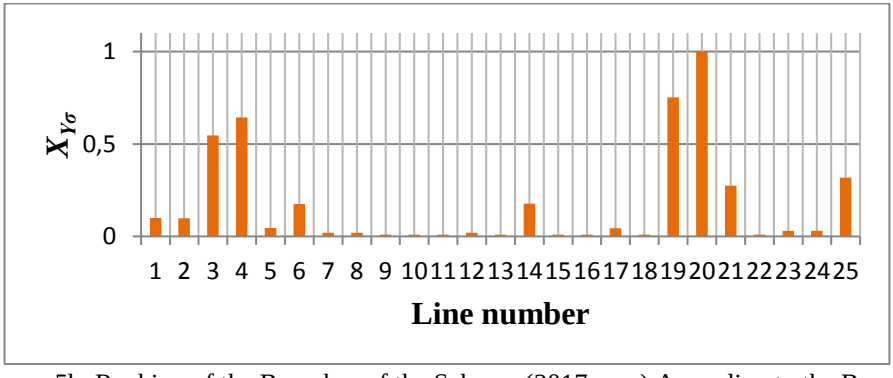

Figure 5b. Ranking of the Branches of the Scheme (2017 year) According to the Branch Weakness Indicators, Based on Singular Analysis of the Bus Admittance Matrix

The approaches also give calculations for the scheme for 2020 (fig. 2): Sensory nodes appeared: a, b, c, f, g, i, j, k, l, m, n, o, s, w, and branches - 1, 3, 6, 7, 8, 10, 11, 13, 15, 16, 17, 18, 21, 23, 24, 29.

After change of a configuration of the scheme results too changed, the number of Sensory nodes decreased that says that the system became steadier.

3 Conclusions

Using the approach offered, it is possible to analyse the power system: identify weaknesses, predict the balance/imbalance of the system under deficit and surplus of electricity to further take measures to achieve a normal balanced mode.

The results obtained of the Latvian energy power system weak point's localization and vulnerability assessment in the design phase allow providing the next.

As it is known, when increasing generation, it is necessary to increase consumption as well. In the case of simulation carried out, excess generation was exported to Lithuania - 1600 MW, separately to each interconnection line, each of 400 MW (4 lines in total).

While generating a wind farm, 15% of the total generated power at 5 nodes, the voltage increased to 395 kV, in the result of which voltage goes beyond the allowed value $U>>1,05U_{nom}$.

Therefore, simulating with the increased part of the Wind Power Station (WPS) in order to balance the system, it is required to increase the part of reacting power.

In the case of increasing the generation from the wind farm to 30% of the total generated power, the situation worsens: at some nodes, the voltage increases to 405 kV.

Based on the conducted researches and mathematical simulations on model schemes of the Latvian energy system, a critical level of permissible increase in the share of generation from wind parks was revealed, exceeding of which can lead to violation of the static stability of the energy system as a whole.

References

[1] Criteria and Countermeasures for Voltage Collapse. CIGRE TF 38.02.12. Final report // Electra. – 1991. – № 124 – P. 118–132.

[2] Approaches to the Security Analysis of Power Systems: Defence Strategies Against Malicious Threats / E. Bompard [et al.] // Office for Official Publications of the European Communities. – 2007. – 51 p.

[3] Voropay, N.I. Analysis of the systemic failures of the mechanisms in the EPS / N.I. Voropay, D.N.Efimov, V.I. Reshetov – 2008. – № 10. – C. 12–24.

[4] Wasley, R.G. Identification and ranking of critical contingencies in dependent variable scale / R.G. Wasley, M. Danesdoost // IEEE Trans. Power Appar. and Syst. – 1983. – Vol. 102, № 4. – P. 881–892.

[5] Analysis of electric power systems of inhomogeneities /O.N. Voytov. – Novosibirsk: Science; Sib. Dep-of RAN, 1999. – 256 c.

[6] Gamm, A. Z. Sensors and weaknesses in the electric power systems / A. 3. Gamm, I. I. Golub. – Irkutsk: Science; Sib, 1996. – 99 c.

[7] Electromechanical transient processes in electrical systems. - Riga 2012-P.22.

[8] Nepomnyaschiy, V., Gerhards, J., Mahņitko, A., Lomane, T. Reliability of Latvian Power System's 330 kV Substations. Latvian Journal of Physics and Technical Sciences, 2014, Vol.51, Iss.3, pp.15-23. ISSN 0868-8257. Available from: doi:10.2478/lpts-2014-0016

[9] Papkov, B., Gerhards, J., Mahņitko, A. System Problems of Power Supply Reliability Analysis Formalisation. In: 2015 IEEE 5th International Conference on Power Engineering, Energy and Electrical Drives (POWERENG): Proceedings, Latvia, Riga, 11-13 May, 2015. Riga: Riga Technical University, 2015, pp.225-228. ISBN 978-1-4673-7203-9. e-ISBN 978-1-4799-9978-1. e-ISSN 2155-5532. Available from: doi:10.1109/PowerEng.2015.7266324

[10] Soboļevskis A., Zicmane I., Murach V. "Vulnerability assessment of electric power system for the case of Latvian EPS", 2015 56th International Scientific Conference on Power and Electrical Engineering of Riga Technical University, Riga, 2015.
[11] Soboļevskis A., Zicmane I., "Analysis of vulnerability of the Latvian electrical power system" 2016 16 IEEE International Conference on Environment and Electrical Engineering, La Palazzina de' Servi, Florence, Italy, 2016.
[12] Soboļevskis A., Zicmane I., "Assessing the Impact of Registering of Weak Points Calculating the Power System Operating Modes", 2016 57th International Scientific Conference on Power and Electrical Engineering of Riga Technical University, Riga, 2016.
[13] Soboļevskis A., Zicmane I., "Prediction Of Latvian Electrical Power System For Reliability Evaluation Including Wind Energy" 17th IEEE International Conference on Environment and Electrical Engineering, , Milan, Italy, 2017 (Accepted).
[14] Kovalenko S. Power System Static Stability Assessment Methods, Criteria and Algorithms. Doctoral thesis. – Riga: RTU, 2013.- 142 pp.

10TH INTERNATIONAL CONFERENCE ON SUSTAINABLE ENERGY AND ENVIRONMENTAL PROTECTION (JUNE 27TH – 30TH, 2017, BLED, SLOVENIA), MODELLING AND SIMULATION
J. Krope, A.Ghani Olabi, D. Goričanec & S. Božičnik

University of Maribor Press

Effect of Strut + Wall Injection Techniques on the Flow-Field of Circular-Shaped Multi-Strut Scramjet Combustor

GAUTAM CHOUBEY & KRISHNA MURARI PANDEY

Abstract The multi-strut injector is one of the most favourable candidates for the mixing improvement between the hydrogen and the high speed air, and its parametric investigation has drawn an increasing observation among the researchers. Hence the flow-field characterises of a typical multi-strut based scramjet combustor have been investigated numerically. Besides, for validation purpose, the results of single strut scramjet engine have been compared with experimental data available in the open literature. The addition of multi-strut enhances the flow-field characterises as well as the performance of the engine than that of single strut engine. Additionally, the presence of different strut + wall injector on the performance of multi-strut scramjet engine has also been investigated. The obtained results show that the combination of wall 1, wall 2 and multi-strut improves the performance of scramjet as compared to other multi-strut + wall injection scheme due to higher penetration depth.

Keywords: • scramjet • H2 fuel • multi-strut • mixing efficiency • strut + wall injection •

CORRESPONDENCE ADDRESS: Gautam Choubey, Research Scholar, National Institute of Technology Silchar Assam India, Department of Mechanical Engineering, 788010, e-mail: gautam_dadaa@yahoo.com. Krishna Murari Pandey, Ph.D., Professor, National Institute of Technology Silchar Assam India, Department of Mechanical Engineering, 788010, e-mail: kmpandey2001@yahoo.com.

https://doi.org/10.18690/978-961-286-058-5.10 ISBN 978-961-286-058-5

Available at: http://press.um.si.

1 Introduction

An air-breathing hypersonic propulsion system, such as a scramjet engine, is one of the most effective propulsion systems for producing a large thrust. There are no moving parts in Scramjet engine and shock wave present inside the engine helps in the compression process rather than compressors, as in gas turbine engine. At the same time, supersonic combustion as well as mixing, is one of the most crucial problems which are faced by the hypersonic air-breathing propulsion system. The short residence time of the mixture (in the order of milliseconds) is the key reason for which the flame-holding mechanism in the scramjet combustor cannot fulfil the necessity for cruising a long time in near-space [1, 2]. Hence, a good fuel injection technique with a high amount of mixing as well as penetration plays an important role for fast and most significantly effective combustion. During the recent years, different fuel injections [3-14] have been investigated both experimentally as well computationally in order to enhance the mixing rate and combustion phenomena within the scramjet engine.

Computational Fluid Dynamics approach [15] is one of the significant methods to accelerate experimental investigations, complete parametric studies and confirm whether design variations are advantageous for experimental testing. Simultaneously, it also presents notable perception into complicated flow phenomena such as interactions of shock wave/boundary layer, separations, interactions of turbulence/chemistry model and mode transition and, thus remarkably enhancing the flow-path design technique for proportionately lower costs compared to expensive experimental investigations alone [16-18]

As the flow-phenomena in multi-strut scramjet combustor during the presence of different wall injector have not discussed previously, hence the objective of the present work is to study computationally the effect of different wall injectors on the flow-filed of multi-strut scramjet combustor. The combination of different multi-strut + wall injection scheme and their effect on the performance of multi-strut injector is also studied in details in this paper.

2 Physical model and numerical method

Fig. 1 represents the schematic diagram, of single strut scramjet engine. The entry of preheated air takes place in 50 mm X 40 mm cross-section combustion at Mach number 2.0. In order to compensate for the growth of boundary layer at x = -9 mm, the top wall of the combustion chamber diverges with an angle of 3º. A strut is placed at Y = 25 mm, whose height and length is 6 mm and 32 mm respectively. The position of the strut from the entrance of the combustor is almost 77 mm in the horizontal direction. The injection of H_2 takes place sonically through 15 holes of diameter 1 mm, and 1.6 mm apart from the centre of strut base.

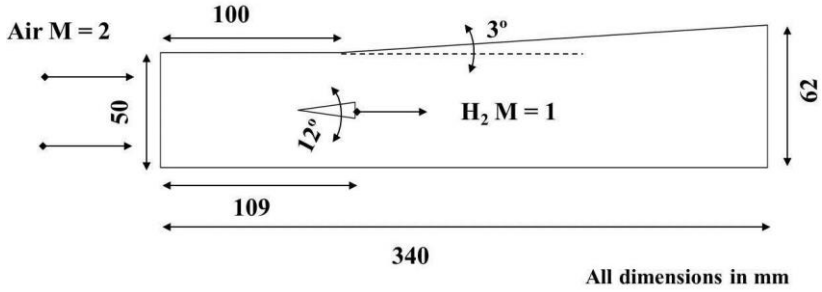

Figure 1 Schematic diagram of DLR supersonic combustion chamber [19-21]

Again for multi-strut scramjet engine, two additional struts are introduced along with central strut for flame holding as well fuel injection process [22]. The overall length of the combustor is 800 mm. The combustor configuration is exactly similar to experimentally investigate DLR combustor. Here the injection of fuel takes place through multiple holes of the struts. Here also the combustor chamber is uniform up to 90 mm and then it diverges at angle 3º in order to avoid the separation of boundary layer.

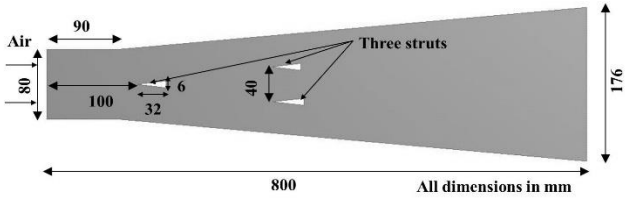

Figure 2 Schematic diagram of multi-strut scramjet combustor

2.1 Numerical method

The 2D compressible RANS equations, the SST k-ω turbulence model, and the finite-rate/eddy-dissipation reaction model are used in order to reveal the flow-field of multi-strut scramjet combustor. Here the preference is given to the RANS equations [23] because they can resolve on coarser meshes and also allow simplifying of steady flow calculations as compared to other computational techniques such as direct numerical simulation, large eddy simulation and detached eddy simulation. As in the present work, the key interest is concentrated on separated flows; hence Menter SST k-ω [24] is selected as turbulence model. This is because, for separated flow case, SST k-ω model is more precise than that of k- ε model. Again, the combination of species transport [25] and finite rate/eddy dissipation reaction model is the combustion model which is mainly used in the present simulation. The selection of these models mainly depends on their simplicity and satisfactorily proper modelling of the burned gas including perfectly oxidised species of H_2 fuel. Additionally, Hydrogen combustion which includes single step chemical reaction is preferred in current simulation because it is satisfactory for estimating the overall performance parameters with considerably lower computational cost [26].

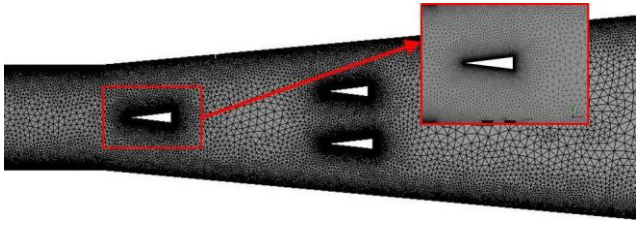

Figure 3 2D unstructured triangular meshes

The computational grids were unstructured and generated by the commercial software ANSYS ICEM-CFD, [27] and the calculation was primarily carry forward on a base grid with 121346 elements respectively. The grids were clustered more densely near the strut as well as the wall region for resolving the boundary layer accurately [Fig. 3]. The boundary conditions for the present model are shown in table 1.

Table 1 Boundary conditions [28]

Variables	Air	H_2
Pressure (Pa)	101325	101325
Temperature (K)	340	250
Mach number (M)	2	1
Mass fraction of H_2 (Y_{H2})	0	1
Mass fraction of O_2 (Y_{O2})	0.232	0
Mass fraction of H_2O (Y_{H2O})	0.032	0
Mass fraction of N_2 (Y_{N2})	0.736	0

3 Validation

The computationally obtained flow patterns characteristic show a reasonable agreement with the experimental observation and are hence reported. The deflection of incoming supersonic flow takes place at the tip of the wedge which is then followed by the formation of two shocks symmetrically on each side. Again, separation of the boundary layer (formed along the walls) takes place at the base of the strut and also the formation of two symmetric shear layers occur, due to the low pressure in the recirculation region that converge towards the centreline. At the same time, two expansion fans are formed due to flow divergence at both corners of the strut. Additionally, the H_2 jet is under-expanded because of the presence of low-pressure region and as a result, diamond-shaped jets are noticed in the computation which can also be seen in the experiment.

Fig. 4(c) shows the experimental and computational pressure variation along the length of the single strut scramjet engine. The impingement of shock on the wall is the primary

reason for the sudden increase in pressure which can be easily noticed from the graph. As the walls are considered as a smooth surface for the computational purpose, hence slight variations are noticed between the simulation and experimental results. The variations of velocity at y = 0.025 m for single-strut with CFD simulation as well as experimental observation are shown in Fig.4 (d). The CFD results specify qualitative as well as quantitative similarity with DLR experimental outcome along with a minimum speed and stronger acceleration in the downward direction [29, 30].

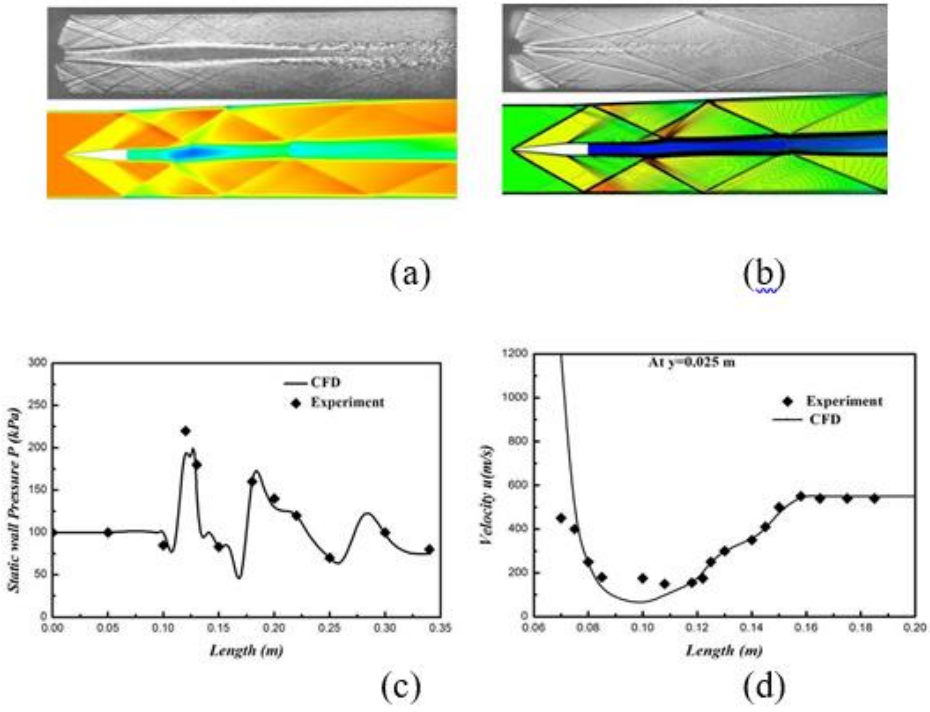

Figure 4 Schlieren image of hydrogen injection [19-21] and CFD predicted (a) Mach number contour (b) density contour for single strut injection (c) Wall pressure distribution for single-strut experimentally[19-21] and with CFD simulation and (d) Horizontal velocity distributions along the middle of the channel at y = 0.025 m

4 Results and discussion

As the current computational simulation represent adequate similarity with the experimental shadowgraph image, pressure as well as velocity variations in the open literature [19-21], hence similar mesh technique mechanism is applied for carry out the rest of the simulation work.

4.1 Multi-strut + wall

When hydrogen is injected from multi-strut as well wall 1 injector, then the formation of shock wave take place from the prime edge of the strut which is then followed by the interaction with the boundary layer as well as the formation of separation region on the bottom wall of combustor. Bow shock formation mainly occurs downstream the strut injector due to normal injection from wall 1 injector. Simultaneously, existence of high pressure region is also noticed close to the fuel injection area due to the initiation of combustion phenomena. As compared to the other parts of the combustor, lower Mach number value is observed in the separation as well as recirculation region.

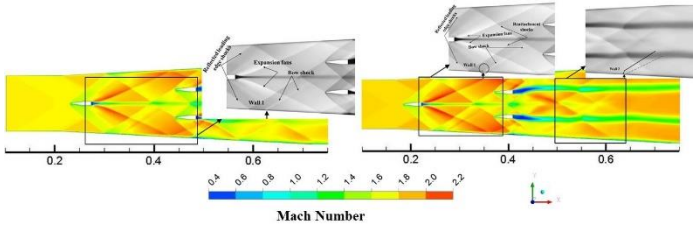

(a) (b)

Figure 5 Effect of (a) *multi-strut + wall 1* (b) *two-strut + wall 1+ wall 2* injector on Mach no contour of two-strut scramjet combustor

With the addition of wall 2 injector along with wall 1 and multi-strut injector vortices are formed near the middle section of the combustor. As a result, there is an improvement in mixing and also the flow is accelerated to higher supersonic speed. The high pressure region is thickened near the wall due to combination of *multi-strut + wall 1+ wall 2* injection which also generates high vortex as well helps in better hydrogen/air mixing. Hence the combination of *multi-strut + wall 1+ wall 2* injection will boost to a wider temperature and robust combustion area adjacent to the wall.

Again, the interaction among the shock waves takes place due to the presence of *multi-strut + wall 1 + wall 2 + wall 3 injector*. These shock waves are mainly generated form the wall injection locations. At the same time, the interaction between the shock wave and boundary layer leads to the formation of separation region on both the wall of the combustor. But the length of the separation region formed by three wall injectors exceeds the length of separation region formed by wall 1 as well as wall 2 injector.

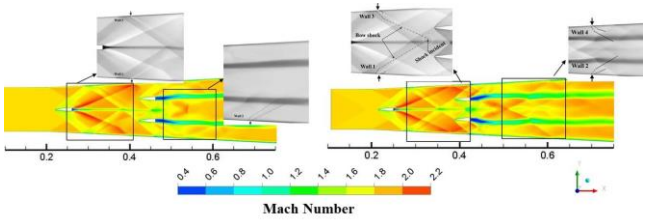

(a) (b)

Figure 6 Effect of (a) *multi-strut + wall 1+ wall 2 + wall 3* (b) *multi-strut + wall 1+ wall 2 + wall 3 + wall 4* injector on Mach no contour of two-strut scramjet combustor

The formation of complex flow-field occurs due to the introduction of wall 4 injector inside the scramjet engine. As a result, the strong shock wave train (formed due to presence of wall injector) is pushed out the combustor section due to stronger combustion phenomena which occurs due to the combination of *multi-strut wall 1+ wall 2 + wall 3+ wall 4* injector. Here also the formation of large separation region along with low Mach number takes place on both the wall of combustor.

4.2 Mixing efficiency

The mixing efficiency can be defined as [31, 32]

$$\eta_{mix}\ (x) = \frac{\int \alpha \rho u Y_{H_2} dA}{\dot{m}_{H_2}(x)}$$

where *A* indicates the channel cross section. The denominator represents the total amount of fuel injected upstream of this section. The quantity α in the numerator is given as

$$\alpha = \begin{Bmatrix} 1/\Phi: & \Phi \geq 1, \\ 1: & \Phi < 1 \end{Bmatrix}$$

The mixing efficiency plot for different injection scheme for $\Phi = 1$ is represented in Fig. 7.

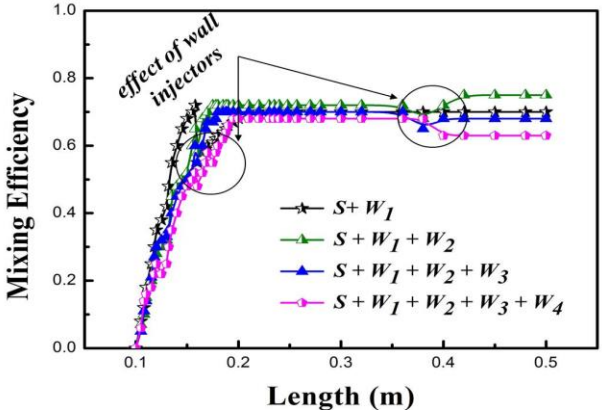

Figure 7 Mixing efficiency plot for different strut + wall configuration where *S* = Multi-strut, W_1 = Wall 1, W_2 = Wall 2, W_3 = Wall 3, W_4 = Wall 4

5 Conclusions

In the current study, the effects of wall injection on the presence of Multi-strut have been investigated numerically. The computational methods used in this paper can be utilised to show the wave systems in the typical single strut scramjet engine, and the results show fairly qualitative agreement with the experimental outcome. Additionally ,the combination of *multi-strut + wall 1+ wall 2* injectors yields better air-H_2 mixing as they boost to a higher penetration depth as compared to other injection schemes. Mixing efficiency is also found to be maximum for *multi-strut + wall 1+ wall 2* injector.

Acknowledgements

The authors would also like to express great gratitude to the Department of Mechanical Engineering of National Institute of Technology (NIT Silchar), Assam, India for providing Computational Fluid Mechanics Lab facilities to carry out the research work. It was extremely helpful for the completion of this work.

References

[1] D Cecere, A Ingenito, E Giacomazzi, L Romagnos C, Bruno, "Hydrogen/air supersonic combustion for future hypersonic vehicles", International Journal of Hydrogen Energy, vol.36, pp. 11969-11984, 2011 doi: 10.1016/j.ijhydene.2011.06.051

[2] "Scramjet combustor development" Dr. Satish Kumar & Team Head, Hypersonic Propulsion Division & Dy. Project Director, HSTDV, DRDL, Hyderabad

[3] K. M Kim, S W Baek , C Y Han, "Numerical study on supersonic combustion with cavity-based fuel injection", International Journal of Heat and Mass Transfer vol. 47, pp. 271–286,2004

[4] W Huang, Li Yan, "Numerical investigation on the ram-scram transition mechanism in a strut-based dual-mode scramjet combustor", International journal of hydrogen energy, vol. 41,pp. 4799- 4807,2016

[5] W Huang, Z. G Wang, L Yan, W. D Liu, "Numerical validation and parametric investigation on the cold flow field of a typical cavity-based scramjet combustor", Acta Astronautica vol.80, pp. 132–140,2012 doi:10.1016/j.actaastro.2012.06.004.

[6] W. Huang, L. Jin , Li Yan , Jian-guo Tan, "Influence of jet-to-cross flow pressure ratio on non-reacting and reacting processes in a scramjet combustor with backward-facing steps", International journal of Hydrogen energy vol.39, pp.21242-21250,2014

[7] W. Huang , Ming-hui Li, Li Yan, "Mixing augmentation mechanism induced by the pseudo shock wave in transverse gaseous injection flow fields", International journal of Hydrogen energy vol. 41, pp.10961-10968,2016

[8] M B Gerdroodbary, M Mokhtari, K Fallah, H Pourmirzaagha, "The influence of micro air jets on mixing augmentation of transverse hydrogen jet in supersonic flow". International journal of Hydrogen energy vol.41, pp.22497-22508, 2016

[9] N. K Mahto, G. Choubey , L Suneetha , K. M Pandey, "Effect of variation of length-to-depth ratio and Mach number on the performance of a typical double cavity scramjet combustor", Acta Astronautica, vol.128,pp.540-550,2016 doi:10.1016/j.actaastro.2016.08.010

[10] G. Choubey, K M Pandey, "Effect of variation of angle of attack on the performance of two-strut scramjet combustor", International Journal of Hydrogen Energy vol. 41(26), pp.11455–11470,2016 doi:10.1016/j.ijhydene.2016.04.048

[11] M B Gerdroodbary, M Mokhtari, K Fallah , H Pourmirzaagha, "Characteristics of transverse hydrogen jet in presence of multi air jets within scramjet combustor", Acta Astronautica , vol 132, pp. 25–32,2017

[12] Z-W Huang, G-q He, F Qin, X-g Wei, "Large eddy simulation of flame structure and combustion mode in a hydrogen fueled supersonic combustor", International journal of Hydrogen energy vol.40, pp. 9815-9824,2015

[13] C Fureby, K Nordin-Bates, K Petterson , A Bresson, V Sabelnikov , "A computational study of supersonic combustion in strut injector and hyper mixer flow fields", Proceedings of the Combustion Institute, vol.35, pp. 2127–2135,2015

[14] J Hu, J Chang, W Bao, Q Yang, J Wen, "Experimental study of a flush wall scramjet combustor equipped with strut/wall fuel injection", Acta Astronautica vol.104, pp. 84–90, 2014

[15] J. H Ferziger and M Peri, "Computational methods for fluid dynamics", 2002 (Chapter 7)

[16] M. A. Vyas, W.A. Engblom, N.J. Georgiadis, C.J. Trefny, V.A. Bhagwandin, "Numerical simulation of vitiation effects on a hydrogen fueled dual-mode scramjet", NASA/TM-2010-216756, 2010

[17] J.S. Shang, "Computational fluid dynamics application to aerospace science", Aeronautical Journal, vol.113, pp. 619–632, 2009

[18] W Huang, W-d Liu, S-b Li, Z-x Xia, Jun Liu, Z-g Wang, "Influences of the turbulence model and the slot width on the transverse slot injection flow field in supersonic flows", Acta Astronautica vol.73, pp.1–9, 2012

[19] W. Waidmann , F Alff , M Bohm , U Brummund , W Clauss, and M Oschwald, "Experimental investigation of hydrogen combustion process in a supersonic combustion ramjet (SCRAMJET)" DGLR, Jahrestagung, Erlangen, Germany, pp. 629–638 (1994)

[20] W. Waidmann , F Alff , M Bohm, U Brummund, W Clauss, and M. Oschwald, "Supersonic combustion of hydrogen/air in a scramjet combustion chamber". Space Technology, vol15(6) pp.421-429,1995 doi: 10.1016/0892-9270(95)00017-8

[21] W. Waidmann, U. Brummund, and J. Nuding, "Experimental investigation of supersonic ramjet combustion (Scramjet)", 8th Int. Symp. on Transport Phenomena in Combustion, Taylor & Francis, Boca Raton, FL.(1996)
[22] S. Kumar, S. Das, S. Sheelam, "Application of CFD and the Kriging method for optimizing the performance of a generic scramjet combustor", Acta Astronautica, vol.101 pp.111–11, 2014
[23] W Huang, L Ma, Z G Wang, M Pourkashanian, D. B Ingham, S B Luo, J Lei, "A parametric study on the aerodynamic characteristics of a hypersonic wave rider vehicle", Acta Astronautica vol.69, pp. 135–140,2011
[24] F.R Menter, "Two-Equation Eddy-Viscosity Turbulence Models for Engineering Applications", AIAA Journal,vol. 32(8), pp. 1598–1605,1994 doi: 10.2514/3.12149
[25] J Tu, G. H Yeoh, and C Liu, "Computational Fluid Dynamics: A Practical Approach," Elsevier, Butterworth–Heinemann, Oxford, UK, (2008).
[26] K Kumaran , V Babu, "Investigation of the effect of chemistry models on the numerical predictions of the supersonic combustion of hydrogen", Combustion and Flame, vol 156, pp. 826–841,2009 doi:10.1016/j.combustflame.2009.01.008
[27] ANSYS. ANSYS Fluent 14.0 theory guide, Canonsburg, PA 15317, ANSYS, Inc.2011
[28] M. Oevermann, "Numerical investigation of turbulent hydrogen combustion in a scramjet using flamelet modelling", Aerospace Science & Technology vol.4,pp.463-480,2000 doi:10.1016/S1270-9638(00)01070-1
[29] G. Choubey, K. M Pandey, "Investigation on the effects of operating variables on the performance of two-strut scramjet combustor", International Journal of Hydrogen Energy vol.41 (45), pp. 20753–20770, 2016 doi: 10.1016/j.ijhydene.2016.09.157
[30] G. Choubey G, K. M Pandey, "Effect of parametric variation of strut layout and position on the performance of a typical two-strut based scramjet combustor", International Journal of Hydrogen Energy 2017 doi: 10.1016/j.ijhydene.2017.03.014
[31] A Rajasekaran and V Babu, "Numerical Simulation of Three-Dimensional Reacting Flow in a Model Supersonic Combustor", Journal of Propulsion and Power, vol.22, pp. 820-827,2006 doi: 10.2514/1.14952
[32] R A Baurle, T Mathur , M. R Gruber, and K. R Jackson, "A Numerical and Experimental Investigation of a Scramjet Combustor for Hypersonic Missile Applications", AIAA Paper 1998-3121, 1998

10TH INTERNATIONAL CONFERENCE ON SUSTAINABLE ENERGY AND ENVIRONMENTAL PROTECTION (JUNE 27TH – 30TH, 2017, BLED, SLOVENIA), MODELLING AND SIMULATION
J. Krope, A.Ghani Olabi, D. Goričanec & S. Božičnik

University of Maribor Press

Identifying Energy Consumers Behaviour by Using Energy Big Data Analytics

ADRIANA REVEIU, SIMONA VASILICA OPREA & ADELA BÂRA

Abstract It has been more and more recognized that behavioural factors of the energy consumers are of a great importance in achieving energy conservation and efficiency, beside technological improvements and policy regulations.

Development of Internet of things, advanced communication networks and big data storage and analytics facilitated digitization of traditional energy systems. In this conditions, large amounts of energy production and consumption data are available. These assure the framework to implement energy big data analytics. Decision support based on data analysis plays an important role in management of energy systems.

The aim of this paper is to propose a model for identifying profiles of energy consumers, based on their energy consuming behaviour and energy appliances used, by exploiting energy big data analytics. The energy consumption patterns of different consumers are heterogeneous, because their energy usage decision is usually affected by various factors. Understanding the energy consumption behaviour of different sort of users is important for both power companies and energy consumers.

Keywords: • energy efficiency • modelling energy consumer profile • energy big data • IoT.• Analytics •

CORRESPONDENCE ADDRESS: Adriana Reveiu, Ph.D., Assoc. Prof., Bucharest University of Economic Studies, Faculty of Cybernetics, Statistics and Economic Informatics, 6 Romana Place, 1st District, Bucharest, Romania, e-mail: reveiua@ase.ro. Simona Vasilica Oprea, Ph.D., Assistant Professor, Bucharest University of Economic Studies, Faculty of Cybernetics, Statistics and Economic Informatics, 6 Romana Place, 1st District, Bucharest, Romania, e-mail: simona.oprea@csie.ase.ro. Adela Bâra, Ph.D., Professor, Bucharest University of Economic Studies, Faculty of Cybernetics, Statistics and Economic Informatics, 6 Romana Place, 1st District, Bucharest, Romania, e-mail: bara.adela@ie.ase.ro.

https://doi.org/10.18690/978-961-286-058-5.11 ISBN 978-961-286-058-5

Available at: http://press.um.si.

1 Introduction

Important efforts were developed to decrease energy consumption, by designing a high number of energy efficiency technologies and appliances, and by developing public policies aiming to stimulate energy saving. Energy consumers can now invest in technologies, in order to reduce the demand of energy, such as: rooftop solar photovoltaic systems, plug-in electric vehicles, home energy management systems, and new battery storage technologies. These technologies can make energy infrastructure more reliable, efficient and less polluting. [1]

Beside technological developments and policy regulations, an important approach aiming to conserve energy is consumers' behaviour. The energy consumption patterns record high variance because of the multitude of factors influencing the consumers' decisions. In addition, the salvage potential of domestic energy is considerable, as stated in [2]. So that, it is important to understand the behaviour of energy consumers, in order to influence it, because this is an efficient solution to decrease energy consumption.

On the other hand, development of Internet of things, advanced communication networks and big data storage and analytics facilitated digitization of traditional energy systems. So that, traditionally energy system is being replaced by the smart energy system, which includes intelligent components aiming to manage and analyse large amount of heterogonous data, about the entire energy management channel. As a consequence, large amounts of energy production and consumption data are generated, stored and are available for future processing and analysis. These assure the framework to implement decision support systems in energy based on energy big data analytics, in order to decrease energy consumption.

For studying and modelling energy consumers' behaviour, both economic and sociologic approaches have been used. It attempts to understand the consumers' motivations and habits in using energy.

2 Modelling Consumers Behaviour

Energy consumers' behaviour have been studied deeply from various perspectives: economic, engineering, sociological, and psychological. [3,4,5] The people behaviour and habits is different in their homes and at workplaces. [6]

Energy consumption in itself is not a behaviour, but it is a consequence of behaviours, like: turning the lights off, lowering thermostat levels, and so on. Behavioural researches have proved that consumers are not quite as rational as they are often assumed to be in economic modelling approaches. [7]

Economic related researches show that behavioural factors have a major importance in determining energy efficiency [8], and that economic parameters, e.g. prices, costs,

explain only a part of observed behaviour [9]. This indicates a need for further research into behavioural influences affecting energy consumption.

Three dimensions related to energy consumers' behaviour could be identified: time, spatial and user dimensions.

Time dimension describes the end-user consumption behaviour at various granularity time levels: a minute, an hour, a day, a week, a season or a year.

User dimension considers the consuming behaviours related to the specific behaviour of each person from a household, or from a company. Behavioural factors influencing energy consumers are both objective and subjective. [10] Objective factors are not linked to the people decisions or personal selections. Objective factors are related to households' characteristics, rooms' size, family size and income level. Objective factors could be identified easier than the subjective ones. Subjective factors are specific to individuals' daily behaviour and habits in consuming energy, like: level of understanding of energy saving issues, life style and cultural background, social norms, past experience, perceptions of quality, and trust-based information networks.

Spatial dimension tackles about the specific geographical and environmental conditions, energy price, local policies influencing energy consumption in households, and surrounding environment.

3 Support IT Solutions for Energy Big Data System

Information and communication technologies in general, in particular the emerging information technologies, namely: big data analytics, internet of things, and cloud computing are increasingly used into the whole process of energy sector from production to consumption. [11]

Firstly, Internet of Things (IoT) is an overall infrastructure enabling advanced services, by creating a physical and virtual interconnection of things, based on existing and evolving interoperable information and communication technologies [12].

Secondly, cloud computing is a complex technology, with virtually unlimited capabilities in terms of storage and processing power.

Thirdly, big data analytics techniques can manage and integrate various types of real time and historical data, acquired from different sources, aiming to be used on the fly. By using big data analytics technologies we could continuously improve the collection, aggregation, processing and use of data to improve the energy systems.

The framework of proposed solution for energy big data system setting up is depicted in the figure 1.

The sensing layer contains sensors aiming to provide energy related data about consumers' behaviour and environmental conditions, by using user, spatial and time dimensions.

The interconnecting layer aims to integrate and to adapt data received from the sensing layer and data from other sources, like: weather data, socio-demographic and behavioural data of energy consumers, and so on. IoT is the supporting technology used by this layer, in order to acquire real time data from sensors and to interconnect them.

Data layer has as main tasks to store, to manage and to integrate data acquired from various data sources. The supporting technologies for this layer are: database management systems and cloud computing technologies.

Big data analytics layer aims to provide, for the enhanced energy service layer, the framework for discovering appropriate knowledge and data processing, from available data, in the right time. Enhanced energy services layer is the beneficiary layer of the framework and comprises energy related services, including the service for identifying energy consumers' profile.

Figure 10. Framework of proposed solution

Big data in the energy sector, named energy big data [10] have to meet the "4V" characteristics, namely: volume, velocity, variety, and value.

Energy big data mean a huge volume of data. In the case of energy smart systems, using a lot of smart metering devices, the gathered amount of data about energy consumption is impressive. Analytical processing should be used in order to manage and to make useful this volume of energy related data.

Velocity of energy big data refers to the speed of data collection, processing and analysis. Unless the traditional energy systems, where data are usually processed after a significant time interval, an intelligent energy system needs to process both current data and historical data, almost in real time. This is why speed up data processing is a critical issue in the energy big data systems. This task is fulfil with the support of IoT solution for data gathering, cloud computing technologies, and data mining a real time decision support system could be developed.

Data used in an energy big data system have a higher degree of data variety, comparing with the data from traditional energy systems. This is true because the data sources and data types are heterogeneous in an energy big data system; a part of data being structured, and some of them being unstructured.

Data from an energy big data is valued only if they could be analysed and interpreted in the right format and in time, to be available for supporting decisions.

4 Identifing Energy Consumers' Behaviour by Using Energy Big Data

In the last years, some researchers proposed models aiming to explore householders' energy consumption behaviour and the influencing factors. But, they didn't provide a conceptual framework that can be implemented to understand what major influential factors affect consumers' energy use characteristics in a particular building, and how the influence their energy use behaviour. [13]

This paper aims to use energy big data analytics technologies as supporting tools, in order to develop a framework which can be used on various types of buildings, locations and weather conditions to identify the influential factors of energy consumers' behaviour.
Several behavioural models and theories were developed, some of the most complex are: attitude-behaviour-context (ABC) model, motivation-opportunity-ability (MOA) model, and Triandis' model [14].

Unlike the first two models, Triandis model considers not only the objective and subjective factors influencing consumers' behaviour, but also consumers' habits and routine, maybe the most important component of human behaviour. [15]

According to Triandis, behaviour is partially influenced by the intention, partially by the habits, and somewhat by the situational constraints and environmental conditions. Triandis model uses six factors: attitudes, contextual factors, personal capabilities (affects and intentions), social factors and habits to model the behavioural influence factors.

Attitudes are distinctly from rational personal decisions, and may include both positive and negative emotional responses of different situations.

Personal capabilities refer to affects and intentions.

Affects suppose an instinctive behavioural responses to a specific situation and existing emotional antecedents.

The intention is influenced by social and affective factors, as well as by rational deliberations.

Social factors include: norms, roles, public policies and self-concept.

Norms refer to social rules about what should and should not be done.

Roles are related to personal believe about behaviours, appropriate for persons having a particular positions in a group.

According with Triandis model, self-concept refers to the behaviours that the person does or does not engage in.

Habits consider the frequency of past and current behaviours.

To fulfil the research tasks we adapted Triandis interpersonal behaviour model to describe energy consumers' behaviour, as presented in figure 2.

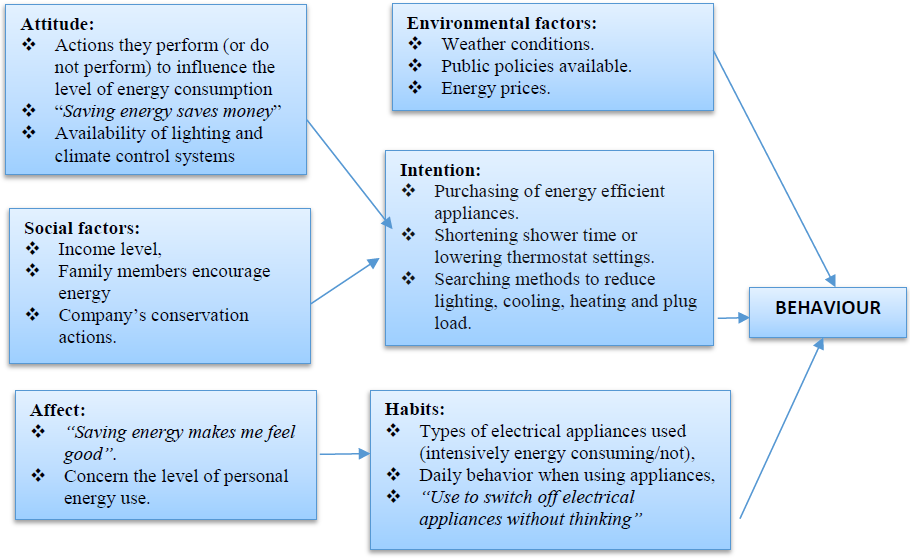

Figure 11. Framework for interpersonal behaviour model for energy consumers

5 Conclusive Remarks and Future Work

The paper proposes a solution for acquiring, integrating, management and modelling data about energy consumers' behaviour and attitudes, aiming to influence energy saving. Defining a framework for identifying energy consumers' behaviour is the first step of our ongoing research. In a next phase, the model will be implemented in order to identify statistical significant groups of energy consumers with common characteristics and to evaluate the impact of changing their behaviour for energy saving.

Acknowledgement

This work was supported by a grant of the Romanian National Authority for Scientific Research and Innovation, CNCS/CCCDI – UEFISCDI, project number PN-III-P2-2.1-BG-2016-0286 "Informatics solutions for electricity consumption analysis and optimization in smart grids" and contract no. 77BG/2016, within PNCDI III.

References

[1] A. R. Carrico, M. P. Vandenbergh, P. C. Stern, and T. Dietz, "US climate policy needs behavioural science.", *Nature Clim. Change*, no. 5, pp. 177–179, 2015.

[2] European Commission. Communication from the commission—action plan for energy efficiency: realising the potential. European Commission Report, COM (2006) 545 Final, 2006.

[3] K. Zhou and S. Yang, "A framework of service-oriented operation model of China's power system.", *Renew Sustain Energy Rev*, no. 50, pp. 719–25, 2015.

[4] Z. Rupert, W. Wehrmeyer, and R. Murphy, "The energy efficiency behaviour of individuals in large organisations: A case study of a major UK infrastructure operator", *Energy Policy*, no. 104, pp. 38–49, 2017.

[5] A. Reveiu, I. Smeureanu, M. Dardala, R. Kanala, "Modelling Domestic Lighting Energy Consumption in Romania by Integrating Consumers Behavior", *Procedia Computer Science*, no. 52(1), pp. 812-818, December 2015.

[6] N. Murtagh, M. Nati, W.R. Headley, B. Gatersleben, A. Gluhak, A., M.A. Imran, D. Uzzell, "Individual energy use and feedback in an office setting: a field trial." *Energy Policy*, no. 62, pp. 717–728, 2013.

[7] C. Wilson and Dowlatabadi, "Models of decision making and residential energy use.", *Annu. Rev. Environ. Resour*., no. 32, pp. 169–203, 2007.

[8] E. Cagno, and A.Trianni, "Evaluating the barriers to specific industrial energy efficiency measures: an exploratory study in small and medium-sized enterprises." *J. Clean. Prod.*, no. 82, pp. 70–83, 2014.

[9] S. Sorrell, "Reducing energy demand: a review of issues, challenges and approaches.", *Renew. Sustain. Energy Rev*., no. 47, pp. 74–82, 2015.

[10] K. Zhou, S. Yang, "Understanding household energy consumption behavior: The contribution of energy big data analytics", *Renewable and Sustainable Energy Reviews*, no. 56, pp. 810–819, 2016.

[11] S. M. R. Islam, D. Kwak, M. H. Kabir, M. Hossain and K. S. Kwak, "The Internet of Things for Health Care: A Comprehensive Survey," in *IEEE Access*, vol. 3, pp. 678-708, 2015.

[12] International Telecommunication Union, "Overview of the internet of things." [Online]. Available: https://www.itu.int/rec/T-RECY. 2060-201206-I, 2012.

[13] D. Li, C. C. Menassa, A. Karatas, "Energy use behaviors in buildings: Towards an integrated conceptual framework", *Energy Research & Social Science*, no. 23, pp. 97–112, 2017.

[14] M. Martiskainen, *Affecting consumer behaviour on energy demand*, Sussex Energy Group, 2007.

[15] H.C. Triandis,"Values, attitudes and interpersonal behavior", in Nebraska Symposium on Motivation: Beliefs, attitudes and values. University of Nebraska Press, pp. 195-259, 1980.

10TH INTERNATIONAL CONFERENCE ON SUSTAINABLE ENERGY AND ENVIRONMENTAL PROTECTION (JUNE 27TH – 30TH, 2017, BLED, SLOVENIA), MODELLING AND SIMULATION
J. Krope, A.Ghani Olabi, D. Goričanec & S. Božičnik

University of Maribor Press

Numerical Analysis of Scramjet Combustor with Innovative Designs of Strut Injector

OBULA REDDY KUMMITHA, KRISHNA MURARI PANDEY & RAJAT GUPTA

Abstract In this research paper passive method has been considered to improve the mixing and combustion efficiency of scramjet combustor. For this the modified and innovative strut injector designs have been developed from the reference of DLR scramjet. The newly introduced strut injector models are named as rocket and double arrow shape strut injectors. The numerical analysis of computational domains with innovative strut injectors has been carried out by considering the ANSYS – FLUENT 15.0, which is a numerical simulation tool. Shear stress transport model (SST k-ω model) has been considered for turbulence modelling under high speed flows. From the numerical results it is observed that the compressed air entered into the combustion chamber is at higher pressure than the basic DLR scramjet model and it reduces the ignition delay. And also it is found that with rocket and double arrow strut model the boundary layer separation and vortices formation is increases and it gives the better mixing of fuel and air and finally it improves the combustion efficiency.

Keywords: • scramjet • optimization • passive techniques • mixing efficiency • combustion efficiency •

CORRESPONDENCE ADDRESS: Obula Reddy Kummitha, GITAM University, School of Technology, Mechanical Engineering Department, Rudraram, Patancheru Mandal, Hyderabad, Telangana, Medak Dist. – 502329, India, e-mail: obulareddy.bec10@gmail.com. Krishna Murari Pandey, Ph.D., Professor, National Institute of Technology Silchar Assam India, Department of Mechanical Engineering, 788010, e-mail: kmpandey2001@yahoo.com. Rajat Gupta, National Institute of Technology Silchar, Mechanical Engineering Department, NIT Road, Dist Cachar, Silchar, Assam 788010, India, e-mail: rguptanitsri@gmail.com.

https://doi.org/10.18690/978-961-286-058-5.12 ISBN 978-961-286-058-5

Available at: http://press.um.si.

1 Introduction

The study of supersonic combustion ramjet (SCRAMJET) is one of the most interesting and ongoing research on aerospace technology. In present years, the study of combustion phenomenon in supersonic flows creates and promotes a huge interest in the further development of scramjet engines [1]. Most of the countries are interested and doing more research work in the field of scramjet combustion engines due to its more applications and advantages in the field of aerospace and relative fields (military missiles, etc.,) [2,3]. Pandey K M et al. [4,5] performed a numerical and computational study on mixing characteristics of scramjet combustor. For their study, they observed that in order to achieve efficient combustion in the scramjet combustor, it is necessary to enhance and accelerate the mixing between fuel and air as well as to reduce the pressure losses in the combustion. K. kumaran and V. Babu [6] in their work found that multi step chemistry model gives the better approximations than the single step model. Waidmann W, et al, were performed experimental investigation of hydrogen combustion process in a supersonic combustion ramjet and found that the efficient mixing of fuel and air is greatly affected by the shock layer formation and vertex development in the flow dynamics [7,8,9]. From this we can understand that the importance of computational fluid dynamics to predict the boundary layer separation and the formation of vertex and to analyze the flow characteristics that are used for evaluation of efficient combustion in the scramjet combustor[10].

Choubey G and Pandey KM [11] investigated the effect of angle of attack variation on scramjet combustor performance with two strut fuel injector. Three angle of attack (α = 3^o, 0^0 and -3^o) were considered and simulation had performed using RANS and SST k-w turbulence model. From the numerical results they found that the scramjet model with 0^o angle of attack had smallest ignition delay as compared to the other two models. And also found that the mixing phenomenon and combustion efficiency was high in the case of 0^o angle of attack.

Farah A.L et al. [12] analyzed numerically the influence of multi staged injection of hydrogen fuel in a supersonic scramjet combustor along with centrally located wedge shaped strut injector by considering Reynolds-averaged Navier-Stokes (RANS) equations and SST k-w turbulence model by using ANSYS CFS-12 code. The internal flow field of scramjet combustor with multiple complex shock waves analyzed and compared with the experimental schlieren images available in open literature and found a good agreement between the numerical and experimental results. And also they found that the mixing of fuel and supersonic air was enhanced with increased in formation of vortices and bow shocks with multi staged injection.

Both mixing and combustion phenomenon are complex process and directly proportional to each other, with increase in mixing of fuel and supersonic air combustion efficiency also will increases. Hence, the major objective and challenging task in scramjet technology is mixing enhancement of fuel and supersonic air. In view of highly expensive

and safety precautions many researchers are performed numerical study on scramjet technology.

Combustor geometry and location of fuel injection strut and injection scheme are have an important role in a supersonic scramjet combustor. Zun Cai et al. [13] analyzed the effect of fuel injection scheme and combustor geometry on the combustion performance in supersonic flows. In this research paper numerical simulations were carried out to investigate the effect of rear wall-expansion cavity which is attached to the wall of the combustor. Different chemical reaction mechanisms also considered. From the numerical analysis they found that the scramjet combustor with a rear wall expansion cavity configuration showed a better ability for the prevention of thermal chocking than the other configurations of combustor under the same fuel injection scheme. It was found that the supersonic combustion for a rear wall expansion cavity configuration was highly sensitive to the fuel injection scheme and location of strut, but not that much considerable sensitive to the injection pressure. And also they found that flame stabilization was achieved with combined fuel injection scheme (upstream injection of the cavity in addition to the direct injection on the rear wall).

The objective of the present work is to study the combustion flow dynamics of basic and modified versions of the DLR scramjet engine named as rocket and double arrow strut scramjet models. In this paper, how the combustion flow dynamics are being variable with flow geometry has been reported. Finite rate/eddy dissipation chemistry model along with SST k-ω turbulence model were considered for the better and more accurate results prediction of combustion flow dynamics.

2 Mathematical And Numerical Modeling

The supersonic scramjet engine combustion process is greatly affected by the turbulence, hence the complete Navier - Stokes equations have been considered in the approximate numerical analysis of combustion flow dynamics. The supersonic scramjet combustion flow dynamics are characterized by the evolution of boundary layer formation and shock waves, for this two dimensional Navier-Stokes equations have been defined as follows [14].

Mass conservation (continuity equation):

$$\frac{\partial \rho}{\partial t} + \frac{\partial}{\partial x_i}(\rho u_i) = 0 \tag{1}$$

Momentum conservation:

$$\frac{\partial}{\partial t}(\rho u_i) + \frac{\partial}{\partial x_i}(\rho u_i u_j) = -\frac{\partial P}{\partial x_i} + \frac{\partial}{\partial x_i}(\tau_{ij}) \tag{2}$$

Energy equation:

$$\frac{\partial}{\partial t}(\rho e_t) + \frac{\partial}{\partial x_i}(\rho h_t u_j) = \frac{\partial}{\partial x_i}(\tau_{ij} u_i - q_i) \tag{3}$$

2.1 Turbulence modelling

Turbulence modelling is the most important part in combustion problems and its physics involved at the molecular level and causes for mixing of fuel and air. Great coupling is involved in between turbulence and combustion in terms of mixing, dissipation, and diffusion and chemistry reaction rate. In order to evaluate the heat of reaction, combustion stability, species transport and flame aerodynamics, the turbulence governing equations with the function of stress tensor must be modelled. Shear stress transport k-ω turbulence model has been considered and the governing transport equations of turbulent kinetic energy (k) and turbulent dissipation rate (ω) are defined as follows [14].

$$\frac{\partial k}{\partial t} + U_i \frac{\partial k}{\partial x_i} = \frac{\partial}{\partial x_i}[(\vartheta + \sigma_k \vartheta_t)\frac{\partial k}{\partial x_i}] + P_k - C_\mu \omega k \tag{4}$$

$$\frac{\partial \omega}{\partial t} + U_i \frac{\partial \omega}{\partial x_i} = \frac{\partial}{\partial x_i}[(\vartheta + \sigma_\omega \vartheta_t)\frac{\partial \omega}{\partial x_i}] + \gamma \frac{\omega}{k} P_k - \beta \omega^2 + (1 - F_1)\frac{2\sigma_\omega}{\omega}\frac{\partial k}{\partial x_i}\frac{\partial \omega}{\partial x_i} \tag{5}$$

In Eq.4, the left hand side terms are defined as temporal change and convective terms of turbulent kinetic energy. Right hand side first term of Eq.4 represents the diffusive transport of turbulent stresses. Production of turbulent kinetic energy is represented by P_k and the last term is defined as dissipation of turbulent kinetic energy. Similarly the Eq.5 also can be understood in a similar manner except the last two terms. The blending function F_1 is defined as

$$F_1 = (\arg_1^4)$$

Where,

$$\arg_1 = \min\left[\max\left(\frac{\sqrt{k}}{C_\mu \omega y}, \frac{500\vartheta}{y^2\omega}\right), \frac{4\rho\sigma_{\omega 2}k}{CD_{k\omega}y^2}\right]$$

Where, y represents the normal distance to the wall and $CD_{k\omega}$ is defined as a positive portion of the cross diffusion term.

$$CD_{k\omega} = \max\left(2\rho\sigma_{\omega 2}\frac{1}{\omega}\frac{\partial k}{\partial x_i}\frac{\partial \omega}{\partial x_i}, 10^{-20}\right)$$

2.2 Combustion modelling

Combustion is defined as the rapid chemical reaction and is involved in rapid turbulence creation, hence it requires more attention to model and simulate the combustion flow dynamics. In ANSYS-Fluent the finite rate chemistry turbulence model with eddy dissipation is one of the best and most utilized combustion modelling approach which is mainly used in the present research work. The global one step chemical reaction of hydrogen combustion has been considered in this paper for its capable of predicting the overall performance parameters with considerably less computational cost for the scramjet combustor [6], and the reaction equation is as follows:

$2H_2 + O_2 \rightarrow 2H_2O$

2.3 Geometry modelling and mesh generation

Basic or a standard reference scramjet model has been considered from the experimental test rig of DLR scramjet model [3, 4, 5]. The modified and innovated rocket and double arrow strut models were created with reference to the basic DLR scramjet model. The computational domains of the basic DLR scramjet strut model and the newly introduced innovated models are developed by the design modular and mesh was generated by the mesh modular tool defined as pre-processor tool of ANSYS-FLUENT and the computational domains are shown in Fig.1.

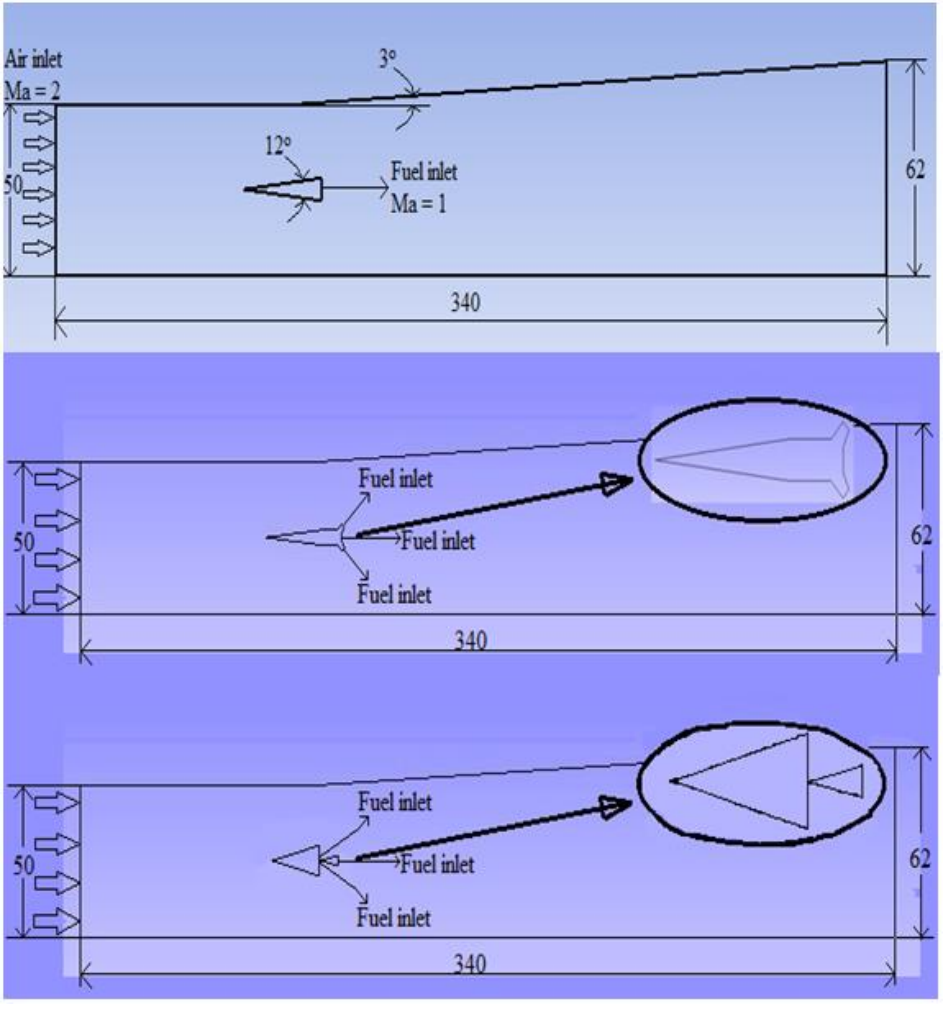

Fig. 1 Basic DLR scramjet model, rocket and double arrow strut model

2.4 Grid Independence study

Grid independence study is the process of finding the finest and best grid size, in which further grid refinement will not change the obtained solution. Three cases have been considered to generate the mesh for computational domains and are defined as fine mesh, coarse mesh and medium mesh.

Grid independence study can be performed by plotting a graph in between the obtained solution and number of elements. Initially the solution has been carried out with 36000 elements (coarse) and the simulation has been extended with 50000 (medium) and 65000

(fine mesh). A plot has been generated to study the variation of results with respect to the variation of grid size and it is observed that the solution remains constant after 79600 elements.

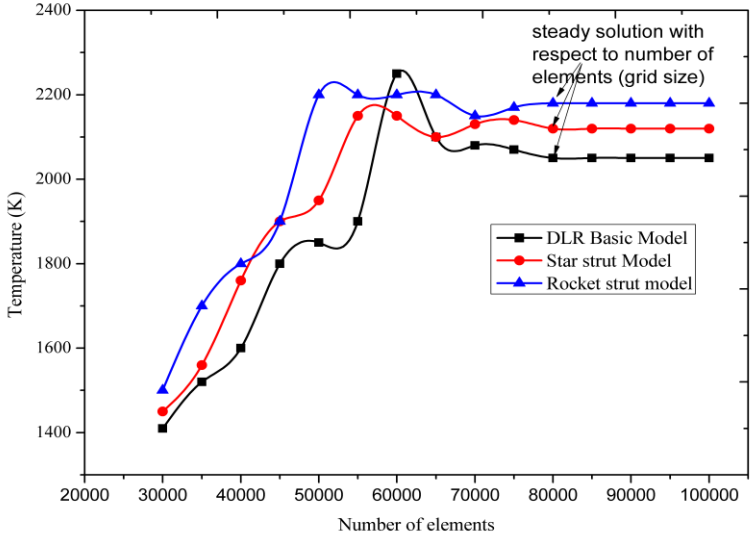

Fig.2 Grid independence study

2.5 Initial and boundary conditions

The solution of numerically simulated problems greatly depends on type of initial and boundary conditions assigned. In this problem, air enters into the isolator section at a Mach number of 2 and fuel is injected at a sonic speed. Air and fuel inlets are defined with Dirichlet boundary conditions and no slip boundary condition is used to define the walls of computational domain. Neumann boundary condition is used to define the outflow wall of the domain. All the variables used at inlet and outlet boundary conditions are defined in the following table.

Table 1. Style and Font Size

Variable	Air	H_2
Ma	2.0	1.0
u (m/s)	730	1200
T (K)	340	250
P (Pa)	100000	100000
ρ (kg/m^3)	1.002	0.097
Y_{O2}	0.232	0
Y_{N2}	0.736	0
Y_{H2O}	0.032	0
Y_{H2}	0	1

3 Validation of results

The computational fluid dynamics results of any numerical problem should be compare and validate with the experimental data available in open literature. In this research paper, numerical results have been compared and validation has been done with the DLR experimental data available in open literature [7-9]. From the numerical results and DLR experimental schlieren images it is observed that the shock waves are developed at the edge of tip of the strut and the same undergoes to multiple reflection in between the strut and combustion chamber walls and develops a shock train (Fig.3). It is identified that the shock train development and reflection location of oblique and expansion shocks of both numerical and experimental are almost similar (Fig.3).

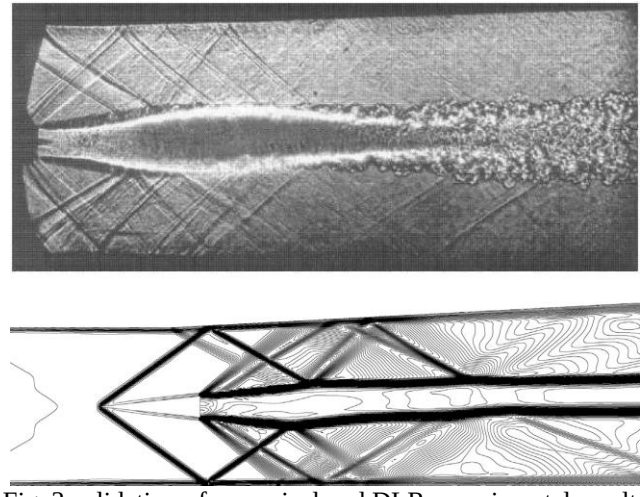

Fig. 3 validation of numerical and DLR experimental results

4 Results and discussion

The numerical analysis of scramjet combustor with different designs fuel injection strut has been analysed with finite volume second order upwind discretization scheme and finite rate eddy dissipation chemistry turbulence model.

Experimental and numerical results comparison of basic DLR scramjet model has been made and it is found that the numerical results are almost similar with experimental results and the same has been reported in validation section.

The variation of static pressure along combustor lower wall and middle of the combustor is shown in fig.4.

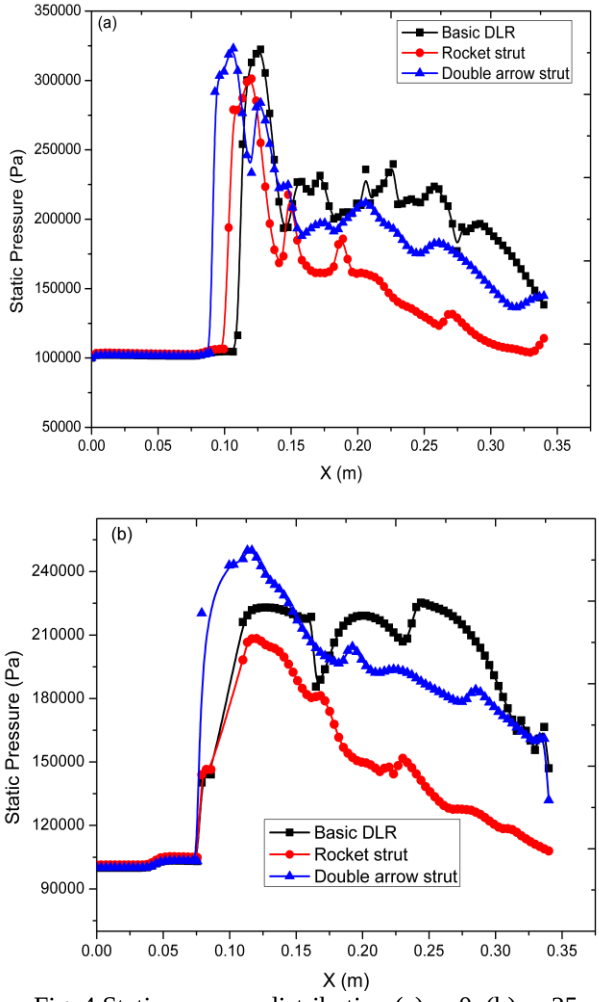

Fig. 4 Static pressure distribution (a) y=0, (b) y=25

From the Fig.4, it is observed that the static pressure of the compressed air for double arrow strut before enter into the combustion chamber is higher as compared to the other two cases. In Fig.4 (a), the peak and lower points in pressure curve represents the multiple reflections of shock waves.

The computational flow field is more illustrated by plotting velocity variations at different sections along the length of the combustor (Fig.5). From the velocity profiles it is identified that the velocity of compressed air decreases from the inlet of isolator to the inlet of combustion chamber. And also it is observed that the velocity of combustion

products increases from x=108 mm to the x=275 mm by converting pressure energy into kinetic energy (Fig.5).

From the comparison of different strut injectors velocity it is identified that the rate of conversion of pressure energy into kinetic energy is more for the case of double arrow strut.

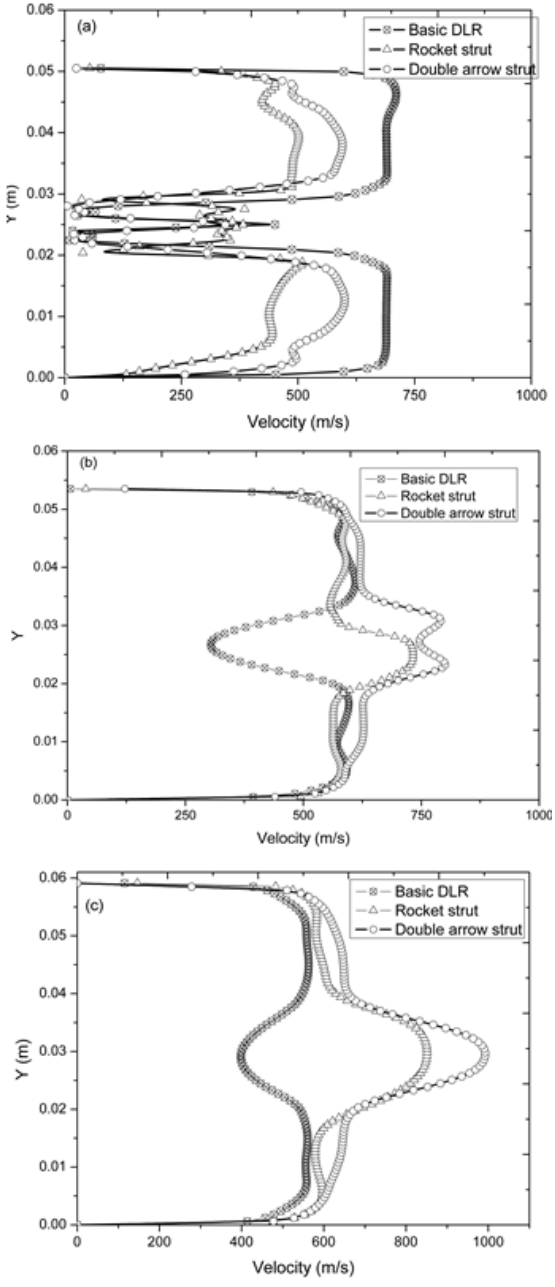

Fig. 5 Velocity profiles at different sections (a) x=108, (b) =167 and (c) = 275 mm

The mixing and combustion of fuel and supersonic air has been studied by analyzing the combustion chamber flow characteristics like pressure, velocity and temperature. The temperature plot for different strut case has been shown in Fig. 6.

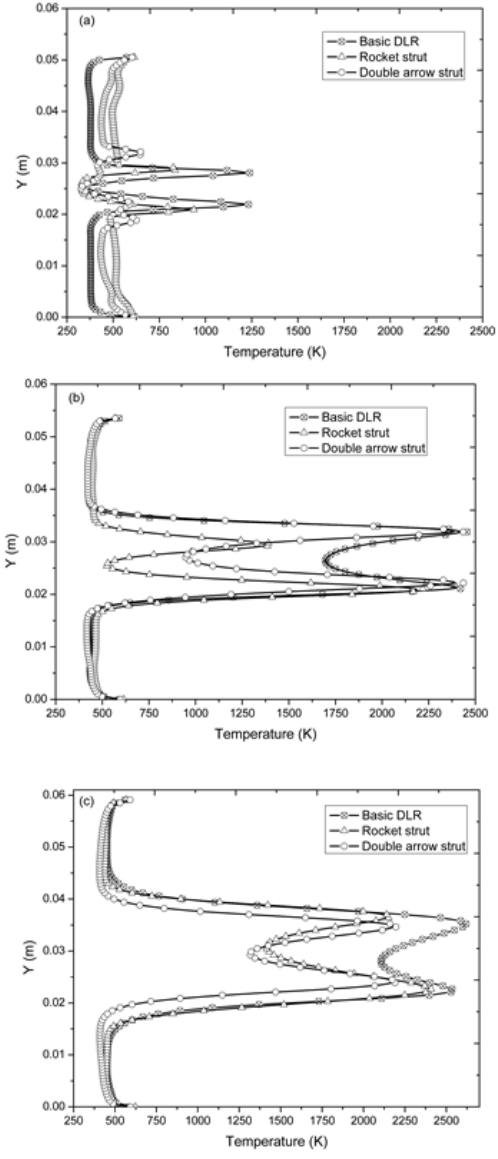

Fig.6 Temperature profiles at different sections (a) x=108, (b) =167 and (c) = 275 mm

From the temperature profiles it is identified that the temperature increases along the length of the combustor. With increase in combustion width for double arrow strut and rocket strut it has been observed that fuel and air mixing is more as compared to the other two cases up to x = 245 mm.

From the temperature and velocity profiles it is observed that double and rocket strut has extra oblique shocks due to inclined injection of fuel.

5 Conclusion

Numerical analysis of scramjet combustor with different fuel injector designs has been analyzed and predicted the flow characteristics like shock waves, pressure distribution, velocity profile and temperature flow field. Numerical results has been compared with the experimental and found a good agreement qualitatively and quantitatively. From the pressure profiles it has been identified that the inlet pressure of compressed air for the both double arrow and rocket strut is greater than that of basic DLR scramjet model and it leads to decrease in ignition delay and increases the tendency of early combustion. From the velocity and temperature profiles it is found that combustion zone has been increased due to inclined injection of fuel into the main stream. From all the contours and plots it has to be concluded that the mixing and combustion efficiency can be enhanced with these types of fuel injection struts having an inclined fuel injection technique

References

[1] Scramjet combustor development Dr. Satish Kumar & Team Head, Hypersonic Propulsion Division & Dy. Project Director, HSTDV, DRDL, Hyderabad.

[2] Cecere D, Ingenito A, Giacomazzi E, Romagnos L, Bruno C. Hydrogen/air supersonic combustion for future hypersonic vehicles. *Int J Hydrogen Energy*, vol. 36: pp. 11969-84, 2011.

[3] Pandey KM, Roga S, Choubey G. Computational analysis of hypersonic combustor using strut injector at flight mach 7. *Combust Sci Technol* vol. 187(9): pp. 1392-407, 2015.

[4] Pandey KM, Sivasakthivel T. CFD analysis of mixing and combustion of a scramjet combustor with a planer strut injector. Int J Environ Sci Dev (2011);2: 102-8.

[5] Pandey KM, Sivasakthivel T. CFD analysis of hydrogen fuelled mixture in scramjet combustor with a strut injector by using fluent software. Int J Eng Technol, vol.3, pp.109-15, 2011.

[6] Kumaran K, Babu V. Investigation of the effect of chemistry models on the numerical predictions of the supersonic combustion of hydrogen. Combust Flame, vol. 156, pp. 826-41, 2009.

[7] Waidmann W, Alff F, Bohm M, Brummund U, Clauss W, Oschwald M. Experimental investigation of hydrogen combustion process in a supersonic combustion ramjet (SCRAMJET)" DGLR. Jahrestag Erlangen, pp. 629-38, 1994.

[9] Waidmann W, Alff F, Bohm M, Brummund U, Clauss W, Oschwald M. Supersonic combustion of hydrogen/air in a scramjet combustion chamber, Space Technol, vol. 15(6), pp. 421-9, 1995.

[10] Waidmann W, Brummund U, Nuding J. Experimental investigation of supersonic ramjet combustion (Scramjet). In: 8th int. Symp. on transport phenomena in combustion. Boca Raton, FL: Taylor & Francis; 1996.

[11] Choubey G, Pandey KM, Effect of variation of angle of attack on the performance of two srtut scramjet combustor, International journal of Hydrogen energy, 2016.

[12] L. Abu-Farahn, O.J. Haidn, H.-P. Kau, Numerical simulations of single and multi-staged injection of H2 in a supersonic scramjet combustor, Propulsion and power research, 3(4), 2014, 175-186.

[13] Zun Cai, Zhenguo Wang, Mingbo Sun, Xue-Song Bai, Effect of combustor geometry and fuel injection scheme on the combustion process in a supersonic flow, Acta Astronautica 129 (2016) 44–51.

[14] Obula Reddy Kummitha, Lakka Suneetha, K.M. Pandey, Numerical analysis of scramjet combustor with innovative strut and fuel injection techniques, International journal of hydrogen energy 2017,
http://dx.doi.org/10.1016/j.ijhydene.2017.01.213

10TH INTERNATIONAL CONFERENCE ON SUSTAINABLE ENERGY AND ENVIRONMENTAL PROTECTION (JUNE 27TH – 30TH, 2017, BLED, SLOVENIA), MODELLING AND SIMULATION
J. Krope, A.Ghani Olabi, D. Goričanec & S. Božičnik

University of Maribor Press

Automated Scenario Generation by P-Graphs

EVA KONIG & BOTOND BERTOK

Abstract Uncertain availability limits the applicability of renewable energy sources. The effects of the installation of new technologies can be analysed only by methods that are capable of systematically considering the general consequences of these uncertainties. One of the most detailed and applied method is the scenario analysis. However, if there are more consequences of an uncertainty that have an effect on several components of the system, then even enumerating and considering all the possible scenarios are complex questions. A tool based on the P-graph framework is proposed herein according to a superstructure approach. Software-based generation of all the possible scenarios is possible by applying the tools of the P-graph method. Originally, the P-graph framework has been developed for designing engineering processes and systems where the method provides the technically feasible alternative structures involved in a superstructure. As an analogy, we propose to algorithmically generate the scenarios as the combinations of the possible consequences of the uncertainties. This proposed method will be illustrated by a case study that involves feasible technologies utilizing renewable energy sources.

Keywords: • P-graph • scenarios • process synthesis • uncertainty • renewable energy sources •

CORRESPONDENCE ADDRESS: Eva Konig, Assistant, University of Pannonia, Faculty of Information Technology, Egyetem utca 10., 8200 Veszprem, Hungary, e-mail: konig@dcs.uni-pannon.hu. Botond Bertok, Ph.D., Associate Professor, University of Pannonia, Faculty of Information Technology, Egyetem utca 10., 8200 Veszprem, Hungary, e-mail: bertok@dcs.uni-pannon.hu.

https://doi.org/10.18690/978-961-286-058-5.13 ISBN 978-961-286-058-5

Available at: http://press.um.si.

1 Introduction

Utilization of renewable sources in energy generation has become crucial in the latest decade. Although, the availability of these renewable sources, such as wind, biomass, or solar source, is much more localized than the fossil based power sources. Therefore the conversion from fossils to renewable sources is not trivial, since not only the related technology is different but the system should be decentralized as well [6]. Another issue related to the usage of renewable sources is in the uncertain availability of them. In order to tackle this problem, a lot of different stochastic approaches have been developed in the recent years [7]. The appearance of these new type of sources effects the global and national energy markets as well as the national and international energy management strategies [8]. One of the most prevalent technology the application of PV modules even in the level of single households and the industry as well [9]. In this paper, we present an approach that is capable of considering the stochastic energy consumption as well as the uncertain availability of renewable sources and we will highlight its advantages through a case study that contains solar energy sources in the level of a single household in Hungary.

2 The p-graph framework

The P-graph method has been developed on the basis of graph theory and was at first applied for solving process network synthesis (PNS) problems arose in chemical process design [1]. Process synthesis can be formulated as a MILP generally solved by a branch-and-bound algorithm what results in linear programming sub-problems. In contrast the P-graph framework provides algorithmic tools for constructing the MILP problems and it is capable of determining not only the optimal but the n-best suboptimal solutions as well.

The P-graph framework stands on three cornerstones, specifically the graph representation, the five axioms stating the properties of the combinatorically feasible solutions, and the effective algorithms. The latter covers the algorithm for maximal structure generation (MSG) [2], the solution structure generation (SSG) [1], [3], [5] as well as an accelerated branch and bound algorithm (ABB) to determine the optimal the n-best suboptimal structures [4].

The SSG algorithm provides all the feasible alternative structures, which is illustrated in Figure 1. and Table 1.

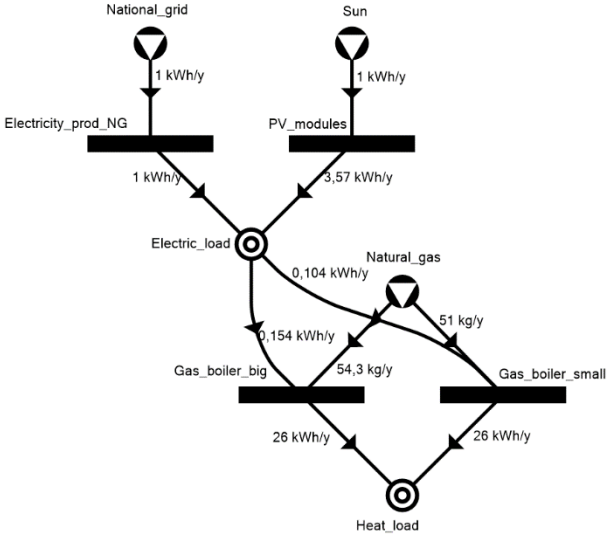

Figure 1. P-graph representation of the operating units for the case study.

Table 1. Combinatorially feasible structures for the case study generated by algorithm SSG

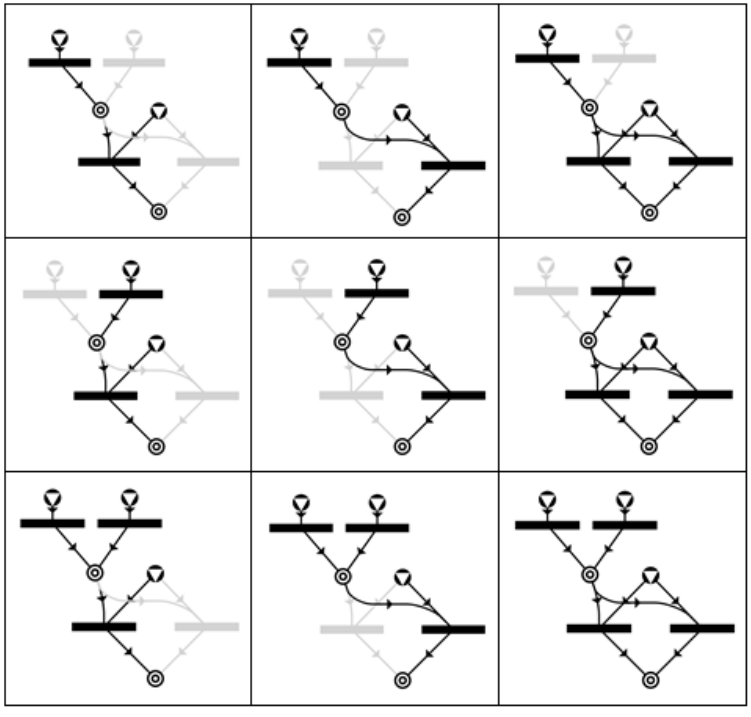

Figure 1. shows a structure that has two required products and each of them can be generated by nonempty combinations of two different equipments, therefore the analysis of the problem may yield to any of the 9 potentially feasible alternative structures, which are presented in Table 1. All of these alternatives are embedded in Figure 1 and can be enumerated automatically by algorithm SSG implemented in the software P-Graph Studio [10].

3 Case study

In order to illustrate the expediency of the above detailed method, let us consider a Hungarian household with a family of four-five people in a 150 m^2 ground-space house. The goal is to plan a system that is able to fulfil the electric and the cumulative heat requirements of the house with the least cost invested per year by a 15-year-long pay-out period. We considered two possibilities for generating each type of power, namely, for heating we have two different gas boilers, a bigger one with better performance and a smaller one with slightly worse performance and, for electricity we can buy it from the national grid or we can invest into PV modules [see Figure 1.].

For further analysis, we considered three scenarios where the difference between the scenarios is in the required flow of the electric and heat load. The capacities were scaled based on the average consumption of such households in Hungary, and these values are set in the first scenario with 50% probability. The second scenario presents the economical consumption with 30% probability and the third scenario presents the wasting consumption with 20% probability [see Figure 2.]. The above problem can be formulated as a two stage where the upper stage represent the investments, and the lower stage the operation in case of different scenarios; see Figure 2. The two-stage problem may yield to $9^3 = 729$ feasible alternatives that causes an enormous classical scenario tree with 729 leaves, whose compressed version is illustrated in Figure 3. The first column of the scenario tree represents the investment in the 9 alternative structures given in Table 1. However, according to the process synthesis approach proposed herein, the 729 alternatives do not have to be expounded as a decision tree, since each of them are taken into account by the process synthesis algorithms implemented the software P-graph Studio based on the initial structure represented in Figure 2. Moreover, all the 729 alternatives can be exhaustively enumerated by algorithm SSG if needed.

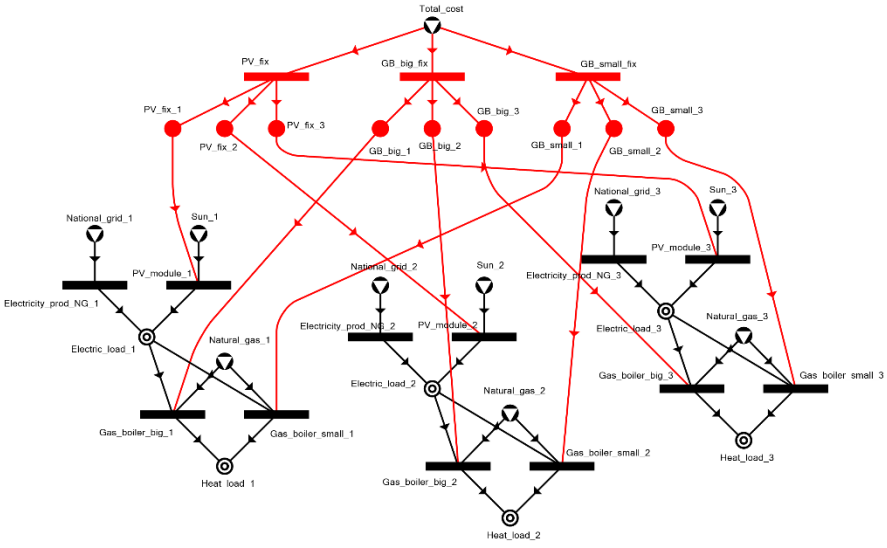

Figure 2. P-graph representation of the two stage decision problem for the case study.

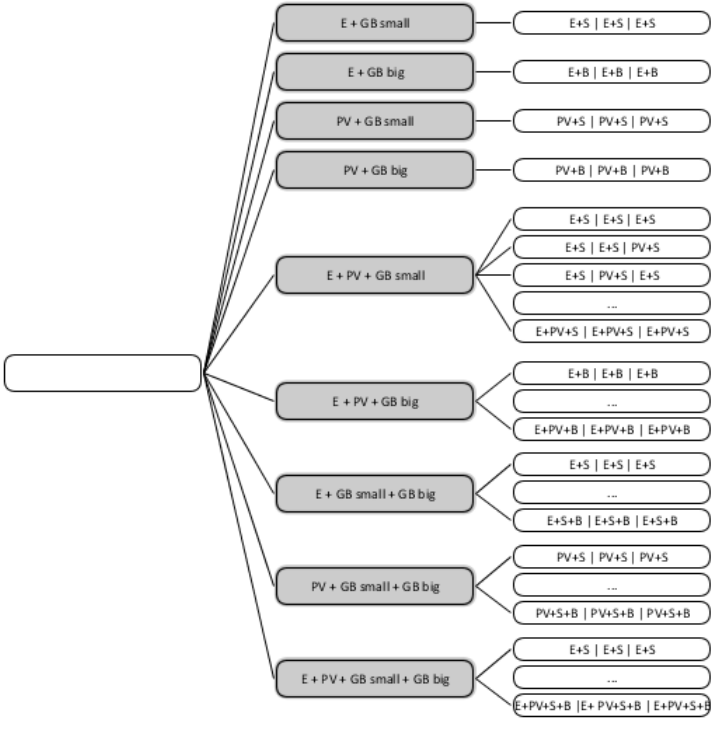

Figure 3. The compressed scenario tree of the same problem represented in Figure 2.

4 Conclusion

We have presented an approach capable of either implicitly taking into account or explicitly enumerate all the possible feasible structural alternatives for a multistage decision problem based on the compact graphical representation and synthesis algorithms provided by the P-graph framework. We have highlighted its advantages through a practical case study of planning an energy system for a household.

Acknowledgements

We acknowledge the financial support of Széchenyi 2020 under the EFOP-3.6.1-16-2016-00015.

References

[1] F. Friedler et al. "Graph-theoretic approach to process synthesis: axioms and theorems." Chemical Engineering Science, vol. 47.8, pp. 1973-1988, 1992
[2] F. Friedler et al. "Graph-theoretic approach to process synthesis: polynomial algorithm for maximal structure generation." Computers & Chemical Engineering vol. 17.9, pp. 929-942, 1993
[3] F. Friedler et al. "Combinatorial algorithms for process synthesis." Computers & Chemical Engineering, vol. 16, pp- 313-320, 1992.
[4] F. Friedler, J. B. Varga, and L. T. Fan. "Decision-mapping: a tool for consistent and complete decisions in process synthesis." Chemical Engineering Science, vol. 50.11, pp. 1755-1768, 1995.
[5] M. S. Peters et al. Plant design and economics for chemical engineers. Vol. 4. New York: McGraw-Hill, 1968.
[6] A Battaglini et al. "Development of SuperSmart Grids for a more efficient utilisation of electricity from renewable sources." Journal of cleaner production vol. 17.10, pp. 911-918, 2009
[7] T. A. Nguyen and M. L. Crow. "Stochastic optimization of renewable-based microgrid operation incorporating battery operating cost." IEEE Transactions on Power Systems vol. 31.3, pp. 2289-2296, 2016
[8] M. Mureddu et al. "Green power grids: How energy from renewable sources affects networks and markets." PloS one, vol. 10.9 e0135312, 2015
[9] F. Najibi and T. Niknam. "Stochastic scheduling of renewable micro-grids considering photovoltaic source uncertainties." Energy Conversion and Management, vol. 98, pp. 484-499 2015
[10] http://p-graph.org/

10TH INTERNATIONAL CONFERENCE ON SUSTAINABLE ENERGY AND ENVIRONMENTAL PROTECTION (JUNE 27TH – 30TH, 2017, BLED, SLOVENIA), MODELLING AND SIMULATION
J. Krope, A.Ghani Olabi, D. Goričanec & S. Božičnik

University of Maribor Press

Methodology for Determining the Propagation of Vibrations Through the Gear Body

RIAD RAMADANI, STANISLAV PEHAN & ALEŠ BELŠAK

Abstract Methodology for determining the propagation of vibrations through the gear body is presented. The source of vibrations is gear meshing. The vibrations transmitted from the contact area to the shaft and other components can be reduced by the gear body structure itself. The main problem is to carry out proper measurements. To ensure the access to the measuring points a new test rig is made, which makes it possible to obtain necessary data from the rotated and lubricated gears. To obtain the data about the vibration intensity at different observing points on the gear ring and on the hub, a new methodology is developed. Vibrations are estimated by measuring displacements, accelerations and sound pressure. The signals are analyzed in time and frequency domain. Experimental results confirm that the gear body structure has an impact upon vibrations of gears in general.

Keywords: • gear • vibration • measuring • test rig • signal analysis •

CORRESPONDENCE ADDRESS: Riad Ramadani, Assistant, University of Prishtina, Faculty of Mechanical Engineering, Bregu i diellit, p.n. 10000 Prishtina, Kosovo, e-mail: riad.ramadani@uni-pr.edu. Ph.D. student, University of Maribor, Faculty of Mechanical Engineering, Smetanova ulica 17, 2000 Maribor, Slovenia, Stanislav Pehan, Ph.D., Associate Professor, University of Maribor, Faculty of Mechanical Engineering, Smetanova ulica 17, 2000 Maribor, Slovenia, e-mail: stanislav.pehan@um.si. Aleš Belšak, Ph.D., Assistant Professor, University of Maribor, Faculty of Mechanical Engineering, Smetanova ulica 17, 2000 Maribor, Slovenia, e-mail: ales.belsak@um.si.

https://doi.org/10.18690/978-961-286-058-5.14 ISBN 978-961-286-058-5

Available at: http://press.um.si.

1 Introduction

Gear noise and vibrations are caused mainly by tooth meshing [1]; while gears are in mesh, the meshing stiffness changes and causes vibration. Vibrations, excited by gear meshing, are transmitted to the housing by shafts and bearings, which creates unwanted noise and instability. Therefore, to figure out how to control gear noise and vibration is of great significance.

In this paper, the reduction of vibrations through gear body modification is presented. The gear body is designed with a lattice structure, the structure is optimized using topology optimization. The optimized gear is produced by additive manufacturing. For vibration measurement, a completely new test rig is designed and developed. Different test rigs have been used to measure noise and vibration [2–4], but the new test rig makes it possible to simultaneously measure displacement, accelerations and sound pressure while the gear rotates. Displacements are measured in different directions using strain gauges positioned on the gear ring and hub. Acceleration is measured on the steel block and sound pressure is measured with a microphone placed close to the tested gear. The signals taken from sensors are analyzed in time, frequency and time-frequency domains. These domains are useful to analyze gear vibrations [5–7]. The frequency domain is obtained using Fast Fourier Transform [8] and the time-frequency domain is obtained using Short Time Fourier Transform [9].

2 Gear test rig design

A completely new test rig for testing gear noise and vibrations is designed and developed. The test rig consists of two heavy steel blocks; they are firmly connected with two connecting shafts, which form together a very rigid structure. Bearings are placed in steel blocks. When changing the tested gears, it is not even necessary to touch the bearings. Both units, the one with the test gears and the one with the drive gears, are lubricated. The test gear unit and the drive gear unit are connected with two interrupted shafts. In the shaft system, an elastic element is integrated. The test rig is designed in such way that it makes it possible to assemble the sensors directly to the gear ring and hub. The torque is applied and measured with a special torque wrench. With additional accessories, consisting of a housing, a one-way clutch bearing and a gear, the torsional torque is set. When the rigid coupling is tightened to transmit the torque from one shaft to another, the locking block and accessories for working torque should be removed from the test rig. The drive of the test rig consists of an electromotor (P=0.37 kW) and a frequency regulator used to regulate the rotating frequency. The rotating frequency of the gear can vary from 0 to 1000 min^{-1}.

The final design of the test rig is shown in Figure 1.

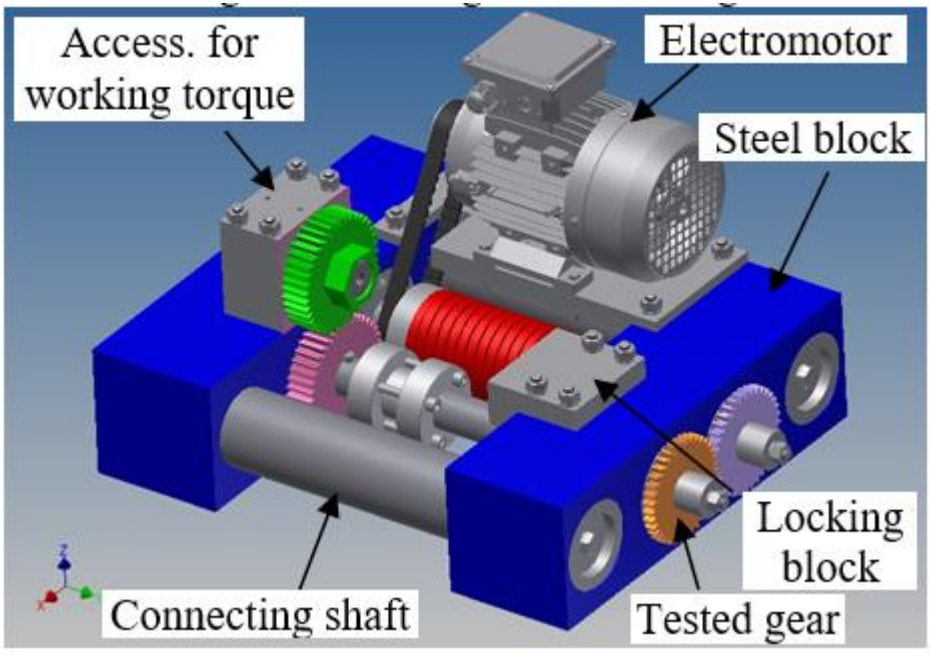

Figure 1. Design of test rig

2.1 Gears used as a research object

Two gears are used as a research object, one with a full solid body used as a reference gear and another one with a lattice structure shown in Figure 2. The module of the gear is 2.5 mm, the number of teeth is 34 and the width is 10 mm. The gear body is designed with a cube diagonal lattice structure. The ProTOp topology optimization software is used to optimize the lattice structure [10]. The whole gear is produced using Selective Laser Melting (SLM). SLM allows a part to be built additively, layer by layer, from powder metal to a solid structure [11, 12]. By this technique, a product can be produced on the basis of a CAD model. Consequently, this is an appropriate manufacturing process to produce complex geometries and structures, as e.g. the above mentioned gear body structure. The tooth flank is grinded in the same tolerances as the reference gear. The gear with the lattice structure is lighter by 36.3 % if compared with the gear with a full solid body. The printed titanium gear is shown in Figure 2.

Figure 2. Photo of printed gear

3 Test procedure

For measuring vibrations of a spur gear pair, the National Instruments NI PXI 4472 system and the PCB accelerometer (model 356A32) are used. Accelerometers are placed on the steel block and on the oil housing. Vibrations of the gear are measured in radial direction in the steel block and in the oil housing.

For sound pressure measurements, the National Instruments NI PXI 4472 system and the AP 7046 microphone are used. The microphone is placed close to the tested gears.

Displacements are measured using a set of strain gauges mounted on the gear ring and hub. Displacements are measured in different directions, e.g. in the tooth root, and in radial and tangential directions.

The TML 1-11 3L strain gauges are used and the Data Acquisition equipment is NI SCXI 1314 and NI USB 6255.

Strain gauges are connected with a slip ring of the type MZ056-S20. The slip ring consists of a stator and a rotor part and it is mounted at the end of the shaft. It allows the transmission of the electric signal from the rotary part to the stationary part. The contact between the rotary and the stationary part is gold-gold. The signal taken from strain gauges will be transmitted through the slip ring to the data acquisition equipment with minimal noise.

The test rig is placed on the table; rubber is placed between the table and the steel blocks of the test rig as a vibrations damping element.

The rubber hardness is medium 33 Shore. The layout of the mesurement procedure is shown in Figure 3.

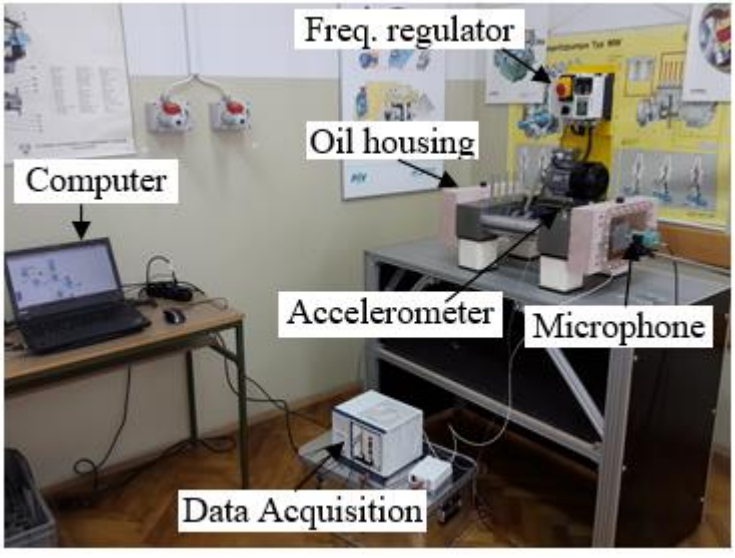

Figure 3. Layout of vibration measurement

The slip ring and the strain gauges assembled on the gear are shown in Figure 4.

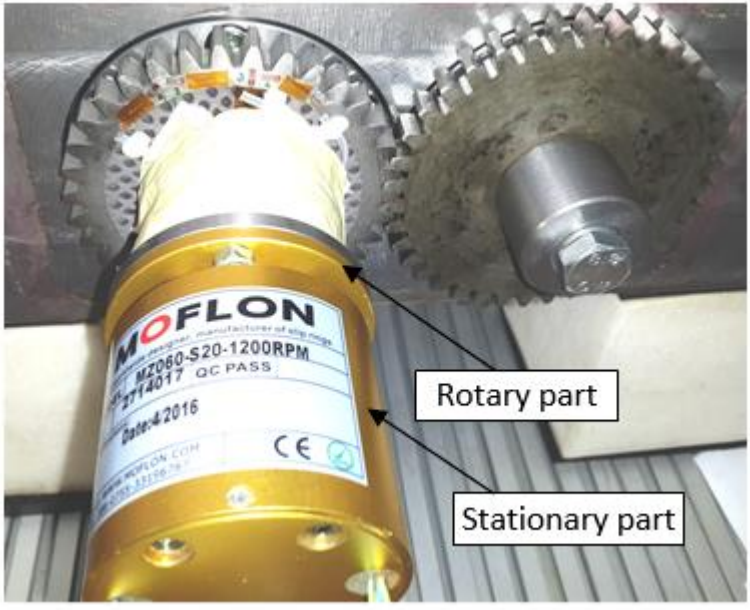

Figure 4. Slip ring and tested gear

4. Frequency domain analysis

The frequency domain is the domain where amplitudes are expressed as a series of sine waves. The measured vibrations are always in the time domain and they need to be transformed to the frequency domain. The Fourier Transform is usually applied for the conversion from time to frequency domain.

The Fourier Transform is a frequency domain representation of function. The purpose of the Fourier Transform of a waveform is to separate the waveform into a sum of sinusoids of different frequencies. A practical signal x(t) can be represented in the frequency domain by its Fourier Transform X(t), given by expression [13]

$$X(f) = \int_{-\infty}^{+\infty} x(t) \cdot e^{-j2\pi ft} dt \tag{1}$$

For a computer implementation, a Discrete Fourier Transform (DFT) is obtained through numerical integration of eq. (1) [13]

$$X(f_k) = \sum_{i=0}^{N-1} x(t_i) e^{-j2\pi f_k t_i} \left(t_{i+1} - t_i\right) \quad k = 0,1,\ldots,N-1 \tag{2}$$

The Fast Fourier Transform (FFT) is a computational algorithm that reduces the computing time of the Discrete Fourier Transform (DFT). The computing time for the FFT is proportional to $N \log_2(N)$. For example, a transform of 1024 points using FFT is about 100 times faster than if using DFT, which represents a significant speed increase. The FFT spectra produce peaks at identified typical frequencies, in the case of gears the gear mesh frequency is known as the basic frequency. If the peaks appear at the fundamental gear mesh frequency and other peaks appear at first, second or third harmonics, this is an indication that some changes are present [14].

For tested gears, time signals are acquired from accelerometers placed on the steel block. The applied torque is and the number of rotations is . The center distance of the gear pair is . The time signal for the gear with a full solid body is presented in Figure 5. The frequency spectrum for the gear with a full solid body is presented in Figure 6.

Figure 7 shows the time signal for the gear with a lattice structure, whereas Figure 8 shows the frequency spectrum for the gear with a lattice structure.

When comparing the frequency spectrum of acceleration for the gear with a full solid body presented in Figure 6 and the gear with a lattice structure presented in Figure 8, it is shown that the lower amplitude with the distribution of components is evident in the frequency spectrum of the gear with a lattice structure.

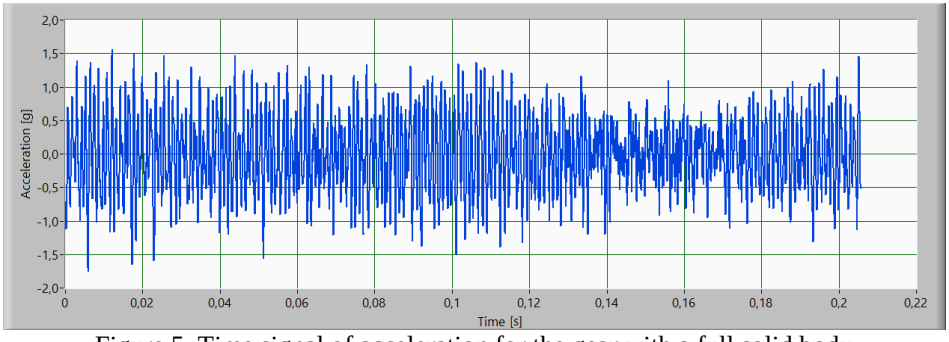

Figure 5. Time signal of acceleration for the gear with a full solid body

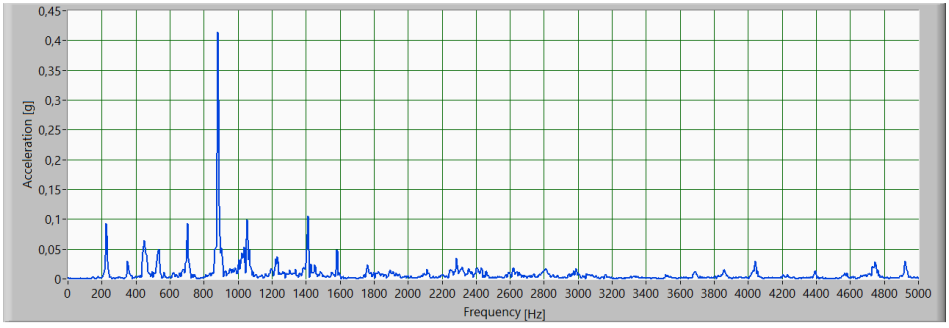

Figure 6. Frequency spectrum of acceleration for the gear with full solid body

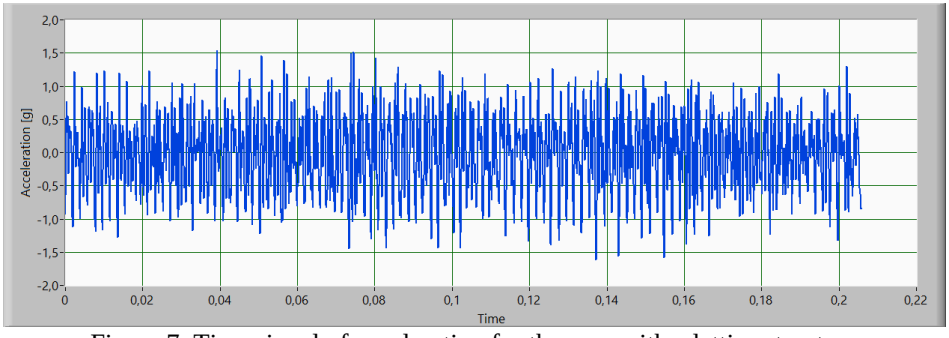

Figure 7. Time signal of acceleration for the gear with a lattice structure

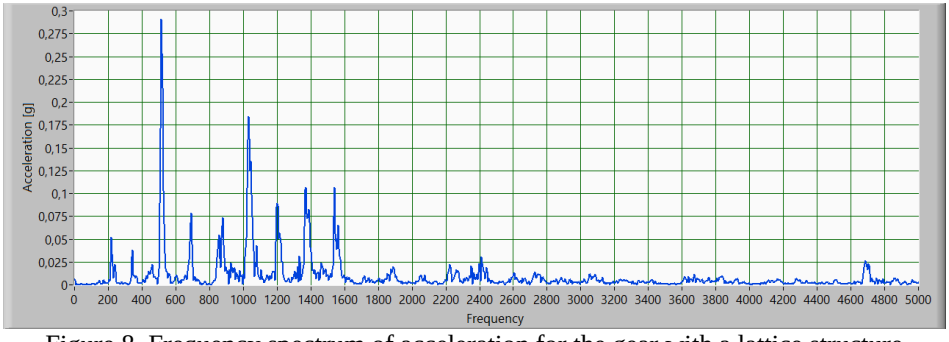

Figure 8. Frequency spectrum of acceleration for the gear with a lattice structure

5 Time-frequency analysis

In the spectrum of the frequency domain it is possible to determine, which frequencies were present in the signal but it is not possible to know the time when those frequencies appeared. The Time-Frequency Analysis introduces a time variable and makes it possible to determine how those frequencies of nonstationary signals change with time, and what the levels of signal energy are [9].

The Short Time Fourier Transform (STFT) is a linear time-frequency transformation and it is widely used for analyzing nonstationary signals. The basic idea of STFT is to divide a signal into short time segments, and then the Fourier analysis is carried out for each segment separately. It is assumed that signals are stationary within each segment. The Short Time Fourier Transform is obtained in the following way: For any signal $x(t)$, let`s suppose that $w(\tau - t)$ is a window function centered at time t, to produce a segmented signal $x(\tau) \cdot w(\tau - t)$, where τ is time variable. By applying the Fourier Transform to such segmented signals, a Short Time Fourier Transform is as follows [15]:

$$STFT_x(t, f) = \int_{-\infty}^{+\infty} x(\tau) \cdot w(\tau - t) e^{-j2\pi f\tau} d\tau \tag{3}$$

A time window position must be selected in order to take the whole time domain in consideration.

For the gear with a full solid body, the time-frequency spectrogram is presented in Figure 9. For the gear with a lattice structure, the time-frequency spectrogram is presented in Figure 10

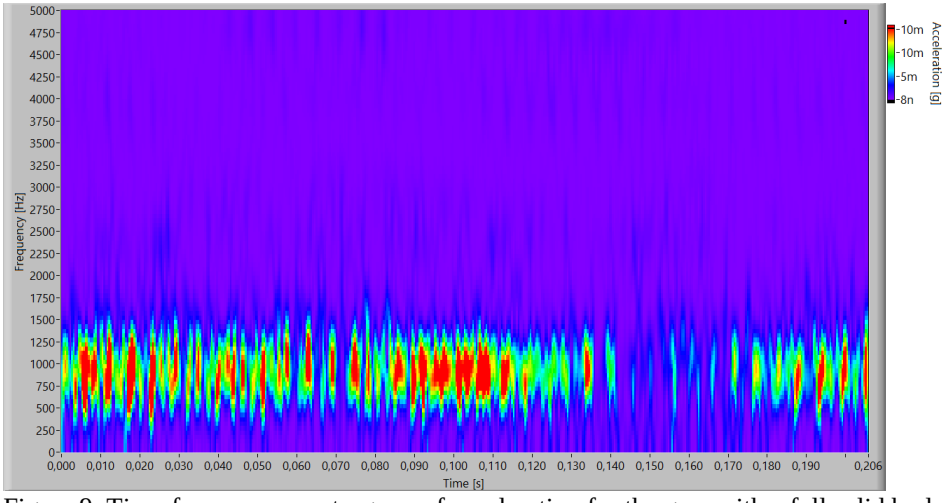

Figure 9. Time-frequency spectrogram of acceleration for the gear with a full solid body

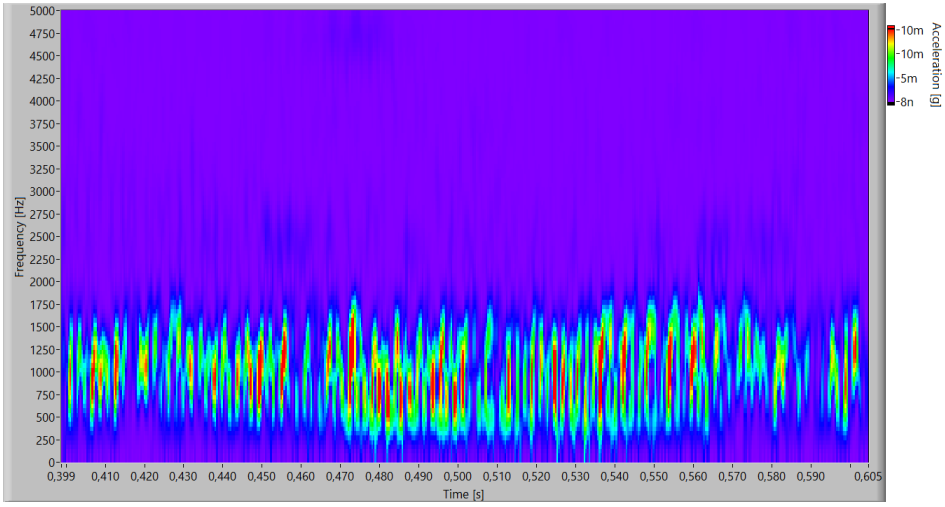

Figure 10. Time-frequency spectrogram of acceleration for the gear with a lattice structure

When comparing the time-frequency spectrogram of acceleration for the gear with a full solid body presented in Figure 9 and the gear with a lattice structure presented in Figure 10, it is shown that the lower amplitude with the distribution of components is evident in the frequency spectrogram of the gear with a lattice structure. For the gear with a full solid body presented in Figure 9, it is shown that the frequency component is not stable during time.

6 Conclusion

In this study, a way of gear vibration reduction is presented, based on the gear body structure modification. The body structure is designed with a lattice structure. The whole gear has been produced by additive manufacturing. Experiments have proven that the lattice structure can effectively reduce gear vibration. A completely new test rig has been designed and developed for vibration measurement. The test rig makes it possible to simultaneously measure displacement, acceleration and sound pressure. The time signals are analyzed in the frequency and time-frequency domains. It is shown in the frequency spectrum and in the time-frequency spectrogram that amplitudes are lower in the gear with the lattice structure than in the reference gear.

References

[1] J. D. Smith, *Gear Noise and Vibration*: Taylor & Francis, 2003.

[2] A. P. Arun, A. P. Senthil Kumar, B. Giriraj, and A. F. Rahaman, "Gear Test Rig – A Review," *International Journal of Mechanical & Mechatronics Engineering IJMME-IJENS*, vol. 14, pp. 16–26, 2014.

[3] M. Åkerblom, "Gear Test Rig for Noise and Vibration Testing of Cylindrical Gears," *Proceedings OST-99 Symposium on Machine Design. Stockholm, pp. 183–199*, 1999.
[4] S. Li, "Experimental investigation and FEM analysis of resonance frequency behavior of three-dimensional, thin-walled spur gears with a power-circulating test rig," *Mechanism and Machine Theory*, vol. 43, pp. 934–963, 8// 2008.
[5] A. Belsak and J. Flasker, "Method for detecting fatigue crack in gears," *Theoretical and Applied Fracture Mechanics*, vol. 46, pp. 105–113, 10// 2006.
[6] A. Belsak and J. Flasker, "Detecting cracks in the tooth root of gears," *Engineering Failure Analysis*, vol. 14, pp. 1466–1475, 12// 2007.
[7] O. D. Mohammed and M. Rantatalo, "Dynamic response and time-frequency analysis for gear tooth crack detection," *Mechanical Systems and Signal Processing*, vol. 66–67, pp. 612–624, 1// 2016.
[8] R. L. Allen and D. Mills, *Signal Analysis: Time, Frequency, Scale, and Structure*: Wiley, 2004.
[9] B. Boashash, *Time Frequency Analysis*: Elsevier Science, 2003.
[10] ProTOp Documentation [Online].
[11] E. O. Olakanmi, R. F. Cochrane, and K. W. Dalgarno, "A review on selective laser sintering/melting (SLS/SLM) of aluminium alloy powders: Processing, microstructure, and properties," *Progress in Materials Science*, vol. 74, pp. 401–477, 10// 2015.
[12] C. Yan, L. Hao, A. Hussein, P. Young, J. Huang, and W. Zhu, "Microstructure and mechanical properties of aluminium alloy cellular lattice structures manufactured by direct metal laser sintering," *Materials Science and Engineering: A*, vol. 628, pp. 238–246, 3/25/ 2015.
[13] E. O. Brigham, "The Fast Fourier Transform and Its Applications," *Prentice Hall. Michigan*, 1988.
[14] J. I. Taylor, *The Vibration Analysis Handbook: A Practical Guide for Solving Rotating Machinery Problems*: VCI, 2003.
[15] Z. Feng, M. Liang, and F. Chu, "Recent advances in time–frequency analysis methods for machinery fault diagnosis: A review with application examples," *Mechanical Systems and Signal Processing*, vol. 38, pp. 165–205, 7/5/ 2013.

10TH INTERNATIONAL CONFERENCE ON SUSTAINABLE ENERGY AND ENVIRONMENTAL PROTECTION (JUNE 27TH – 30TH, 2017, BLED, SLOVENIA), MODELLING AND SIMULATION
J. Krope, A.Ghani Olabi, D. Goričanec & S. Božičnik

University of Maribor Press

Using Multiple Regression Technique for Forecasting Energy Consumption of University Sector Buildings

KHURAM PERVEZ AMBER, MUHAMMAD WAQAR ASLAM, ANILA KOUSAR, MUHAMMAD YAMIN YOUNIS, SYED KASHIF HUSSAIN & BILAL AKBAR

Abstract Energy managers of English universities are responsible for preparing energy budget forecasts. A simple, easier, and less time consuming but reliable forecasting model for different types of buildings is therefore desired. In this paper, using four years real data sets for one dependent variable, i.e. daily electricity consumption and six explanatory variables, a single mathematical equation for forecasting daily electricity usage of two major types of university campus buildings (i.e. academic and office) has been developed using Multiple Regression (MR) technique through SPSS software. For the purpose of this study, two such buildings are selected, both located at London South Bank University in London. The predicted test results demonstrate that out of six explanatory variables, three variables, i.e. surrounding temperature, weekday index and building type are significant. The model demonstrates a normalized root mean squared error (NRMSE) of 11% and 12 % for the office and academic buildings respectively.

Keywords: • Electricity forecasting • Academic • Office • Buildings • Multiple Regression •

CORRESPONDENCE ADDRESS: Khuram Pervez Amber, Ph.D., Assistant professor, Mirpur University of Science and Technology, Department of Mechanical Engineering, Mirpur, 10250, AJK, Pakistan, e-mail: khuram.parvez@must.edu.pk. Muhammad Waqar Aslam, Ph.D., Assistant professor, Mirpur University of Science and Technology, Department of Computer Systems Engineering, Mirpur, 10250, AJK, Pakistan, e-mail: waqaraslam271@gmail.com. Anila Kousar, M.Sc., Lecturer, Mirpur University of Science and Technology, Department of Electrical Engineering, Mirpur, 10250, AJK, Pakistan, e-mail: anila.pe@must.edu.pk. Muhammad Yamin Younis, Ph.D., Assistant professor, Mirpur University of Science and Technology, Department of Computer Systems Engineering, Mirpur, 10250, AJK, Pakistan, e-mail: yamin.596@gmail.com. Syed Kashif Hussain, M.Sc., Assistant professor, Mirpur University of Science and Technology, Department of Computer Systems Engineering, Mirpur, 10250, AJK, Pakistan, e-mail: kashif.me@must.edu.pk. Bilal Akbar, Ph.D., Assistant professor, Mirpur University of Science and Technology, Department of Mechanical Engineering, Mirpur, 10250, AJK, Pakistan, e-mail: belalakbar@googlemail.com.

https://doi.org/10.18690/978-961-286-058-5.15 ISBN 978-961-286-058-5

Available at: http://press.um.si.

1 Introduction

Energy management systems have gained a rapid recognition in England's Higher Education (HE) sector after the Higher Education Funding Council for England (HEFCE) imposed a 43% carbon reduction target for its all member universities. As per this target, all the English Universities must reduce their carbon emissions by 43% by 2020 against the baseline year, i.e. 2005[1]. Fig. 1 shows variation in the sector's CO_2 emissions for the period 2008/09 to 2014/2015. It is evident that electricity (63%) and gas (33.3%) are the major sources of sector's emissions. It can also be observed that annual reduction in sector's emission is too slow (2.17% per year). During this period, the sector has been able to reduce its total carbon emissions only by 8%.

About 98% of these CO_2 emissions are associated with energy use in the buildings of HE sector. The literature review [2] and current statistical data available from Higher Education Statistics Agency (HESA) [3] suggests that electricity and natural gas are mainly responsible for the sector's emissions.

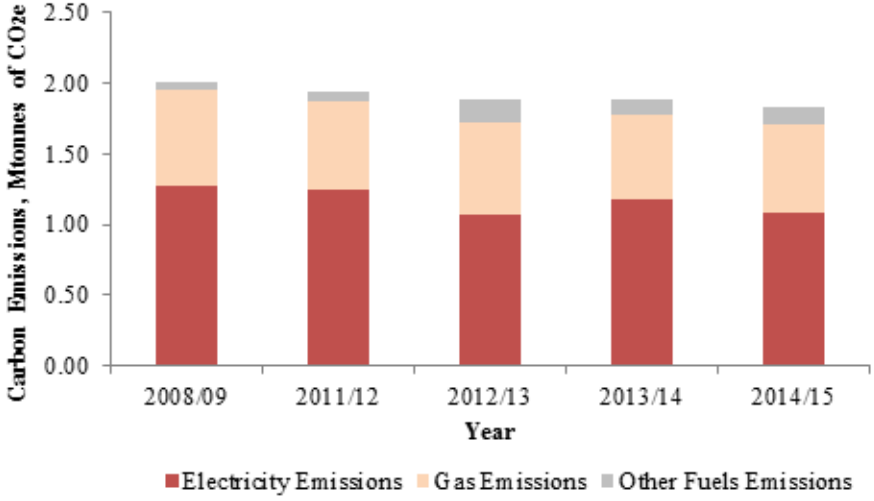

Figure 1 Variation of CO_2 emissions of the England's HE sector [3]

Energy consumption in university buildings is mainly driven by various factors such as building type, building age, occupancy, etc. Nearly 68% space of a typical university campus in England is occupied by two major building categories, i.e. academic (42%) and office (26%) [4,6].

The sector's slow declining trend of carbon emissions clearly indicates that the universities need to explore more and more energy saving opportunities.

Reliable energy consumption forecasting plays a critical role in successful implementation of energy management systems. It further helps in planning where planning is seen as backbone of an organization's operations. Many organizations have failed because of lack of forecasting or faulty forecasting technique on which the planning was based [5]. Among different forecasting techniques, Multiple Regression (MR) is a simple, reliable and a quick technique [34, 37, 39, and 41]. A number of researchers [9-42] have used this technique in their studies.

This research aims to facilitate the energy management teams of universities by providing a simple, quick and reliable energy consumption forecasting model using Multiple Regression (MR) technique in the form of a simple mathematical equation.

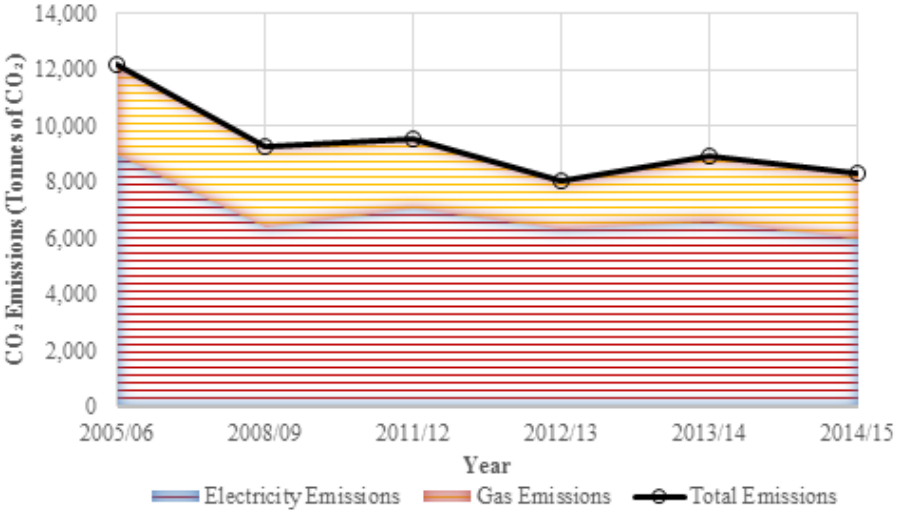

Figure 2 Variation of annual CO_2 Emissions of LSBU [3]

London South Bank University (LSBU) has to meet a target of 43% reduction in its CO_2 emissions by 2020 against the base year 2005/06. Fig. 2 shows variation in its CO_2 emissions for years 2008/09 to 2014/15. It is evident that due to University's imperative initiatives, it has been able to reduce its CO_2 emissions by 32% in 2014/15 compared to 2005/06.

2 Methods

This section presents methods and details of different stages such as data collection, model development and its testing.

2.1 Data Collection

The following data for the explanatory and dependent variables for the period Jan. 2007-Dec. 2011 were used:

Dependent variable: y=Daily electricity usage, Wh/m^2;

Explanatory variable 1: x_1 =Daily mean surrounding temperature, K

Explanatory variable 2: x_2 =Daily mean global irradiance, W/m²

Explanatory variable 3: x_3 =Daily mean humidity, %

Explanatory variable 4: x_4 =Daily mean wind velocity, m/s

Explanatory variable 5: x_5= Weekday Index (proxy variable for weekday type)

Explanatory variable 6: x_6 = Building Type (proxy variable for building type)

2.2 Data Analysis

Buildings Description

All the relevant information of both buildings (academic and office) such as building area, operating hours, built year etc. were collected from the office of energy manager through on site interview with the LSBU's energy manager [35].

Electricity consumption data

Table 1 shows the stats of electricity consumption for non-working days (NWD) and working days (WD) for the two buildings. Followings are the observations drawn from Table 1:

Electricity consumption patterns of both buildings are nearly identical and show drops during summer period which are mainly due to low heating demand during summer months and vice versa for winter months. This indirectly refers to electricity consumption in the heating equipment such as pumps, boilers, air handling units etc.

Table 1. Statistics of electricity consumption (Wh/m^2) on working and non-working days

	Non-Working Day		Working Day	
	Office	**Academic**	**Office**	**Academic**
Min	155	127	229	168
Max	311	404	479	550
Mean	222	220	374	357
Median	221	204	375	349
N	577	577	1,249	1,249

The consumption patterns (low in summer and high in winter) further suggest that surrounding temperature has a noteworthy effect on daily electricity usage of buildings. As both buildings are naturally ventilated (i.e. there is no cooling demand during summer), therefore, only seasonal load is heating which is during winter.

During summer months, heating plant and its accessories are switched off because of which electricity consumption drops to the base load. Other factors such as occupancy have limited effect as these remain somewhat constant during both winter and summer periods.

Weather data

In this study, daily mean values of surrounding temperature, global irradiance, wind velocity and humidity for the Central London region were available from the Kings College's Environment Research Group's website in the form of MS Excel files [7].
Table 2 presents the stats for all these four weather variables. It is evident that daily mean surrounding temperature in the London region remained in the range of -1°C to 28°C whereas humidity remained in the range of 81% to 100%. Peak value for global irradiance was 307 W/m^2 and for wind velocity it was 6m/s.

Buildings Occupancy Data

A proxy variable, i.e. weekday index has been selected to represent the building's occupancy. It has a value of 1 and 0 for working and non-working days respectively. For this variable, it was important to have an accurate data of working and non-working days for years 2007 to 2011. A list of public holidays was available for this period [8].

Table 2. Statistics of weather parameters dataset

	Ambient Temp., (K)	Solar Radiation (W/m^2)	Relative Humidity (%)	Wind Speed (m/s)
Min	272	0	51	0
Max	301	307	100	6
Mean	286	76	81	2
Median	286	52	81	2
Mode	291	11	85	2
N	1826	1826	1826	1826

Building Type

Office building has been assigned a dummy value of 1 whereas academic building has a value of 2.

2.3 Regression analysis

For forecasting daily electricity usage of both buildings, Multiple Regression (MR) technique has been employed using SPSS software.

Compared to other methods such as neural networks, MR method is quite simple, reliable and faster technique for forecasting purposes [37] and has been widely employed by the researchers [9-42] for forecasting the energy consumption of buildings.

Catrina et.al [37] used MR method to predict heating energy consumption of buildings based on three main factors that influence a building's heat consumption. These factors include; the building global heat loss coefficient, the south equivalent surface and the difference between the indoor set point temperature and the sol-air temperature. A detailed error analysis showed that the model presents a very good accuracy with R^2 = 0.987.

Mastrucci et al. [40] employed MR method to forecast electricity and natural gas consumption of domestic buildings in Netherland. In this study, they investigated the effect of different variables of the buildings such as type of dwelling, building age, floor area, and occupancy on the buildings natural gas and electricity consumption. To assess the predictive power of the model, they used R^2 and Mean Square Error (MSE). R^2 values for natural gas and electricity models were found to be 0.718 and 0.817 respectively.

Capozzoli et.al [42] analysed annual heating energy consumptions of eighty school buildings in the north of Italy and developed a MR model to estimate energy consumption of these schools. They used nine different influencing variables and tested the predictive

power of their model based on Mean Absolute Percentage Error (MAPE). The results of this study suggested that the MR model was a decent model a R^2 = 0.85 and MAPE of 15%.

3 Result analysis

The proposed model's equation for predicting daily electricity usage (Wh/m²) of the office or academic building is given by Eq. (1)

$$E_d = 1299 - 3.7x_1 + 145.3x_5 - 12.7x_6 \quad (1)$$

Where;

x_1 = Daily mean surrounding temperature, K
x_5 = Weekday Index (0 for non-working days, 1 for working days)
x_6 = Building type (1 for office and 2 for academic)

The MR model equation clearly demonstrates that there is a negative linear relationship among daily electricity consumption and surrounding temperature.

Table 3 Statistics of real and forecasted electricity consumption (Wh/m^2) for year 2011

	Office Building				Academic Building		
	Real	Forecast	Diff.		Real	Forecast	Diff.
Min	155	173	-12%		158	174	-10%
Max	426	438	-3%		390	402	-3%
Mean	311	324	-4%		299	309	-4%
Median	347	359	-3%		321	333	-4%
N	365	365			365	365	

This is true as high temperature will reduce heating demand of the buildings which means heating equipment and its accessories will not run. It also suggests that daily electricity consumption on a working day will exceed by 145.3 Wh/m^2 than that on a non-working day.

The proposed model has R^2 value of 0.72 demonstrating a decent predictive power of model.

4 Discussion

The predicted values of daily electricity usage were compared with the real daily electricity usage of both buildings for 365 days of year 2011. Table 3 and Fig. 3 demonstrate the comparison between real and forecasted daily electricity usage. It is clear

that the difference between Max, Mean and Median values of real and predicted consumption for both the buildings is less than -5%. This authenticates the accuracy of forecasting of the proposed model. Only in the case of 'minimum value', the difference between real and forecasted values is somewhat considerable i.e. -12% and -10% for office and academic buildings respectively which shows that the base energy consumption values have dropped slightly.

4.1 Error Analysis of the proposed MR model

The proposed MR model has been assessed on the basis of the following two errors.

- Normalized Root Mean Square Error (NRMSE)
- Mean Absolute Percentage Error (MAPE)

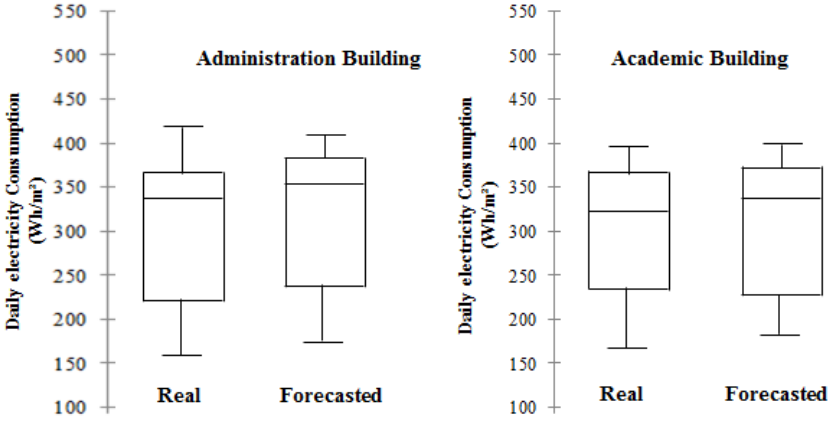

Figure 3 Box plot comparison of real and predicted daily electricity consumption of two types of buildings

Table 4 Error comparison of MR model

Error Type	Office building	Academic building
RMSE	29 Wh/m^2	31 Wh/m^2
NRMSE (%)	11%	12%
MAPE (%)	7.28%	7.84%

It is apparent from Table 4, that the model performs slightly better for the office building compared to the academic building, however, the difference of error for predicting electricity consumption for two building types is minimal, i.e. 1%.

4.2 Limitations of the Models

The followings are the major limitations of this study.

- Unavailability of real occupancy data;
- Model has not been tested for similar type of buildings
- Model assumes that building's operating conditions remains same.

5 Conclusions

A multiple regression model has been developed to forecast electricity consumption of academic and administration type buildings. The model offers NRMSE of 11% for office building and 12% for academic building. Energy managers of universities can use this model to forecast energy consumption of their campus buildings.

Acknowledgements

Authors would like to pay special gratitude towards the Energy Manager, Mr. Anuj Saush at LSBU for providing information and electricity data.

References

[1] Amber, K. P., and John Parkin. "Barriers to the uptake of combined heat and power technology in the UK higher education sector." International Journal of Sustainable Energy 34.6 (2015): 406-416.

[2] Hawkins, D., et al. "Determinants of energy use in UK higher education buildings using statistical and artificial neural network methods." International Journal of Sustainable Built Environment 1.1 (2012): 50-63.

[3] HESA, Higher Education Statistics Agency, Environmental Information, Estates Management Statistics Tables, [Online]. Available at: (https://www.hesa.ac.uk/index.php?option=com_heicontacts&Itemid=87) (accessed: 10 October 2016) (online).

[4] Amber, K. P., M. W. Aslam, and S. K. Hussain. "Electricity consumption forecasting models for administration buildings of the UK higher education sector." Energy and Buildings 90 (2015): 127-136.

[5] Chand, S., The Importance of Forecasting in the Operations of Modern Management, 2016, Available at: (http://www.yourarticlelibrary.com/management/the-importance-of-forecasting-in-the-operations-of-modern-management/3504/) (accessed on: 26 September 2016). (online)

[6] Amber, K. P., and M. W. Aslam. "Energy-related environmental and economic performance analysis of two different types of electrically heated student residence halls." International Journal of Sustainable Energy (2016): 1-16.

[7] ERG, Environmental Research Group, KCL London Air, ERG, Environmental Research Group, 2013, Available at: http://www.londonair.org.uk/(accessed: 2 February 2013). (Online)

[8] Project Britain Bank Holidays. [Online]. Available at: http://projectbritain. com/bankholidays.html (accessed: 18 January 2013), 2012
[9] Pulido-Arcas, Jesús A., Alexis Pérez-Fargallo, and Carlos Rubio-Bellido. "Multivariable regression analysis to assess energy consumption and CO 2 emissions in the early stages of offices design in Chile." Energy and Buildings 133 (2016): 738-753.
[10] Fumo, Nelson, and MA Rafe Biswas. "Regression analysis for prediction of residential energy consumption." Renewable and Sustainable Energy Reviews 47 (2015): 332-343.
[11] Kaza, Nikhil. "Understanding the spectrum of residential energy consumption: a quantile regression approach." Energy policy 38.11 (2010): 6574-6585
[12] Swan, Lukas G., and V. Ismet Ugursal. "Modeling of end-use energy consumption in the residential sector: A review of modeling techniques." Renewable and sustainable energy reviews 13.8 (2009): 1819-1835.
[13] Saha, G. P., and J. Stephenson. "A model of residential energy use in New Zealand." Energy 5.2 (1980): 167-175.
[14] Hirst, Eric, Richard Goeltz, and Janet Carney. "Residential energy use: Analysis of disaggregate data." Energy Economics 4.2 (1982): 74-82.
[15] Bentzen, Jan, and Tom Engsted. "A revival of the autoregressive distributed lag model in estimating energy demand relationships." Energy 26.1 (2001): 45-55.
[16] Zhang, Fan, et al. "Time series forecasting for building energy consumption using weighted Support Vector Regression with differential evolution optimization technique." Energy and Buildings 126 (2016): 94-103.
[17] Yun, Bai, and Chuan Li. "Daily natural gas consumption forecasting based on a structure-calibrated support vector regression approach." Energy and Buildings (2016).
[18] Dong, Bing, et al. "A hybrid model approach for forecasting future residential electricity consumption." Energy and Buildings 117 (2016): 341-351.
[19] Lomet, Aurore, Frédéric Suard, and David Chèze. "Statistical modeling for real domestic hot water consumption forecasting." Energy Procedia 70 (2015): 379-387.
[20] Mavromatidis, Lazaros Elias. "A review on hybrid optimization algorithms to coalesce computational morphogenesis with interactive energy consumption forecasting." Energy and Buildings 106 (2015): 192-202.
[21] Williams, Kristopher T., and Juan D. Gomez. "Predicting future monthly residential energy consumption using building characteristics and climate data: A statistical learning approach." Energy and Buildings 128 (2016): 1-11.
[22] Massana, Joaquim, et al. "Short-term load forecasting in a non-residential building contrasting models and attributes." Energy and Buildings 92 (2015): 322-330.
[23] Friedrich, Luiz, Peter Armstrong, and Afshin Afshari. "Mid-term forecasting of urban electricity load to isolate air-conditioning impact." Energy and Buildings 80 (2014): 72-80.
[24] Aranda, Alfonso, et al. "Multiple regression models to predict the annual energy consumption in the Spanish banking sector." Energy and Buildings 49 (2012): 380-387.
[25] Wang, Huilong, et al. "Short-term prediction of power consumption for large-scale public buildings based on regression algorithm." Procedia Engineering 121 (2015): 1318-1325.
[26] Sandels, Claes, et al. "Day-ahead predictions of electricity consumption in a Swedish office building from weather, occupancy, and temporal data." Energy and Buildings 108 (2015): 279-290.
[27] Li, Qi, et al. "Calibration of Dynamic Building Energy Models with Multiple Responses Using Bayesian Inference and Linear Regression Models." Energy Procedia 78 (2015): 979-984.

[28] Eleftheriadou, A., A. Sfetsos, and N. Gounaris. "The suitability of high resolution downscaled seasonal models for the energy assessment of the building sector." Energy and Buildings 111 (2016): 176-183.
[29] Christiansen, Nils, et al. "Electricity consumption of medical plug loads in hospital laboratories: Identification, evaluation, prediction and verification." Energy and Buildings 107 (2015): 392-406.
[30] Fan, H., I. F. MacGill, and A. B. Sproul. "Statistical analysis of driving factors of residential energy demand in the greater Sydney region, Australia." Energy and Buildings 105 (2015): 9-25.
[31] Catalina, Tiberiu, Vlad Iordache, and Bogdan Caracaleanu. "Multiple regression model for fast prediction of the heating energy demand." Energy and Buildings 57 (2013): 302-312.
[32] Crompton, Paul, and Yanrui Wu. "Energy consumption in China: past trends and future directions." Energy economics 27.1 (2005): 195-208.
[33] Hawkins, D., et al. "Determinants of energy use in UK higher education buildings using statistical and artificial neural network methods." International Journal of Sustainable Built Environment 1.1 (2012): 50-63.
[34] K.P. Amber, "Development of a Combined Heat and Power Sizing Model for the Higher Education Sector of the United Kingdom", (Unpublished doctoral thesis), London South Bank University, London, United Kingdom, October, 2013.
[35] A. Saush, "On-site interview with Energy Manager of London South Bank University", June 17, 2011.
[36] International Standards Organization (ISO), [Online]. Available at: (http://www.iso.org/iso/home.htm), (accessed: 13 January 2016).
[37] Catalina, Tiberiu, Vlad Iordache, and Bogdan Caracaleanu. "Multiple regression model for fast prediction of the heating energy demand." Energy and Buildings 57 (2013): 302-312.
[38] Amiri, Shideh Shams, Mohammad Mottahedi, and Somayeh Asadi. "Using multiple regression analysis to develop energy consumption indicators for commercial buildings in the US." Energy and Buildings 109 (2015): 209-216.
[39] Fumo, Nelson, and MA Rafe Biswas. "Regression analysis for prediction of residential energy consumption." Renewable and Sustainable Energy Reviews 47 (2015): 332-343.
[40] Mastrucci Alessio, Baume Olivier, Stazi Francesca, Leopold Ulrich. Estimating energy savings for the residential building stock of an entire city: a GIS-based statistical downscaling approach applied to Rotterdam. Energy Build2014;75:358–67
[41] Braun, M. R., H. Altan, and S. B. M. Beck. "Using regression analysis to predict the future energy consumption of a supermarket in the UK." Applied Energy 130 (2014): 305-313.
[42] Capozzoli, Alfonso, Daniele Grassi, and Francesco Causone. "Estimation models of heating energy consumption in schools for local authorities planning." Energy and Buildings 105 (2015): 302-313.

10TH INTERNATIONAL CONFERENCE ON SUSTAINABLE ENERGY AND ENVIRONMENTAL PROTECTION (JUNE 27TH – 30TH, 2017, BLED, SLOVENIA), MODELLING AND SIMULATION
J. Krope, A.Ghani Olabi, D. Goričanec & S. Božičnik

University of Maribor Press

Effect of Flow Direction and Operating Condition of Cooling Stream on Fischer-Tropsch Synthesis Performance in Catalytic Micro-Based Reactor

WANTHANA CHAIWANG, APICHAYA THEAMPETCH, NUTTHAWOOT JERMKWAN, THANA SORNCHAMNI, PHAVANEE NARATARUKSA & CHAIWAT PRAPAINAINAR

Abstract Fischer-Tropsch synthesis (FTs) has been reported that heat removal is one of the crucial issues owing to highly exothermic reaction. Therefore, operation of FTs in micro-based reactor can lead to the improvement of heat transport from reaction to cooling medium. Then, micro-based reactor could provide more accurate operating condition of pressure and temperature. Hence, in this work a concept of microreactor and heat exchanger integration into a single module was studied. A microreactor/heat exchanger simulation model composed of three reaction channels and three cooling channels were modelled using computational fluid dynamic. Effect of cooling stream direction, and flow rate and inlet temperature on FT reaction performance were focused. The simulation results showed that co-current direction presented more desirable in term of temperature profile in the reactor than that of counter-current direction, especially for higher cooling inlet temperature as it gave higher conversion and gave nearly isothermal operation.

Keywords: • microreactor • Fischer-Tropsch • heat exchanger • catalytic reaction • computational fluid dynamic •

CORRESPONDENCE ADDRESS: Wanthana Chaiwang, M.Eng., King Mongkut's University of Technology North Bangkok, Department of Chemical Engineering, 1518 Pracharat1 Rd., Wongsawang, Bangsue, 10800 Bangkok, Thailand, e-mail: wanthana.chw@gmail.com. Apichaya Theampetch, M.Eng., King Mongkut's University of Technology North Bangkok, Department of Chemical Engineering, 1518 Pracharat1 Rd., Wongsawang, Bangsue, 10800 Bangkok, Thailand, e-mail: a.theampetch@gmail.com. Nutthawoot Jermkwan, M.Eng., King Mongkut's University of Technology North Bangkok, Department of Chemical Engineering, 1518 Pracharat1 Rd., Wongsawang, Bangsue, 10800 Bangkok, Thailand, e-mail: jermkwan.n@gmail.com. Thana Sornchamni, Ph.D., PTT Research and Technology Institute, Analytical & Petrochemical Research Department, Sanapthup, Wangnoi, 13170 Ayutthaya, Thailand, e-mail: thana.s@pttplc.com. Phavanee Narataruksa, Ph.D., Associate Professor, King Mongkut's University of Technology North Bangkok, Department of Chemical Engineering, Research and Development Center for Chemical Engineering Unit Operation and Catalyst Design, 1518 Pracharat1 Rd., Wongsawang, Bangsue, 10800 Bangkok, Thailand, e-mail: phavanee.n@eng.kmutnb.ac.th. Chaiwat Prapainainar, Ph.D., Assistant Professor, King Mongkut's University of Technology North Bangkok, Department of Chemical Engineering, Research and Development Center for Chemical Engineering Unit Operation and Catalyst Design, 1518 Pracharat1 Rd., Wongsawang, Bangsue, 10800 Bangkok, Thailand, e-mail: chaiwat.r@eng.kmutnb.ac.th.

https://doi.org/10.18690/978-961-286-058-5.16 ISBN 978-961-286-058-5

Available at: http://press.um.si.

1 Introduction

Fischer Tropsch synthesis (FTs) is one of the key processes in gas to liquid (GTL) technology for converting syngas (CO and H_2) into long chain hydrocarbons. The products derived from FTs are regarded as ultra-clean and high quality transportation fuels due to their high cetane number [1, 2]. Taking into account highly exothermic characteristic of FT reaction ($\Delta H \approx -165\ kJ/mol$) [3, 4]. Heat removal is an important issue for FT reactor design process. In this case, microreactor technology could provide predominant advantage over conventional reactors. Microchannel reactors are typically fabricated with external heat exchange line. However, the idea of microchannel reactor coupled with micro heat exchanger was recently introduced [4]. Integrating heat exchange channel into the microchannel reactor could provide possibility for continuous operation in conventional scale [5]. Nowadays, various microchannel reactor design and fabrication were presented [2, 6, 7]. However, a few investigations have been carried out for microchannel reactor coupled with micro channel heat exchanger [4, 8]. Moreover, the lack of information about coolant flow direction design in the compact micro-heat exchanger/reactor is noticeable. In this work, the idea of microchannel reactor coupled with heat exchange channel and the effect of flow direction of cooling stream on FT reaction performance are presented.

2 Methodology

As mentioned above, the concept of microchannel reactor coupled with heat exchanger was performed. This idea was inspired by plate heat exchanger operation as shown in Figure.1 (a). Hydrodynamic behavior of fluids and FT reaction performance can be studied by using computational fluid dynamics (CFD) tecnique with COMSOL Multiphysics 3.5a. The governing equations in this work were Navier-stoke, Mass and Energy transfer equations.

2.1 Simulation Model

Model geometry in this study is shown in Figure 1. It comprises of three reaction channels and three cooling channels. Stainless steel 316 was selected as reactor material. The cross section of the flow channels is 0.6mm×0.5mm based on micromachining technology and the length of channel is 71.3. Channel spacing is 0.3 mm length between reaction channels and cooling channels is 1.5 mm.

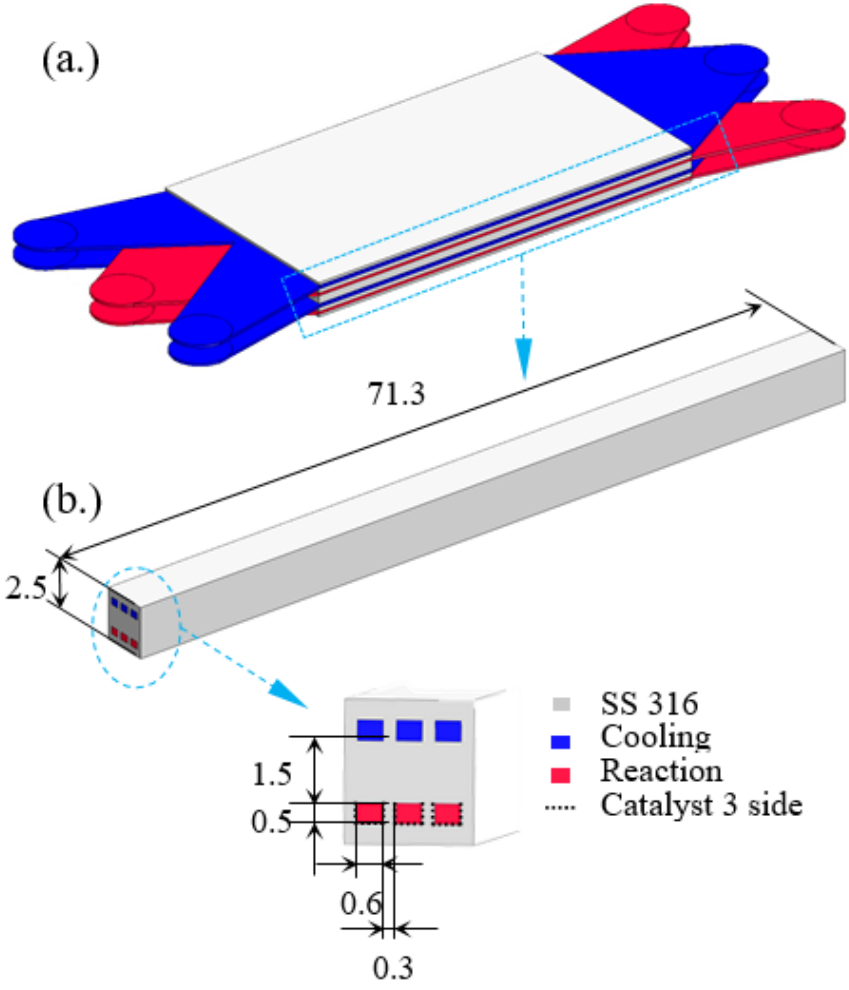

Figure 1. Microreactor/heat exchanger geometry: (a.) overall reactor model, (b.) simulation model of reaction channels coupled with cooling channels

2.2 Kinetic Data of the Model

Lumped kinetics in this study was Langmuir form from Almeida et al. [3] work based on 20%Co-0.5%Re/γ-Al_2O_3 with 35 μm of catalyst thickness coated on the wall of catalytic flow channels. Almeida et al. exhibited six reactions to predict reaction rates. Equations

set comprised of reaction of light hydrocarbons (C1–C4), long-chain hydrocarbons (C5+) and side reaction (water gas shift), as shown in Equation (1) – (9) [3]. Lumped kinetic for long-chain hydrocarbons was tetradecane ($C_{14}H_{30}$). Kinetic constants are shown in Table 1.

$$CO + 3H_2 \xrightarrow{k_{C1}} CH_4 + H_2O \tag{1}$$

$$2CO + 5H_2 \xrightarrow{k_{C2}} C_2H_6 + 2H_2O \tag{2}$$

$$3CO + 7H_2 \xrightarrow{k_{C3}} C_3H_8 + 3H_2O \tag{3}$$

$$4CO + 9H_2 \xrightarrow{k_{C4}} C_4H_{10} + 10H_2O \tag{4}$$

$$14CO + 30H_2 \xrightarrow{k_{C5+}} C_{14}H_{30} + 14H_2O \tag{5}$$

$$CO + H_2O \xrightarrow{k_{CO2}} CO_2 + H_2 \tag{6}$$

$$R_n = \frac{k_{C_n} P_{CO}^{\beta} P_{H_2}}{(1 + K_{CO} P_{CO})^2}, \quad \begin{matrix} \beta = 1 (n < 5), \\ \beta = 1.2 (n = 5) \end{matrix} \tag{7}$$

$$k_{C_n} = k_{C_n,473} \cdot exp\left(\frac{-E_A}{R} \cdot \left(\frac{1}{T} - \frac{1}{473} \right) \right) \tag{8}$$

$$K_{CO} = K_{CO,473} \cdot exp\left(\frac{\Delta H_{CO}}{R} \cdot \left(\frac{1}{T} - \frac{1}{473} \right) \right) \tag{9}$$

$$R_{CO_2} = k_{CO_2} P_{H_2O}^{0.35} \tag{10}$$

Table 1. Kinetics constant in this work [3]

Species	E_A [kJ·mol^{-1}]	k_{473} [mol$_{co}$/(kg$_{cat}$·s·atm^2)]
C_1	110.2	1.96×10^5
C_2	110.2	1.29×10^4
$C_{3,4}$	110.2	1.83×10^4
C_{5+}	62.6	$1.69 \times 10^{5,a}$
CO_2	120	$1.07 \times 10^{-5,b}$
	ΔH [kJ·mol^{-1}]	K_{473} [atm^{-1}]
CO	11.2	5.27 × 104

[a] [mol$_{co}$/(kg$_{cat}$·s·atm$^{2.2}$)]
[b] [mol$_{co}$/(kg$_{cat}$·s·atm$^{0.35}$)]

2.3 Operating Conditions

In the system, reaction was operated at 10atm, 508K and 0.002 g·min·Ncm^{-3}. Syngas mole ratio (H_2:CO:N_2) used in this study was 0.6:0.3:0.1. This feed composition was validated by a simulation model with the same geometry and conditions and compared with the results from Almeida's work [3]. Heat of reaction was calculated using Equation (11). Then, overall heat of reaction in the system was a sum of every reaction in system. Heat of reaction is shown in Table 2.

$$Q_{rxn} = R_n \times H_{rxn} \tag{11}$$

Selected cooling medium in this study was water at 35atm. At this condition, it was to ensure that, under high pressure, water would be in liquid phase to avoid phase change in the system. The flow direction of cooling stream was set as co-current and counter-current.

Table 2. Calculated heat of reactions

Reactions	H_{rxn} [kJ·mol^{-1}]
(1)	-205.91
(2)	-346.6
(3)	-498.85
(4)	-651.35
(5)	-2,171.56
(6)	-40.923

Flow rates of cooling stream were calculated from energy balance using Equation (12). The flow rates were calculated based on the assumption that reactor would be operated in order to keep the reaction condition at 508K, Therefore, the outlet temperature of cooling stream was set to be at 508K. Consequently, corresponding flow rates can be determined according to inlet temperature of cooling stream. Cooling stream inlet temperature was varied from 298K to 507K. In the case of low cooling stream inlet

temperature, it was to lower cooling stream flow rate and lower the cost of heating cooling stream to the desired temperature. Cooling stream flow rate with different inlet temperature is shown in Table 3.

$$Q_{cool} = m_c C_p \Delta T_c \tag{12}$$

Table 3. Cooling stream flow rate at different inlet temperatures

T_C, inlet [K]	Flow rate [ml·min^{-1}]
507	0.0708
498	0.0072
398	0.00802
298	0.00495

Assumptions in this work were steady state, ideal gas, no gravitational force and the reaction occurred at the surface of the wall of flow channels [9]. The objective in this work was trying to maintain the operating condition the reaction close to isothermal condition.

3 Results

In order to investigate heat exchange performance of the microreactor/heat exchanger, temperature within microchannel of reaction and cooling stream can be presented. As mentioned above, the effect of cooling stream flow direction including co-current and counter current on FTs reaction performance were focused in this section.

3.1 Results of Co-current Direction

In co-current of cooling stream direction, temperature profile along channel length in every cases were shown in Figure 2. It can be seen that the higher the different of temperature between reaction and cooling stream, the lower the outlet temperature of reaction stream. At the entrance of the flow channels, heat from exothermic reaction is transferred to cooling stream causing higher cooling stream temperature and temperature of two streams reached the same point before leaving the reactor. As a result, reaction temperature was out of desired temperature range for Fischer-Tropsch reaction. Therefore, in case of co-current, cooling stream should be fed with the temperature close to reaction temperature in order to keep the reaction condition near desired temperature.

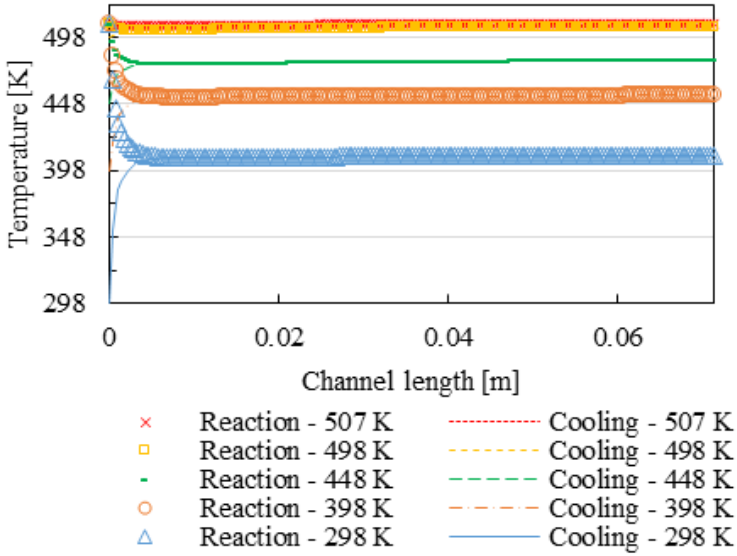

Figure 2. Temperature profile along reaction and cooling channel in case of co-current with different inlet temperatures.

In Figure. 3, conversion of reactions when operated with different cooling stream inlet temperature is shown. At 298K of cooling stream inlet temperature, reaction temperature was too low causing lower conversion when compared to the case of using cooling stream with 507K. However, it should be noted that, at too low operating condition, the conversion still increased because the results were from mathematical simulation model. The kinetic of reaction when operated at out of reaction temperature range may propel reaction in the simulation model, but it will not give the similar results in experiment.

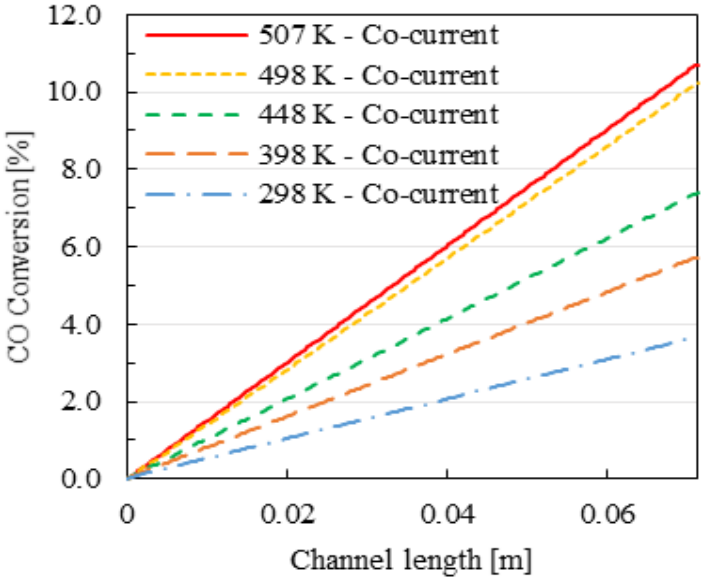

Figure 3. CO conversion along reaction channel in the case of co-current with different inlet temperatures.

3.2 Results of Counter-current Direction

In counter-current of cooling stream direction, temperature profile along channel length in every cases are shown on Figure 4. Temperature of reaction and cooling channel at steady state are very close due to heat transfer along channel length. Outlet temperature of reaction are close to inlet temperature of cooling channels channel and vice versa. When changing inlet temperature of coolant, lower cooling stream inlet temperature has effect on reaction channel causing lower reaction temperature. In order to operate the reaction close to isothermal, cooling stream should be fed with inlet temperature close to reaction temperature. Even though, temperature gradient between the reaction channels and cooling channels are low but the operation can be carried out with higher cooling stream flow rate.

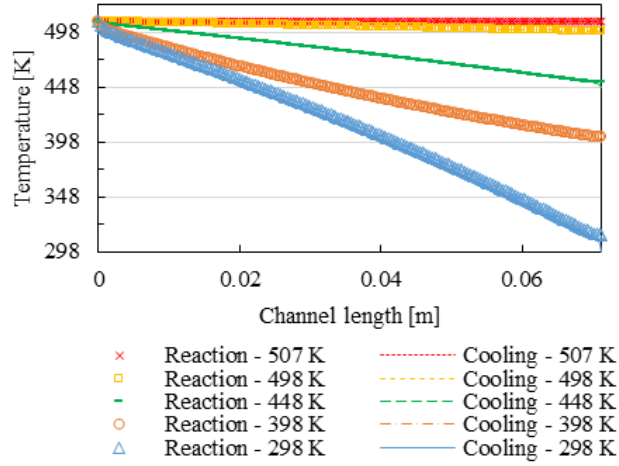

Figure 4. Temperature profile along reaction and cooling channel in case of counter-current with different inlet temperatures.

For CO conversion, the results are not different from the case of co-current stream direction when cooling stream inlet temperature is close to reaction temperature. CO conversion can be seen in Figure 5.

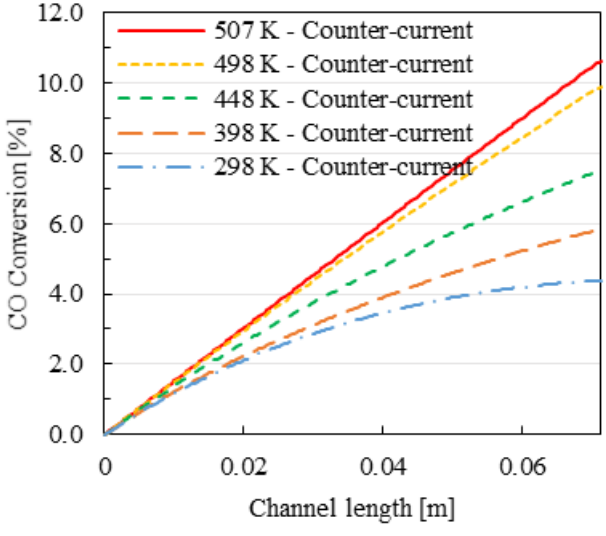

Figure 5. CO conversion along reaction channel in the case of counter-current with different inlet temperatures.

When compare the results from co-current and counter-current cooling stream direction, in order to control temperature in the range of reaction, co-current stream direction showed more desirable temperature profile than counter-current case as the outlet temperature can be closer to isothermal as it can be seen from the flat temperature profiles when reaction and cooling stream reached the same point.

3.3 Effect of Increased Cooling Stream Flow Rate

From the previous session, it can be seen that cooling stream inlet temperature should be close to reaction temperature. Therefore, a case of cooling stream with 498K was selected to study to investigate the effect of cooling stream flow rate. This was on the basis that to operate the system with lower cooling stream feed temperature in order to obtain near isothermal operation by increasing cooling stream feed flow rate. In this part, cooling feed flowrate was increased to two and five folds of the flow rate obtained from energy balance calculation. The results are shown in Figure 6 for co-current case and in Figure 7 for counter-current case. From Figure 6 for the case of co-current stream direction, it can be seen that temperature profile of reaction stream decreased at the entrance of the channel, then gradually increased when reaction stream and cooling stream reached the same point. Temperature of both streams increased as the reaction goes on and heat from the reaction is released to the cooling stream. The results from lower flow rate gave higher reaction temperature in the system but all the cases gave the system temperature in desired temperature range.

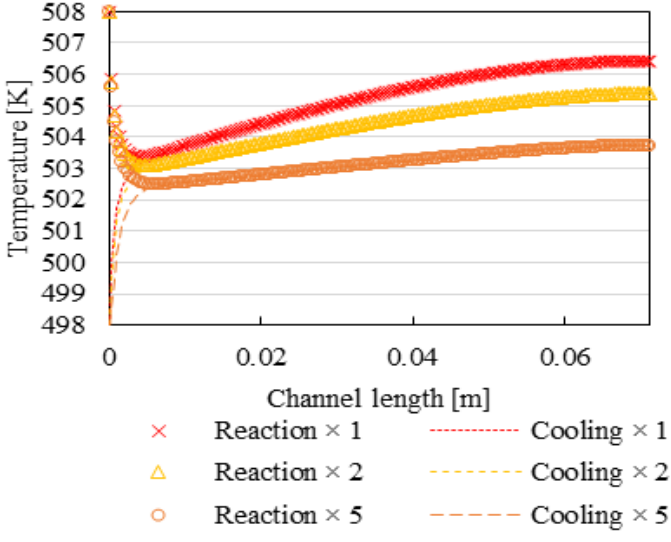

Figure 6. Temperature profile along reaction and cooling channel in case of co-current with 498K cooling stream inlet temperature with increasing cooling stream flow rate.

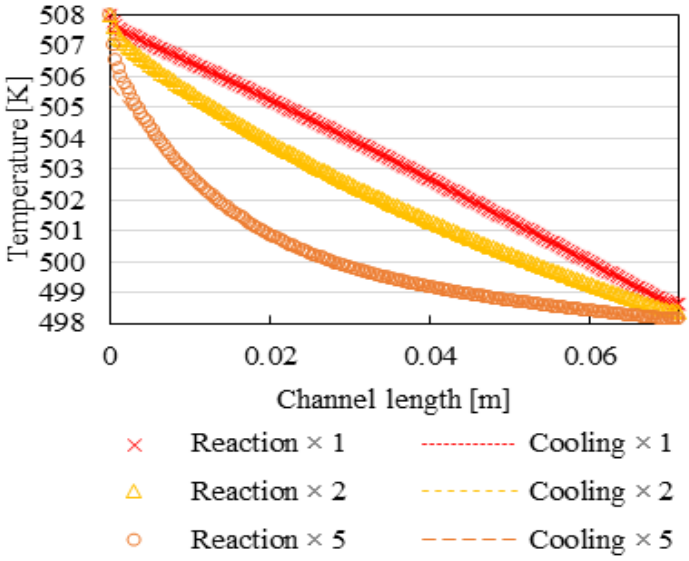

Figure 7. Temperature profile along reaction and cooling channel in case of counter-current with 498K cooling stream inlet temperature with increasing cooling stream flow rate.

Figure 7 shows temperature profile along channels length in case of counter-current cooling stream direction. The results are different from co-current case. Temperature of reaction stream dropped along length of channel and reached the lowest temperature at the cooling stream inlet temperature. When increased cooling stream flow rate, temperature profile dropped more sharply than the case of lower flow rate. When consider the effect of cooling stream inlet temperature on CO conversion, it has insignificant effect to CO conversion when increasing cooling stream flow rate. However, when the system operated with co-current, CO conversion is higher than that from counter-current around 10% at the outlet of the flow channels as can be seen in Figure 8 and Figure 9.

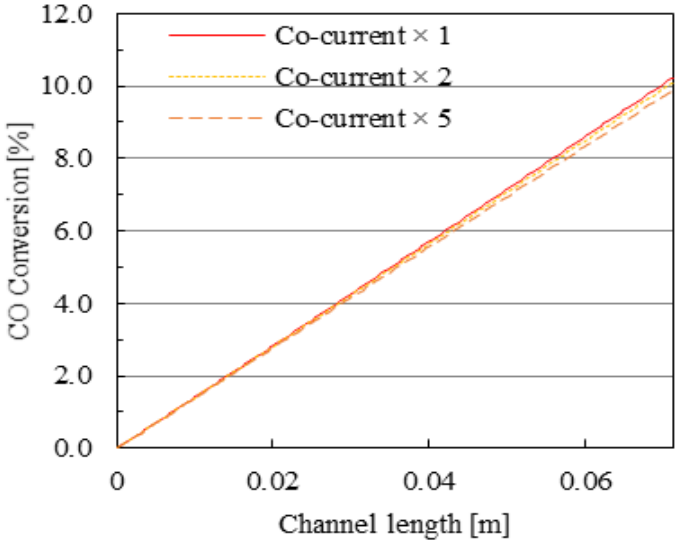

Figure 8. CO conversion along reaction and cooling channel in case of co-current with 498K cooling stream inlet temperature with increasing cooling stream flow rate.

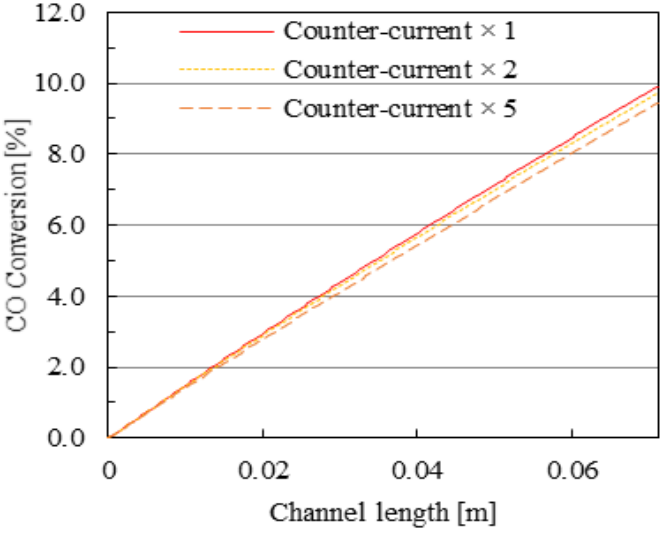

Figure 9. CO conversion along reaction and cooling channel in case of counter-current with 498K cooling stream inlet temperature with increasing cooling stream flow rate.

4 Conclusion

In this work, the idea of microreactor/heat exchanger was presented. The effect of flow direction of cooling stream on FT reaction performance was focused. The results showed that co-current direction presented higher temperature difference, especially for inlet position although conversion of reactant were relatively closed compare to counter-current case. But, when decrease cooling stream inlet temperature, it would be significantly effect CO conversion. So, the system should be operated with cooling stream inlet temperature close to desired temperature for reaction. Co-current direction also gave more stable system temperature than that of counter-current operation.

Acknowledgements

The authors would like to acknowledge PTT Research and Technology Institute for the financial support to this research and Faculty of Engineering, KMUTNB.

References

[1] M.R. Rahimpour, S.M. Jokar, and Z. Jamshidnejad, "A novel slurry bubble column membrane reactor concept for Fischer–Tropsch synthesis in GTL technology," *Chemical Engineering Research and Design*, vol. 90, pp. 383–396, Mar. 2012.

[2] L.C. Almeida, F.J. Echave, O. Sanz, M.A. Centeno, G. Arzamendi, L.M. Gandía, E.F. Sousa-Aguiar, J.A. Odriozola, and M. Montes, "Fischer–Tropsch synthesis in microchannels," *Chemical Engineering Journal*, vol. 167, pp. 536–544 , Mar. 2011.

[3] L.C. Almeida, O. Sanz, D. Merino, G. Arzamendi, L.M. Gandía, and M. Montes, "Kinetic analysis and microstructured reactors modeling for the Fischer–Tropsch synthesis over a Co–Re/Al_2O_3 catalyst," *Catalysis Today*, vol. 215, pp. 103–111, Oct. 2013.

[4] M.-S. Shin, N. Park, M.-J. Park, K.-W. Jun, and K.-S. Ha, "Computational fluid dynamics model of a modular multichannel reactor for Fischer–Tropsch synthesis: Maximum utilization of catalytic bed by microchannel heat exchangers," *Chemical Engineering Journal*, vol. 234, pp. 23–32, Dec. 2013.

[5] F. Hayer, H. Bakhtiary-Davijany, R. Myrstad, A. Holmen, P. Pfeifer, and H.J. Venvik, "Characteristics of integrated micro packed bed reactor-heat exchanger configurations in the direct synthesis of dimethyl ether," *Chemical Engineering and Processing: Process Intensification*, vol. 70, pp. 77–85, Aug. 2013.

[6] D. Mei, L. Liang, M. Qian, and X. Lou, "Modeling and analysis of flow distribution in an A-type microchannel reactor," *International Journal of Hydrogen Energy*, vol. 38, pp. 15488–15499, Nov. 2013.

[7] D.M. Murphy, A. Manerbino, M. Parker, J. Blasi, R.J. Kee, and N.P. Sullivan, "Methane steam reforming in a novel ceramic microchannel reactor," *International Journal of Hydrogen Energy*, vol. 38, pp. 8741–8750, Jul. 2013.

[8] M.-S. Shin, N. Park, M.-J. Park, J.-Y. Cheon, J.K. Kang, K.-W. Jun, and K.-S. Ha, "Modeling a channel-type reactor with a plate heat exchanger for cobalt-based Fischer–Tropsch synthesis," *Fuel Processing Technology*, vol. 118, pp. 235–243, Feb. 2014.

[9] E.B. A.-M. Hilmen, O.A. Lindvåg, D. Schanke, S. Eri, and A. Holmen, "Fischer–Tropsch synthesis on monolithic catalysts of different materials", *Catalysis Today*, vol. 69, pp. 227–232,

10TH INTERNATIONAL CONFERENCE ON SUSTAINABLE ENERGY AND ENVIRONMENTAL PROTECTION (JUNE 27TH – 30TH, 2017, BLED, SLOVENIA), MODELLING AND SIMULATION
J. Krope, A.Ghani Olabi, D. Goričanec & S. Božičnik

University of Maribor Press

Modeling of Monolith Reactor for Steam Methane Reforming: Comparison Between Surface Reaction Model and Thin Catalyst Layer Model

PIYANUT INBAMRUNG, CHAIWAT PRAPAINAINAR, SABAITHIP TUNGKAMANI, GORAN N. JOVANOVIC, THANA SORNCHAMNI & PHAVANEE NARATARUKSA

Abstract This article presents an approach for development of mathematical models to simulate reaction performance of a monolith reactor for SMR. A single square channel was modelled by using COMSOL software. Two different models for simulation were constructed. The first one was assumed that the SMR reactions took place on the wall surfaces or surface reaction model. The second model was taking into account of the reaction both at the surface and inside a thin catalyst layer. In order to validate the two models, a set of SMR experiments was carried out in a bench-scale monolith. The Ni metal catalyst was prepared and coated on the monolith structure. The reaction was operated under atmospheric pressure and 600°C with a H_2O:CH_4 molar feed ratio of 3:1. In order to find the most suitable model to reconcile the experimental data, an objective function of $\sum(C_{\text{mod}} - C_{\text{exp}})^2$ based on $r = kC_A C_B$ was defined. The values of rate constant for both the surface reaction model and the thin catalyst layer model are 1.45×10^{13} $m^4mol^{-1}s^{-1}$ and 1.10×10^{14} $m^3mol^{-1}s^{-1}$, respectively. The Chi-square values for the surface model and thin catalyst layer model are 1.8019 and 0.5595, respectively. The thin catalyst layer model can better represent the experimental data than the surface model.

Keywords: • Monolith reactor • Surface reaction • Steam Methane Reforming • Thin catalyst layer • CFD •

CORRESPONDENCE ADDRESS: Piyanut Inbamrung, Ph.D., student, King Mongkut's University of Technology North Bangkok, Department of Chemical Engineering, , Bangkok, 10800, Thailand, email: p.inbamrung@gmail.com. Chaiwat Prapainainar, Ph.D., Assistant Professor, King Mongkut's University of Technology North Bangkok, Department of Chemical Engineering, Bangkok, 10800, Thailand, email: chaiwat.r@eng.kmutnb.ac.th. Sabaithip Tungkanani, Ph.D., Assistant Professor, King Mongkut's University of Technology North Bangkok, Department of Industrial Chemistry, Bangkok, 10800, Thailand, email: sabaithip.t@sci.kmutnb.ac.th. Goran N. Jovanovic, Ph.D., Profresor, Oregon State University, School of Chemical Biological and Environmental Engineering, Corvallis, OR 97331, USA, email: goran.jovanovic@oregonstate.edu. Thana Sornchamni, Ph.D., PTT Research and Technology Institute, Analytical & Petrochemical Research Department, Wangnoi, Ayutthaya, 13170, Thailand; email: thana.s@pttplc.com, Phavanee Narataruksa, Ph.D., Associate Professor, King Mongkut's University of Technology North Bangkok, Department of Chemical Engineering, Bangkok, 10800, Thailand, email: phavanee.n@eng.kmutnb.ac.th.

https://doi.org/10.18690/978-961-286-058-5.17 ISBN 978-961-286-058-5

Available at: http://press.um.si.

1 Introduction

The major industrial process for hydrogen production is steam methane reforming (SMR). Traditionally, nickel is the metal of catalyst for SMR in industrial application. The overall of SMR reaction could be described by reaction (1).

$$CH_4 + H_2O \leftrightarrow CO + 3H_2 \quad (1)$$

The SMR commercialization process mostly adopts the packed-bed or fixed-bed reactor with contact times larger than one second. The conventional reactors is limited either by mass transport, or by heat transport to or from the reaction region. To conduct this process more efficient, various experimental simulation studies of syngas or hydrogen production by using microstructured have been performed.

The intensification of the SMR process by using monolith reactors or microstructured reactors should be enable on the one hand to solve pressure drop problem and on the other hand to reduce substantially the size of process units [1]. In monolith reactors, the support material is coated with a washcoat layer containing the precious metal catalyst particles. The washcoat provides a large surface area for the chemical reaction. Poulikakos and Kazmierczak (1987) indicated that a porous mixture at the channel wall has an impact on the fluid flow and the heat transfer capability of a single channel investigation [2].

In this content, two models were studied for the validation of model using rate constant. The rate constant was varied and was simulated in order to find the optimum rate constant with respect to the experiment via the objective function. To investigate the fundamental transport phenomena inside a catalytic reactor, numerical simulations with detailed reaction schemes were applied. Two different models for simulation were constructed. There are the surface reaction model and the thin catalyst layer model. The SMR experiments was carried out in a bench-scale monolith reactor. The NAM catalyst (base on Ni metal component) was prepared and coated on the monolith structure.

2 Methodology

Two models for simulation were constructed. Firstly, surface reaction model was created with reaction occurring on surface assumption which no diffuse into catalyst layer. Secondly, the thin catalyst layer was created based on the reaction taking place on surface and inside the thin catalyst layer. The two models were simulated by changing the value of rate constant. In this work, the overall reaction rate was studied relying on the power law with first order assumption.

$$r = kC_{CH_4}C_{H_2O} \quad (2)$$

The objective function was defined as equation (3) in order to optimize the rate constant for each model,

$$obj = \sum_{i}^{n} \left(C_{\text{mod}} - C_{\text{exp}} \right)^2 \tag{3}$$

where, C_{mod} is methane concentration from simulation and C_{exp} is methane concentration from the experiment. In order to compare with the experiment, the Chi-square was used for analysis. The Chi-square value was calculate from equation (4),

$$\chi^2 = \sum_{i}^{k} \frac{\left(C_{\text{mod},i} - C_{\text{exp},i} \right)^2}{C_{\text{exp},i}} \tag{4}$$

where, χ^2 is the Chi-square value. This value was used for the model validation.

2.1 Simulation

The fluid behaviour of two models were investigated by using software COMSOL Multiphysic V3.5a. The Computational Fluid Dynamics (CFD) governing equations comprised of Navier-Stokes equations for flow and species balances. A single square channel of monolith with 3D model was created for surface reaction model and 2D asymmetric model was used for thin catalyst layer model creation. The basic simulation conditions was shown in Table 1.

Table 1. Basic conditions for simulation

Descriptions	Value
Channel hydraulic diameter of modelled reactor [m.]	0.0015
Channel length of modelled reactor [m.]	0.10
Total mole flow rate [mol/s]	3.64×10^{-6}
Inlet velocity [m/s]	0.05
Reaction temperature [K]	873
Operating pressure [atm.]	1

The rate constants were varied for the two model calculations in order to find an optimum point for the objective function stated.

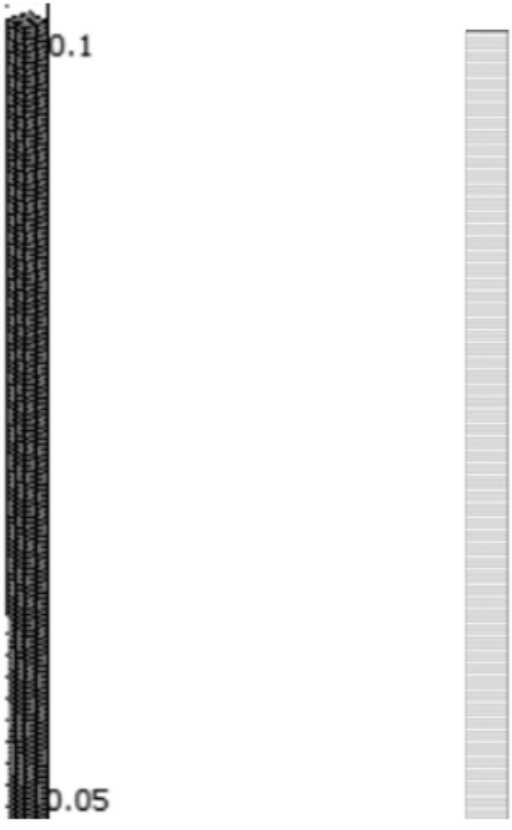

Figure 1. Computational domain (a) 3D-Surface model (b) 2D-Thin catalyst layer

2.2 Experiment

Square ceramic monolith with dimensions of 1.5 mm x 1.5 mm and 16 channels has been employed as substrate for coating deposition. The 16 channels of monolith was varied length as 2, 4, 5, 6, 7, 8, 9, and 10 cm. Experiments of steam methane reforming reaction have been carried out on the dipped Ni/Al_2O_3-MgO coating at atmosphere pressure. The average of catalyst density was approximately 7 $g.m^{-2}$. Figure 2 showed the thin washcoated on ceramic monolith wall which has average thickness 38.5 μm. The wall coated monolith was placed in an electric tube furnace reactor (Carbolite Model.VST12/600/3216P1) and its temperature was measured by a thermocouple type K. The gas flow rate was controlled by mass flow controllers (Kofloc® Model 8500MC). Inlet deionized water flow rate was controlled by a peristaltic pump (Watson-Marlow®

Model 323). Product stream was separated using condenser and desiccant trap with the temperature of 273K. The compositions of gas product were analysed by gas chromatograph (Agilent® Model GC-7890A). Prior to reaction operation, the catalyst coating has been reduced by flowing H_2/N_2 stream into the reactor with the temperature ramped from room temperature to 873K in about 12 h. After that, an experimental investigation was carried out under the conditions of reaction temperature of 873K, atmospheric pressure, and feed reactant molar ratio $H_2O:CH_4:N_2$ of 3:1:0.5.

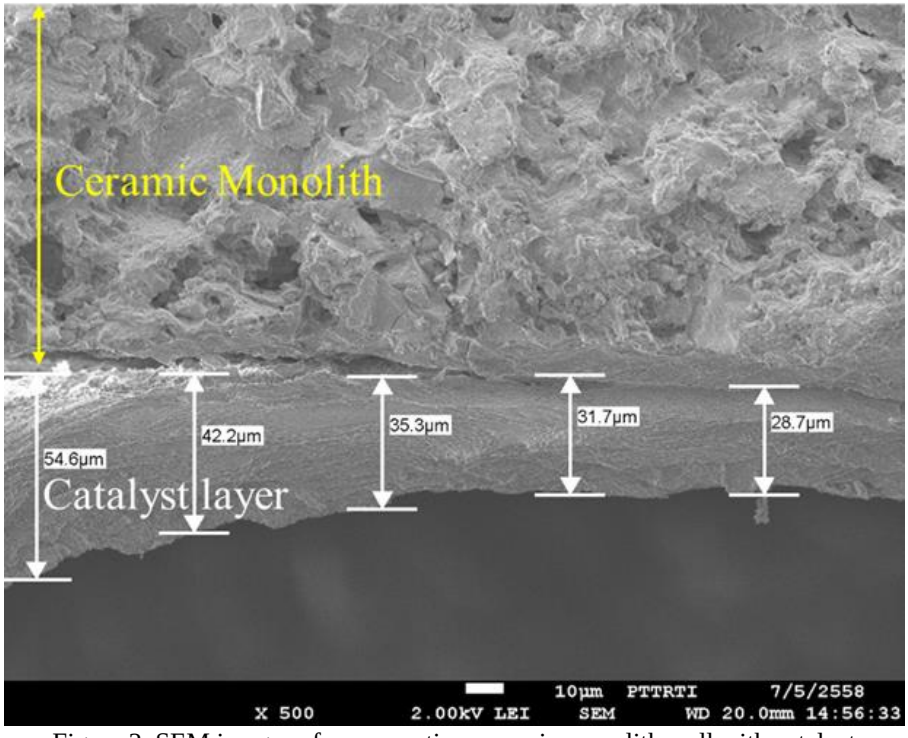

Figure 2. SEM images of cross-section ceramic monolith wall with catalyst

2.3 Result and Discussion

The results of rate constant analysis for surface reaction model was shown Figure 3. It presents the optimized rate constant at the minimum value of 1.45×10^{13} $m^4mol^{-1}s^{-1}$. Figure 4 presented the optimized rate constant as of 1.10×10^{14} $m^3mol^{-1}s^{-1}$.

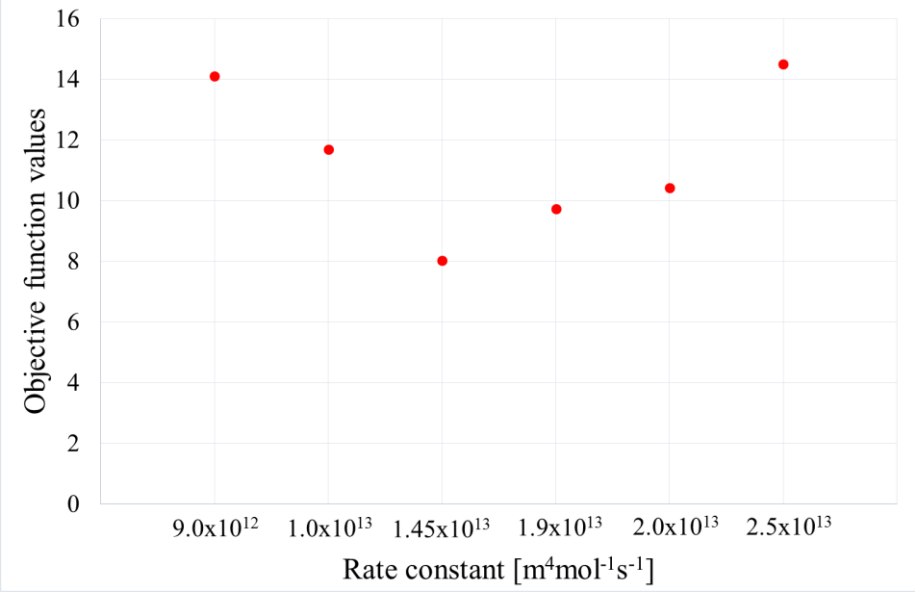

Figure 3. Optimized rate constant of surface reaction model

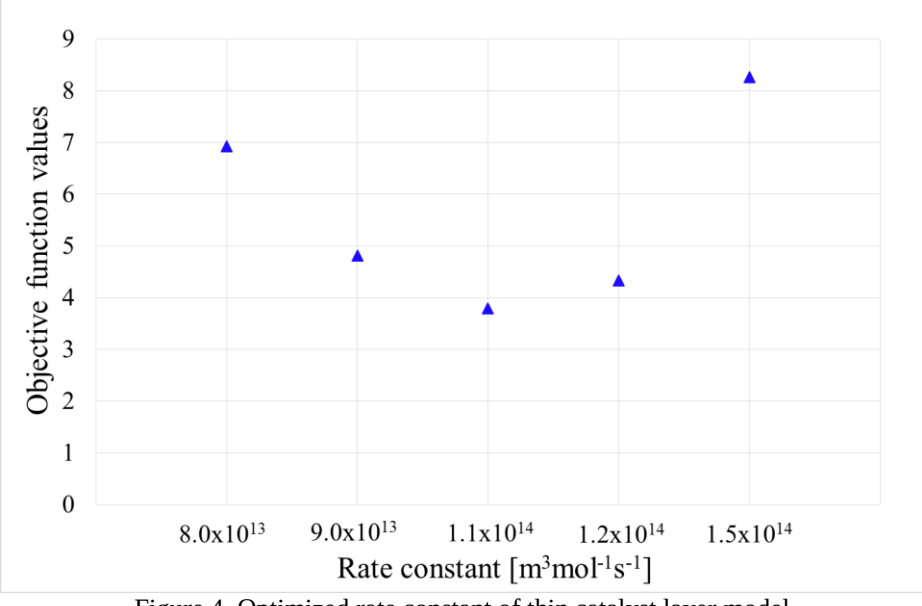

Figure 4. Optimized rate constant of thin catalyst layer model

The obtained optimum rate constant for two models were investigated. The methane concentration profile of two models were compared with the experimental results as shown in Figure 5. The results show that the methane concentration profile from the thin layer model stays closer to the concentration data from the experiment. This happened because the thin catalyst layer model has a thickness layer closed to the coated catalyst layer from the experiment. Although, the catalyst layer is very thin, but it has an impact on catalytic performance. The Chi-square values for the surface model and thin catalyst layer model are 1.8019 and 0.5595, respectively. It can be evidenced that the thin catalyst layer model can better explain the experimental data than the surface model.

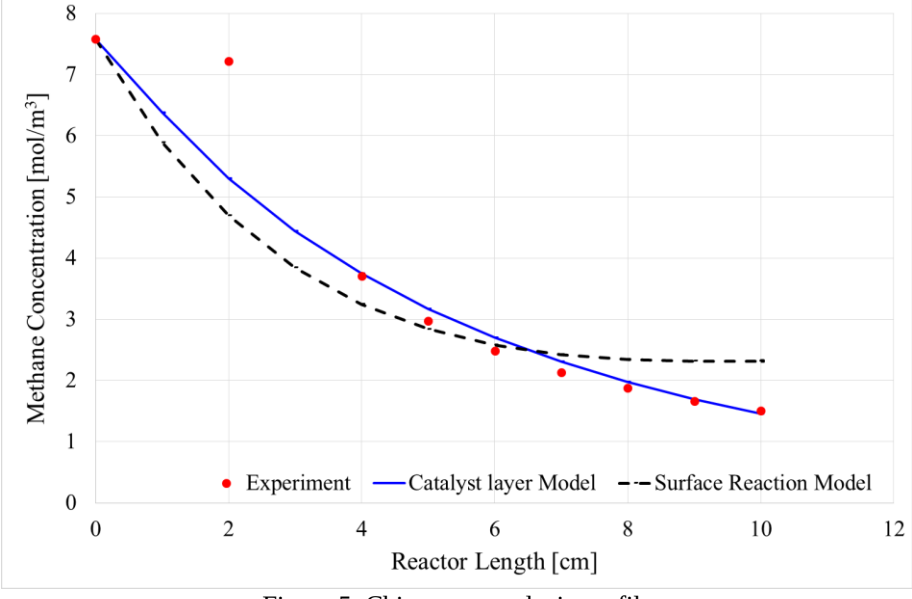

Figure 5. Chi-square analysis profile

2.4 Conclusion

Two different models were numerically constructed. The first one was assumed that the SMR reactions took place on the wall surfaces or surface reaction model. The second model was taking into account of the reaction both at the surface and inside a thin catalyst layer stick to the walls. The values of rate constant that gave the minimum values of the objective function for both the surface reaction model and the thin catalyst layer model, are 1.45×10^{13} $m^4mol^{-1}s^{-1}$ and 1.10×10^{14} $m^3mol^{-1}s^{-1}$, respectively. The Chi-square testing showed that the thin catalyst layer model better explained the experiment more than the surface reaction model.

Acknowledgements

The authors would like to acknowledge Research and Researcher for Industry (RRI) Grant no. PHD56I0046, Thailand and PTT Research and Technology Institute for the financial support to this research.

References

[1] M. Mbodji , J.M. Commenge, L. Falk, D. Di Marco, F. Rossignol, L. Prost, S. Valentin, R. Joly, and P. Del-Gallo, "Steam methane reforming reaction process intensification by using a millistructured reactor: Experimental setup and model validation for global kinetic reaction rate estimation," *Chemical Engineering Journal*, vol. 207-208, pp. 871-884, Aug. 2012.

[2] D. Poulikakos and M. Kazmierczak, "Forced Convection in a Duct Partially Filled With a Porous Material," J. Heat Transfer, vol. 109(3), pp. 653-662, Aug. 1987.

10TH INTERNATIONAL CONFERENCE ON SUSTAINABLE ENERGY AND ENVIRONMENTAL PROTECTION (JUNE 27TH – 30TH, 2017, BLED, SLOVENIA), MODELLING AND SIMULATION
J. Krope, A.Ghani Olabi, D. Goričanec & S. Božičnik

University of Maribor Press

Numerical Analysis of a Non Steady State Phenomenon During the Gas Ignition Process in the Condensing Boiler

MANUEL MOHR, MARKO KLANČIŠAR, TIM SCHLOEN, NIKO SAMEC & FILIP KOKALJ

Abstract The paper presents the most appropriate numerical approach for the investigation of the ignition phenomena of premixed confined combustion in the condensing boiler. A transient simulation with the coupling of the burning velocity model (BVM) was sufficient enough to fully describe the phenomena that are responsible for the ignition sequence and the flame stabilization. In the investigation, four different ignition power loads were applied. Also, the ratio between oxidizer (air in our case) and the fuel (methane - CH4) was based on the normal combustion process for the described device. The numerical results were validated with the experimental set up results and they are showing very good correlation with the experimental case. The described method tested on device already in production, is to be used in the development process of the next generations of gas fired products.

Keywords: • Premixed combustion • Computational Fluid Dynamics • Burning Velocity Model • Ignition • Condensing Gas Boiler •

CORRESPONDENCE ADDRESS: Manuel Mohr, M.Sc., Max Weishaupt GmbH, Max-Weishaupt-Straße 14, 88477 Schwendi, Germany, e-mail: FG.Mohr@weishaupt.de. Marko Klancisar, Ph.D., Max Weishaupt GmbH, Max-Weishaupt-Straße 14, 88477 Schwendi, Germany, e-mail: FG.Klancisar@weishaupt.de. Tim Schloen, Ph.D., Max Weishaupt GmbH, Max-Weishaupt-Straße 14, 88477 Schwendi, Germany, e-mail: fg.dr.schloen@weishaupt.de. Niko Samec, Ph.D., Full Professor, University of Maribor, Faculty of Mechanical Engineering, Smetanova ulica 17, 2000 Maribor, Slovenia, e-mail: niko.samec@um.si. Filip Kokalj, Ph.D., Senior Lecturer, University of Maribor, Faculty of Mechanical Engineering, Smetanova ulica 17, 2000 Maribor, Slovenia, e-mail: filip.kokalj@um.si.

https://doi.org/10.18690/978-961-286-058-5.18 ISBN 978-961-286-058-5

Available at: http://press.um.si.

1 Introduction

The ignition process is a key step in the reliable functioning structure of a gas fired condensing boiler. In transitional periods with low heat demand or for the specific device versions with manual dispensing operation, the number of burner starts per day are in the high double digits. In the development of a new gas fired condensing boiler, a safer and more reliable ignition process plays a major role. The main reason is the fact that the ignition process is influenced by various boundary conditions. These include not only the geometry of the combustion chamber, but also the pressure drop across the heat exchanger and the exhaust gas conduit, the fan power, the fuel air ratio and the ambient conditions. Using a numerical model, the ignition process is to be mapped virtually to achieve the ability of making early prediction of the ignition behavior in future development projects. In addition, the influence of the spark ignition position as well as the influence of the energy released at the spark ignition is a major issue during the development process of a gas condensing boiler with premixed combustion. It has to be ensured that no detonations occur due to a delayed ignition. It is of great interest to build up a numerical model which is able to consider all this influences to the ignition process. To reach a reliable evaluation of the numerical results, these are validated by experimental tests. Subject of this investigation is the gas fired condensing boiler WTC-GW 15-B from Max Weishaupt GmbH, Germany, which has a nominal combustion capacity of 14 kW. Evaluation criteria for the ignition process in the numerical model and the experimental tests are the pressure profiles. As can be seen in other numerical investigations of the ignition process like in [1], [2] and [3] the pressure results and heat release rates of numerical investigations are consistent with experimental results. This is a major objective in the present investigations.

2 Ignition process and flame propagation simulation using the burning velocity model

2.1 The burning velocity model

The ignition process is always a non-stationary event, that is the process starting from the mixing of the reactants to the stationary burning flame. [4] For this reason, the numerical reproduction of the ignition process should be carried out only with the help of unsteady simulations, which, depending on the model size, require high computing power to achieve meaningful calculation times. In order to obtain efficient and less computationally intensive description of the ignition the Burning Velocity Model (BVM) was used, which is integrated part of the ANSYS CFX 15.0. In preliminary studies it was found out that there are advantages using the BVM combustion model over other combustion models when illustrating an ideal premixed combustion with respect to the computing time, the level of detail of the numerical model and the definition of time step. One reason for this lies in the low degree of rigidity of the system of equations in the BVM model describing the reaction mechanisms in the flame by means of a global reaction progress variable $\tilde{c}$, presented in [4] and [7]. Reaction progress variable is

calculated based on the following transport equation and is of the magnitude from 0 to 1 [5]:

$$\frac{\partial(\overline{\rho}\tilde{c})}{\partial t} + \frac{\partial \overline{\rho}\tilde{u}_j\tilde{c}}{\partial x_j} = \frac{\partial}{\partial x_j}\left[\left(\overline{\rho D} + \frac{\mu_T}{\sigma_c}\right)\frac{\partial \tilde{c}}{\partial x_j}\right] + \overline{w_c} \quad (1)$$

The source term on the right side of Equation (1) is calculated as follows:

$$\overline{w_c} = \overline{S_c} - \frac{\partial}{\partial x_j}\left((\overline{\rho D})\frac{\partial \tilde{c}}{\partial x_j}\right)$$

$$\text{with } \overline{S_c} = \overline{\rho_u} \cdot S_T \cdot |\nabla \tilde{c}| \quad (2)$$

The low rigidity in the system of equations lies in the turbulent flame velocity S_T, which varies only within a few orders of magnitude. In ANSYS CFX 15.0, several calculation approaches for the turbulent flame velocity are available, whereupon in the present studies the Zimont approach is being used [5]:

$$S_T = A \cdot G \cdot u'^{3/4} \cdot S_L \cdot \lambda_u^{-1/4} \cdot l_t^{1/4} \quad (3)$$

This turbulent flame velocity is one the one hand dependent from the laminar flame velocity S_L and on the other hand from the turbulence field in the flow (parameters u' and l_t). The dependence of flame propagation from the fuel ratio is then taken into consideration with help of the laminar flame velocity S_L. Within these studies, the beta function is used, which defines the maximum value of the laminar flame velocity at a fuel ratio of φ = 1.06. For leaner and richer mixtures, the laminar flame velocity decreases approximately in parabolic form [8] and [9], whereupon above φ = 1.64 and below φ = 0.56 the flame propagation is defined as zero trend [5]. The consideration of the temperature and pressure dependence of the laminar flame velocity is omitted, as these factors can be considered negligible in the present investigations. With use of the parameter G in eq. (3), reduction of the flame velocity up to the flame extinction brought on by very high turbulence intensities can be represented and adjusted in the model. The user can choose to fine tune this flame extinction parameter

$$\varepsilon_{cr} = 15 \cdot \nu \cdot g_{cr}^2 \quad (4)$$

which describes the critical dissipation rate. The remaining parameters in Equation (3) A and λ_u represent a modeling constant (A = 0.5) and the thermal diffusivity of unburned mixture.

2.2 Integrated ignition model

A further advantage in the modeling of the ignition process, the BVM model proves to be superior over other combustion models as it contains the possibility to initialize the combustion reaction. With this integrated spark ignition model it is possible to setup ignition timing and the spark position. In addition, the temperature due to release of the ignition spark can be taken into account in the model. Due to the fact that this combustion model doesn't use an Arrhenius equation, no activation energy level has to be exceeded to initiate combustion. The ignition model inside the BVM represents a zero dimensional initial value problem, which brings a reaction progress within the ignition radius r_K into the fluid volume [5]:

$$\frac{d}{dt} r_K(t) = \frac{\rho_u}{\rho_b} \cdot S_{T,k} \tag{5}$$

From Equation (5) it is apparent that the growth of the ignition core is assumed to be approximately spherical. By specifying a transition radius, it is defined how many time steps should pass after the ignition time until the reaction progress is transmitted to the combustion model. To ensure that the ignition core can be properly resolved by the computational mesh at the moment of ignition, the initial volume of the core should be large enough.

2.3 Turbulence modeling and energy equation

For modeling of turbulent structures in the combustion chamber, the k-ε turbulence model is used. The level of turbulence in the combustion chamber is considered low and there are no major rotation areas expected. The numerical model is adiabatic so that the representation of heat loss into the surroundings and heat transfer processes in the combustion chamber housing are not taken into consideration. Because the flow inside the combustion chamber can be considered as a dynamically incompressible flow, the numerically robust thermal energy equation is used [5].

3 Gas fired condensing boiler setup

3.1 Geometrical model

In order to perform the basic investigations for numerical illustration of the ignition process with reasonable simulation times, the geometric model of the gas-fired condensing boiler is simplified, without excessively restricting the information value of the ignition model. In upper first section of the Figure 1, there is an overview of the flue gas volume in the gas fired condensing boiler. One can recognize the inlet collector of the combustion chamber and the subsequent heat exchanger. In order to investigate the ignition process and the flame propagation, the volume of the combustion chamber is sufficient enough so that in the first step (second section of the Figure 1) the whole heat exchanger domain can be removed. After first simulations, it was apparent that further

simplification of the numerical model to reduce simulation times is useful. It was finally decided that also the inlet collector should be removed to achieve meaningful simulation times and to be able to further refine the mesh inside the combustion chamber. This implies the simplification of a homogenous inflow of the fuel air mixture into the combustion chamber. This does not bring any bigger restriction to the information value since the tests conducted in this paper are purely basic investigations.

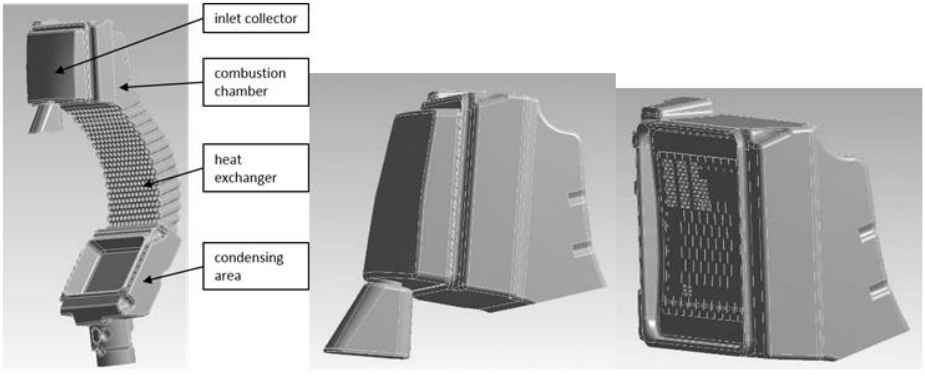

Figure 1: Upper figure: Fluid volume including inlet collector, combustion chamber and heat exchanger; middle figure: Numerical model with simplified fluid volume including just the inlet collector and combustion chamber; lower figure: Final numerical model with simplified fluid volume including just combustion chamber

The final geometric model is in Figure 1 shown in the bottom illustration. On this figure, the distributor plate can be seen on the left side of the combustion chamber. Premixed fuel air mixture enters in the combustion chamber through the narrow circular and elongated openings. With this geometrical simplifications, the complexity of the global computational mesh is significantly scaled down, thereby the simulation time considerably reduced and the optimization of the computational mesh in the important areas of the combustion chamber can be carried out. The ignition position in the numerical model is the same as in the original gas fired condensing boiler and won't be varied as the focus on this essential investigation is to test if a numerical reproduction of the ignition process is possible. The ignition energy in the integrated ignition model is set to 0.2 J as this reflects more or less the energy released in reality.

3.2 Mesh resolution and time step size

To ensure the independence of the numerical solutions from the mesh resolution and the time step of transient simulation, a mesh and time step dependency study is conducted. In the first step, the numerical mesh is gradually refined with use of stationary simulations of the velocity field in the combustion chamber and finally evaluated with the BVM model.

Table 5: Grid size

	Computati-onal mesh 1	Computati-onal mesh 2	Computati-onal mesh 3
Node count	0.601 Mio.	0.864 Mio.	3.084 Mio.
Element count	3.204 Mio.	4.621 Mio.	17.380 Mio.

The velocity field has an impact on all other numerical results, so this is a convenient criterion for evaluating the mesh resolution. The differences in the velocity field of the numerical mesh 1-3 were compared.

In Figure 2 the velocity levels are compared at two key points in the combustion chamber; on the ignition spark position and at the SCOT electrode, every time for different mesh resolution. Therein, the influence of the numerical diffusion can be seen which decreases with increasing degree of refinement of the computational mesh [7]. In comparison to mesh 2 and 3, the flow conditions in the combustion chamber change only slightly, so that the mesh with 0.864 million nodes represents a good compromise between the numerical accuracy and simulation time. In the next step the transient simulations are carried out and the time step size is gradually reduced by step of 0.01s to an order of magnitude that once again provides a good compromise between the simulation complexity and the numerical accuracy. Evaluation for the ignition process is carried out based on the pressure profile in the combustion chamber via the ignition process. In Figure 6, the pressure profiles are compared with the same numerical setup and different time steps. This shows that a time step of 0.001 s is sufficient to represent the pressure profile over the ignition process with sufficient accuracy.

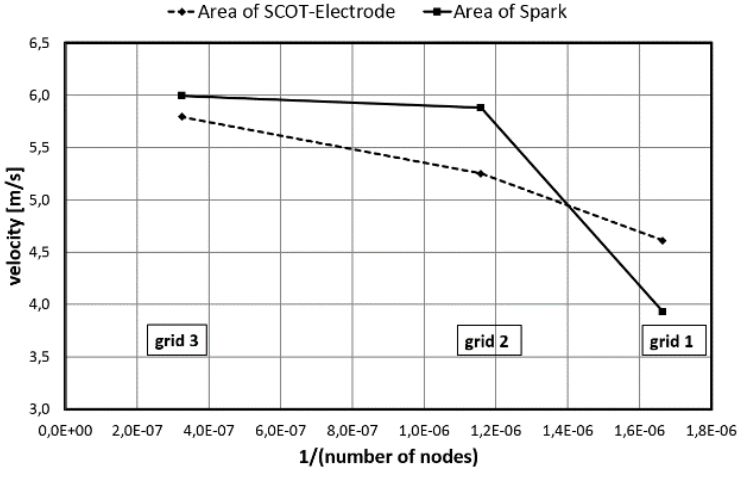

Figure 2: Comparison of the fluid velocity at different grid resolutions on key points inside the combustion chamber

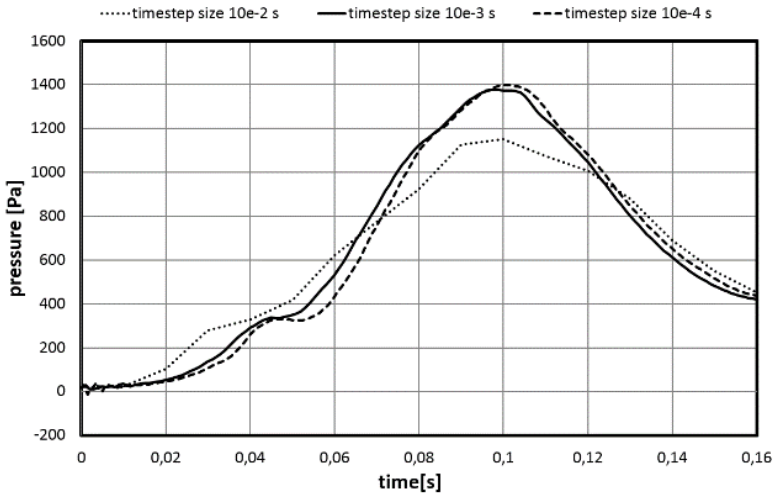

Figure 3: Pressure profiles of the ignition process with different time step sizes

4 Investigations of the ignition process

To evaluate the numerical model, different boundary conditions for the ignition process are defined and at the same time the evaluation of the qualitative changes within the numerical studies is conducted. The variation of ignition boundary conditions includes:

- Ignition timing
- Combustion capacity (power load) at ignition
- Counter pressure in combustion chamber
- Fuel-air ratio

For successful ignition with use of the built-in ignition model, a sufficiently high fuel ratio in the vicinity to the ignition source is necessary. For this reason, the ignition timing is set to 0.25 s, having the equivalence ratio that is defined at the burner inlet in the vicinity if the ignition source before the initialization of the combustion reaction is started. The remaining boundary conditions for the investigations of the influence of the ignition timing on the pressure profile are summarized in Table 2. The counter pressure in the combustion chamber is adjusted by means of the outlet opening. Centered in the outlet plane there is a circular orifice and within the scope of the "back pressure in the combustion chamber" investigations, its diameter is varied. Outside this scope of investigations, the orifice opening is set to 30 mm.

Table 6: Boundary conditions

Parameter	Value
Average mass flow	0.004604 kg/s
Equivalence ratio (φ)	0.7435
Ignition timing	0.25 s
Inlet mixture temperature	296 K
Absolute pressure	95,500 Pa
Static pressure – outlet (rel.)	0 Pa
Throttle diameter	30 mm
Fuel	Methane (CH4)

The results of the variation of the ignition timing are shown in Figure 4. It can be seen that an increase of the ignition delay leads to higher pressure gradient and higher pressure peak. This qualitative change in the pressure profile is to be expected as with increasing ignition delay the fuel air ratio throughout the combustion chamber rises to φ = 0.7435. Thereby the flame velocity is higher in a larger volume of the combustion chamber so that the temperature in the combustion chamber increases faster or rather the density decreases more rapidly. The pressure in the combustion chamber increases because of the back pressure of the fluid volume (choking effect by small outlet).

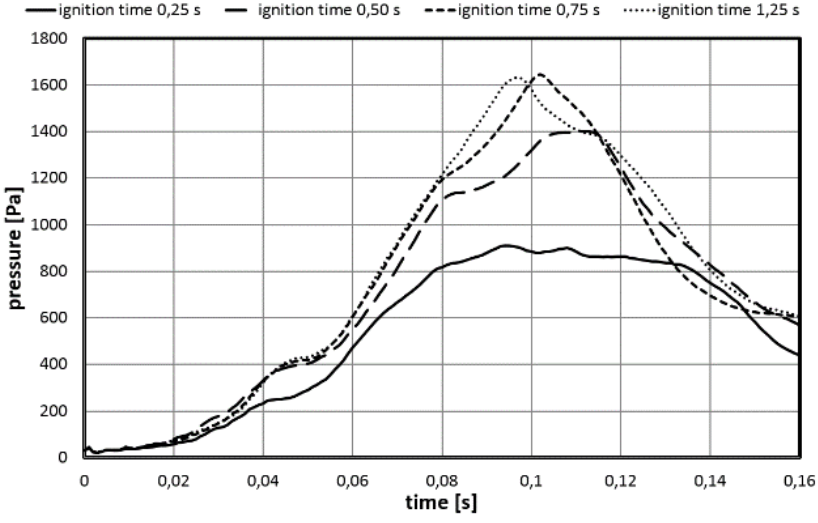

Figure 4: Pressure profiles for different ignition timings

Within the studies on the variation of the ignition, the boundary conditions shown in Table 2 are left constant and changes apply only to the mass flow. The variation of the ignition capacity (load) is carried out within the limits of 55% to 95%. The qualitative change of the pressure variation due to the variation of the mass flow is shown in Figure 5. This shows that with increasing ignition load, the pressure in the combustion chamber

rises rapidly and results in a higher pressure peak. At the same time the velocity level in the combustion chamber increases, which leads to a higher turbulence intensity in the shear layers of the flow. This additionally contributes to the fact that the turbulent flame velocity (see Equation (3)) increases. The higher pressure peak with increasing mass flow effect is mainly due to the higher proportion of fuel in the combustion chamber and the rapid flame propagation.

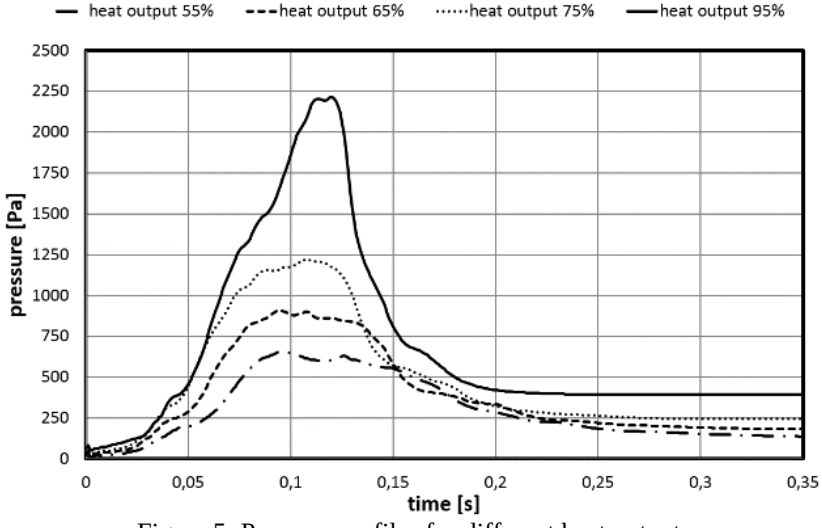

Figure 5: Pressure profiles for different heat outputs

5 Experimental investigations

5.1 Experimental setup

For the validation of numerical results, a geometrically similar model is mandatory. For this reason, a testing bench was constructed with an identical combustion chamber volume. The outlet plane is sealed with an aluminum plate which has a circular opening, as seen in the numerical model. On this device, the plates can be assembled with different circular apertures by means of screw connections, so that they can be varied as in the numerical investigation of the outlet section. Unlike in the numerical model, the experiment does not allow the simplifications due to the fact that the inlet fan, the collector and the gas valve are key components of the experiment. The experimental test setup in shown in Figure 6. Therein, the fan, the gas valve block with gas connection pipe, the inlet silencer, the inlet collector and the combustion chamber is shown.

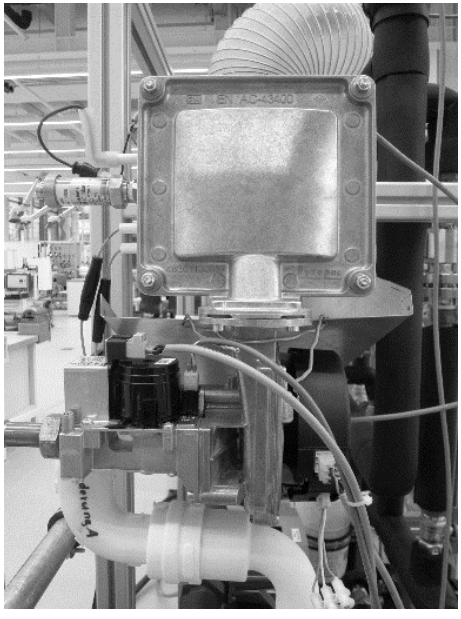

5.2 Experimental results and comparison with numerical investigations

To validate the numerical results, the same conditions for the ignition process are set-up in the experiment, as they appeared in the numerical simulations. In Figure 7 the pressure profiles over the ignition process for the ignition power loads between 55% and 95% are summarized.

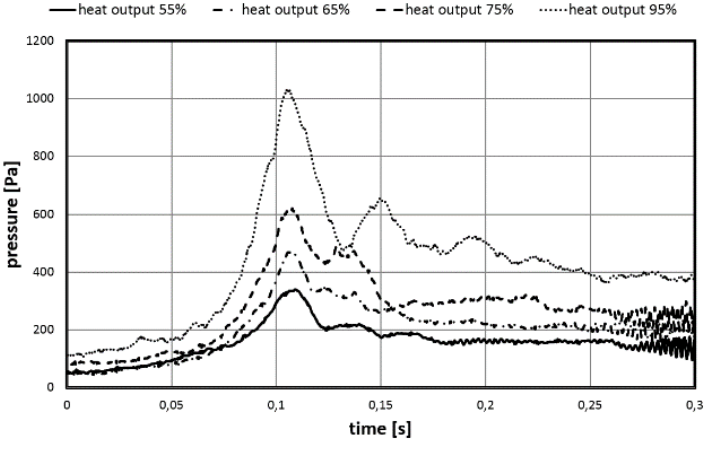

Figure 7: Experimental results – pressure profiles for different heat outputs during ignition

A direct comparison with the pressure profiles of the numerical simulations from Figure 5 shows us that on the one hand, the duration of pressure increase lies in the same temporal order of magnitude as in the numerical investigation and on the other hand, there exists an approximately constant factor (value 2.0) between the pressure peaks of the experimental and numerical results.

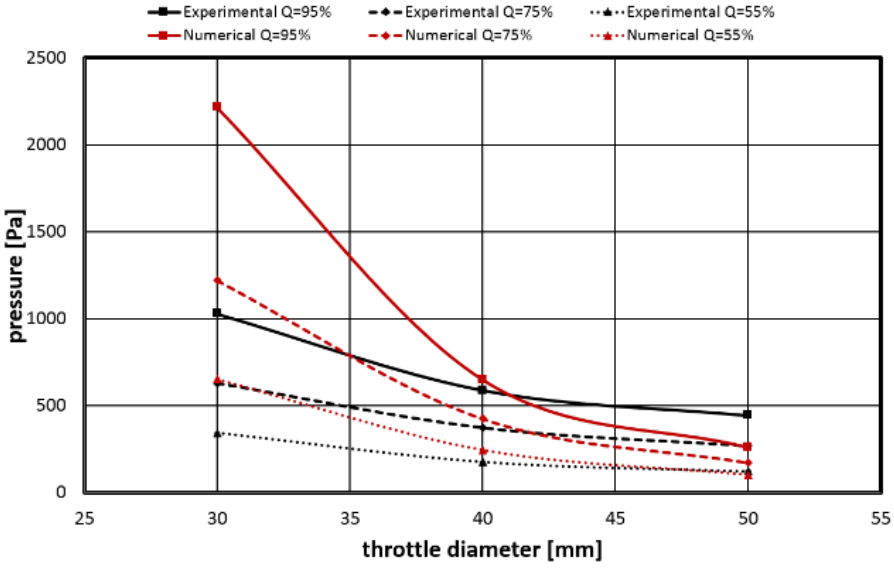

Figure 12: Comparison between pressure peaks for the numerical and experimental investigation using different throttle diameters and heat output

6 Conclusion

A numerical study of transient phenomena during the ignition process in the gas fired condensing boiler has been applied. It can be concluded that ignition time in correlation with different power load have a significant impact on flame stabilization. Furthermore, very good correlations between the pressure profiles of the numerical and experimental studies can be derived. For further investigations the influence of the spark ignition position as well as the influence of the energy released during spark ignition to the pressure profile can be taken into account.

References

[1] Kong S.C. and Reitz R.D. (2003), Numerical Study of Premixed HCCI Engine Combustion and its Sensitivity to Computational Mesh and Model Uncertainties, Combust. Theory Modelling

[2] Sudeshkumar M. P. and Devaradjane G., Development of a Simulation Model for Compression Ignition Engine Running with Ignition Improved Blend
[3] Mikulski M. and Wierzbicki S., Validation of a Zero-Dimensional and 2-Phase Combustion Model for Dual-Fuel Compression Ignition Engine Simulation
[4] Joos F. (2006), Technische Verbrennung, Springer
[5] Ansys CFX 15.0 (2013), Theory guide.
[6] Dinler N. and Yucel N., Combustion Simulation in a Spark Ignition Engine Cylinder: Effects of Air-Fuel Ratio on the Combustion Duration
[7] Ferziger J.H. and Perić. M. (2002), Computational Methods for Fluid Dynamics
[8] Metghalchi M. and Keck J.C. (1982), Burning Velocities of Mixtures of Air with Methanol, Isooctane, and Indolene at High Pressure and Temperature, Elsevier Science Publishing Co., Inc.
[9] Warnatz J. and Maas U. and Dibble R.W. (2001), Verbrennung, Physikalisch-Chemische Grundlagen, Modellierung und Simulation, Experimente, Schadstoffbildung, Springer

10TH INTERNATIONAL CONFERENCE ON SUSTAINABLE ENERGY AND ENVIRONMENTAL PROTECTION (JUNE 27TH – 30TH, 2017, BLED, SLOVENIA), MODELLING AND SIMULATION
J. Krope, A.Ghani Olabi, D. Goričanec & S. Božičnik

University of Maribor Press

Modelling of an Expandable, Reconfigurable, Renewable DC Microgrid for Off-Grid Communities

JOANNE KITSON, SAMUEL J. WILLIAMSON, PAUL HARPER, CHRIS M. MCMAHON, GES ROSENBERG, MIKE TIERNEY, KAREN BELL & BIRAJ GAUTAM

Abstract This paper proposes a DC microgrid system based on multiple locally available renewable energy sources in an off-grid rural community, based on a field study carried out in a rural, off-grid village in Nepal. The site has been assessed as suitable for solar and wind power. Using estimated solar data for the site's location, wind data measured locally, household and population data and typical measured domestic demand profiles, a DC microgrid system model has been constructed. Power flow is controlled using modified DC droop control on each individual energy source to enable optimal power sharing with minimum power dissipation across distribution lines.

Keywords: • DC microgrid • DC droop control • Solar • Wind • Off-Grid Communities •

CORRESPONDENCE ADDRESS: Joanne Kitson, University of Bristol, Faculty of Engineering, Tyndall Avenue, Bristol, BS8 1TH, UK, e-mail: Joanne.Eemg.Kitson@bristol.ac.uk. Samuel J. Williamson, University of Bristol, Faculty of Engineering, Tyndall Avenue, Bristol, BS8 1TH, UK, e-mail: Sam.Williamson@bristol.ac.uk. Paul Harper, University of Bristol, Faculty of Engineering, Tyndall Avenue, Bristol, BS8 1TH, UK, e-mail: Paul.Harper@bristol.ac.uk. Chris M. McMahon, DTU Technical University of Denmark, Anker Engelunds Vej 1 Bygning 101A, 2800 Kgs. Lyngby, Danmark, e-mail: chmcm@mek.dtu.dk. Ges Rosenberg, University of Bristol, Faculty of Engineering, Tyndall Avenue, Bristol, BS8 1TH, UK, e-mail: Ges.Rosenberg@bristol.ac.uk. Mike Tierney, University of Bristol, Faculty of Engineering, Tyndall Avenue, Bristol, BS8 1TH, UK, e-mail: , K. Bell, University of Bristol, School for Policy Studies, 8 Priory Rd, Bristol BS8 1TZ, UK, e-mail: Mike.Tierney@bristol.ac.uk. Biraj Gautam, People, Energy & Environmental Development Association (PEEDA), Devkota Marg, Mid-Baneshwor, Kathmandu-10, P.O.Box 8975, EPC 2157, Nepal, e-mail: biraj@peeda.net.

https://doi.org/10.18690/978-961-286-058-5.19 ISBN 978-961-286-058-5

Available at: http://press.um.si.

1 Introduction

Of the 1.2 billion people who do not have access to electricity, nearly 85% are in rural areas [1], and most of these will require off-grid solutions to achieve the U.N.'s goal of universal energy access by 2030 [2]. For these solutions, renewable generation technologies are often the most appropriate, as they are sustainable and allow local power generation without any requirement for external energy supply. Off-grid renewable solutions are normally on an individual household scale, such as the Solar-Home System (SHS), or community scale solutions, where a single resource powers multiple households such as a micro-hydro scheme. Microgrids have emerged as an opportunity to connect multiple sources and loads that are in close geographic location, and can be either grid-connected or islanded.

Both AC- and DC-based microgrids have been investigated [3], with benefits and drawbacks to each type of system. DC microgrids have advantages of simpler control with no requirement for synchronisation, and are able to integrate renewable sources such as photovoltaics and battery storage easier than AC networks. Primary control for DC microgrids can be based on droop mechanisms, where the output voltage of a source reduces as the power demand increases, mimicking grid attributes [3]. This can be achieved artificially through power electronic interfaces, with further levels of control added as required [4].

This paper proposes and simulates a modular DC microgrid system in which the sources interfaced with the DC grid via droop control. Section 2 describes the overall system layout and design; Section 3 details the case study site; Section 4 presents the results from the simulation of the case study site.

2 DC Microgrid System Overview

The DC microgrid links together sources and loads in a common location; the sources and loads can be scattered across the implementation area, as shown diagrammatically in Figure 13.

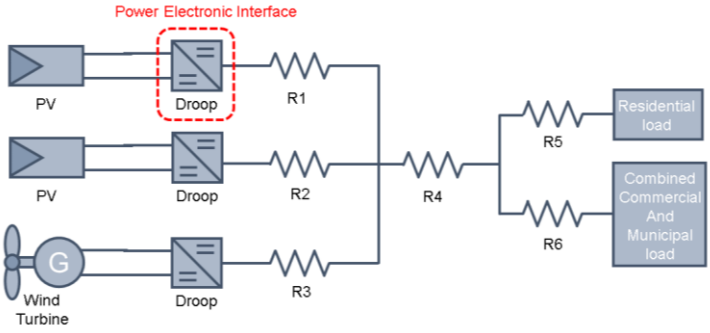

Figure 13. Diagram of off-grid distributed DC multi-source, multi-load system.

Each source is connected onto the grid through a modular power electronic interface. The power electronic interface includes a grid interfacing converter which changes the voltage to the grid level, and uses droop control to manage the power flow onto the grid.

Droop control is used to control the power flow of the system without the need for communication between sources. For DC systems, the converter measures its output power or current and adjusts the output voltage. This is typically implemented as a linear relationship; thus, for sources that are separated by transmission and distribution lines, there is a trade-off between voltage regulation and power sharing. However, a novel system has been proposed in [7], which uses a non-linear droop curve, shown in Figure 15. This allows for good power sharing at low and high power, whilst minimising change in grid voltage. As with a linear droop scheme, this system can be scaled dependent on ratio of available power to maximum power [8]. This scheme is applied in the DC microgrid model, with the Matlab code written for this work is shown in Figure 14.

```
function [Rd,Vref,newVnom,alpha,deltaV] =
droop(Rdmax,Imax,Vnom,Vmin,I)
%INPUTS:
%Rdmax = modulus of maximum droop gain
%Imax = maximum current available
%Vnom = nominal voltage
%Vmin = min acceptable voltage
%I= source's output current
%alpha is the arc co-efficient
alpha=(Rdmax*Imax)/(Vnom-Vmin);
% Rd = a range of droop gain (always negative)
Rd=((I^(alpha - 1)*alpha*(Vmin -
Vnom))/Imax^alpha);
%deltaV is the amount by which Vnom must be shifted
up
deltaV=((alpha-1)*(Vnom-
Vmin)*I^alpha)/(Imax^alpha);
newVnom=Vnom+deltaV;
%OUTPUTS:
Vref=newVnom+Rd*I;
```

Figure 14. Modified DC droop control implemented in embedded Matlab code

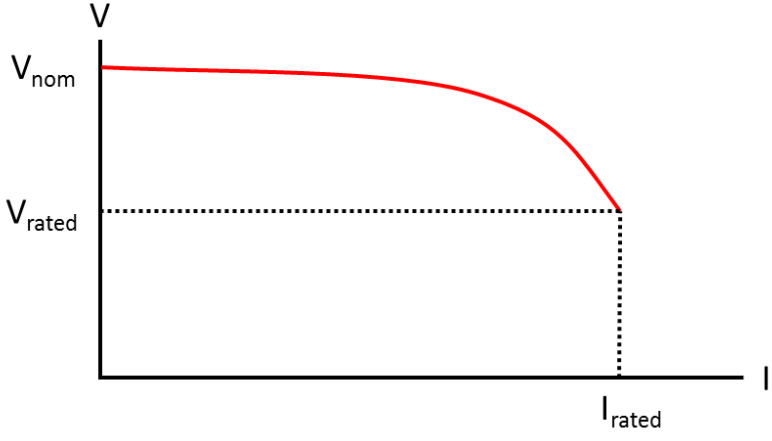

Figure 15. Droop control Curve

The grid transmission and distribution system is constructed from wires, which can be assumed to be simple resistances for low voltage cables. The loads for the DC microgrid are assumed to connect directly onto the grid.

3 Case Study site: Mityal, NEPAL

The DC microgrid system described in Section 2 is simulated through a case study example, informed by data from a field study, carried out in Mityal VDC, Palpa, Nepal [9]. The most pertinent local site details are set out in Table. 7. The survey assessed both existing and potential availability of off-grid supply sources, and provided background information to assist in assessing the future demand and installation requirements for a microgrid in this area.

3.1 Modelled DC microgrid system

A DC microgrid system based on the site study in Mityal, has been created in Simulink. This model considers the change in loads and sources on an hour by hour basis, using the available load, wind and solar data. No energy storage has been included in this model, but it will be used as a basis in future work for specifying the minimum amount of system storage required together with HOMER software [10]

Table. 7 Summary of Information from Field Study Site in Nepal

Site name	Mityal VDC, Palpa, Nepal
Co-ordinates	27°46’ N 83°55’E
Elevation above sea level	957 metres
No. of households (population)	54 (300)
Available renewable energy sources	Solar, wind
Currently installed renewable power	Average SHS 39 W (min 10 W, max. 180W) 2.4 kW solar system on school
Currently installed non-renewable power	Commercial - Rice mill diesel engine 7.4 kW Domestic – wood, liquid petroleum gas (LPG)
Domestic power demand (daily average)	6.61 kW average (summer), 3.91 kW (winter)
Domestic energy demand per day	58.53kWh (summer), 30.05kWh (winter)
Current total commercial energy demand per day	86.6kWh (rice mill, water pump, office equipment)
Current municipal services demand	2kW for health posts, police station
New renewable installations recommended by PEEDA to meet current demand	Three 5kW wind turbines (total 15 kW), 16 solar panels of 310 W each (aggregate of 5 kW solar)

In order to maintain the Simulink model’s relative simplicity a version scaled to $1/10^{th}$ of the full hybrid wind-solar installation recommended by the field report [9] with typical site loads is created. The model’s main features are set out in Table 8. and employ 1.5

kW wind turbine and 500 W solar based on models previously compiled by the authors [6], [11]. The main features of the DC multi-source multi-load system are listed in Table 8.

Table 8. Summary of Power Sources, Loads and DC Network Simulation Parameters

Simulated Network Characteristics (10:1)	**Details**
Wind turbine	1.5 kW rated
25 x SLP020 20 W solar panels	aggregate solar power: 500 W
Transmission/distribution resistances (Figure 13)	R1, R2 = 4.3 mΩ, R3 = 8.5 mΩ, R4 = 420 mΩ R5, R6 = 150 mΩ
DC distributed network	400 V rated +/- 5% at source
System voltage drop	≤ 10%
Domestic load	5.85 kWh in 1 day
Commercial load	8.66. kWh in 1 day
Municipal load	1.20 kWh in 1 day

3.2 Modelling Demand over 24 hours

The field study has provided estimates of the composite domestic, commercial and municipal energy demand per day (Table. 7). However, the instantaneous power demand will follow an irregular pattern over the course of a day.

Domestic Instantaneous Power Demand

Figure 16 shows the typical rural domestic consumption pattern over a 24-hour period in October, based on measured data from Bhanbhane, Gulmi, Nepal in 2012 [12]. It exhibits typical Nepalese rural domestic consumption patterns over a day, and therefore has been adapted for use in modelling the rural load considered in this work. The measured power over the course of a day on one household gave rise to a total energy consumption of 0.39 kWh; this has been normalised to 1 kWh energy consumption over the course of 24 hours as shown in Figure 16

The scaled profile varying domestic demand over the course of a day, shown in Figure 16 was used as an input to the load model in Simulink. Based on a given power

consumption profile and measured grid voltage, a signal could be generated to control a controlled current source emulating a load, as shown in Figure 17.

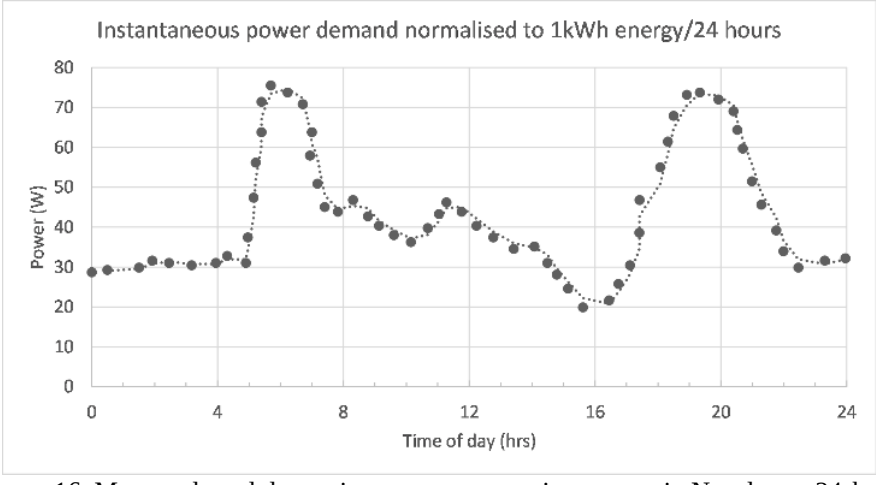

Figure 16. Measured rural domestic power consumption pattern in Nepal over 24-hour period (normalised to 1 kWh)

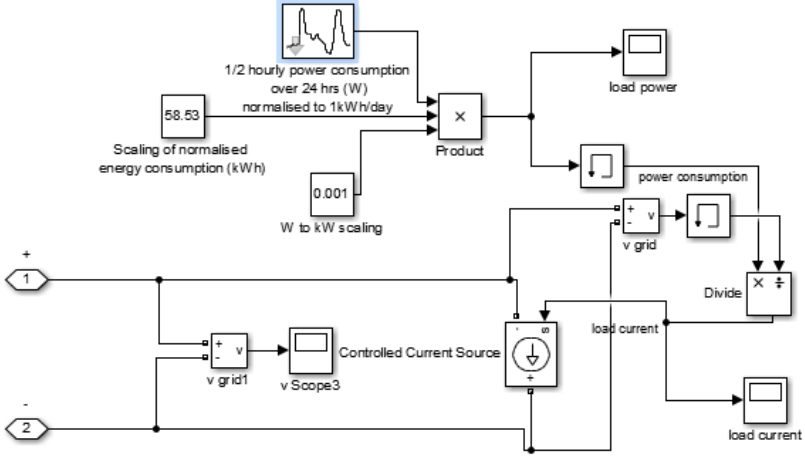

Figure 17. Simulating 24-hour domestic load with scaled variable power consumption

Commercial and Municipal Power

The commercial and municipal power consumption is more predictable than domestic over the course of 24 hours and is shown in Figure 18. The commercial load is comprised

of a water pump, rice mill, and office requirements (photocopy machine and printer). The municipal load comprises office lighting and equipment requirements for a health post, police station, co-operative, VDC office and forestry office.

The separate and combined commercial and municipal power load over the course of 24 hours is also shown in Figure 18. The composite load is modelled in Simulink as a second load using the same technique as the domestic load.

3.3 Modelling Solar Power

The solar panel models used are taken from [11], their details are set out in Table 8.

Local Solar Data

Using site GPS co-ordinates, daily averaged solar data from NASA [13] is used. The site provides an average insolation energy of 5.22 kWh/m^2/day over the course of a year, increasing in June to 5.8 kWh/m^2/day. Assuming no cloud cover or shading, the insolation power varies diurnally [14] shown in reaching a maximum of 1,012 W/m^2. This is then used as an input to the solar panel models.

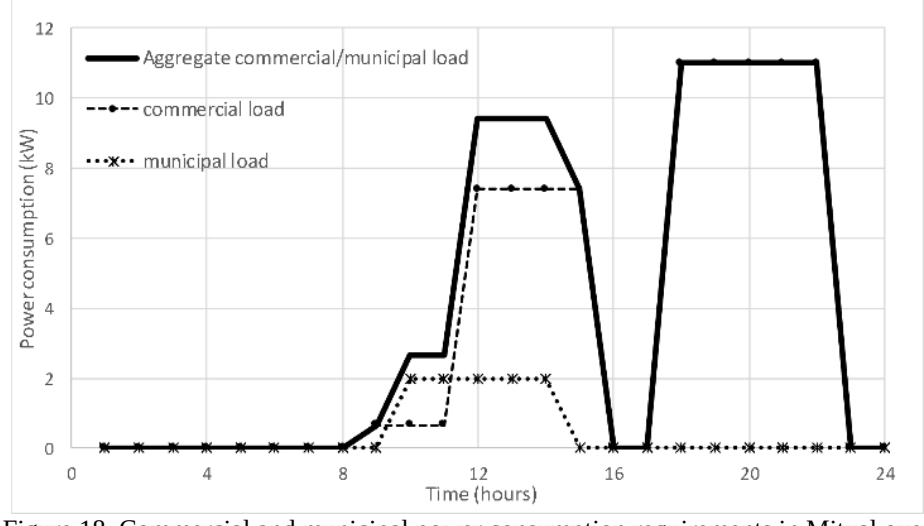

Figure 18. Commercial and municipal power consumption requirements in Mityal over 24 hours

Local Temperature Data

Photovoltaic panel performance is temperature dependent, and is an input for the solar panel model. There is no locally recorded temperature information, so an average temperature based on the site location [15] has been used, which is 28.1 ˚C in June.

3.4 Modelling wind power

Wind data was recorded at the site every 10 minutes, and averaged every 2 hours, over a period of 9 months at 20, 30 and 40m by the Alternative Energy Promotion Centre, Nepal [9]. This averaged wind speed data is combined with gust modelling, using a small Gaussian distributed random signal with a mean of 0 m/s and a variance of 3 m/s, to determine the wind speed. The wind turbine model used in the simulation is a 1.5 kW turbine model [6], with parameters in Table 8.

3.5 Line Resistances

Standard 100 mm^2 Aluminium Conductor Steel Reinforced (ACSR) lines have been selected for the transmission and distribution lines [9], which will have a resistance of 0.30 Ω/km [16]. The distance between the wind turbine and solar panel and the power house, where the solar and wind resource connection points are, is assumed to be 28.3 m and 14.2 m respectively. The approximate distance of the transmission line running between the power house site and the village captured during the field visit and was measured to be 1.4 km. Within Mityal village the total distribution wire length was measured to be 1 km. For simplicity, the composite village demand has been modelled as two separate loads, each with cabling to them of 0.5 km. The transmission and distribution distances are illustrated as resistances in Figure 13, and their details are in Table 8.

3.6 Droop Control Parameters

The droop curve shown in Figure 15 are used in this simulation, with V_{nom} = 420 V and V_{rated} = 400 V. The maximum current, I_{rated} is dependent on the power available to the source, and is scaled, as described in Section 2 and [8].

Droop Curve Scaling

The maximum output power from solar panels is approximately proportional to the product of their power rating and insolation, ignoring temperature effects and will therefore vary. Accordingly, the maximum power available from the solar panel, based on the rated panel power at standard conditions and the insolation, is fed forward into the droop controller, as in Figure 19. This sets the value of the maximum current I_{rated} for droop control at minimum voltage V_{rated}, in Figure 15.

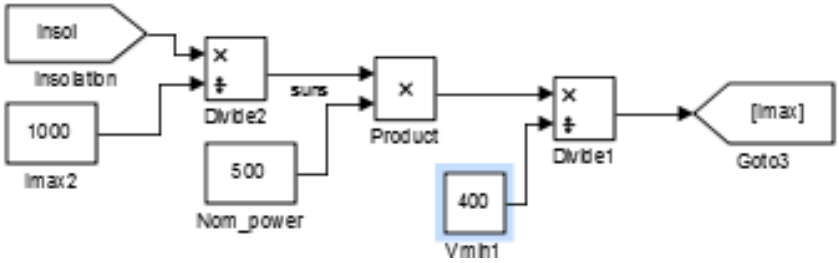

Figure 19. Feed forward of solar power (based on insolation) into droop controller

For the wind turbine, the output power is directly proportional to the cube of the wind speed. As the rated power of the wind turbine at rated speed of 10 m/s is 1.5 kW, the droop control permits the output voltage to range from its nominal 420 V down to a minimum of 400 V at full output power. Therefore, I_{rated} for the wind turbine droop control is 3.947 A at 10 m/s wind speed.

4 Case Study Simulation Results

The system model is shown below over a period of 10 hours 11am – 9pm Figure 20 (top) shows the current being drawn from the solar source; the square shape is attributable to the combined commercial/municipal load profile. Figure 20 (middle) illustrates the decrease in droop control voltage reference with insolation (bottom).

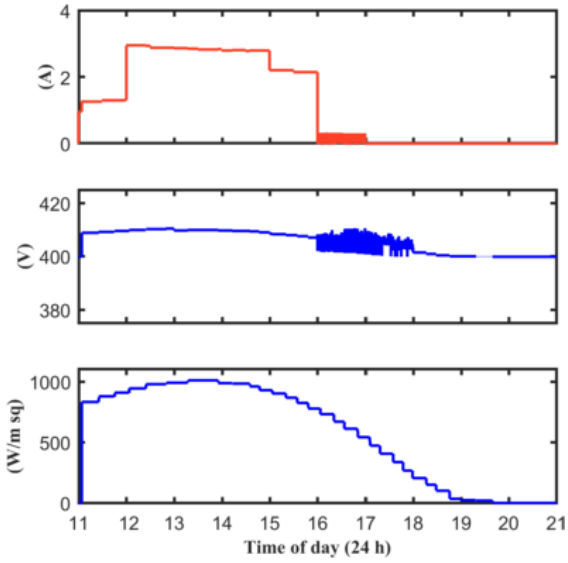

Figure 20. Solar output: current (top), droop control reference (middle), insolation (bottom)

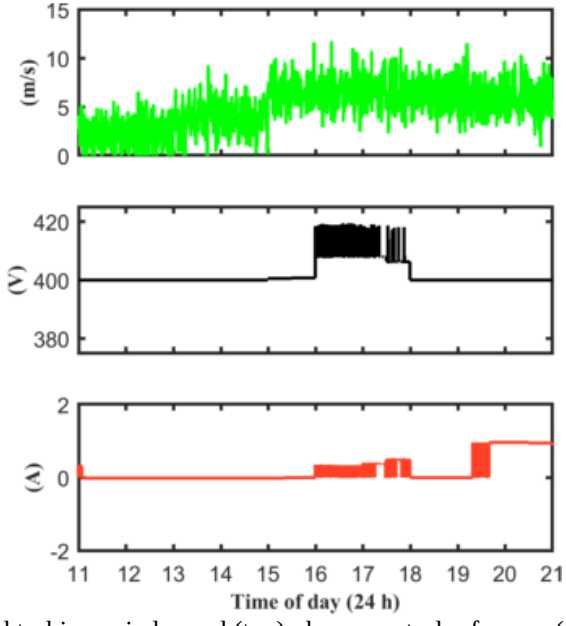

Figure 21. Wind turbine: wind speed (top), droop control reference (middle), current (bottom)

Figure 21 sets out data for the wind turbine. Between 1100-1500 hours, wind speed (top) is lower, therefore the droop reference voltage (middle) is at its minimum of 400V. During 1600-1800 hrs most of the load current is being drawn from solar, therefore the droop reference voltage Figure 21 (middle) is higher.

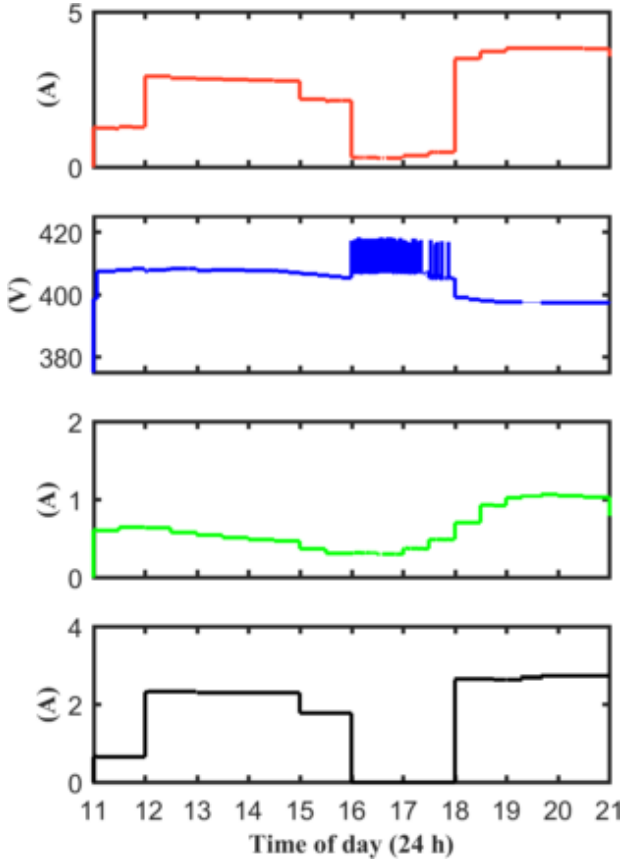

Figure 22. Grid and Loads: grid current (top), grid voltage (middle), domestic load (green), commercial load (bottom)

Figure 22 shows the grid current and voltage, and load currents during 1100-2100 timeframe. It will be noted from this that there is a slump in grid voltage at high loads, particularly 1800-2100 hrs as there is no storage to provide additional power during periods of demand-supply mismatch.

5 Conclusions

This paper has presented a DC microgrid system, interfacing renewable sources using a power electronic interface with droop functions. A case study site in Mityal, Nepal is simulated to demonstrate the performance of the system to variable generation and loads. The simulation has illustrated power sharing between wind and solar sources through droop control and in response to changing parameters over the course of a day such as loads and insolation. Future work in this area will focus on specifying the amount of storage required for this system.

Acknowledgements

The funding of this research has been provided by a UK EPSRC Global Challenges Project Institutional Sponsorship Grant.

References

[1] "World Energy Outlook http://www.worldenergyoutlook.org/publications/weo-2016/," *International Energy Agency*, 2016.
[2] "UN Sustainable Development Goals https://sustainabledevelopment.un.org/," 2017.
[3] J. M. Guerrero, "Hierarchical Control of Droop-Controlled AC and DC Microgrids 2014; A General Approach Toward Standardization," *IEEE Trans. on Ind. Elect.*, vol. 58, no. 1, pp. 158–172, Jan. 2011.
[4] J. C. Vasquez, "Voltage Support Provided by a Droop-Controlled Multifunctional Inverter," *IEEE Trans. Indust. Elect.*, vol. 56, no. 11, pp. 4510–4519, Nov. 2009.
[5] V. Salas, "Review of the maximum power point tracking algorithms for stand-alone photovoltaic systems," *Solar Energy Materials and Solar Cells*, 2006.
[6] N. Kishor and J. Fraile-Ardanuy, *Modeling and Dynamic Behaviour of Hydropower Plants, Chapter 11 (Williamson et al)*. IET, 2017.
[7] A. Khorsandi, "An adaptive droop control method for low voltage DC microgrids," in *The 5th Annual PEDSTC Conf.*, 2014, pp. 84–89.
[8] S. J. Williamson, A. Griffo, B. H. Stark, and J. D. Booker, "A controller for single-phase parallel inverters in a variable head pico-hydropower off-grid network," *Sustainable Energy, Grids and Networks, vol. 5, pp 114–124*, 2016.
[9] T. Chand and B. Gautam, "PEEDA Field Study Report in Mityal, Ruksibhanjyang, Palpa district, Nepal, December 2016," People, Energy & Environment Development Association.
[10] "HOMER website: http://www.homerenergy.com/."
[11] J. Kitson, "A photovoltaic panel modelling method for flexible implementation in Matlab/Simulink using datasheet quantities," in *26th IEEE ISIE, 19-21 June 2017 Edinburgh*, 2017.
[12] S. J. Williamson, "Modular and Scalable Low-Head Pico-Hydro Generation for Off-Grid Networks (PhD Thesis)," University of Bristol, 2014.
[13] "NASA Atmospheric Science Data Center, https://eosweb.larc.nasa.gov."
[14] "Sunshine on a Perfectly Cloudless Day, http://biocycle.atmos.colostate.edu/shiny/solar/."

[15] "World Bank Climate Change Portal http://sdwebx.worldbank.org/climateportal/index.cfm?page=country_historical_climate&ThisCCode=NPL."
[16] "Mini Grid Design Manual, ESMAP, Washington DC, 2000."

10TH INTERNATIONAL CONFERENCE ON SUSTAINABLE ENERGY AND ENVIRONMENTAL PROTECTION (JUNE 27TH – 30TH, 2017, BLED, SLOVENIA), MODELLING AND SIMULATION
J. Krope, A.Ghani Olabi, D. Goričanec & S. Božičnik

University of Maribor Press

Modelling and Scale-Up of Hydrogen Production by Electrolyzers for Industrial Applications

LUCAS BONFIM, LAUREANO JIMÉNEZ, MARCELINO GIMENES, SÉRGIO FARIA, THIAGO CAVALI & CID ANDRADE

Abstract Hydrogen production is a promising approach to meet the energy demand for the next years. The hydrogen can be obtained by systems based on electrolyzers that can get hydrogen from the water using electricity. Since this is a novel technology, this paper aims to model and scale-up the hydrogen production by finding the best combination of electrolyzers for an industrial demand. A non-linear mathematical model has been prepared to be tested in two different case studies in different scenarios of hydrogen production. The percentage of cost for electricity was between 87% and 95%, depending on the selected technology. The average production cost in large scale determined for the model was around 1.18 US$/kg H2. May be concluded that the production of electrolytic hydrogen from hydroelectricity is, in quantitative terms, reaching similar levels of conventional market technology.

Keywords: • Scale-up • Electrolyzer • Electrolysis • Hydrogen • Modelling •

CORRESPONDENCE ADDRESS: Lucas Bonfim, Ph.D Student, State University of Maringa, Department of Chemical Engineering, Colombo Avenue 5790, Maringa, Brazil, e-mail: pg52814@uem.br. Laureano Jiménez, Ph.D, Associate Professor, Rovira i Virgili University, Department of Chemical Engineering, Països Catalans Avenue 26, Tarragona, Spain, e-mail: laureano.jimenez@urv.cat. Marcelino Gimenes, Ph.D., Associate Professor, State University of Maringa, Department of Chemical Engineering, Colombo Avenue 5790, Maringa, Brazil, e-mail: mlgimenes@uem.br. Sérgio Faria, Ph.D., Associate Professor, State University of Maringa, Department of Chemical Engineering, Colombo Avenue 5790, Maringa, Brazil, e-mail: shbfaria@uem.br. Thiago Cavali, Msc. Student, Technological Federal University of Paraná, Department of Electrical Engineering, Alberto Carazzai Avenue 1640, Cornélio Procópio, Brasil, e-mail: thiagocavali@utfpr.edu.br. Cid Andrade, Ph.D., Associate Professor, State University of Maringa, Department of Chemical Engineering, Colombo Avenue 5790, Maringa, Brazil, e-mail: cmgandrade@uem.br.

https://doi.org/10.18690/978-961-286-058-5.20 ISBN 978-961-286-058-5

Available at: http://press.um.si.

1 Introduction

Industrially, hydrogen production with novel and sustainable systems are required in the near future, due in part to the increase of oil prices and demand and also due to global warming. Appearing as possible solutions, fuel cells and hybrid systems present a promising future in order to meet the demand [1].

Present day researches are oriented on three major ways of producing hydrogen from water: pure thermochemical methods, pure electrolysis methods and hybrid methods [2]. The thermochemical water splitting processes promise to produce hydrogen and oxygen from water and heat without using electricity, but requiring an external heat source, which generally causes several environmental impacts. Until now, the cleanest method of producing hydrogen has been water electrolysis using electricity to split water in oxygen and hydrogen according to Reation 1 [3].

$$H_2O \rightarrow H_2 + \tfrac{1}{2}O_2 \quad (1)$$

When the technology is well implemented the oxygen generated can be used as a by-product in different applications [3].

The process occurs at an unit named electrolyzer that consists of an anode and a cathode separated by an electrolyte operating according the system represented in Figure 1.

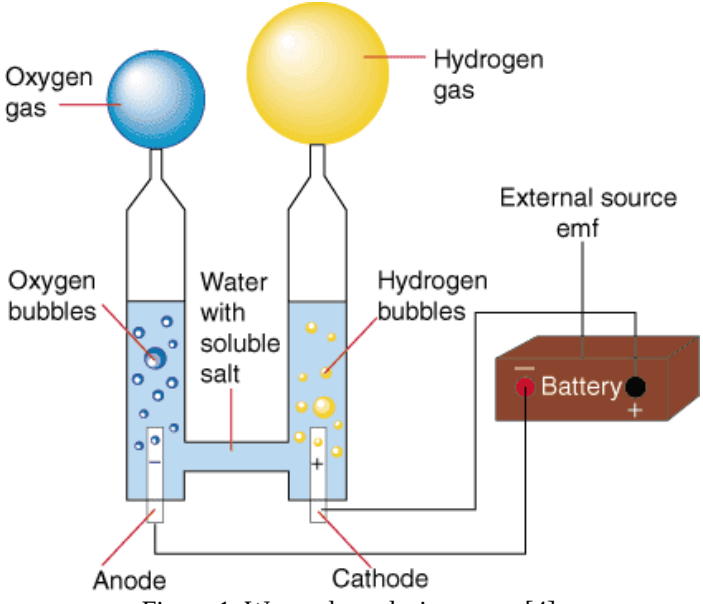

Figure 1. Water electrolysis system [4].

The main limitations related to the hydrogen production by electrolysis are the electrical energy consumption in the process, because nowadays most of electricity is generated using technologies that results in greenhouse gas emission, and the pilot scale of production where the technology find itself [5]. Therefore, the water electrolysis represents 4% (65 million tonnes) of global hydrogen production while natural gas reforming represents 48%, by-product from chemicals production 30% and coal gasification 18% [6]. A largely use of renewable sources is expected the overcoming of the limitations and a larger use of the water for electrolysis in the next years [7].

In Europe, the use of electrolytic hydrogen is expected to evolve gradually from industrial exploitation to wide deployment in hydrogen refueling infrastructure around 2020, but this growth depends of the evolution of energy systems and regulatory frameworks [8]. With advances in production capacity of the electrolyzers the hydrogen will be used as an alternative fuel in transports, energy storage, grid services and on chemical industry [8].

The much lower cost of hydrogen from renewable generation in 2030 compared to the 2012 levels, is a result of both CAPEX (capital expenditure) and OPEX (operating expenses) reduction and efficiency improvements in electrolyzers [9]. The capital costs involved are linked to the structure of hydrogen production module composed by a hydrogen generator and separator (a) and components of the structure (b) (transformers, electronics interface, pressure regulating valves, pipes, etc.) illustrated in Figure 2.

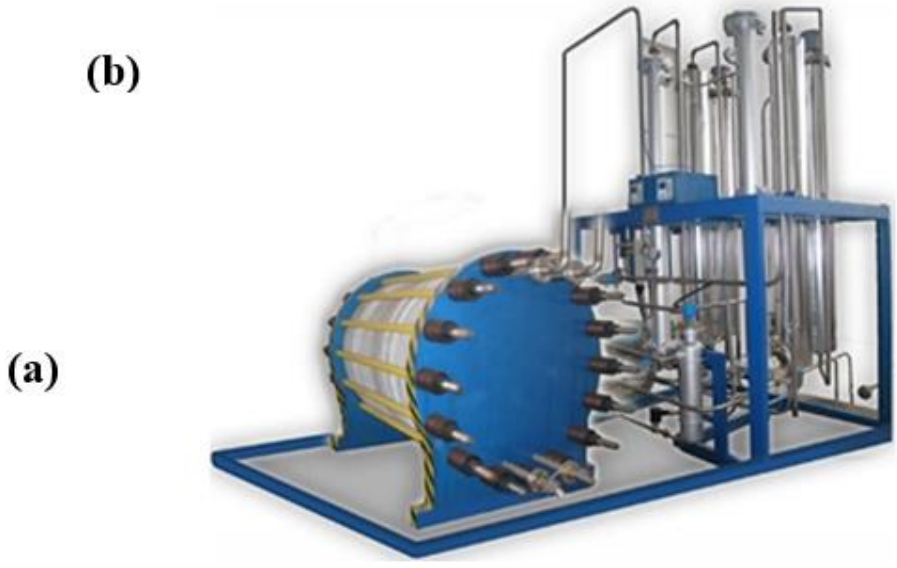

Figure 2. Example of hydrogen production module by electrolysis [10].

The main operating costs are associated with electricity consumption, as described previously, cooling water and compression energy to store the products.

Different types of electrolyzers can be find in the literature, each of them have a distinct reaction mechanism to produce hydrogen [7]. In this paper, we consider and compare the two more commons and improved ones: Polymer Electrolyte Membrane (PEM) electrolyzers and Alkaline electrolyzers.

In PEM electrolyzers the electrolyte is a polymer. The water reacts with the anode producing oxygen and hydrogen ions (Reaction 2). After the reaction, the oxygen is released as a gas, the electrons flow through an external circuit and the ions H^+ pass across the membrane to the cathode, where these ions combine with electrons from the external circuit and form hydrogen gaseous (Reaction 3)[1]:

$$2H_2O \rightarrow O_2 + 4H^+ + 4e^- \quad (2)$$

$$4H^+ + 4e^- \rightarrow 2H_2 \quad (3)$$

PEM electrolyzers typically produce hydrogen with 99.99 % v/v of purity and are commercially used in *low-scale* applications. The production capacity is around 0.06 ~ 30 Nm^3 H_2/hr with an efficiency range of 67-82% [8].

The alkaline electrolyzers operate with the transport of hydroxide ions from cathode to anode through a gas-tight working as electrolyte (Reactions 4 and 5). The alkaline electrolyzers are the most used technology in a *worldwide level* because this type of process is mature and the electrolyzers are reliable and safe. The produced hydrogen has a purity of 99.7 % v/v and the production capacity of alkaline electrolyzers is around 760 Nm^3 H_2/hr [8].

$$OH^- \rightarrow O_2 + H_2O + 4e \quad (4)$$

$$4H_2O + 4e^- \rightarrow 2H_2 + 4OH \quad (5)$$

Face to the limitation of scale for the discussed technology, the main objective of this work is to obtain a technical consensus from a panel of independent industry experts with regard to the current state-of-the-art cost of producing hydrogen from water electrolysis for scaled up scenarios.

2 Methodology

The methodology is based on three main steps to elaborate a techno-economic project of a set of scaled up electrolyzers modules. The steps are indicated in Figure 3 described hereafter.

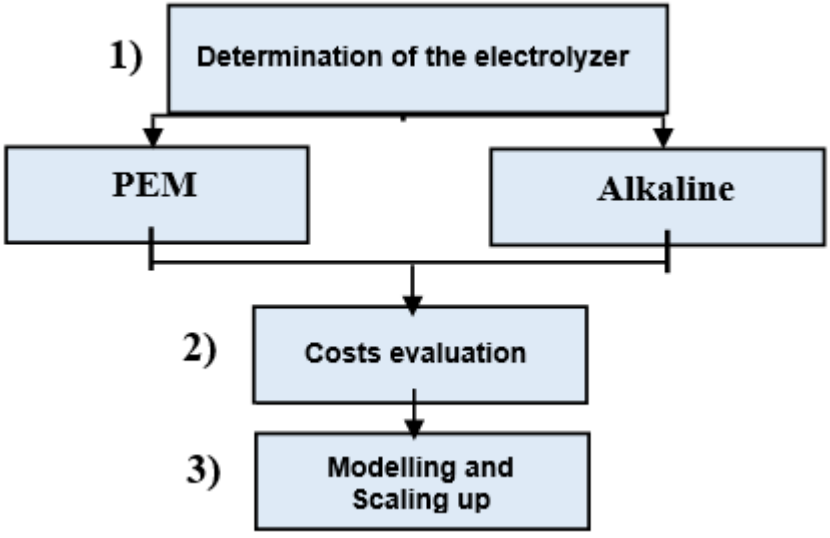

Figure 3. Steps of the scaling up methodology.

2.1 Determination of the electrolyzer

Aiming to approach different types of electrolyzers it is necessary to compare and select the appropriate one for the application.

Table 1 compares the main characteristics associated to the different electrolyzers and it is notable that the system size range is the factor responsible for constraint the electrolyzer selected.

Table 1. Overview of Alkaline and PEM electrolyzers [8].

Electrolyzer	Alkaline	PEM
System size range ($Nm^3 H_2/h$)	0.25 - 760	0.01 - 240
System size range ($kg H_2/h$)	22 - 67,800	0.89 - 22,300
Energy consumption (kW)	1.8 - 5,300	0.2 - 1,150
Hydrogen purity (%)	99.5 - 99.9	99.9

2.2 Costs evaluation

For any techno-economic analysis of a process is important to describe a scenario where the system is going to be implemented. According with a study realized in Europe by the *E4tech Sàrl with Element Energy Ltd* this work takes into account a representative data

sets for different types of regulatory and pricing environment, values from five European member states selected for detailed analysis [8]. The different countries present significant variations in different parameters listed next (*i.e.*, plant capacities, pressure out, electricity price, etc.). The evaluation using CAPEX and OPEX is adopted.

2.2.1 CAPEX

Most process plants have a non-linear relationship between the cost of the plant and its production capacity. The annualized cost of investment and implementation of an electrolytic hydrogen plant is modelled by Eq. 6 [11].

$$C_{CAPEX} = P_C^{\,n} crf \tag{6}$$

Where C_{CAPEX} is the annualized capital cost of the plant (US$) and P_C is the capacity (kilograms per year). Sources in the industry have confirmed that a power law relationship with an exponent n of between 0.6 and 0.7 seems to hold for a wide range of capacities in today's market up to about 1,000 kg/day [11]. The C_{CAPEX} is multiplied by a capital recovery factor (*crf*) which is a function of the interest rate (i) and a plant lifetime (t) in years. (Eq. 7).

$$crf = \left(\frac{i(1+i)^t}{(1+i)^t - 1} \right) \tag{7}$$

2.2.2 OPEX

Operational costs include planned and unplanned maintenance, as well as overhaul, but not the electricity cost. Often these costs are provided as a percentage of initial capital expenditure. All available data points suggest OPEX values of 2-5% of the annualized CAPEX per year, with no distinction between different technologies. Extrapolating to the extreme boundary case, the operational costs are provided by Eq. 8.

$$C_{OPEX} = 0.05\,C_{\mathrm{CAPEX}} \tag{8}$$

Where the C_{OPEX} takes into consideration compression, storage, and dispensing costs. Beyond, we still have to account with the cost of electricity which are a major contributor to the overall cost of water electrolysis. Electricity represents nearly 80% of the electrolysis cost considering current state-of-the-art technology [11].

2.2.3 Electricity cost

The water electrolysis unit considered in this work is going to use one of the electrolyzers presented by E4Tech and Element Energy review. More details can be find in *Study on development of water electrolysis in the EU - Final report* [8].

The specific system energy requirement is used to determine the electricity cost to produce hydrogen as a function of the electricity price. These demands of electricity are shown in Tables 2 and 3 for the Alkaline and PEM electrolyzers respectively.

Table 2. Alkaline electrolyzers understudy [8].

Electrolyzer	Plant capacity (kg H_2/h)	System electricity consumption (F_c) (kWh/kg H_2)
Customised1	29,450	51.0
G256	15,170	59.5
Customised2	17,850	52.3
HyStat60	5,350	57.8
Model120	7,140	52.4
Customised3	67,800	51.2
Customised4	43,280	50.0
Container	5,350	57.8
EV150	20,080	58.7

Table 3. PEM electrolyzers understudy [8].

Electrolyzer	Plant capacity (kg H_2/h)	System electricity consumption (F_c) (kWh/kg H_2)
Development	1,780	55.6
E60 cluster	21,410	54.5
EL30/144	320	55.6
HPac40	210	53.4
Hogen C30	2,680	64.5
SILYZER200	22,300	60.0

The Tables present information as name provided by companies, besides electrolyzer information as model capacity and electric consumption. Then, a product between the consumption factor F_c and the electricity price P_e (US$/kWh) can express the total electricity cost $C_{electricity}$ as show in Eq. 9.

$$C_{electricity} = F_c P_e \tag{9}$$

Finally, Eq. 10 can evaluate the total annualized cost (TAC) for an electrolyzer.

$$TAC = C_{CAPEX} + C_{OPEX} + C_{electricity} \quad (10)$$

Where the *TAC* represents the costs associated to a single electrolyzer module. The next step will determine the configuration necessary to attempt the scaled up system.

2.3 Modelling and scale-up

For industrial scale production are usually required a set of modules operating in parallel according with their single capacity. Parallel electrolyzers can be installed with some sharing of utilities such as power electronics and controls and possibly other balance-of-plant components. Working with multiple units in parallel also has benefits, as it allows for maintenance and unscheduled shutdowns of individual electrolyzer units and leaves the rest of the plant operational.

The number of electrolyzers required to attempt the annual demand (*D*) can be determined according with Eq. 11, where *j* designate the alkaline electrolyzers and *k* the PEM electrolyzers.

$$N_{j,k} = \frac{D}{P_{j,k}} \quad (11)$$

Then, it is necessary to determine the best configuration of electrolyzers capable of providing the necessary demand. In fact, an optimal combination between the electrolyzers can be found using non-linear programming techniques able of minimize the value of *TAC* in the following model *M*.

$$(M)_{\min} TAC = f\left(P_C, P_e, F_C, N_j, N_k\right)$$

$$s.t. \quad \sum_{j=1}^{9} N_j^{Alkaline} P_{Cj} y_j + \sum_{k=1}^{6} N_k^{PEM} P_{Ck} y_k \geq D$$

$$N_j, N_k \in \mathrm{I}$$

$$y_j, y_k \in \{0,1\}^n$$

$$\sum y_j = 1$$

$$\sum y_k = 1$$

The model is constrained to supply the demand of hydrogen (*D*) and allows to combine alkaline and PEM electrolyzers. The model was implemented and solved using the *Microsoft Excel* complex solver.

3 Results and discussion

Once presented the model for scale up the production, two case studies are evaluated for a lifetime plant of 5 years operating 8600 h/year with an interest equal 20 %. A demand of 20,000 and 70,000 ton H_2/year are adopted for cases 1 and 2, respectively, according references.

The case studies combine the results obtained for single electrolyzers in model M. Table 4 presents the results for single electrolyzers operating with their maximum capacity.

Table 4. Electrolyzers' *TAC* and production.

Electrolyzer	Total Annualized cost (US$/year)	Production (kg H_2/year)
Customised1	272,530,595	253,270,000
G256	163,840,654	130,462,000
Customised2	169,575,092	153,510,000
HyStat60	56,321,886	46,010,000
Model120	68,152,840	61,404,000
Customised3	628,752,101	583,080,000
Customised4	392,373,758	372,208,000
Container	56,321,886	46,010,000
EV150	213,832,338	172,688,000
Development	18,119,950	15,308,000
E60 cluster	211,775,704	184,126,000
EL30/144	3,294,524	2,752,000
HPac40	2,087,000	1,806,000
Hogen C30	31,521,908	23,048,000
SILYZER200	242,634,029	191,780,000

The results of single electrolyzers confirm that usually Alkaline electrolyzers present higher total costs than PEM electrolyzers due to higher production potential. The percentage of cost for electricity was calculated between 87% and 95%, depending on the selected technology. PEM electrolyzers presented higher costs with electricity. The average production cost in large scale determined for the model was around 1.18 US$/kg H_2. In the maximum capacity, some electrolyzers can produce amounts of hydrogen

above the stipulated demand, however, the model can select electrolyzers operating under their maximum capacity.

3.1 Case study 1: photovoltaic-wind power plant for hydrogen production

First case is based on a photovoltaic-wind power plant construction for electric and hydrogen production. Studies in Oman describe that energy costs of photovoltaic-wind solar hybrid system were found around 0.2 US$/kWh [12]. The best configuration find by the developed model is presented in Table 5.

Table 5. Best scale-up for case 1.

Electrolyzer	Units	TAC (US$/year)	Production (kg H_2/year)
Development	1	18,119,950	15,308,000
EL30/144	2	5,616,973	4,692,000
Total	3	23,736,923	20,000,000

When a demand of 20,000 ton H_2/year is required, three units of PEM electrolyzers are required to supply the low demand of a photovoltaic power plant.

3.2 Case study 2: glycerol reforming for hydrogen and power production

Second case is based on a glycerol reforming for hydrogen and power production plant with low carbon dioxide emissions. The hydrogen & power production costs are around 0.04 US$/kWh [13].

This cost can be lower as a result of the regionality of the study and the best configuration in this case is presented in Table 6 for a higher demand.

Table 6. Best scale-up for case 2.

Electrolyzer	Units	TAC (US$/year)	Production (kg H_2/year)
HyStat60	1	56,321,886	46,010,000
Hogen C30	1	31,521,908	23,048,000
HPac40	1	1,088,568	942,000
Total	3	88,932,362	70,000,000

When a demand three and a half times bigger than case 1 is required, the total annualized cost can increase more than this factor. In fact, the TAC increases in a factor of 3.74. In this case, three units are also required, but in function of the higher demand, one alkaline

electrolyzer is required, in addition to two PEM electrolyzers producing smaller amounts of hydrogen.

Both demands in industrial scale are possible and can be attend using multiple parallel electrolyzer modules. The model defines some electrolyzers working with their maximum capacity in cases 1 and 2, but one can note that electrolyzers *EL30/144* and *HPac40* produce values under their single capacity, as presented in Table 1.
Some extra considerations can be noted from our results, as the possibility of use combined technologies of electrolyzers to obtain lower costs and the production margin achieved with electrolyzers that do not operate in their maximum capacity.
As demonstrated, the current state-of-the-art of hydrogen from water electrolysis can be scaled-up to industrial scenarios, being competitive with conventional market technologies.

4 Conclusions and pesrpectives

A non-linear mathematical model has been prepared to modelling and scale-up production of hydrogen via electrolysis in terms of production capacity and costs evaluation. The model is comprised of several modules which dealing the total production cost: electricity consumption, investment, operation and maintenance.

The production cost model was applied to two different case studies in different scenarios of hydrogen production. The first case of lower production gave preference to PEM electrolyzers while the second one required hybrid technology. The percentage of cost for electricity was between 87% and 95%, depending on the selected technology. The average production cost in large scale determined for the model was around 1.18 US$/kg H_2.

Finally, it may be concluded that the production of electrolytic hydrogen from hydroelectricity is, in quantitative terms, reaching similar levels of conventional market technologies. Perspectives of the work show that the results must be compared with other studies reported in the literature for similar production levels and even for others with more favourable conditions in terms of economy of scale.

Acknowledgements

The authors gratefully acknowledge the financial support from CAPES (Brazilian Federal Agency for Support and Evaluation of Graduate Education), from the Spanish Ministry of Education and Competiveness (CTQ2016-77968-C3-1-P, MINECO/FEDER).

References

[1] A. Basile, and A. Iulianelli, *Advances in Hydrogen Production, Storage and Distribution*. Cambridge: Woodhead Publishing, 2014.

[2] M. Ball, and M. Wietschel, *The Hydrogen Economy: Opportunities and Challenges*. Cambridge: University Press, 2009.

[3] M. M. Rashid, M. K. Al Mesfer, H. Naseem, and M. Danish "Hydrogen Production by Water Electrolysis: A Review of Alkaline Water Electrolysis, PEM Water Electrolysis and High Temperature Water Electrolysis" *International Journal of Engineering and Advanced Technology*, vol. 4, pp. 80-93, Feb. 2015.

[4] V. A. M. Longo, *Produção biológica de hidrogênio*. In english: *Biological production of Hydrogen*. Florianópolis: UFSC, 2008.

[5] H. Al-Kalbani, J. Xuan, S. García and H. Huang, " Comparative energetic assessment of methanol production from CO_2: Chemical versus electrochemical process" *Applied Energy*, vol. 165, pp. 1-13, Jan. 2016.

[6] M. A. Laguna-Bercero, "Recent advances in high temperature electrolysis using solid oxide fuel cells: A review" *Journal of Power Sources*, vol. 203, pp. 4–16, Jan. 2012.

[7] M. Ball, and M. Wietschel "The future of hydrogen – opportunities and challenges" *International Journal of Hydrogen Energy*, vol. 34, pp. 615-627, Dec. 2008.

[8] E4TECH, ELEMENT ENERGY. *Study on development of water electrolysis in the EU*. Final report. 160 p. 2014.

[9] A. Contreras, F. Posso, and T. N. Veziroglu "Modeling and simulation of the production of hydrogen using hydroelectricity in Venezuela" *Journal of Hydrogen Energy*, vol. 32, pp. 1219–1224, Dec. 2006

[10] Angstrom advanced hydrogen solutions & technology, 2017. Angstrom Advanced Hydrogen Generating Plant by Water Electrolysis. Available at angstromadvancedhydrogen.wordpress.com/angstrom-advanced-tech/water-electrolysis [Accessed 05/16/2017].

[11] U.S. Department of Energy Hydrogen Program, 2009. *Current State-of-the-Art Hydrogen Production Cost Estimate Using Water Electrolysis*. Available at https://www.hydrogen.energy.gov/pdfs/46676.pdf [Accessed 05/16/2017].

[12] M. Qolipoura, A. Mostafaeipoura, and O. M. Tousib, " Techno-economic feasibility of a photovoltaic-wind power plant construction for electric and hydrogen production: A case study" *Renewable and Sustainable Energy Reviews*, vol. 78, pp. 113-123, Apr. 2017.

[13] A. M. Cormos, and C. C. Cormos " Techno-economic and environmental performances of glycerol reforming for hydrogen and power production with low carbon dioxide emissions" *International Journal of Hydrogen Energy*, vol. 42, pp. 7798–7810, Dec. 2016.

10TH INTERNATIONAL CONFERENCE ON SUSTAINABLE ENERGY AND ENVIRONMENTAL PROTECTION (JUNE 27TH – 30TH, 2017, BLED, SLOVENIA), MODELLING AND SIMULATION
J. Krope, A.Ghani Olabi, D. Goričanec & S. Božičnik

Effect of Insulators on the a-IGZO TFT Performance

MOHAMED LABED, NOUREDINE SENGOUGA & SLIMANE CHALA

Abstract Indium Gallium Zinc Oxide (IGZO) thin films have attracted significant attention for application in thin-film transistors (TFTs) due to their specific characteristics, such as high mobility and transparency. The performance a-IGZO thin film transistors (TFTs) with four different insulators (SiO2 Si3N4, Al2O3 and HfO2) are examined by using numerical simulation. It is found that the output performance is significantly enhanced with high relative permittivity of the insulator. The HfO2 gate insulator gives the best performance: lower threshold voltage and subthreshold, and higher field effect mobility, on current and Ion/Ioff ratio.

Keywords: • a-IGZO • TFT • Simulation • Insulators • Stability.•

CORRESPONDENCE ADDRESS: Mohamed Labed, Ph.D. student, University of Biskra, Physics Department, Laboratory of Metallic and Semiconducting Materials, BP 145 RP, 07000 Biskra, Algeria, e-mail: m.labed@univ-biskra.dz. Nouredine Sengouga, Ph.D., Professor, University of Biskra, Physics Department, Laboratory of Metallic and Semiconducting Materials, BP 145 RP, 07000 Biskra, Algeria, e-mail: n.sengouga@univ-biskra.dz. Slimane Chala, Ph.D. Student, University of Biskra, Physics Department, Laboratory of Metallic and Semiconducting Materials, BP 145 RP, 07000 Biskra, Algeria, e-mails: chala_slimane@yahoo.com.

https://doi.org/10.18690/978-961-286-058-5.21 ISBN 978-961-286-058-5

Available at: http://press.um.si.

1 Introduction

Transparent amorphous oxide semiconductors (TAOS) is a very active field compared with the conventional transparent oxide semiconductors (TOS) such as ZnO, In_2O_3, IZO. Amorphous Indium gallium zinc oxide (a-IGZO) is the most promising AOS due to high mobility, large band gap, high transparency and room temperature deposition. a-IGZO has a wide application especially thin films transistors (TFT). TFT based on a-IGZO replaced the conventional TFTs based on a-Si, ZnO or organic semiconductors [1], [2]. The instability of a-IGZO TFTs following a stress is a sensitive issue. The ongoing research is trying to understand the reasons of this instability such as negative bias illumination stress [3] or positive bias stress[4]. Several ways are used to reduce the impact of instability by structure optimization [5], using a passivation layer [6], or treatment after deposition [7].

In this work, numerical simulation is used to understand the effect of the insulator type on the operation a-IGZO TFT and the threshold (V_{th}) instability. The numerical simulation is carried out using the ATLAS software which is a very powerful tool to simulate and study electronic devices. ATLAS gives us a hand to vary many parameters which allows us to model the experimentally observed phenomenon. The numerical study allows the understanding of the effect of insulators without the contribution of other parameters such as interface states between semiconductors and insulator or fixed charge in the insulator material which cannot be control by experimental work. Furthermore, numerical simulation decreases the cost and time required by measurement and it is obvious that a careful study of insulators and instability effects is very difficult to be achieved experimentally.

2 Method

Four structures with the same parameters but using different insulators layer: SiO_2, Si_3N_4, Al_2O_3 and HfO_2 were studied. The schematic a-IGZO TFT structure studied in this work is shown in Figure 1. It consists of an a-IGZO active layer (20 nm), an insulator layer (100 nm) and a silicon wafer substrate (n^{++}) as a gate. The length (L) and the width (W) of the channel are 30 and 180 μm, respectively. The source and the drain are 5 nm thick and made of titanium (Ti).

3 Physical model

The numerical simulation is a powerful tool to understand the physics of electronic devices and materials. It is also a cheap and effective tool to optimize the semiconductor device conception and operating mode. The Poisson and the continuity equations describe the electronic phenomena inside semiconductors and the electrical transport mechanisms involved.

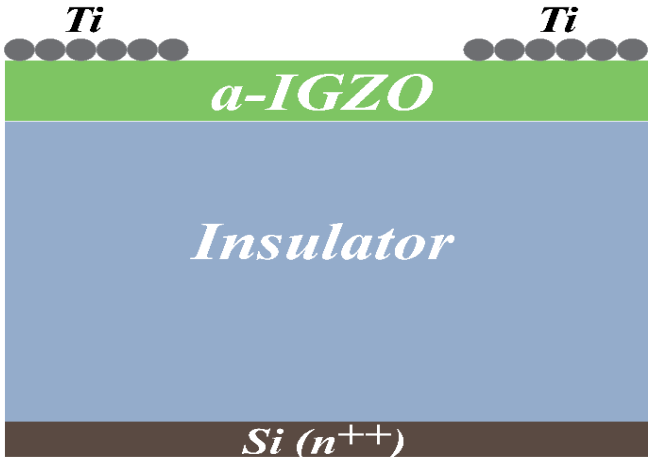

Figure 1. Schematic View of The a-IGZO TFT Structure Used in This Work.

The numerical resolution is the best way to solve the Poisson and the continuity equation system and get information about the effect of the various parameters (physical and structural) included in the device operation.

Usually the a-IGZO density of gap states is formed by donor tail state $g_{vt}^{D}(E)$ with exponential decay from E_v , a donor Gaussian distribution $g_G^D(E)$ with a maximum located at 2.9 eV (from E_v) and another narrow acceptor tail state $g_{ct}^{A}(E)$ near E_C. These distributions are expressed as follows [8, 9]:

$$g_{vt}^{D}(E) = N_{td} \times exp\left(\frac{E_V - E}{W_{td}}\right) \quad (1)$$

$$g_{G}^{D}(E) = N_{gd} \times exp\left(\frac{-(E - E_{gd})^2}{W_{gd}}\right) \quad (2)$$

$$g_{ct}^{A}(E) = N_{ta} \times exp\left(\frac{E - E_c}{W_{ta}}\right) \quad (3)$$

Figure 2 shows the different components used usually to model of the density of states in the a-IGZO.

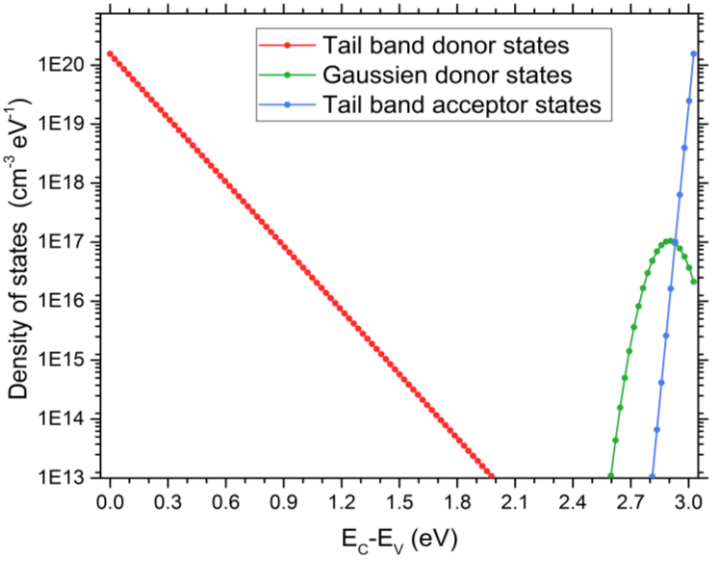

Figure 2. Density of States in a-IGZO

The Poisson's equation relates the electro-static potential to the space charge density and is given by:

$$div(\varepsilon \nabla \psi) = -\rho = -q(p - n + n_{tail} - p_{tail} + n_{gd} - p_{ga} + N_d) \tag{4}$$

where ψ is the electrostatic potential, ε is the local permittivity, ρ is the local space charge density, n and p are the free carrier's densities, N_d is the n-channel doping concentration. n_{tail}, p_{tail} and n_{gd} are charge states in the band gaps.
The continuity equations for both electrons and holes, are expressed in the dynamic regime as [10]:

$$\frac{\partial n}{\partial t} = \frac{1}{q} div(\overrightarrow{J_n}) + G_n - R_n \tag{5}$$

$$\frac{\partial p}{\partial t} = -\frac{1}{q} div(\overrightarrow{J_P}) + G_P - R_p \tag{6}$$

At the stationary regime $\frac{\partial n}{\partial t} = \frac{\partial p}{\partial t} = 0$.

$\overrightarrow{J_n}$ and $\overrightarrow{J_p}$ are the electron and hole current densities, G_n and G_p are the optical generation rates for electrons and holes which are neglected in this study. R_n and R_p are the total recombination rates for electrons and holes in Gaussian and tail states, and q is the electron charge. In the drift-diffusion model, the current densities are expressed in terms of the quasi Fermi levels ϕ_n and ϕ_p as

$$\vec{J}_n = -q\mu_n n \nabla \phi_n \tag{7}$$

$$\vec{J}_p = -q\mu_p p \nabla \phi_p \tag{8}$$

where $\mu_n$and μ_p are electron and hole mobilities, respectively. The quasi-Fermi levels are linked to the carries concentration and the potential through

$$n = n_i \exp\left(\frac{\psi - \phi_n}{K_B T}\right) \tag{9}$$

$$p = n_i \exp\left(\frac{\psi - \phi_p}{K_B T}\right) \tag{10}$$

Table1. The Physical Parameters of The Different Layers of The a-IGZO

Layer	Parameters	Designation	Value
IGZO	$N_C(cm^{-3})$	Effective DOS in CB	5×10^{18}
	N_V (cm-3)	Effective DOS in VB	5×10^{18}
	$E_g\ (eV)$	Band gap	3.05
	$\chi\ (eV)$	Electronic affinity	4.16
	ε	Relative permittivity	10
	L(µm)/W(µm) /T(nm)	Length/Wide/ Thickness	180/40 /20
	$\mu_n\ (\frac{cm^2}{V\ s})$	Free electron mobility	15
	$\mu_p\ (\frac{cm^2}{V\ s})$	Free hole mobility	0.1
SiO_2	$E_g(eV)$	Band gap	9
	ε_{ox}	Relative permittivity	3.9
Si_3N_4	$E_g(eV)$	Band gap	5.3
	ε_{ox}	Relative permittivity	7.5
Al_2O_3	$E_g(eV)$	Band gap	8.8
	ε_{ox}	Relative permittivity	9.3
HfO_2	$E_g(eV)$	Band gap	6
	ε_{ox}	Relative permittivity	22.0
S/D contacts (Ti)	d(nm)	Thickness	5
	$\Phi_{Ti}(eV)$	Work function	4.33
Gate Si ploy (n++)	d(nm)	Thickness	5
	$\Phi_{p-Si}(eV)$	Work function	4.58

The physical parameters in Table 1 were used in the continuity equation and this last is solved for different applied gate voltage ranging from -10 to 20 V. The drain voltage was fixed 0.1 V. the transfer characteristic $(I_{DS} - V_{GS})$ is plotted on a semi-logarithmic scale

4 Results And Discussion

To understand the effect of the insulator on the operation a-IGZO TFTs the Poisson and continuity equations were solved using physical properties. The values of defect on the band gap are $1.55x10^{20}$ $cm^{-3}eV^{-1}$ for tail band acceptor and donor. Gaussian donor states are $6.5x10^{17}$ $cm^{-3}eV^{-1}$. The transfer characteristic (I_{DS}-V_{GS}) are plotted on a linear and semi-logarithmic scales in Figure 3. The threshold voltage (V_{th}) and mobility field-effect (μ_{FE}) extracted from the linear plot while Ion, I_{on}/I_{off} and subthreshold swing (SS) from the transfer characteristics plot.

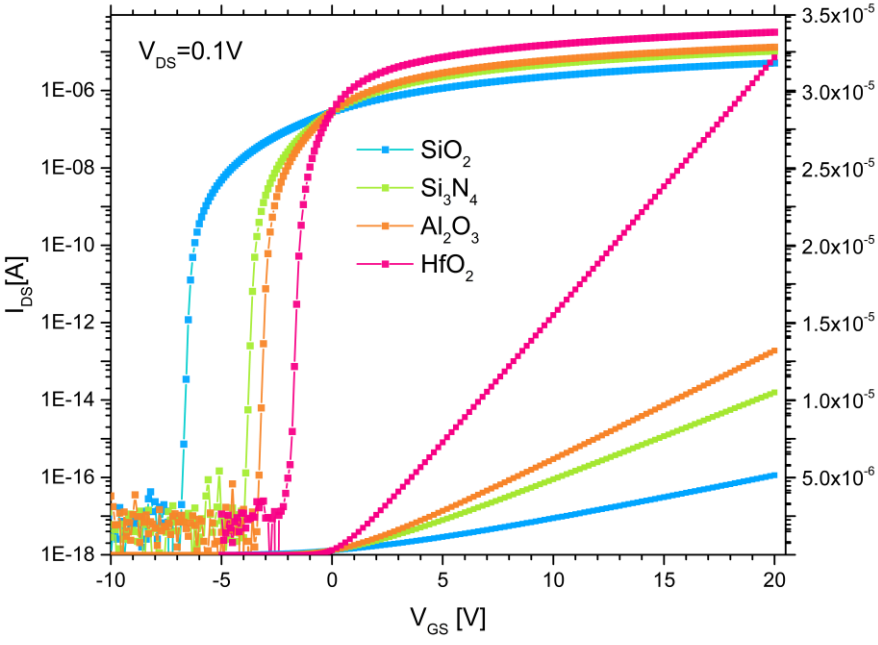

Figure 3. The Transfer Characteristics for Diffrent Insulators Layers

The output parameters are summarized in Table 2.

Table 2. The Effect of Different Insulators Layer on The Output Parameters of The TFT

	SiO_2	Si_3N_4	Al_2O_3	HfO_2
V_{th} (V)	-1.70	-0.60	-0.43	0.23
μ_{FE} ($cm^2\ s^{-1}\ V^{-1}$)	7.87	8.21	9.50	13.73
I_{on} (A)	4.44 x10^{-6}	9.10 x10^{-6}	1.5 x10^{-5}	2.81 x10^{-6}
I_{on}/I_{off}	5.87 x10^{11}	1.43 x10^{12}	2.07 x10^{12}	5.06 x10^{12}
SS (V dec^{-1})	0.13	0.11	0.10	0.09

Using different types of insulators has a noticeable on the a-IGZO TFT performance. The output parameters for IGZO/SiO_2 TFT V_{th}, μ_{EF}, I, I_{on}/I_{off} and SS are -1.70V,7.87 $cm^2\ s^{-1}\ V^{-1}$, 4.44x10^{-6}A, 5.87x10^{11} and SS 0.13 $Vdec^{-1}$ respectively. The IGZO/Si_3N_4 TFT show better performance than IGZO/SiO_2 TFT which were V_{th}, μ_{EF}, I, I_{on}/I_{off} and SS 0.60V,8.21 $cm^2\ s^{-1}\ V^{-1}$, 9.10x10^{-6}A, 1.43x10^{12} and SS 0.13 $Vdec^{-1}$ respectively. IGZO/Al_2O_3 TFT show higher than IGZO/SiO_2 and IGZO/Si_3N_4 when was V_{th}, μ_{EF}, I, I_{on}/I_{off} and SS are -0.43V, 9.50 $cm^2\ s^{-1}\ V^{-1}$, 1.54x10^{-5}A, 2.07x10^{12}. The IGZO/HfO_2 had the optimal performance compared with other TFT in this study where V_{th}, μ_{EF}, I, I_{on}/I_{off} and SS are 0.23 V, 13.73 $cm^2\ s^{-1}\ V^{-1}$, 2.81x10^{-6}A, 5.06x10^{12} and SS 0.09 $Vdec^{-1}$ respectively. The high relative permittivity insulator leads to a higher TFT performance. To further understand this behaviour we extracted and plotted the internal parameters (electron concentration and electric field) in figures 4 and 5 respectively.

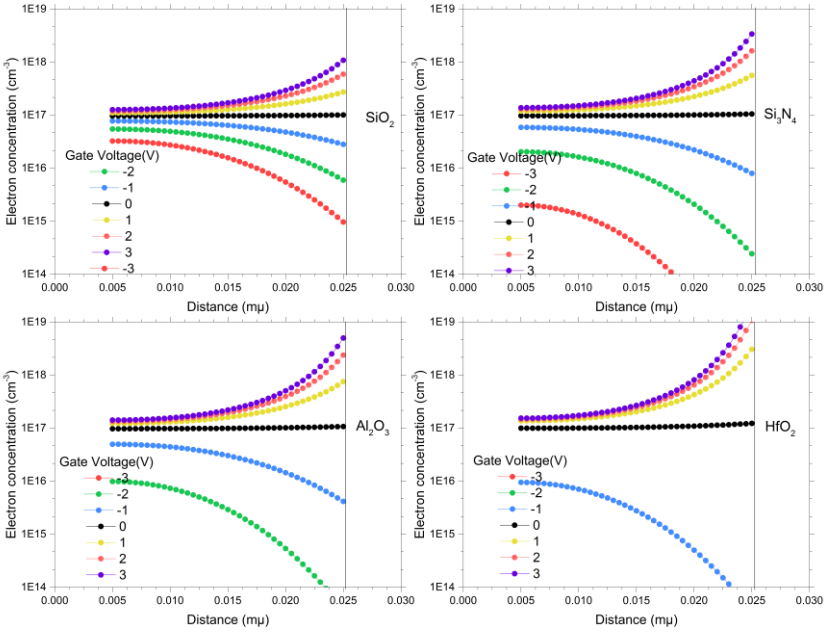

Figure 4. The Electron Concentration for Different Gate Insulators

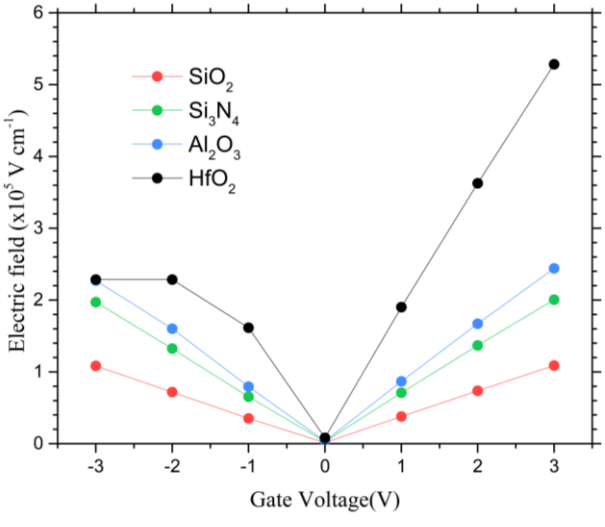

Figure 5. The Electric Field for Different Gate Insulators

The type of insulator affects electron accumulation at the interface between the semiconductor and the insulator and hence affect V_{th} and I_{on}. When the electron concentration surpasses $1x10^{14}$ cm^{-3} the TFT passes to the ON regime. For SiO_2 insulators -3 V was enough to make electron accumulate at interface due to low electric field as shown in figure 5. This makes a-IGZO/SiO_2 TFT work in the negative region. At 3 V a low electron concentration at the interface makes a-IGZO/SiO_2 TFT has the smallest I_{on}. The a-IGZO/Si_3N_4 TFT work on at -2 V gate voltage when electron concentration surpasses $1x10^{14}$ cm^{-3}. We notice that the electric field show a higher value than SiO_2. At 3V a-IGZO/Si_3N_4 archived high concentration more than a-IGZO/SiO_2 TFT while less than a-IGZO/Al_2O_3 and a-IGZO/HfO_2 TFT. For a-IGZO/Al_2O_3 TFT, it works at -1 V which gives a better performance than a-IGZO/SiO_2 and a-IGZO/Si_3N_4. The a-IGZO/HfO_2 TFT achieved the optimal performance in this work since it works at 0 V gate voltage with high electron concentration at the interface for positive gate voltages. The low concentration for negative gate voltage is due to a higher electric field. Those different values of electron concentration related with effect of electric flied. High electric field causing high electron concentration and gives high Ion value while low value of electric filed lets electrons accumulate at the interface which makes the TFT work for negative gate voltages. This property is useful for electronics devices.

5 Conclusion

The type of insulator deeply affect the performance of a-IGZO TFTs. The high relative permittivity gives the optimal performance. The HfO_2 achieve high and optimal performance which make it the right insulator for a-IGZO TFTs.

Acknowledgements

Mohamed Labed et *al.* would like to thank the University of Biskra for its support.

References

[1] K. Nomura, H. Ohta, A. Takagi, T. Kamiya, M. Hirano, and H. Hosono, "Room-temperature fabrication of transparent flexible thin-film transistors using amorphous oxide semiconductors.," Nature, vol. 432, no. 7016, pp. 488–492, 2004.

[2] T. Kamiya, K. Nomura, and H. Hosono, "Present status of amorphous In–Ga–Zn–O thin-film transistors," Sci. Technol. Adv. Mater., vol. 11, no. 4, p. 44305, 2010.

[3] H. Oh, S. M. Yoon, M. K. Ryu, C. S. Hwang, S. Yang, and S. H. K. Park, "Photon-accelerated negative bias instability involving subgap states creation in amorphous In-Ga-Zn-O thin film transistor," Appl. Phys. Lett., vol. 97, no. 18, 2010.

[4] K. Domen, T. Miyase, K. Abe, H. Hosono, and T. Kamiya, "Positive-Bias Stress Test on Amorphous In–Ga–Zn–O Thin Film Transistor: Annealing-Temperature Dependence," J. Disp. Technol., vol. 10, no. 11, pp. 975–978, 2014.

[5] K. Dongsik, J. Hyunkwnag, K. Yongsik, B. Minkyung, J. Jaeman, K. Jeahyeong, K. Woojoon, H. Inseok, M. K. Dong, and H. K. Dae, "Effect of the Active Layer Thickness on the Negative Bias Illumination Stress-induced Instability in Amorphous InGaZnO Thin-film Transistors," J. Korean Phys. Soc., vol. 59, no. 21, p. 505, 2011.

[6] K. Yamada, K. Nomura, K. Abe, S. Takeda, and H. Hosono, "Examination of the ambient effects on the stability of amorphous indium-gallium-zinc oxide thin film transistors using a laser-glass-sealing technology," Appl. Phys. Lett., vol. 105, no. 13, pp. 2012–2016, 2014.

[7] J. S. Park, J. K. Jeong, Y. G. Mo, H. D. Kim, and S. Il Kim, "Improvements in the device characteristics of amorphous indium gallium zinc oxide thin-film transistors by Ar plasma treatment," Appl. Phys. Lett., vol. 90, no. 26, pp. 2012–2015, 2007.

[8] M. Kimura, T. Nakanishi, K. Nomura, T. Kamiya, and H. Hosono, "Trap densities in amorphous- InGaZn O4 thin-film transistors," Appl. Phys. Lett., vol. 92, no. 13, pp. 1–4, 2008.

[9] Y. Ueoka, Y. Ishikawa, J. P. Bermundo, H. Yamazaki, S. Urakawa, M. Fujii, M. Horita, and Y. Uraoka, "Density of States in Amorphous In-Ga-Zn-O Thin-Film Transistor under Negative Bias Illumination Stress," ECS J. Solid State Sci.

10TH INTERNATIONAL CONFERENCE ON SUSTAINABLE ENERGY AND ENVIRONMENTAL PROTECTION (JUNE 27TH – 30TH, 2017, BLED, SLOVENIA), MODELLING AND SIMULATION
J. Krope, A.Ghani Olabi, D. Goričanec & S. Božičnik

University of Maribor Press

Optimization-Based Determination of a Building's Instantaneous Base Temperature

MATJAŽ PREK, VINCENC BUTALA & GORAZD KRESE

Abstract The base temperature of a building represents the maximum outside temperature at which no cooling is required to maintain the thermal comfort inside the building. The determination of base temperature represents one of the central problems with the use of cooling degree days since, in addition to the characteristics of the building, it is also dependent on internal and external heat gains, which vary throughout the day.

In this paper, we present an optimization-based approach for determining the instantaneous base temperature of a building. The approach is based on a grey-box modelling technique which considers the effect of solar radiation and air humidity. The free parameters of the model are derived from the data of electricity demand for building cooling and the building site weather data by applying a derivative-free optimization method. The proposed approach is verified on a set of artificially generated data.

Keywords: • base temperature • energy use disaggregation • HVAC • pattern search • grey-box model •

CORRESPONDENCE ADDRESS: Matjaž Prek, Ph.D., Assistant Professor, University of Ljubljana, Faculty of Mechanical Engineering, Aškerčeva cesta 6, 1000 Ljubljana, Slovenia, e-mail: matjaz.prek@fs.uni-lj.si. Vincenc Butala, Ph.D., Professor, University of Ljubljana, Faculty of Mechanical Engineering, Aškerčeva cesta 6, 1000 Ljubljana, Slovenia, e-mail: vincenc.butala@fs.uni-lj.si. Gorazd Krese, Ph.D., Assistant, University of Ljubljana, Faculty of Mechanical Engineering, Aškerčeva cesta 6, 1000 Ljubljana, Slovenia, e-mail: gorazd.krese@fs.uni-lj.si.

https://doi.org/10.18690/978-961-286-058-5.22 ISBN 978-961-286-058-5

Available at: http://press.um.si.

1 Introduction

The key targets of the European Union (EU) 2030 Energy Strategy is to reduce greenhouse gas (GHG) emissions by at least 30% compared to 1990 levels, increase the share of renewable energy sources in final energy consumption to at least 27% and achieve an energy efficiency increase of at least 27%. Improving the energy performance of buildings is the key to achieve these goals, as buildings are responsible for 40 % of energy consumption and 36 % of CO2 emissions in the EU [1], [2]. Although space heating is still the dominant energy demand for buildings in most European countries, special attention should be paid to space cooling, since the energy consumption it accounts for (mostly electric energy) [3], [4] is growing rapidly as a consequence of global warming.

A fundamental influence on the energy efficiency of the building takes place in the planning phase, since poorly thought-out planning leads to mistakes that can be costly or impractical to repair. The effect of an energy efficient air conditioning system is nullified if the building has architectural and construction conditioned high cooling loads [5]. Since in this phase a general estimation is more important than accuracy, simple methods for determining energy use in buildings are more suitable than computer simulations since the latter are computationally demanding, expensive and time-consuming. Among the simple methods for evaluating [6], [7] and analysis [8]–[10], as well as forecasting [11]–[14] of weather related energy consumption in buildings, the cooling degree day (CDD) method stands out, since cooling degree days capture both the extremity and duration of outdoor temperatures.

Cooling degree days are defined as the sum of positive differences between the outdoor air temperature (dry-bulb) and a reference temperature over a certain time period. The reference temperature represents the threshold at which it becomes necessary to cool the building; this is also called the base temperature. The most widely used are the so-called general base temperatures, which are usually defined by the competent institution in individual countries (e.g. UK 15.5°C [15], USA 18.3°C [16]). The base temperature represents the set indoor temperature, lowered due to internal (people, lights, appliances and equipment) and external (through wall structures, fenestration, infiltration) heat gains and, is as such, specific for each building. Its determination represents a central problem, since in addition to thermal characteristics of the building it also depends on solar radiation, humidity and internal heat gains, which vary throughout the day. These effects and their interactions have not yet been resolved in a satisfactory and generally applicable way. Currently the solar radiation assumed by the classic degree day methodology is based on averages, not peak values. One big weakness is also that this method presupposes only a linear dependence between cooling energy consumption and sensible cooling loads and so neglects latent loads, which are, like loads due to solar gains, more distinctive at higher temperatures

In this work, an approach for determining the instantaneous base temperature of a building, based on an optimization-based grey-box modelling procedure taking into account the influence of solar radiation and air humidity, is presented and verified.

2 Methodology

2.1 Model derivation

Our primary objective was to develop a tool, which would enable an easy and reliable determination and analysis of building cooling energy use. Therefore, our main guideline for model derivation was that its use requires minimal information about the building and the installed air-conditioning system or that the required information is easily accessible. Consequently, a grey-box model based on the following assumption has been developed:

- Quadratic dependence between the chiller electricity demand and cooling load.
- The heat losses within the cold distribution systems are negligible.
- The air conditioned rooms of the building are treated as one zone.
- The set indoor temperature is constant.
- All transparent (and opaque) building envelope elements have the same constant thermal and optical characteristics.
- Long-wave radiation heat exchange of the external building surfaces with the atmosphere and the surrounding surfaces is negligible.
- Transmission heat gains through transparent building envelope elements (fenestration) are negligible.
- Air exchange provided solely by mechanical ventilation.
- Infiltration is negligible.
- Mass flow rate of (fresh) outside air is constant.
- Air dehumidification though thermal condensation.
- Thermal condensation dehumidification dew point temperature is constant.
- Internal heat gains are constant and emitted solely by means of convection.

These assumptions resulted in the following expressions for predicting the building electricity demand for cooling:

$$P_{ch}(t) = B_0 + B_1 \cdot \dot{Q}_L(t) + B_2 \cdot \dot{Q}_L{}^2(t) \quad (1)$$

$$\begin{aligned}\dot{Q}_L(t) = &\sum_{i=1}^{N_{st}} A_{st,i} U_{st} \left(\vartheta_o(t-\Delta t) - \vartheta_i\right) + \\ &+ F_{st,sol} \sum_{i=1}^{N_{st}} A_{st,i} G_{glob.i}(t-\Delta t) + \\ &+ F_{st,ak} \left(\vartheta_i - \delta t/\tau \sum_{k=t-\tau}^{t} \vartheta_o(k)\right) + \\ &+ F_{ok,sol} \sum_{i=1}^{N_{ok}} A_{ok,i} G_{glob.i}(t) + \\ &+ \dot{m} c_p \left(\vartheta_o(t) - \vartheta_i\right) + S_{not} + \\ &+ \tfrac{1}{2} \dot{m} r_0 \left(x_o(t) - \bar{x}_{coil} + \left|x_o(t) - \bar{x}_{coil}\right|\right)\end{aligned} \quad (2)$$

where, P_{ch} is the instantaneous electricity demand of the vapour-compression refrigeration system (chiller) serving the building, B_0-B_2 are the regression coefficients of the chiller model, $\dot{Q}_L$ is the instantaneous cooling load of the building, N_{st} is the number of the opaque building envelope elements, $A_{st,i}$ is the area of the i-th opaque building envelope element, U_{st} is the thermal transmittance (U-value) of the opaque building envelope elements, ϑ_o is the outside air temperature, ϑ_i is the indoor air temperature, Δt is the heat gain time lag, $F_{st,sol}$ is the solar gain decrement factor for opaque building envelope elements, $G_{glob,i}$ is the global solar radiation incident on the i-th building envelope element, $F_{st,ak}$ is thermal response factor of the opaque building elements, δt is the data time-step, τ is the thermal response period, $F_{st,ok}$ is the solar gain decrement factor for transparent building envelope elements, N_{ok} is the number of the transparent building envelope elements, $A_{ok,i}$ is the area of the i-th transparent building envelope element, $\dot{m}$ is the mass flow rate of the supplied outside air, c_p is the specific heat capacity of dry air, r_0 is the enthalpy of vaporization of water at 0 °C, x_o is the absolute humidity of outside air, $\bar{x}_{coil}$ is the dehumidification threshold (dew point) absolute humidity, and S_{not} is the internal heat gains surrogate factor.

2.2 Parameter estimation

Problem definition

The presented grey-box model (Equations (1) and (2)) consists of $12+N_{st}+N_{ok}$ parameters. However, the model parameters can only be defined uniquely if the areas of all the building envelope elements are known. In addition to this, we also excluded the regression coefficient B_0 from the parameter estimation procedure, since it represents only the electricity demand of the vapour-compression refrigeration system at minimal cooling power. Thus, the developed grey-box model has the free parameters listed in Table 9.

Table 9. Free parameters of the grey-box model

Parameter	Symbol
w_1	B_1
w_2	B_2
w_3	U_{st}
w_4	$F_{st,ak}$
w_5	$\dot{m}$
w_6	$F_{st,sol}$
w_7	$F_{ok,sol}$
w_8	$\bar{x}_{coil}$
w_9	S_{not}
w_{10}	Δt
w_{11}	τ

The estimation of the parameters represents an optimization problem, since we are searching for a set of values, for which the model prediction error is minimal. For this purpose we defined the following objective function:

$$f_{obj}(\underline{w}) = \sum_{t=t_1}^{t_{N_p}} \left| P_{ch}(t) - \hat{P}_{ch}(t, \underline{w}) \right| \tag{3}$$

$$\underline{w} = (w_1, w_2, \ldots, w_{11}) \in \Re \tag{4}$$

where, f_{obj} is the optimization objective function, $\underline{w}$ is the vector of parameter values, N_p is the number of considered examples (data points), P_{ch} is the actual chiller electricity demand, and $\hat{P}_{ch}$ is chiller electricity demand predicted by the model.

Optimization procedure

To ensure that only physically and technically possible parameter values are considered during the optimization procedure, the solution search space has to limited by constraints. Beside setting lower and upper bounds for each free parameter (Table 10), we also imposed two inequality constraints. The first constraint (Equation (5)), which is a nonlinear inequality constraint, prevents the model from predicting electricity demand values smaller than the regression coefficient B_0. On the other side the second (linear) inequality constraint (Equation (6)) ensures that the (sensible) cooling loads can take only positive values.

Table 10. Lower and upper bounds of the model free parameters

L. bound	Par.	U. bound	Unit	Ref.
-1≤	w_1	≤0	[1]	-
0≤	w_2	≤1	$\left[\frac{1}{kW}\right]$	-
0.15≤	w_3	≤6	$\left[\frac{W}{m^2K}\right]$	[17], [18]
0≤	w_4	$\leq \frac{130Wh/(m^2K)}{60h\cdot 1000} A_{ac}$	$\left[\frac{kW}{K}\right]$	[19]
$\frac{0.24\cdot V_{ac}}{3600\cdot 1000} \leq$	w_5	$\leq \frac{A_{ac}}{5000}$	$\left[\frac{t}{s}\right]$	[20], [21]
0≤	w_6	≤1	[1]	-
0≤	w_7	≤1	[1]	-
0.6≤	w_8	≤2	$\left[\frac{dag}{kg}\right]$	-
0≤	w_9	$\leq 0.1\frac{kW}{m^2}\cdot A_{ac}$	[kW]	[22]
0≤	w_{10}	≤24	[h]	[23]
0≤	w_{11}	≤144	[h]	[24]

$$
\begin{aligned}
0 < w_1 + w_2 \Big\{ & \sum_{i=1}^{N_{st}} A_{st,i} w_3 \left(\vartheta_o\left(t - w_{10}\right) - \vartheta_i\right) + \\
& + w_6 \sum_{i=1}^{N_{st}} A_{st,i} G_{glob.i}\left(t - w_{10}\right) + \\
& + w_4 \left(\vartheta_i - \delta t / w_{11} \sum_{k=t-w_{11}}^{t} \vartheta_o(k)\right) + \\
& + w_7 \sum_{i=1}^{N_{ok}} A_{ok,i} G_{glob.i}\left(t\right) + \\
& + w_5 c_p \left(\vartheta_o\left(t\right) - \vartheta_i\right) + w_9 \Big\}
\end{aligned}
\tag{5}
$$

$$
\begin{aligned}
0 < & \sum_{i=1}^{N_{st}} A_{st,i} w_3 \left(\vartheta_o\left(t - w_{10}\right) - \vartheta_i\right) + \\
& + w_6 \sum_{i=1}^{N_{st}} A_{st,i} G_{glob.i}\left(t - w_{10}\right) + \\
& + w_4 \left(\vartheta_i - \delta t / w_{11} \sum_{k=t-w_{11}}^{t} \vartheta_o(k)\right) + \\
& + w_7 \sum_{i=1}^{N_{ok}} A_{ok,i} G_{glob.i}\left(t\right) + \\
& + w_5 c_p \left(\vartheta_o\left(t\right) - \vartheta_i\right) + w_9
\end{aligned}
\tag{6}
$$

where, A_{ac} is the air-conditioned area of the building, and V_{ac} is the air-conditioned volume of the building.
Because the two time parameters (w_{10}, w_{11}) directly affect the values of the model input variables, their values can only be identified outside the optimization procedure by testing all the possible combinations of the latter

Since our objective function (Equation (3)) is discontinuous, due to the inclusion of latent loads, we could not apply gradient methods to search the solution space. Therefore we opted for the so-called pattern search algorithm [25], which is, like the more prominent genetic algorithms [26], a derivate-free optimization method. At every iteration of the algorithm a discrete mesh, centred at the current incumbent point, is defined. Each iteration consists of two basic steps (Figure 23). During the search step the objective function is evaluated at some finite number of points on the mesh. If the best point found overall is an improvement on the current incumbent point, it becomes the new incumbent; otherwise, the algorithm proceeds to the poll step. The poll step consists of evaluating the objective function at all the points that are immediate neighbours of the incumbent point on the mesh. If the best point found overall by polling is an improvement, it becomes the new incumbent and the mesh resolution step Δ^m is increased for the next iteration, otherwise Δ^m is reduced. The algorithm is considered converged once the Δ^m is shrunk beyond some minimum threshold [27].

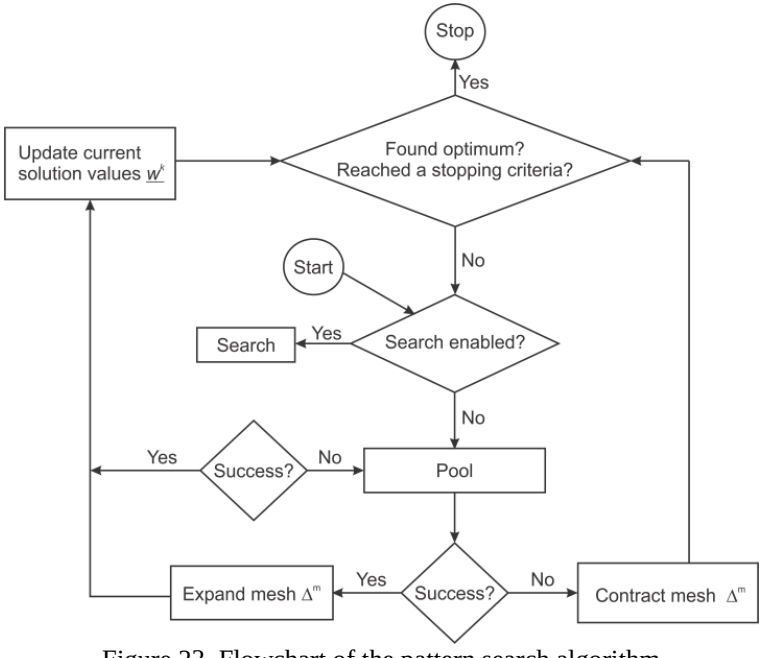

Figure 23. Flowchart of the pattern search algorithm

Base temperature determination

As the base temperature is generally not a measurable variable, it can be determined only indirectly. In our case, we derived the model for predicting the base temperature from the developed grey-box model for predicting the building space cooling electricity demand (Equations (1) and (2)):

$$\dot{Q}_L(t) = 0 \tag{7}$$

$$\begin{aligned}\vartheta_b(t) = \frac{1}{\dot{m}c_p - F_{st,ak}\delta t/\tau}\Big\{&\vartheta_i\left(\dot{m}c_p - F_{st,ak}\right)+\\ &+F_{st,ak}\delta t/\tau\sum_{k=t-\tau}^{t-1}\vartheta_o(k)+\\ &-\sum_{i=1}^{N_{st}}A_{st,i}U_{st}\left(\vartheta_o\left(t-\Delta t\right)-\vartheta_i\right)+\\ &-F_{st,sol}\sum_{i=1}^{N_{st}}A_{st,i}G_{glob.i}\left(t-\Delta t\right)+\\ &-F_{ok,sol}\sum_{i=1}^{N_{ok}}A_{ok,i}G_{glob.i}\left(t\right)-S_{not}+\\ &-\tfrac{1}{2}\dot{m}r_0\left(x_o\left(t\right)-\overline{x}_{coil}+\left|x_o\left(t\right)-\overline{x}_{coil}\right|\right)\Big\}\end{aligned} \tag{8}$$

where, ϑ_b is the instantaneous base temperature of a building.

The algorithm for determining the base temperature of a building is illustrated in Figure 2**Napaka! Vira sklicevanja ni bilo mogoče najti.**. The execution of the algorithm generally requires the use of three sets of data, i.e. the training, the validation and the test dataset. The training set is used by the optimization algorithm to estimate the free parameters of the model (Table 10). The validation dataset serves to verify the adequacy of the parameter values obtained during the optimisation procedure (Equation (9)). At the end the test dataset is applied to assess the performance of the prediction model. We also included a data aggregation function in the base temperature determination algorithm, and introduced the so-called aggregate time *H*, with the intention to establish the maximum admissible time interval, for which a constant base temperature value can be assumed.

$$f_{obj}^{val}(\underline{w}) = 1/N_{p,i}\sum_{t=t_1}^{t_{N_{p,i}}}\left|P_{ch}\left(t\right)-\hat{P}_{ch}\left(t,\underline{w}\right)\right| \tag{9}$$

where, f_{obj}^{val} is the objective function for determining the best parameter values set on the validation dataset, and $N_{p,i}$ is the number of data points in the dataset obtained during the *i*-th aggregation.

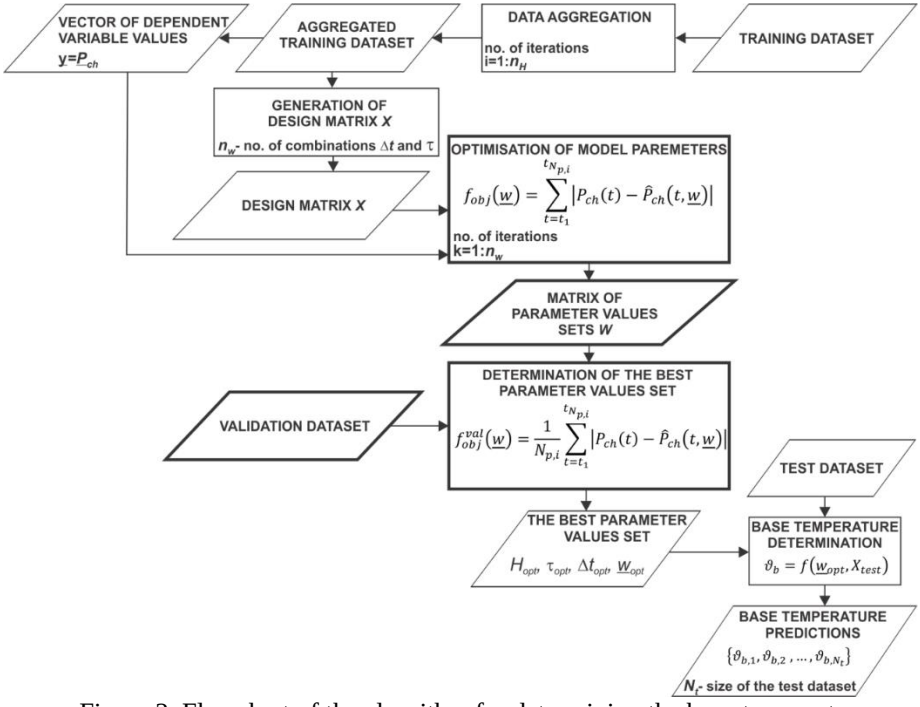

Figure 2. Flowchart of the algorithm for determining the base temperature

3 Varification

The developed grey-box model can only be verified on a set of data, for which we in advance know all the relations between the dependent and independent variables, as well as their values. Since the base temperature of a building cannot be measured, our only option was to use artificially generated data. For this purpose, we have selected EnergyPlus [28], which is an established approach for verifying black-box and grey-box building thermal response models. In order to determine the smallest possible prediction error of the developed model, we designed a simple single-zone building, served by a CAV HVAC system with a fixed air change rate (Table 11).

The training, validation and test datasets were generated using the weather data gathered between 2012 and 2015 at the weather station Ljubljana-Bežigrad, whereby only the data between May 1st and September 30th was considered. In order to obtain the reference (i.e. artificially generated) base temperature values the outside temperature at each considered time step (1 hour) was manipulated individually until the instantaneous cooling loads dropped to zero.

Table 11. Description of the simulated building

Location	Ljubljana
Operating time	0^{00}-23^{59}
Number of user (activity)	18 (0.9 met)
Appliances density [W/m^2]	30
Area conditioned [m^2]	88.62
Volume conditioned [m^3]	310.18
Area of opaque surfaces [m^2]	220.42
Area of windows [m^2]	24.5
Glazing ratio [1]	0.1
U-value of walls [W/m^2/K]	0.372
U-value of roof [W/m^2/K]	0.25
U-value of windows [W/m^2/K]	1.96
G-value of windows [1]	0.691
Shading	no
Number of zones	1
HVAC system	CAV
Set point temperature [°C]	24
Humidity control	no
Heat recovery	mix. chamber
Chiller - type	water cooled
Chiller – capacity [kW]	18
Chiller – COP [1]	5.5

Three out of eleven estimated grey-box model parameters (Table 12) can be compared directly to the EnergyPlus simulation parameters. Namely, the wall *U*-value (w_3), the outdoor air intake rate (w_5) and the internal heat gains (w_9). While there is a good agreement between the reference and the estimated value of the wall *U*-value and the internal gains (i.e. deviation from the reference value 4.4 % and 13 % respectively), the outdoor air intake is underestimated by 34 %. The reason for such deviation lies in the simplifications of the developed grey-box model as well as in the optimization algorithm used to determine the model parameters (no guarantee of convergence to the globally optimal solution). Nevertheless, such deviations do not say much about the quality of the model, since its primary purpose is to predict the base temperature of a building. Therefore, a comparison between the predicted and actual values of the latter is more appropriate and informative.

Table 12. Estimated parameter values for the simulated building

Par.	Unit	Optimisation	EnergyPlus
H	[h]	19	-
w_1	[1]	-0.0122	-
w_2	$\left[\frac{1}{kW}\right]$	0.0114	-
w_3	$\left[\frac{W}{m^2K}\right]$	0.388	0.372
w_4	$\left[\frac{kW}{K}\right]$	0.005	-
w_5	$\left[\frac{kg}{s}\right]$	0.30	0.45
w_6	[1]	0.0001	-
w_7	[1]	0.0969	-
w_8	$\left[\frac{g}{kg}\right]$	8.1	-
w_9	[kW]	4.2866	3.7918
w_{10}	[h]	0	-
w_{11}	[h]	95	-

As can be seen in Figure 24, there is a fair agreement between the predicted and reference base temperature values. Figure 25 also reveals that the prediction error (Equation (10)) is approximately normally disturbed. The relative error for the majority of the data points of the test set lies in the interval between -10 and 10 %. This is, given the simplicity and the purpose of the proposed model, an acceptable outcome.

$$err_{rel} = \frac{\hat{\vartheta}_b - \vartheta_b}{\vartheta_b} \cdot 100\% \tag{10}$$

where, err_{rel} is the relative prediction error, $\hat{\vartheta}_b$ is the predicted value of the base temperature, and ϑ_b is the reference value of the base temperature.

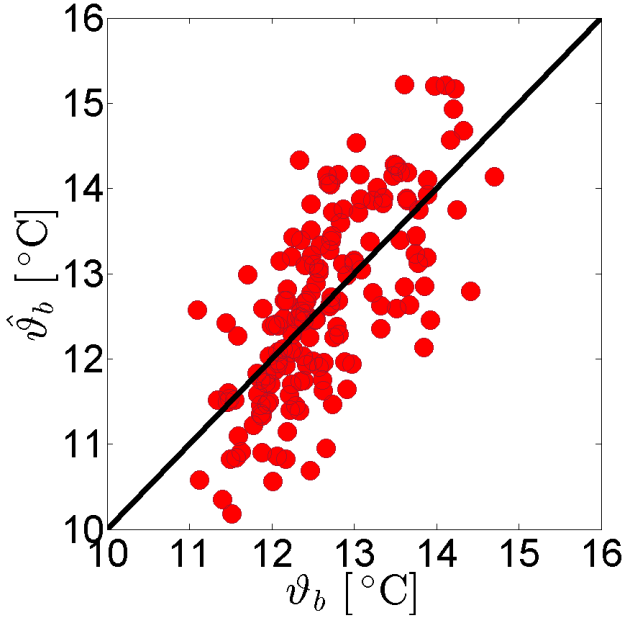

Figure 24. Comparison between the predicted and reference base temperature values on the test dataset

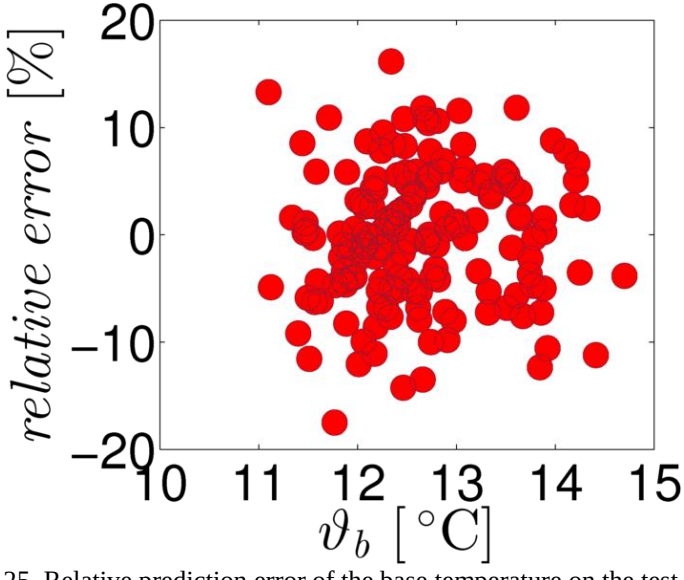

Figure 25. Relative prediction error of the base temperature on the test dataset

4 Conclusions

In this work, we presented and verified an approach for determining the instantaneous base temperature of a building, based on a grey-box modelling technique. The proposed grey-box model considers both the effect of solar radiation and air humidity on the building energy demand for space cooling. The free parameters of the model were estimated by using a derivate-free optimisation method, namely pattern search. To ensure that only physically and technically possible parameter values were considered during the optimization procedure, we limited the solution search space by defining restrictions on the values of individual parameters as well as on their interactions.

The developed model was verified on data generated by the whole building energy simulation program EnergyPlus. The model performed satisfactory and achieved good prediction accuracy on data points not present in the training dataset. Nevertheless, further testing, preferably on data from real systems of higher complexity, is required before final conclusions can be made.

References

[1] European Commision, "Directive 2002/91/EC of the European Parliament and of the Council of 16 December 2002 on the energy performance of buildings," *Off. J. Eur. Union*, pp. 65–71, 2002.

[2] EU, "Directive 2010/31/EU of the European Parliament and of the Council of 19 May 2010 on the energy performance of buildings (recast)," *Off. J. Eur. Union*, pp. 13–35, 2010.

[3] J. Mandelj, G. Krese, M. Prek, and V. Butala, "Impact of HVAC Systems on Building Peak Electricity Load," in *Proceedings of Clima 2013 - 11th REHVA World Congress & the 8th International Conference on IAQVEC*, 2013, p. 9.

[4] G. Krese, J. Mandelj, M. Prek, and V. Butala, "Energy Efficiency Assessment of Existing Buildings Based on Measurements of HVAC Systems Electric Energy Consumption: A Case Study," in *Proceedings of Clima 2013 - 11th REHVA World Congress & the 8th International Conference on IAQVEC*, 2013, p. 8.

[5] G. Krese, J. Mandelj, M. Prek, and V. Butala, "Influence of Building Envelope on the Sensitivity of HVAC System Energy Consumption," in *Proceedings of Clima 2013 - 11th REHVA World Congress & the 8th International Conference on IAQVEC*, 2013, p. 9.

[6] M. Sivak, "Potential energy demand for cooling in the 50 largest metropolitan areas of the world: Implications for developing countries," *Energy Policy*, vol. 37, no. 4, pp. 1382–1384, 2009.

[7] A. Durmayaz, M. Kadıoğlu, and Z. Şen, "An application of the degree-hours method to estimate the residential heating energy requirement and fuel consumption in Istanbul," *Energy*, vol. 25, no. 12, pp. 1245–1256, 2000.

[8] M. Christenson, H. Manz, and D. Gyalistras, "Climate warming impact on degree-days and building energy demand in Switzerland," *Energy Convers. Manag.*, vol. 47, no. 6, pp. 671–686, 2006.

[9] M. Isaac and D. P. van Vuuren, "Modeling global residential sector energy demand for heating and air conditioning in the context of climate change," *Energy Policy*, vol. 37, no. 2, pp. 507–521, 2009.

[10] M. Olonscheck, A. Holsten, and J. P. Kropp, "Heating and cooling energy demand and

related emissions of the German residential building stock under climate change," *Energy Policy*, vol. 39, no. 9, pp. 4795–4806, 2011.

[11] B. E. Psiloglou, C. Giannakopoulos, S. Majithia, and M. Petrakis, "Factors affecting electricity demand in Athens, Greece and London, UK: A comparative assessment," *Energy*, vol. 34, no. 11, pp. 1855–1863, 2009.

[12] M. Hart and R. de Dear, "Weather sensitivity in household appliance energy end-use," *Energy Build.*, vol. 36, no. 2, pp. 161–174, 2004.

[13] E. A. Mohareb, C. A. Kennedy, L. D. D. Harvey, and K. D. Pressnail, "Decoupling of building energy use and climate," 2011.

[14] D. Sailor, "Sensitivity of electricity and natural gas consumption to climate in the U.S.A.—Methodology and results for eight states," *Energy*, vol. 22, no. 10, pp. 987–998, Oct. 1997.

[15] CIBSE, *Degree-Days - Theory and Application - TM41 : 2006*. London: Chartered Institution of Building Services Engineers, 2006.

[16] ASHRAE, *ASHRAE 2013 Handbook – Fundamentals (SI Edition)*., 2013th ed. Atlanta: American Society of Heating, Refrigerating and Air-Conditioning Engineers, 2013.

[17] C. Pöhn, *Bauphysik - Erweiterung 1 Energieeinsparung und Wärmeschutz Energieausweis - Gesamtenergieeffizienz*, 1st ed. Vienna: Springer Vienna, 2007.

[18] J. Kurnitski, *Cost optimal and nearly zero-energy buildings (nZEB) : definitions, calculation principles and case studies*, 1st ed. London: Springer-Verlag London, 2013.

[19] Deutsches Institut für Normung, "DIN V 18599-2:2007-02 - Energetische Bewertung von Gebäuden - Berechnung des Nutz-, End- und Primärenergiebedarfs für Heizung, Kühlung, Lüftung, Trinkwarmwasser und Beleuchtung - Teil 2: Nutzenergiebedarf für Heizen und Kühlen von Gebäudezonen." Deutsches Institut für Normung, Berlin, p. 110, 2007.

[20] H. Recknagel, E.-R. Schramek, and E. Sprenger, *Taschenbuch für Heizung + Klimatechnik 09/10*, 74th ed. München: Deutscher Industrieverlag, 2008.

[21] U. Eicker, *Low energy cooling for sustainable buildings*, 1st ed. Chichester: Wiley, 2009.

[22] Chartered Institution of Building Services Engineers., *CIBSE Guide A – Environmental Design*, 7th ed. London: Chartered Institute of Building Services Engineers, 2006.

[23] K. Fitzner, *Raumklimatechnik Band 4: Physik des Gebäudes*, 16th ed. Berlin: Springer-Verlag Berlin Heidelberg, 2013.

[24] International Organization for Standardization, "ISO 13790:2008 - Energy performance of buildings -- Calculation of energy use for space heating and cooling." International Organization for Standardization, Geneva, p. 2, 2008.

[25] A. R. Conn, K. Scheinberg, and L. N. Vicente, *Introduction to derivative-free optimization*, 1st ed. Philadelphia: Society for Industrial and Applied Mathematics/Mathematical Programming Society, 2009.

[26] D. E. Goldberg, *Genetic algorithms in search, optimization, and machine learning*, 1st ed. Boston: Addison-Wesley Longman Publishing Co., Inc., 1989.

[27] L. M. Rios and N. V. Sahinidis, "Derivative-free optimization: a review of algorithms and comparison of software implementations," *J. Glob. Optim.*, vol. 56, no. 3, pp. 1247–1293, Jul. 2013.

[28] D. B. Crawley, L. K. Lawrie, F. C. Winkelmann, W. F. Buhl, Y. J. Huang, C. O. Pedersen, R. K. Strand, R. J. Liesen, D. E. Fisher, M. J. Witte, and J. Glazer, "EnergyPlus: creating a new-generation building energy simulation program," *Energy Build.*, vol. 33, no. 4, pp. 319–331, 2001.


METTLER TOLEDO
PRINSIS
energetika ljubljana